日中笹川医学奨学金制度＜学位取得コース＞評価書

課程博士：指導教官用

第44期　研究者番号：G4409　作成日　：2024年3月7日

氏　名	馬 快	MA KUAI	性別	F	生年月日　1993/08/25

所属機関（役職）	大阪大学大学院医学系研究科（大学院生）	
研究先（指導教官）	大阪大学大学院医学系研究科腎臓内科学（猪阪　善隆　教授） 国立成育医療研究センター研究所 RI 管理室/移植免疫研究室（李　小康　室長）	
研究テーマ	腎移植における腎臓線維化発生機序の解明と新規治療法の開発に関する研究 Elucidation of the mechanism and development of new therapeutic methods for renal fibrosis after kidney transplantation	
専攻種別	□論文博士	☑課程博士

研究者評価（指導教官記入欄）

成績状況	優 学業成績係数=95	取得単位数 30／30
学生本人が行った研究の概要	腎臓の線維化は、ほとんどの慢性腎臓病の特徴である。腎線維化の動物モデルでは、マウスの左尿管を結紮する一側尿管閉塞（UUO）より確立され、広く基礎研究に使用されている。一方、5-アミノレブリン酸（5-ALA）は、ヘムやプロトポルフィリン IX（PpIX）の重要な前駆体である。我々これまでの研究で、ヘムオキシゲナーゼ（HO）-1 の発現が 5-ALA とクエン酸第一鉄（SFC）により増強されることを明らかにした。本研究では、UUO によって誘発されたマウスの腎線維化および炎症に対する 5-ALA および SFC の保護効果を検証した。	
総合評価	【良かった点】 腎線維化のマウスモデルを確立することができた。評価項目として、病理学、血清学と関連遺伝子の mRNA とタンパク質発現の実験系も併せて確立した。また、5-ALA および SFC マウスへ投与の実験で、その効果が示した。 【改善すべき点】 5-ALA および SFC を用いたマウスへ投与後の効果の作用機序がまだ不明な点があるため、引き続き、検証する必要がある。 【今後の展望】 上記腎線維化のマウスモデルを用いて、5-ALA および SFC の投与での治療評価及びその作用機序を解明することで、将来臨床への応用に目指したい。	
学位取得見込	学位取得見込み	

評価者（李　小康）

日中笹川医学奨学金制度＜学位取得コース＞報告書
研究者用

Supported by 日本財団 THE NIPPON FOUNDATION

第44期　　研究者番号：　G4409　　作成日：2024年3月7日

氏名	马 快	MA KUAI	性別	F	生年月日　1993/08/25
所属機関(役職)	大阪大学大学院医学系研究科（大学院生）				
研究先（指導教官）	大阪大学大学院医学系研究科腎臓内科学（猪阪 善隆　教授） 国立成育医療研究センター研究所RI管理室/移植免疫研究室（李 小康　室長）				
研究テーマ	腎移植における腎臓線維化発生機序の解明と新規治療法の開発に関する研究 Elucidation of the mechanism and development of new therapeutic methods for renal fibrosis after kidney transplantation				
専攻種別	論文博士	□	課程博士	☑	

1）目的（Goal）

Renal fibrosis is the hallmark of most progressive kidney diseases. Unilateral ureteral obstruction (UUO), the ligation of the ureter, most commonly the left ureter, has been widely used to establish animal models of renal fibrosis [1]. 5-aminoacetylacrylic acid (5-ALA), a key precursor of heme and protoporphyrin IX (PpIX), is catalyzed in animal cells by mitochondrial aminoacetylacrylic synthetase using glycine and succinyl-coA [2]. Previous studies demonstrated that heme oxygenase (HO)-1 expression was up-regulated by 5-ALA and sodium ferrous citrate (SFC) [2-5]. HO-1 is known to be a rate determining enzyme in heme metabolism that produces bilirubin and carbon monoxide, which were demonstrated to act as anti-inflammatory factors. The present study aimed to investigate the protective effect of 5-ALA and SFC against UUO-induced renal fibrosis and inflammation in mice.

2）戦略（Approach）

In present study, we used 5-ALA and SFC to treat UUO-induced renal fibrosis and inflammation. For that purpose, mice were randomly divided into five treatment groups: Naive group, 7d UUO model group, 7d UUO + 5ALA/SFC group, 14d UUO model group, 14d UUO + 5ALA/SFC group. 5ALA/SFC was administered to the mice for 7 or 14 days following UUO. At the sampling days, blood and kidney tissue samples were collected for evaluation. Renal tissue was harvested and fixed in 10% formalin or optimal cutting temperature compound for histological examination. For the biochemical and molecular expression assessments, kidney tissues were immediately frozen and stored at 80° C until analysis.

3)材料と方法（Materials and methods）

(1) Animals and unilateral ureteral obstruction model

Specific-pathogen-free inbred male C57BL/6J (B6/J; H-2kb) mice, 8-10 weeks old, were purchased from Japan SLC, Inc. (Shizuoka, Japan). All mice received humane care in accordance with the guidelines of the Animal Use and Care Committee of the National Research Institute for Child Health and Development, Tokyo, Japan (Permission number: A2009-010-C14). All mouse experiments conformed to the National Institutes of Health guidelines for the care and use of laboratory animals. The UUO model was estimated as follows. The abdominal cavity of mice was opened through the left abdominal incision. The left ureter of mice was bluntly separated and double-ligated with 4-0 sutures in the middle and upper 1/3, and the abdominal cavity was closed by layered suture.

(2) Reagents

5-ALA hydrochloride (SBI Pharmaceuticals Co., Ltd., Tokyo, Japan) and SFC (Fe2+) (Eisai Food & Chemical Co., Ltd., Tokyo, Japan) were dissolved in distilled water (DW) at a molar ratio of 5-ALA:SFC of 1:0.5. SFC was diluted in 100mg/kg 5-ALA solution immediately prior to administration.

(3) Treatment protocol

All mice were given adaptive feeding for one week and randomly divided into four groups: Naive group, UUO (7d) group, UUO + 5-ALA/SFC (7d) group, UUO (14d) group and UUO + 5-ALA/SFC (14d) group. 5-ALA/SFC was administered via daily gavage at a dose of 100 mg/kg for 7 and 14 days, respectively. Afterwards, blood, spleen and renal tissues were collected for subsequent experiments on day7 and day14.

(4) Serum biochemical analyses

Serum was collected from whole-blood samples after standing for 30 minutes at 37 ° C and centrifuged at 3000 g for 20 minutes at 4 ° C. The samples were then measured for the blood urea nitrogen (BUN) and serum creatinine (Cr) concentrations with a commercially available kit (Fujifilm, Tokyo, Japan) and an automatic biochemical analyzer (DRI-CHEM 3500i; Fujifilm) according to the manufacturer’s instructions.

(5) Histology and histopathological analyses

Renal 5-μ m-thick sections were prepared and subjected to staining with hematoxylin and eosin (HE) (Muto Pure Chemicals, Tokyo, Japan) for morphological analyses. Slides were then examined by light microscopy (OLYMPUS, Tokyo, Japan).

(6)Masson’s trichrome staining, Sirius red staining

The degree of renal tissue injury was evaluated by Masson’s trichrome staining. The kidney tissues were fixed in 4% paraformaldehyde, embedded in paraffin, and sliced into 4-μ m paraffin sections. Then, sections were treated in xylene, dehydrated with graded ethanol, and stained with Masson (Sigma-Aldrich; Merck KGaA). After staining, the sections were dehydrated with 70 and 90% ethanol. Slides observed with an optical microscope (Olympus, Tokyo, Japan). Histological results were quantified using the WinRoof 7.4 software program (Mitani Corporation, Tokyo, Japan).

1．研究概要(2)(7) Immunohistochemical analysis

(8) RNA purification and quantitative RT-PCR

(9) Western blotting

(10) Statistical analyses

4)実験結果(Results)

(1) 5-ALA/SFC reduced UUO-induced renal dysfunction and tubulointerstitial injury

To determine whether 5-ALA/SFC treatment improves the outcome in acute kidney injury (AKI) and subsequent renal fibrosis, we set up a rodent model of unilateral ureteral obstruction (UUO). Mice were treated with 5-ALA/SFC or acted as controls on day 7 and 14 (Fig. 1A). Blood samples were measured for the blood urea nitrogen (BUN) and serum creatinine (Cr) concentrations with a commercially available kit (Fujifilm, Tokyo, Japan) and an automatic biochemical analyzer (DRI-CHEM 3500i; Fujifilm) according to the manufacturer' s instructions.Compared with naive group, serum BUN in UUO model group on day7 and day14 increased significantly ($p<0.001$ and $p<0.0001$, respectively). 5-ALA/SFC treatment decreased the levels of BUN on day7 and day14 ($p<0.01$and $p<0.0001$, respectively). The levels of Cr also down-regulated markedly by 5-ALA/SFC administration on day14 ($p<0.05$) but had no significant differences on day7 (Fig. 1B). Kidneys of the UUO side and naive group were harvested for histopathology on day 7 and day 14. Hematoxylin and eosin (H&E) staining showed that 5-ALA/SFC attenuated tubular atrophy, tubular dilatation and inflammatory cell infiltration.

(2)5-ALA/SFC exerted protective effects against inflammation

Renal mRNA expression of inflammatory cytokine-related genes, particularly tumor necrosis factor-alpha (TNF-α), inducible nitric oxide synthase (iNOS), interferon-gamma (IFN-γ), interleukin-1 beta (IL)-1β, IL-17, C-C motif chemokine ligand 2 (CCL2), CCL5, CD11c and C-C chemokine receptor type 2 (CCR2), were significantly higher in UUO group on day7 and day14. In contrast, the expression of TNF-α, IL-1β, CCL2, CCL5, IL-17, iNOS and CCR2 was lower in the 7d_A/S group than in the 7d_control group ($p<0.01$, $p<0.05$ and $p <0.01$, respectively). The IFN-γ expression was down-regulated as well but without a significant difference. After the administration of 5-ALA/SFC for 7 days, TNF-α and IL-1β showed notable reductions in expression ($p<0.01$ and $p<0.01$, respectively). The infiltration of neutrophils in liver was assessed using chloroacetate esterase staining of liver specimens.

(3)5-ALA/SFC exerted anti-apoptotic effects.

The mRNA expression of apoptosis-related molecules, particularly Bcl-2-associated X (Bax), caspase-1, caspase-3 and NF-κB, was markedly up-regulated in the 7d_control group compared with Naïve group ($p<0.05$, $p<0.0001$, $p<0.001$ and $p<0.0001$, respectively). The mRNA expression of Bax, caspase-1, caspase-3, caspase-9 and NF-κB showed a significant decrease ($p<0.05$) in the 7d_A/S group on day7 but had no significant differences on day14. Furthermore, the mRNA expression of Bcl-2 in the 7d_A/S group was markedly up-regulated on day7($p<0.05$).

To confirm the anti-apoptosis effect of 5-ALA/SFC, we measured the protein levels of Bax and NF-κB in renal tissues in the Naïve group, 14d_control group and 14d_A/S group by Western blotting. After a densitometric analysis of the signals, we found that the expression of Bax and NF-κB was significantly reduced by the treatment of 5-ALA/SFC ($p<0.05$ and $p<0.05$, respectively).

(4)5-ALA/SFC mitigated UUO-induced tubulointerstitial fibrosis

Picro-Sirius red staining and Masson's trichrome (MT) staining showed markedly decreased tubulointerstitial fibrosis in the 5-ALA/SFC treated group on day 7 and day 14.We then performed IHC staining to evaluate kidney fibrosis. Tubules were surrounded by expanded interstitium with abundant interstitial collagen I and α-SMA. 5-ALA/SFC treatment suppressed tubulointerstitial fibrosis on day 7 and day 14 dramatically.

RT-PCR revealed that 5-ALA/SFC significantly reduced mRNA expression of PDGF, TIMP-1, TIMP-2, Col1α1, Col5α3, MMP9 and α-SMA. To confirm the anti-fibrosis effect of 5-ALA/SFC, we measured the protein levels of TGF-β, Col1α1 and α-SMA in renal tissues in the Naïve group, 14d_control group and 14d_A/S group by Western blotting. After a densitometric analysis of the signals, we found that the expression of TGF-β, Col1α1 and α-SMA was significantly reduced by the treatment of 5-ALA/SFC ($p<0.01$, $p<0.01$ and $p<0.001$, respectively).

(5)5-ALA/SFC promotes renal proliferation through activation of the ERK signaling pathway

To further characterize 5-ALA/SFC-induced renal proliferation, we analyzed the expression and activation of p44 ERK1 and p42 ERK2. This analysis revealed that 5-ALA/SFC significantly increased the levels of phosphorylated (activated) ERK1/2 on day 14.

5)考察(Discussion)

5-ALA/SFC is a very promising treatment of renal diseases and the rational use of it will solve many problems clinically.

6)参考文献(References)

1 Bai Y, Wang W, Yin P, Gao J, Na L, Sun Y, Wang Z, Zhang Z, Zhao C. Ruxolitinib Alleviates Renal Interstitial Fibrosis in UUO Mice. INT J BIOL SCI 2020 2020-01-20; 16(2): 194-203.

2 Fujino M, Nishio Y, Ito H, Tanaka T, Li XK. 5-Aminolevulinic acid regulates the inflammatory response and alloimmune reaction. INT IMMUNOPHARMACOL 2016 2016-08-01; 37: 71-78.

3 Liu C, Zhu P, Fujino M, Zhu S, Ito H, Takahashi K, Nakajima M, Tanaka T, Zhuang J, Li XK. 5-ALA/SFC Attenuated Binge Alcohol-Induced Gut Leakiness and Inflammatory Liver Disease in HIV Transgenic Rats. ALCOHOL CLIN EXP RES 2019 2019-08-01; 43(8): 1651-1661.

4 Hu X, Que W, Hirano H, Wang Z, Nozawa N, Ishii T, Ishizuka M, Ito H, Takahashi K, Nakajima M, Tanaka T, Zhu P, Guo WZ, Li XK. 5-Aminolevulinic acid/sodium ferrous citrate enhanced the antitumor effects of programmed cell death-ligand 1 blockade by regulation of exhausted T cell metabolism in a melanoma model. CANCER SCI 2021 2021-07-01; 112(7): 2652-2663.

5 Negoro H, Chatziantonio C, Razzaque MS. Therapeutic potential of 5-aminolevulinic acid and sodiumferrous citrate for viral insults: relevance to the COVID-19 crisis. EXPERT REV ANTI-INFE 2022 2022-05-01; 20(5): 657-661.

2. 執筆論文 Publication of thesis ※記載した論文を添付してください。Attach all of the papers listed below.

論文名 1 Title	Combinations of anti-GITR antibody and CD28 superagonist ameliorated dextran sodium sulfate-induced mouse colitis.				
掲載誌名 Published journal	Clin Exp Immunol				
	2022 年 6 月	208(3) 巻(号)	340 頁 ～ 350 頁	言語 Language	English
第1著者名 First author	Kuai Ma	第2著者名 Second author	Weitao Que	第3著者名 Third author	Xin Hu
その他著者名 Other authors	Wen-Zhi Guo, Liang Zhong, Daisuke Ueda, Er-Li Gu, Xiao-Kang Li				
論文名 2 Title	A Mesenchymal-Epithelial Transition Factor-Agonistic Antibody Accelerates Cirrhotic Liver Regeneration and Improves Mouse Survival Following Partial Hepatectomy				
掲載誌名 Published journal	Liver Transpl.				
	2022 年 5 月	28(5) 巻(号)	782 頁 ～ 793 頁	言語 Language	English
第1著者名 First author	Kuai Ma	第2著者名 Second author	Weitao Que	第3著者名 Third author	Xin Hu
その他著者名 Other authors	Wen-Zhi Guo, Er-Li Gu, Liang Zhong, Virginia Morello, Manuela Cazzanti, Paolo Michieli, Terumi Takahara, Xiao-Kang Li				
論文名 3 Title	Combinations of anti-GITR antibody and CD28 superagonist induce permanent allograft acceptance by generating type 1 regulatory T cells.				
掲載誌名 Published journal	Sci Adv.				
	2022 年 8 月	3(31)eabo4413 巻(号)	頁 ～ 頁	言語 Language	English
第1著者名 First author	Weitao Que	第2著者名 Second author	Kuai Ma	第3著者名 Third author	Xin Hu
その他著者名 Other authors	Wen-Zhi Guo, Xiao-Kang Li				
論文名 4 Title	Coral calcium carried hydrogen ameliorates the severity of non-alcoholic steatohepatitis induced by a choline deficient high carbohydrate fat-free diet in elderly rats.				
掲載誌名 Published journal	Sci Rep.				
	2023 年 6 月	13(1):11646. 巻(号)	頁 ～ 頁	言語 Language	English
第1著者名 First author	Kuai Ma	第2著者名 Second author	Xin Hu	第3著者名 Third author	Keiki Nambu
その他著者名 Other authors	Daisuke Ueda, Naotsugu Ichimaru, Masayuki Fujino, Xiao-Kang Li				
論文名 5 Title					
掲載誌名 Published journal					
	年 月	巻(号)	頁 ～ 頁	言語 Language	
第1著者名 First author		第2著者名 Second author		第3著者名 Third author	
その他著者名 Other authors					

3. 学会発表 Conference presentation ※筆頭演者として総会・国際学会を含む主な学会で発表したものを記載してください

※Describe your presentation as the principal presenter in major academic meetings including general meetings or international meeting

学会名 Conference	第58回日本移植学会総会		
演　題 Topic	Combinations of anti-GITR antibody and CD28 superagonist generated type 1 regulatory T cells		
開催日 date	2022 年 10 月 14 日	開催地 venue	名古屋
形式 method	☑ 口頭発表 Oral □ ポスター発表 Poster	言語 Language	□ 日本語 ☑ 英語 □ 中国語
共同演者名 Co-presenter	Weitao Que, Xin Hu, Xiao-Kang Li		
学会名 Conference			
演　題 Topic			
開催日 date	年 月 日	開催地 venue	
形式 method	□ 口頭発表 Oral □ ポスター発表 Poster	言語 Language	□ 日本語 □ 英語 □ 中国語
共同演者名 Co-presenter			
学会名 Conference			
演　題 Topic			
開催日 date	年 月 日	開催地 venue	
形式 method	□ 口頭発表 Oral □ ポスター発表 Poster	言語 Language	□ 日本語 □ 英語 □ 中国語
共同演者名 Co-presenter			
学会名 Conference			
演　題 Topic			
開催日 date	年 月 日	開催地 venue	
形式 method	□ 口頭発表 Oral □ ポスター発表 Poster	言語 Language	□ 日本語 □ 英語 □ 中国語
共同演者名 Co-presenter			

4. 受賞（研究業績） Award (Research achievement)

名　称 Award name				
	国名 Country		受賞年 Year of award	年 月
名　称 Award name				
	国名 Country		受賞年 Year of award	年 月

5. 本研究テーマに関わる他の研究助成金受給 Other research grants concerned with your resarch theme

受給実績 Receipt record	□ 有　■ 無
助成機関名称 Funding agency	
助成金名称 Grant name	
受給期間 Supported period	年　月 ～　年　月
受給額 Amount received	円
受給実績 Receipt record	□ 有　■ 無
助成機関名称 Funding agency	
助成金名称 Grant name	
受給期間 Supported period	年　月 ～　年　月
受給額 Amount received	円

6. 他の奨学金受給 Another awarded scholarship

受給実績 Receipt record	■ 有　□ 無
助成機関名称 Funding agency	中国国家留学基金管理委員会
奨学金名称 Scholarship name	国家建設高水平大学公派研究生項目
受給期間 Supported period	2020 年 12 月 ～ 2024 年 12 月
受給額 Amount received	8,160,000 円

7. 研究活動に関する報道発表 Press release concerned with your research activities

※記載した記事を添付してください。Attach a copy of the article described below

報道発表 Press release	□ 有　■ 無	発表年月日 Date of release	
発表機関 Released medium			
発表形式 Release method	・新聞　・雑誌　・Web site　・記者発表　・その他（　　）		
発表タイトル Released title			

8. 本研究テーマに関する特許出願予定 Patent application concerned with your research theme

出願予定 Scheduled	□ 有　■ 無	出願国 Application	
出願内容（概要） Application contents			

9. その他 Others

指導責任者（記名）　李 小康

Clinical and Experimental Immunology, 2022, **208**, 340–350
https://doi.org/10.1093/cei/uxac039
Advance access publication 3 May 2022
Research Article

Clinical & Experimental
IMMUNOLOGY

OXFORD

Research Article

Combinations of anti-GITR antibody and CD28 superagonist ameliorated dextran sodium sulfate-induced mouse colitis

Kuai Ma[1,2], Weitao Que[2], Xin Hu[2], Wen-Zhi Guo[3], Liang Zhong[4], Daisuke Ueda[5], Er-li Gu[1], and Xiao-Kang Li[*,2,3]

[1]Department of Gastroenterology and Hepatology, Jing'an District Central Hospital, Jing'an Branch of Huashan Hospital, Fudan University, Shanghai, China
[2]Division of Transplantation Immunology, National Research Institute for Child Health and Development, Tokyo, Japan
[3]Department of Hepatobiliary and Pancreatic Surgery, The First Affiliated Hospital of Zhengzhou University, Zhengzhou, China
[4]Department of Gastroenterology, Huashan Hospital, Fudan University, Shanghai, China
[5]Division of Hepato-Pancreato-Biliary Surgery and Transplantation, Department of Surgery, Kyoto University Graduate School of Medicine, Kyoto, Japan

*Correspondence: Xiao-Kang Li, Division of Transplantation Immunology, National Research Institute for Child Health and Development, 2-10-1 Okura, Setagaya-ku, Tokyo 157-8535 Japan. Tel: +81 3 3416 0181; Fax: +81 3 3417 2864; E-mail: ri-k@ncchd.go.jp

Abstract

Ulcerative colitis (UC) is one of the two main forms of inflammatory bowel disease (IBD) and is an idiopathic, chronic inflammatory disease of the colonic mucosa with an unclear etiology. Interleukin (IL)-10 has been reported to play a crucial role in the maintenance of immune homeostasis in the intestinal environment. Type 1 regulatory T (Tr1) cells are a subset of CD4$^+$Foxp3$^-$ T cells able to secrete high amounts of IL-10 with potent immunosuppressive properties. In this study, we found that the combination of anti-GITR antibody (G3c) and CD28 superagonist (D665) treatment stimulated the generation of a large amount of Tr1 cells. Furthermore, G3c/D665 treatment not only significantly relieved severe mucosal damage but also reduced the incidence of colonic shortening, weight loss, and hematochezia. Dextran sodium sulfate (DSS) upregulated the mRNA levels of IL-6, IL-1β, IL-17, IL-12, tumor necrosis factor-alpha, C-C chemokine receptor type 5, and Bax in splenic lymphocytes (SPLs) and colon tissues, while G3c/D665 treatment conversely inhibited the increase in mRNA levels of these genes. In addition, G3c/D665 treatment altered the proportion of CD4$^+$ and CD8$^+$ T cells and increased CD4$^+$CD25$^+$Foxp3$^+$ regulatory T cells in SPLs, mesenteric lymph nodes (MLNs), and lamina propria lymphocytes (LPLs). Thus, the combination of G3c and D665 treatment showed efficacy against DSS-induced UC in mice by inducing a large amount of Tr1 cell generation via the musculoaponeurotic fibrosarcoma pathways *in vivo* and relieving inflammatory responses both systematically and locally.

Keywords: anti-GITR antibody, CD28 superagonist, dextran sulfate sodium, inflammatory bowel disease, type 1 regulatory T cells

Abbreviations: Ahr: Aryl hydrocarbon receptors; APCs: activated antigen-presenting cells; CTLs: cytotoxic T cells; CTLA-4: cytotoxic T lymphocyte antigen 4; DSS: dextran sodium sulfate; Ebi3: EBV-induced gene 3; Egr2: early growth response 2; Eomes: eomesodermin; FCM: flow cytometry; GITR: glucocorticoid-induced tumor necrosis factor receptor-related protein; IBD: inflammatory bowel disease; IL: Interleukin; Irf4: Interferon regulatory factor 4; LPLs: lamina propria lymphocytes; Maf: musculoaponeurotic fibrosarcoma; MLNs: mesenteric lymph nodes; PBS: phosphate-buffered saline; Prdm1: PR domain zinc finger protein 1; RT-PCR: real-time polymerase chain reaction; SPLs: splenic lymphocytes; Tbx21: T-box transcription factor 21; TCR: T-cell receptor; Teff: effector T cell; TGF-β: transforming growth factor beta; TLR: Toll-like receptor; Tregs: regulatory T cells; Tr1: Type 1 regulatory T; UC: ulcerative colitis.

Introduction

Ulcerative colitis (UC) is a type of inflammatory bowel disease (IBD) characterized by chronic and repeated episodes of enteropatia with symptoms of abdominal pain, severe diarrhea, rectal bleeding, tenesmus, and extraintestinal manifestation [1]. Although the etiology and pathogenesis of UC are complicated and remain uncertain, studies have demonstrated that UC is closely related to the imbalance in mucosal immunity and changes in the colonic barrier [2]. Previous studies showed that the oral administration of dextran sodium sulfate (DSS) in mice induced colitis with clinical symptoms and histopathological features markedly similar to those of human UC [3]. Therefore, the DSS-induced mouse model has been widely used to assess the effects of therapeutic manipulation of UC. At present, there is no cure for UC, and the main treatments for this disorder remain glucocorticosteroids and immunosuppressive agents. More effective and viable therapies with fewer side effects are thus urgently needed [4].

In recent years, cellular therapies have been explored in various immune-mediated inflammatory diseases (IMIDs), including IBD [5, 6]. The immune system maintains peripheral tolerance and downregulates unwanted inflammatory

Received 14 March 2022; Revised 14 April 2022; Accepted for publication 2 May 2022

responses through specialized subpopulations of T cells, namely regulatory T cells (Tregs). The two best-characterized subsets of CD4$^+$ Tregs are CD25$^+$Foxp3$^+$CD4$^+$ T cells and IL-10-producing Foxp3$^-$CD4$^+$ T cells, Type 1 regulatory T (Tr1) cells [7]. Foxp3$^+$ Tregs are characterized by the constitutive expression of the transcription factor forkhead box protein 3 (Foxp3) and the expression of the IL-2 receptor a-chain (CD25) [8]. Tr1 cells represent a subset of CD4$^+$Foxp3$^-$ T cells able to suppress colitogenic T cell responses mainly through the production of high amounts of the cytokine IL-10 with potent immunosuppressive properties [9]. IL-10 has been reported to play a crucial role in the maintenance of the intestinal microbe-immune homeostasis [10]. In addition to CD25$^+$Foxp3$^+$ Tregs, Tr1 cells are potential candidates for cellular therapy in mucosal diseases [5]. Previous studies have reported that Tr1 cells can be generated from murine and human CD4$^+$ T cells *in vitro* [11, 12], but no effective pharmacological approaches have been able to expand antigen-specific or disease-specific Tr1 cells *in vivo*. In the present study, we found that combinations of anti-GITR antibody (G3c) and CD28 superagonist (D665) treatment induced large amounts of IL-10/IFN-γ-co-producing CD4$^+$Foxp3$^-$ Tr1 cells in mice. Furthermore, Tr1 cells contribute to the immunomodulatory effect of protecting against colitis via the high production of IL-10.

In the present study, we determined the protective role of the combinations of G3c and D665 treatment on DSS-induced UC in mice by evaluating the disease activity index (DAI), colon lengths, and pathological changes. To clarify the variation in the proportion and phenotype of immune cells after G3c/D665 treatment, we performed a flow cytometry (FCM) analysis with splenic lymphocytes (SPLs), mesenteric lymph nodes (MLNs), and colon lamina propria lymphocytes (LPLs). Furthermore, cytokine levels were detected by real-time polymerase chain reaction (RT-PCR). The key role of Tr1 cells in G3c/D665 treatment against UC was further elucidated.

Materials and methods

Animal model

Male C57BL/6JJmsSLc (B6/J; H-2k^b) mice 8–10 weeks old, purchased from Shizuoka Laboratory Animal Center (Shizuoka, Japan), were maintained under specific-pathogen-free conditions in a feeding room with automatically controlled light and temperature according to the guidelines of the Institutional Animal Care and Use Committee. All animal procedures were authorized by the National Research Institute for Child Health and Development (permission no. A2009-010-C12).

Mice were randomized into three groups: a naïve group, a 3.5% DSS-control group and a 3.5% DSS + G3c/D665-treated group. Acute colitis of mice was induced with 3.5% DSS (molecular weight, 36 000–50 000; MP Biomedicals, Irvine, CA) for 5 days followed by *ad libitum* drinking water for 3 days. The DSS solutions were dissolved in sterile, distilled water, and prepared fresh every other day. Mice were given a single dose of D665, 1 mg/mice on day 0 and a single dose of G3c, 1 mg/mice on day 3 via intraperitoneal injection as a treated group. G3c and D665 antibodies were purified from the supernatant of hybridomas, gifts from J. Shimizu, Kyoto University, Japan and Dr T. Hunig, University of Wurzburg, respectively. Naïve mice received free water during the study period. Body weight and the DAI were evaluated daily during the colitis induction and recovery phases of the experiment [13]. After mice were sacrificed on day 8, the entire colon was removed from the caecum to the anus, and the colon length was measured as an indirect marker of inflammation.

The DAI

The body weight of mice in each group was recorded daily, as well as the stool consistency and the presence of occult or gross blood per rectum during the experimental period. These parameters were respectively scored by one trained observer blinded to the protocol, and the DAI was calculated as reported previously (Table 1) [14].

Histology and histological scoring

The entire colon was washed with phosphate-buffered saline (PBS), and the distal colon was fixed in 10% formaldehyde solution for 48 h and embedded in paraffin for histological analyses. Sections of the colon (4-mm thick) were prepared and subjected to staining with hematoxylin and eosin (H&E; Muto Pure Chemicals, Osaka, Japan) for morphological analyses. Slides were then examined by light microscopy (OLYMPUS, Tokyo, Japan) in a blinded fashion to assess the inflammation state and blindly scored using a previously published grading system (Table 2) [15].

Table 1: Disease activity index (DAI) scoring.

Score	Weight loss (%)	Stool consistency	Rectal bleeding
0	< 1	Normal	Negative hemoccult test
1	1-5		
2	5-10	Loose stools	Positive hemoccult test
3	10-20		
4	>20	Diarrhea	Gross bleeding

Table 2: Histological injury scoring.

Score	Severity of inflammation	Depth of injury	Crypt damage
0	None	None	None
1	Slight	Mucosal	Basal 1/3 damaged
2	Moderate	Mucosal and submucosal	Basal 2/3 damaged
3	Severe	Transmural	Only surface epithelium intact
4			Entire crypt and epithelium lost

Cell preparation and the flow cytometry analysis

Lymphocyte types among SPLs, MLNs, and LPLs were detected by the LSRFortessa system (BD Biosciences, Franklin Lakes, NJ). Cells were subjected to live/dead staining (Thermo Fisher Scientific, Cleveland, OH) for labeling dead cells and blocked with anti-CD16/CD32 Fc Block antibody to prevent non-specific antibody binding. The following antibodies were purchased from BioLegend (San Diego, CA) and used in the flow cytometry analysis: BV405 anti-mouse CD45 mAb, PE/CF594 anti-mouse CD3 mAb, AF700 anti-mouse CD4 mAb, APC/Cy7 anti-mouse CD4 mAb, AF700 anti-mouse CD8 mAb, and APC/Cy7 anti-mouse CD25 mAb. For intracellular staining, cells were fixed and permeabilized using the transcription factor staining buffer set (eBioscience, San Diego, CA), and then intracellular Foxp3 staining was performed using FITC anti-mouse Foxp3 mAb (eBioscience), PE/Cy7 anti-mouse IFN-γ mAb, APC anti-mouse CTLA-4 mAb, and PE anti-mouse IL-10 mAb purchased from BioLegend. For intracellular cytokine staining, cells were stimulated with 50 ng/ml phorbol 12-myristate 13-acetate (BD Golgi Plug™), 1 mM ionomycin (Sigma–Aldrich, St. Louis, MO), and Brefeldin A (eBioscience) in complete medium for 4 h, followed by surface and intracellular staining. The stained cells were analyzed with the FlowJo software program (Version 10.5.0; BD Biosciences).

Total mRNA preparation and quantitative RT-PCR (qRT-PCR)

Total mRNA was extracted from frozen SPLs, MLNs, and colon tissues using a RNeasy Mini Kit (Qiagen, Valencia, CA). Each 0.8-μg aliquot of mRNA was reverse-transcribed to cDNA using a Prime Script RT reagent Kit (RR037A; Takara, Shiga, Japan). qRT-PCR was performed by the SYBR® Green system using an Applied Biosystem PRISM7900 apparatus (Thermo Fisher Scientific). The PCR cycle conditions for the SYBR® Green system were 50 °C for 2 min, 95 °C for 2 min, 45 cycles of 95 °C for 15 s, and 60 °C for 60 s. The comparative cycle threshold (Ct) method was used to determine the relative gene expression, and the results of target genes (Table 3) were normalized by subtracting the Ct value of 18S rRNA, with the fold change calculated by comparative CT.

Western blot analyses

In brief, frozen SPLs in three groups were homogenized in RIPA buffer containing 1% protease inhibitor cocktail-1 and 1% protease inhibitor cocktail-2 (Sigma–Aldrich) followed by centrifugation in a microfuge at top speed for 30 min. Protein concentrations were assayed using Bio-Rad Protein Assay (Bio-Rad, Hercules, CA). Samples were separated by electrophoresis on 10% polyacrylamide gels and transferred to Immobilon-PVDF (Bio-Rad). After brief incubation with 5% non-fat milk to block non-specific binding, membranes were exposed overnight at 4 °C to specific musculoaponeurotic fibrosarcoma (Maf) (Cell Signaling Technology, Danvers, MA). Maf activity was quantified by a laser densitometric analysis of the radiographic film using the ImageJ software program (NIH, Bethesda, MD).

Statistical analyses

The GraphPad Prism 9 software program (GraphPad, San Diego, CA) was used to calculate statistical significance. A two-way analysis of variance (ANOVA) method and one-way ANOVA method were used to compare the three groups. Data are expressed as the mean ± SD. A value of $P < 0.05$ was considered to be statistically significant (*$P < 0.05$; **$P < 0.01$; ***$P < 0.001$; ****$P < 0.0001$).

Results

G3c/D665 treatment exhibited the potential to attenuate DSS-induced colitis in mice

We evaluated the potential therapeutic effect of G3c/D665 on a DSS-induced mouse colitis model that had been established by orally feeding 3.5% DSS for 5 consecutive days and water

Table 3: Primer sequences for real-time qPCR.

Gene	Forward Primer (5′~3′)	Reverse Primer (3′~5′)
Prdm1	CCCTCATCGGTGAAGTCTA	ACGTAGCGCATCCAGTTG
Eomes	GCGCATGTTTCCTTTCTTGAG	GGTCGGCCAGAACCACTTC
Egr2	GCCAAGGCCGTAGACAAAATC	CCACTCCGTTCATCTGGTCA
Tbx21	AGCAAGGACGGCGAATGTT	GGGTGGACATATAAGCGGTTC
Ahr	AGCCGGTGCAGAAAACAGTAA	AGGCGGTCTAACTCTGTGTTC
TGF-β	ATCCTGTCCAAACTAAGGCTCG	ACCTCTTTAGCATAGTAGTCCGC
Foxp3	CACCCAGGAAAGACAGCAACC	GCAAGAGCTCTTGTCCATTGA
Maf	GCAGAGACACGTCCTGGAGTCG	CGAGCTTGGCCCTGCAACTAGC
TNF-α	AAGCCTGTAGCCCACGTCGTA	GGCACCACTAGTTGGTTGTCTTTG
IL-1β	ACCTTCCAGGATGAGGACATGA	AACGTCACACACCAGCAGGTTA
Bax	GGCTGCTTGTCTGGATCCAA	ATGGTCACTGTCTGCCATGTG
CCR-5	GACATCCGTTCCCCCTACAAG	TCACGCTCTTCAGCTTTTTGCAG
IL-6	GGCGGATCGGATGTTGTGAT	GGACCCCAGACAATCGGTTG
IL-12	AGCACGGCAGCAGAATAAA	CTCCACCTGTGAGTTCTTCAAA
IL-17	CAGCAGCGATCATCCCTCAAAG	CAGGACCAGGATCTCTTGCTG
IL-10	GCTCTTACTGACTGGCATGAG	CGCAGCTCTAGGAGCATGTG
18S	ACATCGACCTCACCAAGAGG	TCCCATCCTTCACATCCTTC

for 3 days. As expected, mice in the 3.5% DSS-control group lost more body weight and exhibited shorter colon lengths and higher DAI scores than the naïve and G3c/D665-treated groups. The improvement of symptoms, such as colonic shortening, weight loss, and hematochezia, in mice treated with G3c/D665 was significant. The colon tissue sections in naïve mice showed no signs of inflammation, while those in the control group showed distortion of crypts, loss of goblet cells, inflammatory cell infiltration, and severe mucosal damage. In contrast, G3c/D665 treatment obviously improved the pathological changes (Fig. 1A). The colons from G3c/D665-treated DSS-colitis mice were relatively normal, exhibiting only slight evidence of inflammatory cell infiltration. These findings were also quantitatively evaluated by a histopathological analysis and scored using a previously published grading system (Fig. 1B). Taken together, these findings indicate that the combination of G3c/D665 treatment effectively attenuated DSS-induced colitis in mice.

G3c/D665 treatment substantially suppressed inflammatory and apoptotic responses in colitis mice

To understand the anti-inflammatory effect of the combinations of G3c/D665 treatment in DSS-induced colitis in mice, we measured the mRNA levels of pro-inflammatory and apoptotic cytokines and chemokines in colon tissues and spleen lymphocytes. The results show that the mRNA levels of pro-inflammatory cytokines (such as TNF-α, IL-6, IL-1β, IL-17, and IL-12), pro-inflammatory chemokines (such as CCR-5) and apoptotic factors (such as Bax) were significantly increased in mice in the control group. However, the increase in these cytokines and chemokines was reduced by G3c/D665 treatment in colon tissues (Fig. 2A). In spleen lymphocytes, the mRNA levels of pro-inflammatory cytokines, such as TNF-α, IL-6, IL-1β, and IL-12, were significantly reduced in the G3c/D665-treated group as well (Fig. 2B). Our data indicated that G3c/D665 treatment conferred profound protection against DSS-induced colitis in association with reduced inflammatory and apoptotic responses, alleviated tissue damage, and the maintenance of intestinal integrity and functionality.

G3c/D665 treatment altered the proportion of CD4$^+$ and CD8$^+$ T cells in SPLs, MLNs, and LPLs.

To clarify the variation in the number and/or phenotype of immune cells after G3c/D665 treatment, we performed an FCM analysis with SPLs, MLNs, and LPLs. Previous studies have shown that CD8$^+$ cytotoxic T cells play a vital role in inducing relapsing colitis [16]. As shown in Fig. 3, in the present study, the proportion of CD8$^+$ cytotoxic T cells among SPLs (P < 0.0001) and MLNs (P < 0.05) was significantly downregulated by the combinations of G3c and D665 treatment compared to the control group, whereas there was no significant change in the LPLs. Furthermore, SPLs, MLNs,

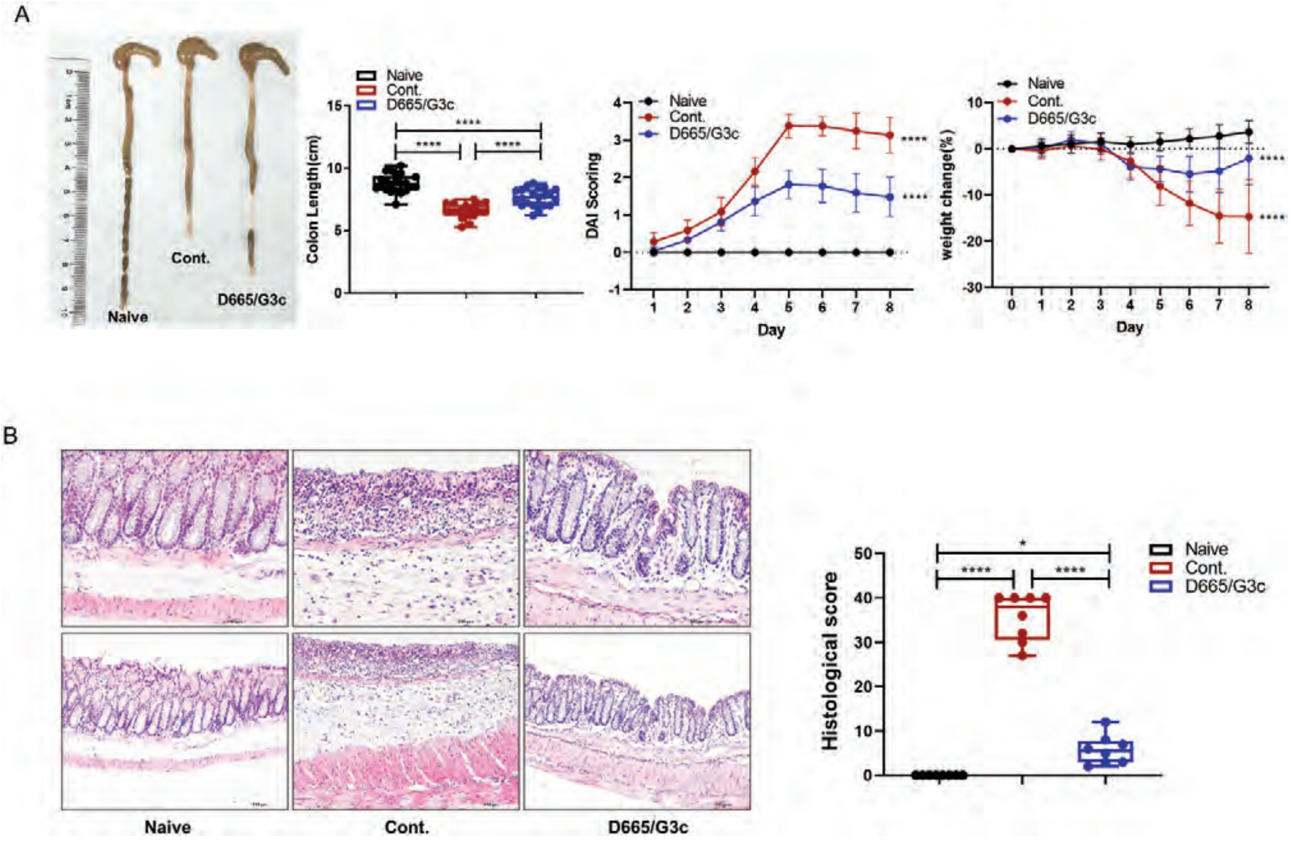

Figure 1: G3c/D665 treatment attenuated DSS-induced damage of colon. (A) The colon gross appearance and length analysis of mice are shown. The DAI of mice and the weight change (%) of mice are also presented. (B) Hematoxylin and eosin (HE) staining of colon specimens in the three groups. Substantial monocyte infiltration, mucosa erosion, goblet cell arrangement disorder, and reduction were seen in the colon specimens of the 3.5% DSS-control group. A Hematoxylin and eosin (HE) analysis of the colon specimens is shown (scale bars = 100 and 200 μm). Each bar represents the mean ± SD. *P < 0.05, ****P < 0.0001.

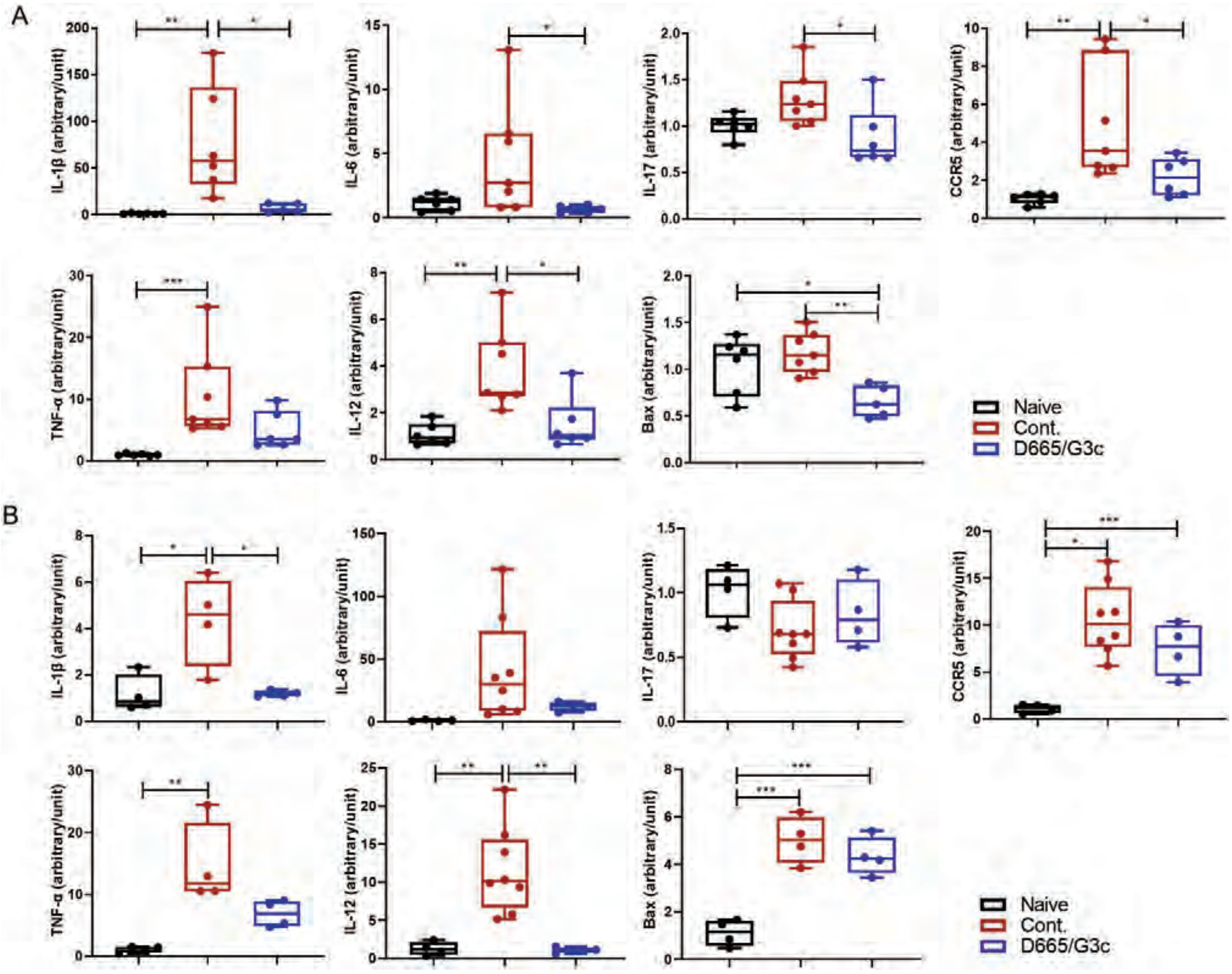

Figure 2: G3c/D665 treatment reduced the mRNA expression of inflammatory and apoptosis cytokine-related genes. (A) Homogenates of colon tissues were analyzed by qRT-PCR as described in the materials and methods. The mRNA expression of inflammatory cytokines-related genes, particularly IL-1β, IL-6, IL-12, IL-17, and CCR-5, was significantly lower in the G3c/D665-treated group than in the control group. The mRNA expression of apoptosis-related gene, such as Bax, was reduced in the G3c/D665-treated group. (B) SPLs were analyzed by qRT-PCR as well. Compared with the control group, the mRNA expression of inflammatory and apoptosis cytokine-related genes, such as IL-1β, IL-12, and Bcl-2, was reduced in the G3c/D665-treated group. Values are expressed as arbitrary units (mean ± SD). *$P < 0.05$, **$P < 0.01$, ***$P < 0.001$.

and LPLs in the G3c/D665 group showed an apparent increase in the proportion of CD4$^+$ T cells compared with the control group.

G3c/D665 treatment led to CD4$^+$CD25$^+$Foxp3$^+$ Treg expansion in DSS-induced colitis

Tregs are a unique subpopulation of CD4$^+$ T cells that play pivotal roles in maintaining immune tolerance, improving the inflammatory intestinal environment, and conferring therapeutic benefits for colitis [17, 18], so we evaluated the population of CD4$^+$CD25$^+$Foxp3$^+$ Tregs in SPLs, MLNs, and LPLs among the three groups.

Our analysis showed that the percentage of CD4$^+$CD25$^+$Foxp3$^+$ Tregs in the G3c/D665-treated group was markedly higher than in the other two groups (Fig. 4A, B). Although the combination of G3c and D665 treatment generated a large number of CD4$^+$CD25$^+$Foxp3$^+$ Tregs according to the FCM analysis, the mRNA expression of Foxp3 gene was not significantly increased in the G3c/D665 group (Supplementary Fig. S1). Both the T cell protein cytotoxic T lymphocyte antigen 4 (CTLA-4) pathway and CD4$^+$CD25$^+$Foxp3$^+$ Tregs are essential for maintaining control of immune homeostasis [19]. We further analyzed CTLA-4 and found that CD4$^+$CD25$^+$Foxp3$^+$ Tregs significantly expressed CTLA-4 in the SPLs, MLNs, and LPLs of the three groups (Fig. 4C, D).

G3c/D665 treatment increased the proportion of Tr1 cells in DSS-induced mouse colitis

Tr1 cells are characterized by their high IL-10-producing capacity and the ability to inhibit T cell responses and colitis [11]. Therefore, we performed an FCM analysis to gain insight into the expression of IL-10$^+$Foxp3$^-$ Tr1 cells and IL-10$^+$IFN-γ$^+$ Tr1 cells gated from CD4$^+$ T cells. Our result showed that the combinations of G3c and D665 treatment generated large amounts of IL-10$^+$Foxp3$^-$ Tr1 cells and IL-10$^+$IFN-γ$^+$ Tr1 cells in the three different lymphocyte types (Fig. 5). To identify the expression of Tr1-related transcription factors (TFs), we extracted TFs known to regulate Tr1 differentiation, including early growth response 2 (Egr2), Aryl hydrocarbon receptors

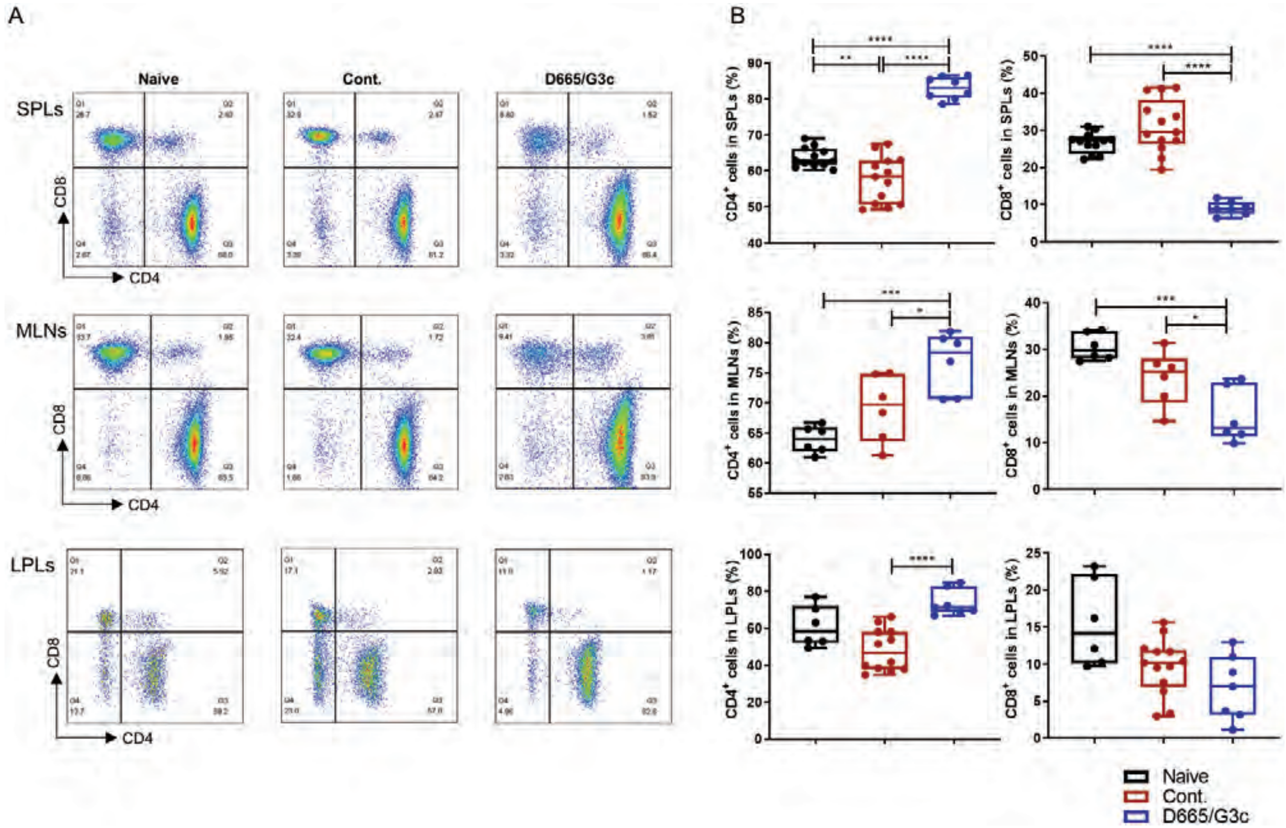

Figure 3: G3c/D665 treatment increased the proportion of $CD4^+$ T cells in SPLs, MLNs, and LPLs. (A) A representative FCM analysis assessing the expression of $CD8^+$ and $CD4^+$ T cells gated on $CD3^+$ T cells in SPLs, MLNs, and LPLs of three groups. (B) The proportion of $CD4^+$ T cells was significantly increased in the G3c/D665-treated group compared to the control group in SPLs, MLNs, and LPLs. The proportion of $CD8^+$ T cells was significantly reduced in the G3c/D665-treated group compared to the 3.5% DSS group in SPLs and MLNs. Data are expressed as the mean ± SD. $^{*}P < 0.05$, $^{**}P < 0.01$, $^{***}P < 0.001$, $^{****}P < 0.0001$.

(Ahr), T-box transcription factor 21 (Tbx21), Eomesodermin (Eomes), PR domain zinc finger protein 1 (Prdm1), transforming growth factor beta (TGF-β), and Maf (Fig. 6, Supplementary Fig. S1). Of these, the mRNA expression of the Prdm1 and Eomes genes was markedly upregulated in the MLNs of the G3c/D665-treated group but showed no significant difference in SPLs or LPLs. In contrast, the mRNA expression of the Ahr gene was shown to be downregulated in MLNs, SPLs, and LPLs of the G3c/D665-treated group, while the Tbx21, Egr2, and TGF-β mRNA expression did not increase as well Supplementary (Fig. S1). The mRNA expression of IL-10 was significantly increased in the SPLs of the G3c/D665-treated group but did not differ markedly among the three groups in MLNs or LPLs. Interestingly, the protein expression of Maf was increased in the SPLs of the G3c/D665-treated group (Fig. 6D) according to Western blotting, but its mRNA expression was not upregulated in any of the three lymphocyte species according to RT-PCR (Supplementary Fig. S1).

Discussion

UC has become a global public health threat, UC patients suffer from a poor quality of life, increased risk of colorectal cancer, and morbidity/mortality associated with colectomy performed for possible symptomatic relief [20]. Despite recent advances and the development of biological therapies, no drugs provide sustained remission of UC at present [21]. Due to substantial advances in our understanding of the biology of regulatory immune cells, novel cell-based therapies to dampen or prevent undesired immune responses in multiple immune diseases, including UC, have been developed. In previous studies on cell therapies for IBD, increased attention has been paid to the use of Foxp3$^+$ Tregs, but there have been few studies on Tr1 cells. Our study showed that Tr1 cells also have several functional properties that may make them particularly well-suited for treating UC or other inflammatory intestinal diseases.

D665 is a unique class of CD28-superagonist monoclonal antibody that has been reported to be capable of activating T cells without overt stimulation of the T-cell receptor (TCR) and selectively activating Tregs in rodents, suggesting an option for the treatment of autoimmune and inflammatory diseases [22]. Glucocorticoid-induced tumor necrosis factor receptor-related protein (GITR) is a transmembrane protein expressed on the surface of multiple types of immune cells and acts as a co-activating molecule that promotes the function of effector T cells and the expansion of Tregs, making it an attractive target for immunotherapy [23, 24]. The important role of GITR in immune system regulation has attracted a lot of attention for immunotherapeutic treatment of cancers and autoimmune diseases and resulted in the development of anti-GITR antibodies [25, 26]. G3c is an anti-GITR antibody that can recognize GITR and have strong co-stimulatory activity for both Tregs and responder T cells [27]. In our previous trials, we found that the use of D665 alone expanded Foxp3$^+$

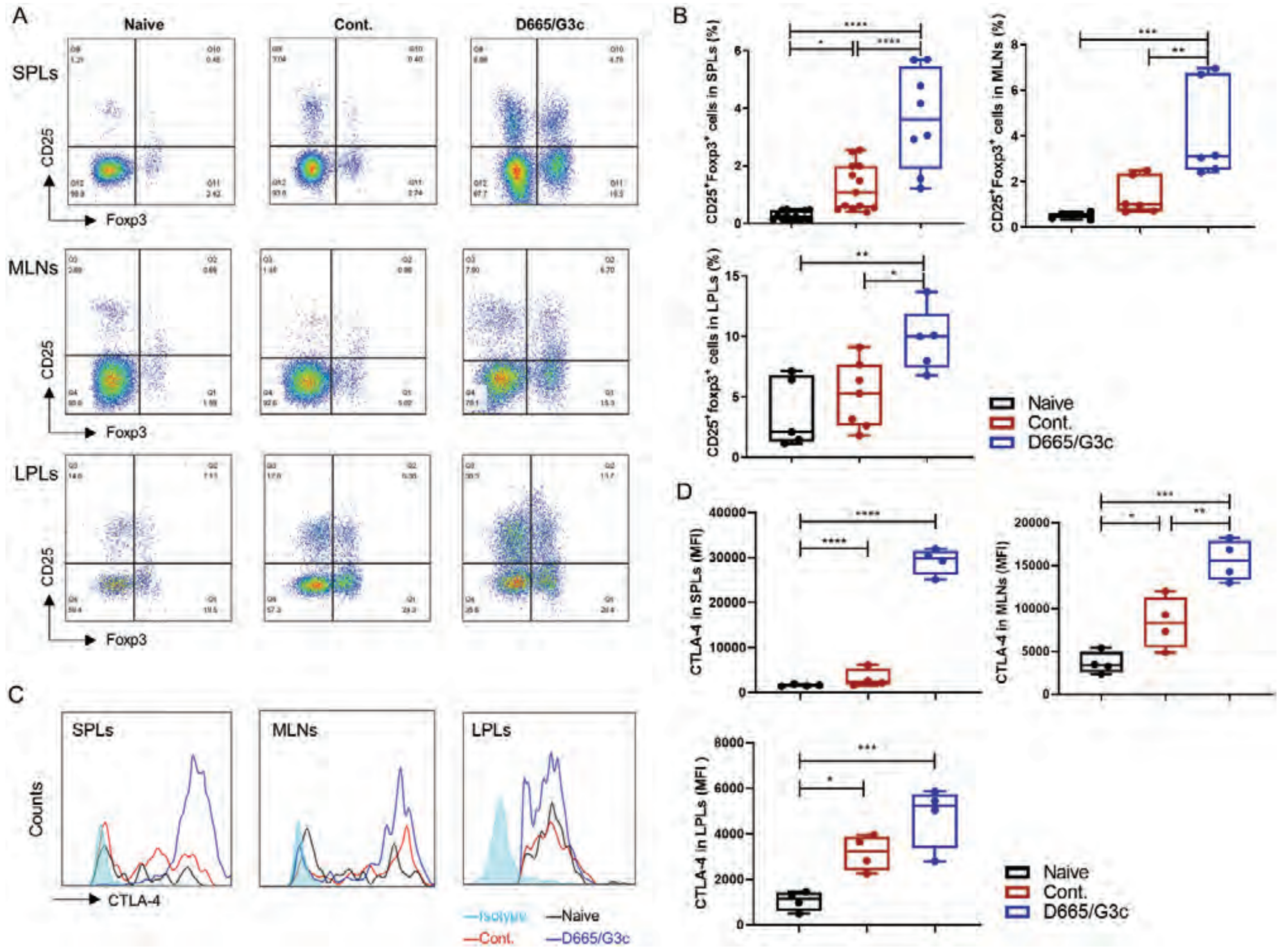

Figure 4: G3c/D665 treatment increased the proportion of CD4⁺CD25⁺Foxp3⁺ Tregs in SPLs, MLNs, and LPLs. (A) A representative FCM analysis assessing the expression of CD4⁺CD25⁺Foxp3⁺ Tregs gated on CD4⁺ T cells in the SPLs, MLNs, and LPLs of the three groups. (B) The proportion of Tregs was significantly increased in the G3c/D665-treated group compared to the control group among SPLs, MLNs, and LPLs. (C–D). A representative FCM analysis assessing the MFI of CTLA-4 expression in the SPLs, MLNs, and LPLs of the three groups gated from CD4⁺CD25⁺Foxp3⁺ Tregs. Data are expressed as the mean ± SD. $^{*}P < 0.05$, $^{**}P < 0.01$, $^{***}P < 0.001$, $^{****}P < 0.0001$.

Tregs, whereas the single-use of G3c could not generate Tregs. In our data, D665 potently expanded Tregs, and the GITR-targeting G3c application further enforced the expansion of Tregs. Large amounts of Tr1 cells were generated after D665 and G3c treatments. G3c played an important role in the induction of Tr1 cells based on D665 treatment. Interestingly, injecting G3c before D665 did not have this effect as well.

To understand the protective effects of G3c/D665 on DSS-induced colitis, mice that had received DSS were given a single dose of D665 1 mg/mice on day 0 and a single dose of G3c 1 mg/mice on day 3 by intraperitoneal injection. This G3c/D665 treatment markedly ameliorated the severity of DSS-induced colitis by inhibiting various pathological manifestations, such as colonic shortening, weight loss, intestinal bleeding, and diarrhea, resulting in a significant reduction in the DAI of the treatment group compared with the non-treated group (Fig. 1A). Furthermore, the degree of mucosal inflammation was markedly improved in mice given G3c/D665 treatment, with observations of decreased mucosal lesions, decreased inflammatory infiltration, and crypt damage microscopically (Fig. 1B).

A hallmark of UC is the dysregulated activation of inflammatory cytokines and components of signaling pathways [28]. Aberrant activation of the immune response and uncontrolled production of inflammatory cytokines has been proven to cause disruption of intestinal barriers, disturbance of intestinal homeostasis, and extensive mucosal injury and inflammation, leading to the development of UC. In response to the commensal microbiota and Toll-like receptor (TLR) signaling, activated antigen-presenting cells (APCs) in the inflamed mucosa of UC produce large amounts of pro-inflammatory cytokines, such as IL-1β, IL-6, IL-12, and TNF-α [28–30]. CCR-5 is a chemokine receptor predominantly expressed on the surface of Th1 polarized T cells and plays an important role in T cell-mediated tissue damage [31]. IL-17 was reported to mediate pro-inflammatory functions including the upregulation of TNF-α, IL-1β, and IL-6 and the recruitment of neutrophils to induce tissue destruction in IBD [28]. In our study, the mRNA levels of pro-inflammatory cytokines (such as TNF-α, IL-6, IL-1β, IL-17, and IL-12), pro-inflammatory chemokines (such as CCR-5), and apoptotic factors (such as Bax) were significantly upregulated in mice in the DSS-control group, as expected (Fig. 2). These indicators were downregulated after treatment, suggesting that G3c/D665 has a significant inhibitory effect on intestinal inflammation and cell necrosis.

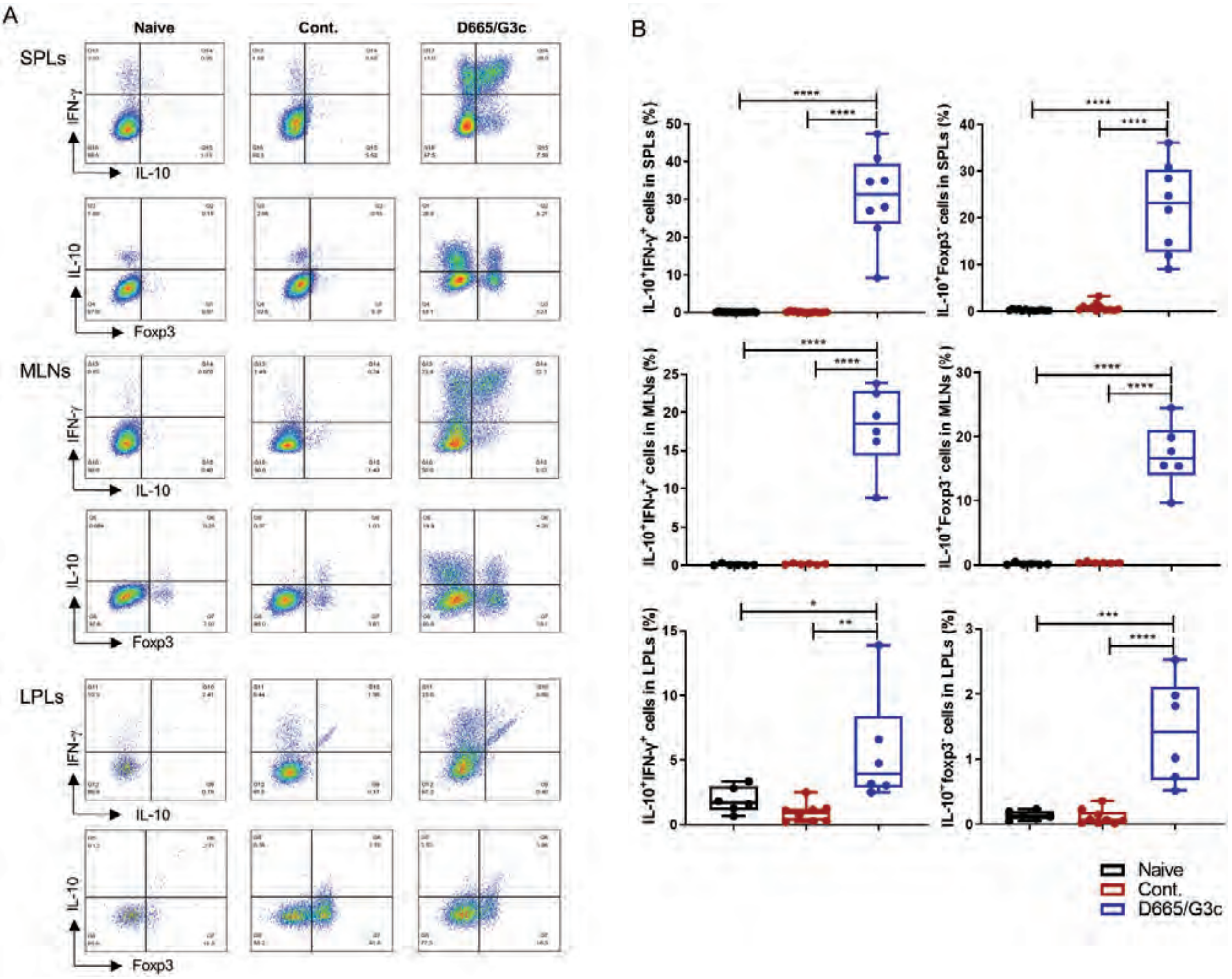

Figure 5: G3c/D665 treatment increased the proportion of IL-10$^+$IFN-g$^+$Tr1 cells and IL-10$^+$Foxp3$^-$Tr1 cells in SPLs, MLNs, and LPLs. (A) A representative FCM analysis assessing the proportion of IL-10$^+$IFN-g$^+$ Tr1 and IL-10$^+$Foxp3$^-$ Tr1 cells gated on CD4$^+$ T cells among the SPLs, MLNs, and LPLs of the three groups. (B) The proportion of IL-10$^+$IFN-g$^+$ Tr1 cells and IL-10$^+$Foxp3$^-$ Tr1 cells was significantly increased in the G3c/D665-treated group compared to the control group among SPLs, MLNs, and LPLs. Data are expressed as the mean ± SD. **P* < 0.05, ***P* < 0.01, ****P* < 0.001, *****P* < 0.0001.

Previous studies have reported that colitis was prevented by *in vivo* antibody depletion of CD8$^+$ T cells but not by that of CD4$^+$ T cells. CD8$^+$ cytotoxic T cells (CTLs) induce relapsing colitis in normal mice, and the cytolytic function of CD8$^+$ CTLs against epithelial cells may initiate the intestinal inflammatory process [16]. Our FCM data showed that CD8$^+$ CTLs were significantly downregulated by G3c/D665 treatment in SPLs and MLNs, whereas there were no significant differences between these two groups in LPLs (Fig. 3). G3c/D665 treatment obviously altered the proportion of CD8$^+$ CTLs and CD4$^+$ T cells, and the proportion of CD4$^+$ T cells in SPLs, MLNs, and LPLs of G3c/D665 group was significantly higher than that in the control group. These results suggest an important role of CD8$^+$ CTLs as initiators of colitis and that G3c/D665 treatment can improve colitis by modulating CD4$^+$ T cell and CD8$^+$ CTL production by modulating systemic or local immunity.

Intestinal mucosal damage caused by UC is associated with mucosal T-cell dysfunction, the imbalance between pro-inflammatory and anti-inflammatory cytokines, and cellular inflammation [28, 32, 33]. CD4$^+$CD25$^+$Foxp3$^+$ Tregs play a critical role in the maintenance of self-tolerance and control of autoimmune diseases and offer a therapeutic option in cases of inflammatory colitis [17, 34, 35]. To clarify the protective activity of G3c/D665 treatment in DSS-colitis, the CD4$^+$CD25$^+$Foxp3$^+$ Treg population was evaluated by FCM. In our study, the combination of G3c and D665 treatment led to the expansion of CD4$^+$CD25$^+$Foxp3$^+$ Tregs in the spleen and MLNs and LPLs of DSS-induced colitis mice (Fig. 4A, B). Cytotoxic T lymphocyte antigen 4 (CTLA-4) (also called CD152) is a key regulator of adaptive immune responses and an inhibitory relative of the T cell co-stimulatory molecule CD28, which has an immunoregulatory function of suppressing the T cell response [36, 37]. Tregs and CTLA-4 have complementary and largely overlapping mechanisms of immune tolerance, and Tregs commonly use CTLA-4 to effect suppression [19]. Our results showed that CD4$^+$CD25$^+$Foxp3$^+$ Tregs significantly expressed CTLA-4 in both SPLs and MLNs, with increased CTLA-4 levels in LPLs, but there was no statistical significance (Fig. 4C, D), indicating that the combination therapy of G3c and D665 partly played a role in the treatment of colitis through Foxp3$^+$ Tregs and CTLA-4.

Tr1 cells regulate responses of both naïve and memory T cells and control inflammasome activity *in vivo* and *in*

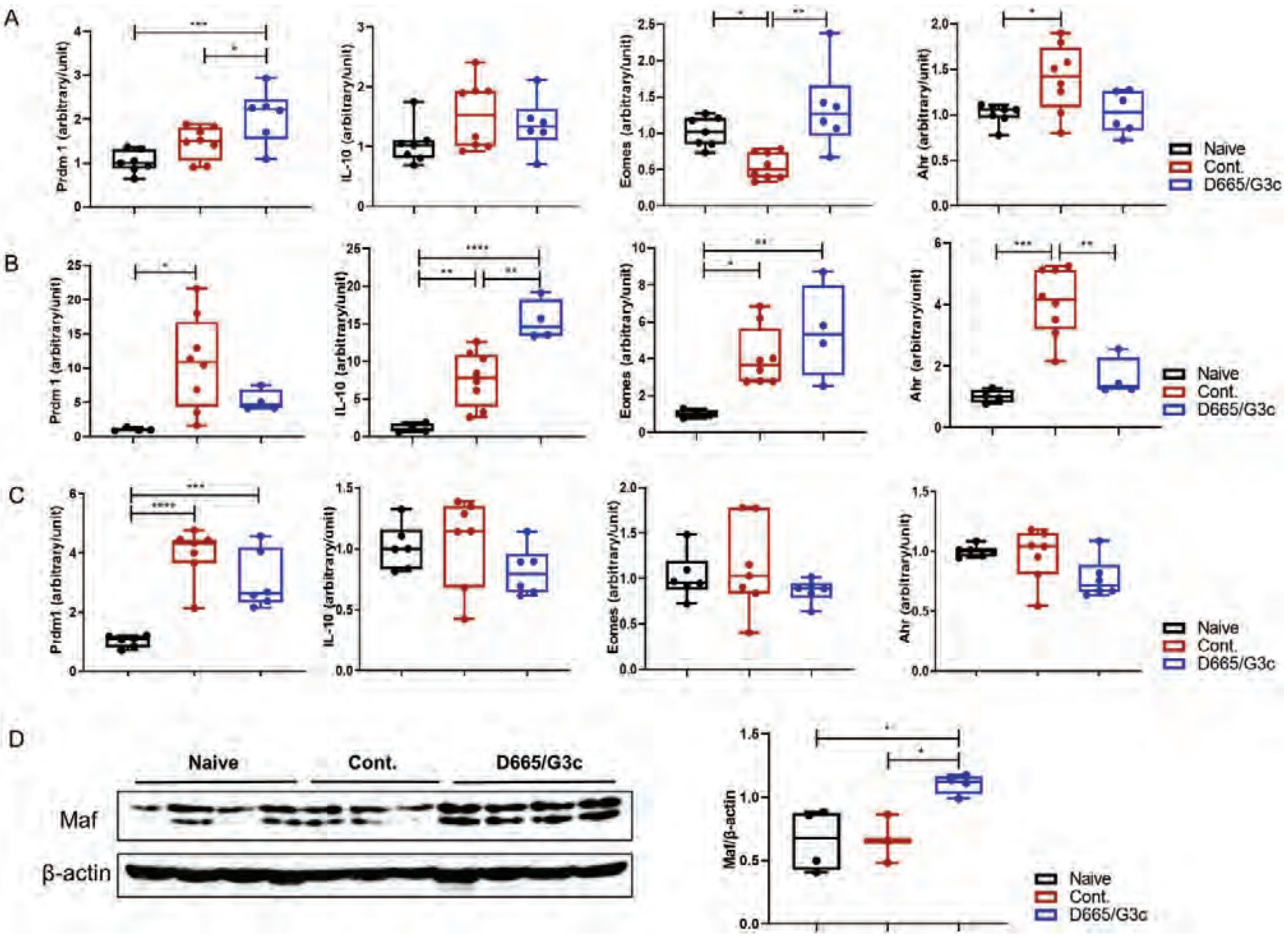

Figure 6: G3c/D665 treatment altered the mRNA expression and protein levels of Tr1 cell-related genes. MLNs (A), SPLs (B) and colon tissues (C) were analyzed by qRT-PCR as described in the materials and methods. The mRNA expression of Tr1 cell-related genes, particularly Prdm1, IL-10, Eomes, and Ahr is shown. (D). A Western blot analysis of the Maf of the SPLs in the three group is shown. Data are expressed as the mean ± SD. $^*P < 0.05$, $^{**}P < 0.01$, $^{***}P < 0.001$, $^{****}P < 0.0001$.

vitro, mainly through the secretion of the immunosuppressive cytokine IL-10 [12]. IL-10 is an anti-inflammatory and immune regulatory cytokine that plays a key role in maintaining immune homeostasis in the gut environment [11, 38]. Furthermore, Tr1 cells have been reported to have a unique ability to promote the development of intestinal goblet cells and repair the epithelial cell barrier function, supporting their use as a cell-based therapy for modulating intestinal inflammation [11]. Previous studies have reported that D665 was able to induce the expansion of CD4$^+$Foxp3$^+$ Tregs *in vivo*, but it has not been reported to induce Tr1 cells thus far [22, 34, 39]. The application of G3c following D665 in our study mediated the expansion of Tregs and the generation of a large number of Tr1 cells. Based on these findings, along with the evidence that aberrant Tregs function and dysregulated control of epithelial homeostasis induce spontaneous intestinal inflammation in gene-knockout mice deficient for IL-10 [40], we hypothesized that Tr1 cells might have unique advantages over CD4$^+$Foxp3$^+$ Tregs in controlling colitis. Our studies showed that the combination of G3c and D665 induced the generation of large amounts of IL-10/IFN-γ-co-producing CD4$^+$Foxp3$^-$ Tr1 cells *in vivo*, and the proliferation of Tr1 cells was much greater than that of CD4$^+$CD25$^+$Foxp3$^+$ Tregs (Fig. 4). Human Tr1-like cells reportedly express the Eomes gene, a T-box transcription factor that controls the cytotoxic functions of CD8$^+$ CTLs and NK cells [41]. Another important transcriptional regulator, Prdm1, has also been shown to promote IL-10 production by Tr1 cells [42]. We assessed the expression of these Tr1 cell-related TFs and found that the mRNA expression of the Prdm1 and Eomes genes was markedly upregulated in MLNs of the G3c/D665-treated group (Fig. 6). A previous study revealed that Maf acted as a growth factor for Tr1 cell development and was critical for IL-10 secretion since IL-27-induced Tr1 cell differentiation was defective in Maf$^{-/-}$ mice [43, 44]. The protein expression of Maf was significantly increased in the SPLs of the G3c/D665-treated group, suggesting that G3c/D665 treatment may promote the generation of Tr1 cells through the Maf pathway.

In a clinical trial in 2006, CD28 superagonist (TGN1412) was reported to result in the instantaneous arrest and uncontrolled T cell activation with cytokine storm [45], but it was later clear that dose-reduction could preferentially address Tregs in humans [46]. The further development of CD28 superagonist (TAB08) has been resumed and is now being evaluated in a phase II study. A previous study has reported that using D665 alone on DSS-induced colitis weakly induced

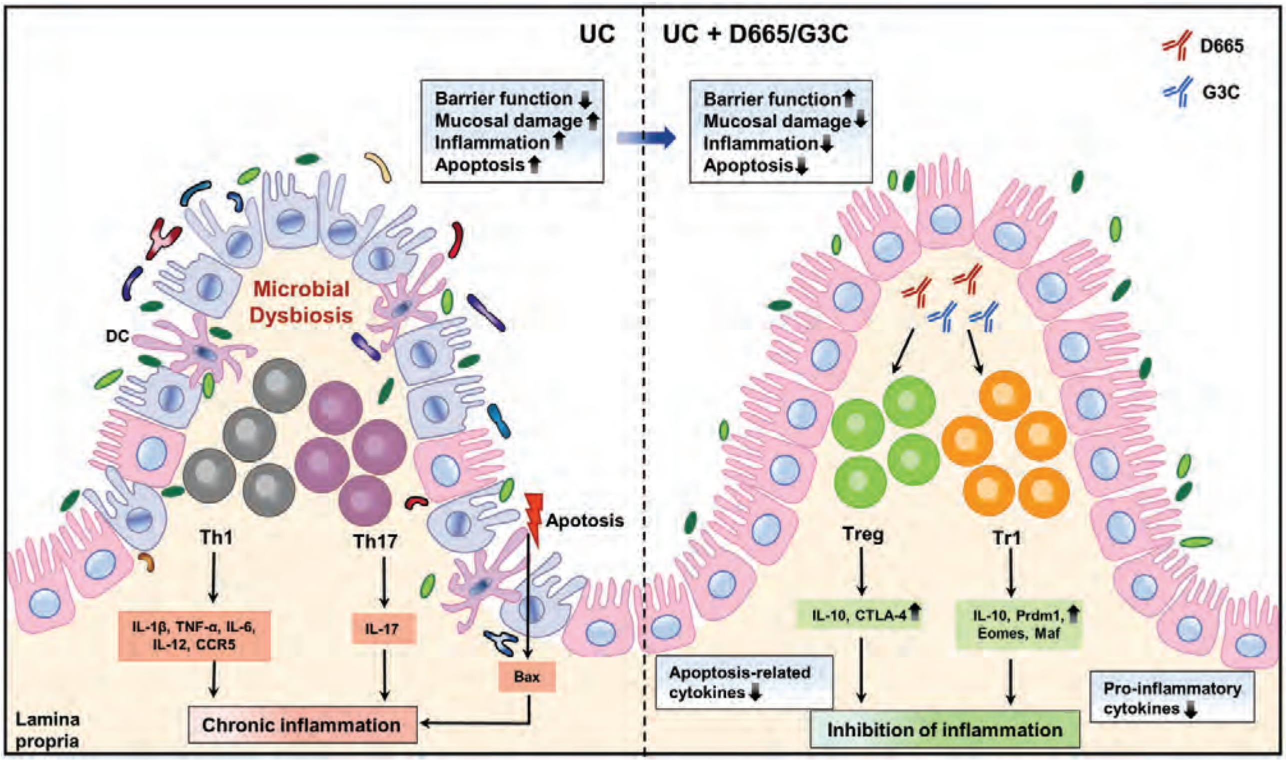

Figure 7: Immune mechanism of G3c/D665 in the treatment of UC. In UC, the intestinal barrier is disrupted, the mucosa is severely damaged, and the balance of intestinal microflora is dysregulated. In the colonic lamina propria, Th1 cells release many pro-inflammatory cytokines, such as IL-1β, TNF-α, IL-6, IL-12, and CCR-5, while Th17 cells release IL-17. The release of apoptotic factor, such as Bax, is also increased in UC. G3c and D665 treatment expands Tregs and Tr1 cells, thereby increasing the release of anti-inflammatory cytokines and decreasing the release of pro-inflammatory cytokines and apoptotic factors. Tregs release IL-10 and CTLA-4, while Tr1 cells release IL-10, Prdm1, Eomes, and Maf. After the administration of G3c and D665, the intestinal barrier is restored, mucosal damage is repaired, and colitis is improved.

the levels of IL-2 and IFN-γ in the spleen and colon but did not result in pathophysiologically relevant levels of cytokine storm [34]. we have not observed any signs of the disorders in the G3c/D665 treated mice with DSS-induced colitis.

Taken together, our data demonstrated that the combination of G3c and D665 treatment targets Tr1 cell generation *in vivo* to reduce the colon damage in DSS-induced mouse colitis by secreting a large amount of IL-10, maintaining and enhancing their regulatory functions (Fig. 7). This represents a major advance towards the therapeutic use of Tr1 cells as cellular therapy and supports the potential of the combination of G3c and D665 as a new auspicious therapeutic option for treating UC in the clinic. Furthermore, harnessing the suppressive potential of Tr1 cells may have important implications for cell therapy of autoimmune, autoinflammatory, and transplantation-related diseases.

Supplementary data

Supplementary data is available at *Clinical and Experimental Immunology* online.

Acknowledgements

The authors are grateful to thank Miss Sato for her invaluable technical assistance. This study was supported by research grants from the Grants of Ministry of Education, Culture, Sports, Science, and Technology of Japan (Grants-in-Aid 17H04277).

Conflicts of interest

All authors of this manuscript have no conflicts of interest to disclose as described by Clinical and Experimental Immunology.

Author contributions

KM, WTQ, XH, WZG, LZ, DU, ELG, and XKL conceived and designed the project; KM acquired the data; KM, WTQ, XH, WZG, LZ, DU, ELG, and XKL analyzed and interpreted the data; KM and XKL wrote the paper. All authors read and approved the final manuscript.

Clinical trial registration

Not applicable.

Ethical approval

Mice were cared for in accordance with the National Research Institute for Child Health and Development guidelines on laboratory animal welfare (permission no. A2009-010-C12). The animal research adheres to the ARRIVE guidelines.

Data availability

Data are available upon reasonable request.

References

1. Ordas I, Eckmann L, Talamini M, et al. Ulcerative colitis. *Lancet* 2012, 380, 1606–19.
2. Geremia A, Biancheri P, Allan P, et al. Innate and adaptive immunity in inflammatory bowel disease. *Autoimmun Rev* 2014, 13, 3–10.
3. Chassaing B, Aitken JD, Malleshappa M, et al. Dextran sulfate sodium (DSS)-induced colitis in mice. *Curr Protoc Immunol* 2014, 104, 15–25.
4. Cao H, Liu J, Shen P, et al. Protective effect of naringin on DSS-induced ulcerative colitis in mice. *J Agric Food Chem* 2018, 66, 13133–40.
5. Cassinotti A, Passamonti F, Segato S. Cell therapy in inflammatory bowel disease. *Pharmacol Res* 2021, 163, 105247.
6. Negi S, Saini S, Tandel N, et al. Translating treg therapy for inflammatory bowel disease in humanized mice. *Cells-Basel* 2021, 10, 1847.
7. Roncarolo MG, Gregori S, Bacchetta R, et al. The biology of T regulatory type 1 cells and their therapeutic application in immune-mediated diseases. *Immunity* 2018, 49, 1004–19.
8. Rudensky AY. Regulatory T cells and Foxp3. *Immunol Rev* 2011, 241, 260–8.
9. Andolfi G, Fousteri G, Rossetti M, et al. Enforced IL-10 expression confers type 1 regulatory T cell (Tr1) phenotype and function to human CD4(+) T cells. *Mol Ther* 2012, 20, 1778–90.
10. Neumann C, Scheffold A, Rutz S. Functions and regulation of T cell-derived interleukin-10. *Semin Immunol* 2019, 44, 101344.
11. Cook L, Stahl M, Han X, et al. Suppressive and gut-reparative functions of human type 1 T regulatory cells. *Gastroenterology* 2019, 157, 1584–98.
12. Battaglia M, Gregori S, Bacchetta R, et al. Tr1 cells: from discovery to their clinical application. *Semin Immunol* 2006, 18, 120–7.
13. Hidalgo-Cantabrana C, Algieri F, Rodriguez-Nogales A, et al. Effect of a ropy exopolysaccharide-producing Bifidobacterium animalis subsp. lactis strain orally administered on DSS-induced colitis mice model. *Front Microbiol* 2016, 7, 868.
14. Cooper HS, Murthy SN, Shah RS, et al. Clinicopathologic study of dextran sulfate sodium experimental murine colitis. *Lab Invest* 1993, 69, 238–49.
15. Dieleman LA, Palmen MJ, Akol H, et al. Chronic experimental colitis induced by dextran sulphate sodium (DSS) is characterized by Th1 and Th2 cytokines. *Clin Exp Immunol* 1998, 114, 385–91.
16. Nancey S, Holvoet S, Graber I, et al. CD8+ cytotoxic T cells induce relapsing colitis in normal mice. *Gastroenterology* 2006, 131, 485–96.
17. Fan L, Qi Y, Qu S, et al. *B*. adolescentis ameliorates chronic colitis by regulating Treg/Th2 response and gut microbiota remodeling. *Gut Microbes* 2021, 13, 1–17.
18. Clough JN, Omer OS, Tasker S, et al. Regulatory T-cell therapy in Crohn's disease: challenges and advances. *Gut* 2020, 69, 942–52.
19. Walker LS. Treg and CTLA-4: two intertwining pathways to immune tolerance. *J Autoimmun* 2013, 45, 49–57.
20. Miao Z, Chen L, Feng H, et al. Baitouweng decoction ameliorates ulcerative colitis in mice partially attributed to regulating Th17/Treg balance and restoring intestinal epithelial barrier. *Front Pharmacol* 2020, 11, 531117.
21. Nunes NS, Chandran P, Sundby M, et al. Therapeutic ultrasound attenuates DSS-induced colitis through the cholinergic anti-inflammatory pathway. *EBioMedicine* 2019, 45, 495–510.
22. Langenhorst D, Tabares P, Gulde T, et al. Self-recognition sensitizes mouse and human regulatory T cells to low-dose CD28 superagonist stimulation. *Front Immunol* 2017, 8, 1985.
23. Riccardi C, Ronchetti S, Nocentini G. Glucocorticoid-induced TNFR-related gene (GITR) as a therapeutic target for immunotherapy. *Expert Opin Ther Targets* 2018, 22, 783–97.
24. Zappasodi R, Sirard C, Li Y, et al. Rational design of anti-GITR-based combination immunotherapy. *Nat Med* 2019, 25, 759–66.
25. He C, Maniyar RR, Avraham Y, et al. . Therapeutic antibody activation of the glucocorticoid-induced TNF receptor by a clustering mechanism. *Sci Adv* 2022, 8, m4552.
26. Petrillo MG, Ronchetti S, Ricci E, et al. . GITR+ regulatory T cells in the treatment of autoimmune diseases. *Autoimmun Rev* 2015, 14, 117–26.
27. Nishioka T, Nishida E, Iida R, et al. In vivo expansion of CD4+Foxp3+ regulatory T cells mediated by GITR molecules. *Immunol Lett* 2008, 121, 97–104.
28. Neurath MF. Cytokines in inflammatory bowel disease. *Nat Rev Immunol* 2014, 14, 329–42.
29. Ng SC, Benjamin JL, McCarthy NE, et al. Relationship between human intestinal dendritic cells, gut microbiota, and disease activity in Crohn's disease. *Inflamm Bowel Dis* 2011, 17, 2027–37.
30. Moschen AR, Tilg H, Raine T. IL-12, IL-23 and IL-17 in IBD: immunobiology and therapeutic targeting. *Nat Rev Gastroenterol Hepatol* 2019, 16, 185–96.
31. Turner JE, Steinmetz OM, Stahl RA, et al. Targeting of Th1-associated chemokine receptors CXCR3 and CCR5 as therapeutic strategy for inflammatory diseases. *Mini Rev Med Chem* 2007, 7, 1089–96.
32. Maynard CL, Weaver CT. Intestinal effector T cells in health and disease. *Immunity* 2009, 31, 389–400.
33. Larabi A, Barnich N, Nguyen H. New insights into the interplay between autophagy, gut microbiota and inflammatory responses in IBD. *Autophagy* 2020, 16, 38–51.
34. Chen J, Xie L, Toyama S, et al. The effects of Foxp3-expressing regulatory T cells expanded with CD28 superagonist antibody in DSS-induced mice colitis. *Int Immunopharmacol* 2011, 11, 610–7.
35. Xu M, Duan XY, Chen QY, et al. Effect of compound sophorae decoction on dextran sodium sulfate (DSS)-induced colitis in mice by regulating Th17/Treg cell balance. *Biomed Pharmacother* 2019, 109, 2396–408.
36. Rowshanravan B, Halliday N, Sansom DM. CTLA-4: a moving target in immunotherapy. *Blood* 2018, 131, 58–67.
37. Hansel TT, Kropshofer H, Singer T, et al. The safety and side effects of monoclonal antibodies. *Nat Rev Drug Discov* 2010, 9, 325–38.
38. Schmitt H, Ulmschneider J, Billmeier U, et al. The TLR9 agonist cobitolimod induces IL10-producing wound healing macrophages and regulatory T cells in ulcerative colitis. *J Crohns Colitis* 2020, 14, 508–24.
39. Schmidt T, Willenborg S, Hunig T, et al. Induction of T regulatory cells by the superagonistic anti-CD28 antibody D665 leads to decreased pathogenic IgG autoantibodies against desmoglein 3 in a HLA-transgenic mouse model of pemphigus vulgaris. *Exp Dermatol* 2016, 25, 293–8.
40. Matharu KS, Mizoguchi E, Cotoner CA, et al. Toll-like receptor 4-mediated regulation of spontaneous Helicobacter-dependent colitis in IL-10-deficient mice. *Gastroenterology* 2009, 137, 1380–90.e1.
41. Gruarin P, Maglie S, De Simone M, et al. Eomesodermin controls a unique differentiation program in human IL-10 and IFN-gamma coproducing regulatory T cells. *Eur J Immunol* 2019, 49, 96–111.
42. Montes DOM, Kumar R, de Labastida RF, et al. Blimp-1-dependent IL-10 production by Tr1 cells regulates TNF-mediated tissue pathology. *PLoS Pathog* 2016, 12, e1005398.
43. Pot C, Jin H, Awasthi A, et al. Cutting edge: IL-27 induces the transcription factor c-Maf, cytokine IL-21, and the costimulatory receptor ICOS that coordinately act together to promote differentiation of IL-10-producing Tr1 cells. *J Immunol* 2009, 183, 797–801.
44. Pot C, Apetoh L, Kuchroo VK. Type 1 regulatory T cells (Tr1) in autoimmunity. *Semin Immunol* 2011, 23, 202–8.
45. Sundqvist KG. CD28 Superagonist shock and blockage of motogenic T cell cascade. *Front Immunol* 2021, 12, 670864.
46. Hunig T. The rise and fall of the CD28 superagonist TGN1412 and its return as TAB08: a personal account. *FEBS J* 2016, 283, 3325–34.

A Mesenchymal-epithelial transition factor-Agonistic Antibody Accelerates Cirrhotic Liver Regeneration and Improves Mouse Survival Following Partial Hepatectomy

Kuai Ma,[1,2] Weitao Que,[1] Xin Hu,[1] Wen-Zhi Guo,[3] Er-li Gu,[2] Liang Zhong,[4] Virginia Morello,[5] Manuela Cazzanti,[5] Paolo Michieli,[5,6] Terumi Takahara,[7] and Xiao-Kang Li[1,3]

[1]Division of Transplantation Immunology, National Research Institute for Child Health and Development, Tokyo, Japan; [2]Department of Gastroenterology and Hepatology, Jing'an District Central Hospital, Jing'an Branch of Huashan Hospital, Fudan University, Shanghai, China; [3]Department of Hepatobiliary and Pancreatic Surgery, The First Affiliated Hospital of Zhengzhou University, Zhengzhou, China; [4]Department of Gastroenterology, Huashan Hospital, Fudan University, Shanghai, China; [5]AgomAb Therapeutics NV, Gent, Belgium; [6]Molecular Biotechnology Center, University of Torino Medical School, Torino, Italy; and [7]Third Department of Internal Medicine, University of Toyama, Toyama, Japan

Small-for-size syndrome (SFSS) is a common complication following partial liver transplantation and extended hepatectomy. SFSS is characterized by postoperative liver dysfunction caused by insufficient regenerative capacity and portal hyperperfusion and is more frequent in patients with preexisting liver disease. We explored the effect of the Mesenchymal-epithelial transition factor (MET)-agonistic antibody 71D6 on liver regeneration and functional recovery in a mouse model of SFSS. Male C57/BL6 mice were exposed to repeated carbon tetrachloride injections for 10 weeks and then randomized into 2 arms receiving 3 mg/kg 71D6 or a control immunoglobulin G (IgG). At 2 days after the randomization, the mice were subjected to 70% hepatectomy. Mouse survival was recorded up to 28 days after hepatectomy. Satellite animals were euthanized at different time points to analyze liver regeneration, fibrosis, and inflammation. Serum 71D6 administration significantly decreased mouse mortality consequent to insufficient regeneration of the cirrhotic liver. Analysis of liver specimens in satellite animals revealed that 71D6 promoted powerful activation of the extracellular signal-regulated kinase pathway and accelerated liver regeneration, characterized by increased liver-to-body weight, augmented mitotic index, and higher serum albumin levels. Moreover, 71D6 accelerated the resolution of hepatic fibrosis as measured by picrosirius red, desmin, and α–smooth muscle actin staining, and suppressed liver infiltration by macrophages as measured by CD68 and F4/80 staining. Analysis of gene expression by reverse-transcription polymerase chain reaction confirmed that 71D6 administration suppressed the expression of key profibrotic genes, including platelet-derived growth factor, tissue inhibitor of metalloproteinase 3, and transforming growth factor-β1, and of key proinflammatory genes, including tumor necrosis factor-α, interleukin-1β, chemokine (C-C motif) ligand 3, and chemokine (C-C motif) ligand 5. These results suggest that activating the MET pathway via an hepatocyte growth factor–mimetic antibody may be beneficial in patients with SFSS and possibly other types of acute and chronic liver disorders.

Liver Transplantation 0 1–12 2021 AASLD.
Received April 12, 2021; accepted September 10, 2021.

Small-for-size syndrome (SFSS) is a common yet underrecognized complication following partial liver transplantation and extended hepatectomy.(1) It is characterized by postoperative liver dysfunction caused by insufficient regenerative capacity and portal hyperperfusion and is more frequent in patients with preexisting liver disease.(2) Approximately one-third of liver transplant recipients who develop early graft failure qualify for SFSS. Small-for-size liver grafts show delayed and impaired regeneration(3) and have greater risks of failure

Abbreviations: agomAbs, agonistic monoclonal antibodies; α-SMA, α–smooth muscle actin; a.u., arbitrary units; CCL3, chemokine (C-C motif) ligand 3; CCl4, carbon tetrachloride; CCL5, chemokine (C-C motif) ligand 5; ELISA, enzyme-linked immunosorbent assay; ERK, including microcirculatory damage, inflammatory injury, and accelerated acute rejection, leading to liver failure with associated coagulopathy, ascites, prolonged cholestasis, and encephalopathy. Because of the persistent organ shortage, living donor liver transplantation is becoming the most viable option for patients with end-stage liver disease. Donor safety always comes first in living donor liver transplantation, and there is a growing momentum for the increased use of small-for-size grafts in association with hepato-regenerative therapies.(4,5)

Hepatocyte growth factor (HGF) is a pleiotropic cytokine of mesenchymal origin that plays a key role in organ regeneration.(6) Its high-affinity receptor, the MET tyrosine kinase, is mainly expressed by epithelial and endothelial cells, but it is also present on some immune cells as well as in various types of myofibroblasts.(7) In the liver, HGF is typically secreted by hepatic stellate cells (HSCs) and plays a key role in hepatic regeneration. Following injury, increased HGF secretion initiates a repair program that limits cell damage, ensures hepatocyte regeneration, inhibits myofibroblast hyperproliferation, and suppresses inflammation, restoring liver function.(8)

extracellular signal-regulated kinase; H & E, hematoxylin-eosin; HGF, hepatocyte growth factor; hMET, human mesenchymal-epithelial transition factor; HSCs, hepatic stellate cells; IgG, immunoglobulin G; IgG1, immunoglobulin G1; IL-1β, interleukin-1β; IP, intraperitoneally; IV, intravenously; mMET, mouse mesenchymal-epithelial transition factor; mRNA, messenger RNA; N/A, Not applicable; PCNA, proliferating cell nuclear antigen; PDGF, platelet-derived growth factor; PSR, picrosirius red; qRT-PCR, quantitative reverse-transcription polymerase chain reaction; RT-PCR, reverse-transcription polymerase chain reaction; SD, standard deviation; SFSS, small-for-size syndrome; TIMP3, tissue inhibitor of metalloproteinase 3; TNF-α, tumor necrosis factor-α.

Address reprint requests to Paolo Michieli, Ph.D., Molecular Biotechnology Center, University of Torino Medical School, Via Nizza 52, I-10126 Torino, Italy. Telephone: +39 11 670 64 99; E-mail: paolo.michieli@unito.it

Address reprint requests to Terumi Takahara, M.D., Ph.D., Third Department of Internal Medicine, University of Toyama, 2630 Sugitani, Toyama, 930-0194 Japan. Telephone: +81 76-434-502; E-mail: terutaka-tym@umin.ac.jp

Address reprint requests to Xiao-Kang Li, M.D., Ph.D., Division of Transplantation Immunology, National Research Institute for Child Health and Development, 2-10-1 Okura, Setagaya-ku, Tokyo, 157-8535 Japan. Telephone: +81-3-3416-0181; FAX: +81-3-3417-2864; E-mail: ri-k@ncchd.go.jp

This study was supported in part by the Ministry of Education, Culture, Sports, Science and Technology of Japan (Grants-in-Aid 16K11064, 24/17H04277, and 18K08558), the National Center for Child Health and Development (Grant 29-09), and Science and Technology Innovation Talents in Henan Universities (no. 19HASTIT003).

Manuela Cazzanti, Paolo Michieli, and Virginia Morello consult for, own stock in, and are employed by AgomAb Therapeutics NV.

DOI 10.1002/lt.26301

Despite the broad therapeutic potential of HGF in liver diseases, its translation to the clinic has been challenging. In fact, HGF does not display ideal drug-like properties: its very short plasma half-life (a few minutes) causes an unfavorable pharmacokinetics because of its high avidity for the extracellular matrix, it has a poor biodistribution; it needs proteolytic activation to acquire biological activity, and once activated it is unstable; lastly, its industrial manufacture is difficult and costly. To overcome the limitations of HGF and to generate a drug that could effectively promote liver regeneration in patients, we generated a series of anti-MET agonistic monoclonal antibodies ("agomAbs") that bind to MET at high affinity and determine MET activation, mimicking the biochemical and biological activity of HGF. AgomAbs combine the powerful therapeutic potential of HGF with the excellent pharmacokinetic, pharmacodynamic, and manufacturing properties of antibodies.

In this study, we explored the therapeutic potential of 71D6, a fully agonistic anti-MET antibody that cross-reacts with rodent, nonhuman primate, and human MET in a mouse model of SFSS.

Materials and Methods

SERUM 71D6 ANTIBODY GENERATION AND CHARACTERIZATION

Serum 71D6 was generated by immunization of *Llama glama* using the SIMPLE antibody platform.(9) A detailed description of its generation and characterization has been published previously.(10) Binding of 71D6 to MET and HGF-mediated and 71D6-mediated MET autophosphorylation and analysis of MET downstream signaling were performed as described.(10)

ANIMAL MODEL

Mouse procedures were authorized by the National Research Institute for Child Health and Development (permission no. A2014-010-C06). The 8-week-old male C57BL/6JJmsSLc mice (Shizuoka Laboratory Animal Center, Shizuoka, Japan) were subjected to repeated subcutaneous injection of 10% carbon tetrachloride (CCl4; Wako) dissolved in olive oil (100 μL/mouse) twice a week for 10 weeks. On the day of the last CCl4 administration, the mice were randomized into 2 arms receiving 3 mg/kg of 71D6 or a control antibody against the F glycoprotein of respiratory syncytial virus(11) (both in the mouse immunoglobulin G1 [IgG1] format). At 2 days after randomization, all of the mice were subjected to 70% hepatectomy by removal of the anterior 2 lobes and posterior left lobe. The 71D6 or control IgG were administered intraperitoneally (IP) at a dose of 3 mg/kg 2 days before hepatectomy and at days 0, 2, 4, 6, 8, 10, and 12. Mice recruited in the trial included main study animals and satellite animals. The spontaneous survival rate of the main study animals was recorded from days 0 to 28. Satellite animals (3 mice per group) were euthanized at 3, 7, and 28 days after hepatectomy. Serum and liver samples were stored at −80°C.

SERUM BIOCHEMICAL MEASUREMENTS

Serum was collected from whole-blood samples after standing for 30 minutes at 37°C and then centrifuged at 1800*g* for 25 minutes at 4°C. Serum samples were then analyzed for serum albumin concentrations using a commercially available kit (Fujifilm) and an automatic biochemical analyzer (DRI-CHEM 3500i; Fujifilm) according to the manufacturer's instructions. Serum HGF concentration was measured using the mouse/rat HGF Quantikine enzyme-linked immunosorbent assay (ELISA) kit (R&D Systems). Serum 71D6 concentration was determined by ELISA as described.(10)

HISTOPATHOLOGICAL AND IMMUNOHISTOCHEMICAL EXAMINATION

Both the liver portion extracted at the time of hepatectomy and that collected at autopsy were processed for histopathological examination. Liver tissues were fixed in 10% formalin for 48 hours, routinely processed, and sliced into sections of 4 μm in thickness. For detection of liver fibrosis, sections were stained with picrosirius red (PSR; Sigma-Aldrich), anti–α-smooth muscle actin (α-SMA) antibodies (AbCam) and anti-desmin antibodies (Boehringer). For detection of macrophage infiltration, sections were stained with antibodies against CD68 (AbCam) and F4/80 (AbCam). For detection of liver proliferation, sections were stained with anti–proliferating cell nuclear antigen (PCNA) antibodies (Dako). Sections were also stained with hematoxylin-eosin (H & E) and periodic acid–Schiff (both from Sigma-Aldrich). After staining, specimens were photographed under a microscope (Olympus). Histological and immunohistochemical results were quantified using WinRoof 7.4 software (Mitani Corporation).

TOTAL MESSENGER RNA PREPARATION AND QUANTITATIVE REVERSE-TRANSCRIPTION POLYMERASE CHAIN REACTION ANALYSIS

Total messenger RNA (mRNA) was extracted from frozen liver tissues using RNeasy Mini Kit (Qiagen). Each 0.8 μg aliquot of mRNA was reverse transcribed to complementary DNA using a Prime Script reverse-transcription (RT) reagent kit (RR037A; Takara). Quantitative reverse-transcription polymerase chain reaction (qRT-PCR) was performed using the SYBR Green system or the primer/probe set system (primer sequences are listed in Table 1) the Applied Biosystem PRISM7900 apparatus (Thermo Fisher Scientific) is a machine which is used to do RT-PCR. The PCR cycle conditions for the SYBR Green system were 95°C for 3 minutes, 45 cycles of 95°C for 3 seconds, and 60°C for 30 seconds. The PCR cycle conditions for the primer/probe set system were 50°C for 2 minutes, 95°C for 15 minutes, 40 cycles of 95°C for 30 seconds, 60°C for 1 minute, and 25°C for 2 minutes. The comparative threshold cycle (ΔΔCt) method was used for determining relative gene expression, and the results of target genes (including fibrosis-related genes and inflammation-related genes) were normalized by subtracting *18S* expression values.

IN VIVO ANALYSIS OF EXTRACELLULAR SIGNAL-REGULATED KINASE ACTIVATION

Frozen liver tissue was homogenized in radio immunoprecipitation assay buffer containing 1% protease inhibitor cocktail-1 and 1% protease inhibitor cocktail-2 (Sigma-Aldrich) followed by centrifugation in a microfuge at top speed for 30 minutes. Protein concentrations were assayed using a Protein Assay kit (Bio-Rad). Samples were separated by electrophoresis on

TABLE 1. Primers and Probes Used in This Study

Genes (PCR)	Forward (5′–3′)	Reverse (5′–3′)	Probe
TIMP3 (SYBR Green)	CACAAAGTTGCACAGTCCTG	TTTGTCGCCTCAAGCTAGA	N/A
PDGF (SYBR Green)	TACAGTTGCACTCCCAGGAAT	CTTCCAGTTGACAGTTCCGCA	N/A
TGF-β (SYBR Green)	ATCCTGTCCAAACTAAGGCTCG	ACCTCTTTAGCATAGTAGTCCGC	N/A
TNF-α (SYBR Green)	AAGCCTGTAGCCCACGTCGTA	GGCACCACTAGTTGGTTGTCTTTG	N/A
CCL5 (SYBR Green)	TGCCCTCACCATCATCCTCACT	GGCGGTTCCTTCGAGTGACA	N/A
IL-1β (SYBR Green)	ACCTTCCAGGATGAGGACATGA	AACGTCACACACCAGCAGGTTA	N/A
18S (SYBR Green)	ATGAGTCCACTTTAAATCCTTTAACGA	CTTTAATATACGCTATTGGAGCTGGAA	N/A
CCL3 (Taqman)	ACCCAGGTCTCTTTGGAGTCAGCGCA	TCCCAGCCAGGTGTCATTTTC	AGGCATTCAGTTCCAGGTCAG
18S (Taqman)	ATCCATTGGAGGGCAAGTCTGGTGC	ATGAGTCCACTTTAAATCCTTTAACGA	CTTTAATATACGCTATTGGAGGCTGGAA

NOTE: Liver-specific expression of profibrotic and proinflammatory genes determined by SYBR green PCR or Taqman PCR as indicated in the table. N/A, Not applicable.

10% polyacrylamide gels and transferred to Immobilon (Bio-Rad) polyvinylidene fluoride. After brief incubation with 5% nonfat milk to block nonspecific binding, membranes were exposed overnight at 4°C to specific phosphorylated anti-p44/p42 extracellular signal-regulated kinase (ERK) antibodies (Cell Signaling Technology). Membranes were washed and exposed to alkaline phosphatase-conjugated secondary antibodies and visualized by incubation in 5% nonfat milk. Phosphorylated p44/p42 ERK activity was quantified by laser densitometric analysis of the radiographic film using ImageJ software (National Institutes of Health, Bethesda, MD).

STATISTICAL ANALYSIS

Prism7 software (GraphPad, San Diego, CA) was used to calculate statistical significance. A 2-way analysis of variance method and Student t test method were used for comparisons between groups. Survival rate analysis was performed using a log-rank (Cox-Mantel) test. Data are expressed as mean ± standard deviation (SD). A value of $P < 0.05$ was considered to be statistically significant.

Results

SERUM 71D6 BINDS TO MET AT HIGH AFFINITY AND PROMOTES MET ACTIVATION, MIMICKING HGF

HGF-mimetic, agonistic anti-MET antibodies were generated by immunization of *L. glama* using the SIMPLE antibody platform.(9) Their biochemical and biological characterizations have been published previously.(10) Among these molecules, which include both partial and full agonists of MET, serum 71D6 represents the most potent fully agonistic antibody. Serum 71D6 was produced as a chimera between variable llama regions and human or mouse IgG1/λ constant regions. Serum 71D6 bound to either the human MET (hMET) or mouse MET (mMET) extracellular domain with the concentration for 50% of maximal effect in the picomolar range (Fig. 1A). Stimulation of immortalized mouse liver cells with 71D6 or HGF resulted in a similar dose-dependent activation of MET and of its downstream signaling (Fig. 1B). An overlapping pattern of MET activation and signaling was observed in MET-expressing human epithelial cells of various origin (not shown).

SYSTEMIC 71D6 ADMINISTRATION RESULTS IN BIOLOGICALLY SIGNIFICANT PLASMA LEVELS

The pharmacokinetic properties of 71D6 were tested in various mouse strains using various routes of administration. In all studies, increasing doses of the antibody were delivered as a single bolus, and antibody levels in plasma were determined at different time points using a MET-based ELISA assay. Table 2 shows the results obtained in a representative study conducted by IP injection. Serum 71D6 concentration reached a peak 8 hours after injection (65 nM at 1 mg/kg and 2638 nM at 30 mg/kg). After 2 days, plasma 71D6 levels showed only a minor deflection (38 nM at 1 mg/kg and 2466 nM at 30 mg/kg). After 8 days, all dose levels except the lowest were still detectable

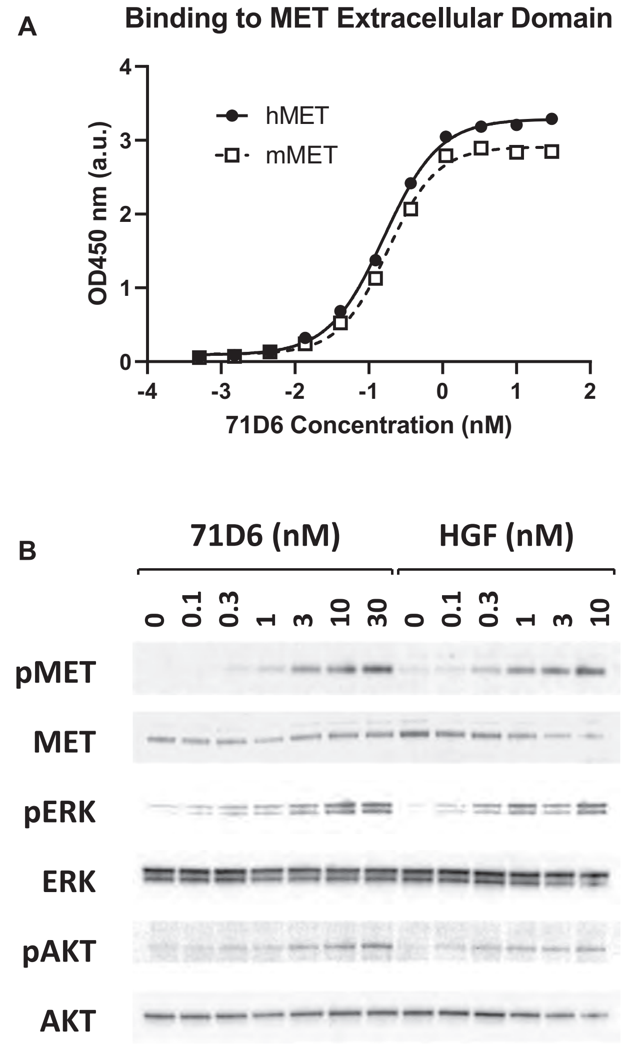

FIG. 1. 71D6 binds to MET at high affinity and elicits MET activation and downstream signaling, mimicking HGF function. (A) 71D6 binding to hMET or mMET extracellular domain was analyzed by ELISA (a.u.). (B) MET activation and downstream signaling induced by HGF or 71D6 was studied in human mouse MLP29 liver precursor cells. Cell lysates were analyzed by Western blotting using antibodies specific for the phosphorylated forms of MET, ERK, and AKT (pMET, pERK and pAKT) as well as antibodies against total MET, ERK, and AKT.

and well in the nanomolar range. Based on these data, the mean plasma half-life of 71D6 corresponded to approximately 5 days (note that recombinant HGF has a half-life of a few minutes in both rodents(12) and humans).(13) Considering that in normal, healthy mice endogenous HGF plasma levels range from 1 to 10 pM(14) and that in the MET phosphorylation assays shown in Fig. 1B both HGF and 71D6 reached saturation at about 10 nM, the concentrations reached following IP injections of 71D6 shown in Table 2 are certainly relevant from a biologic viewpoint.

SERUM 71D6 DISPLAYS A POTENT HEPATOTROPHIC ACTIVITY IN MICE

The biological effects of 71D6 administration were compared with those of recombinant HGF in vivo. In a first experiment, a single bolus of 1 mg/kg of either 71D6 or HGF was administered intravenously (IV) to adult Balb-c mice. Liver-to-body weight ratio and serum albumin levels were measured 4 and 10 days later. As shown in Fig. 2A, 71D6 administration resulted in a marked increase in liver weight both at day 4 (91%) and at day 10 (42%). In contrast, recombinant HGF administration promoted only a minor increase in liver weight (20% at day 4 and 0% at day 10). Serum albumin levels, expression of the synthetic activity of the liver, were invariably higher in the 71D6-treated mice, confirming the superior potency of the antibody. In a second experiment, we aimed at compensating the shorter half-life of HGF with more frequent administration. Because of the challenge of IV injecting the same animals multiple times, IP injection was preferred. Mice were injected IP with either a single bolus of 1 mg/kg 71D6 or with 1 mg/kg recombinant HGF every 12 hours for 5 days. Mice were euthanized at day 6 and subjected to the same analysis as noted previously. Even when administered more frequently, HGF could not match the potent hepatotrophic activity of 71D6. In fact, mice injected with a single bolus of 71D6 displayed a 70% larger liver compared with controls, whereas animals injected repeatedly with HGF showed a modest 10% increase in liver weight (Fig. 2B). Similarly, 71D6 injection resulted in 121% higher albumin levels compared with controls, whereas HGF injection increased serum albumin secretion by 52%. Therefore, 71D6 elicits a significantly more potent hepatotrophic effect in mice compared with recombinant HGF.

SERUM 71D6 PROMOTES LIVER REGENERATION AND INCREASES SURVIVAL IN MICE UNDERGOING CCl4 INJURY AND PARTIAL HEPATECTOMY

Prompted by the previous results, we evaluated the therapeutic effect of 71D6 on liver regeneration in a

TABLE 2. Pharmacokinetic Properties of 71D6

Dose (mg/kg)	Maximum Concentration (nM)	Day 2 Concentration (nM)	Day 8 Concentration (nM)
1	65 ± 3	38 ± 6	0 ± 0
3	271 ± 56	249 ± 70	17 ± 12
10	1265 ± 270	1062 ± 114	257 ± 27
30	2638 ± 327	2466 ± 494	446 ± 45

NOTE: 71D6 concentration in plasma was determined at different time points following IP injection of different dose levels of antibody as a single bolus. Values represent the mean ± standard deviation of at least 3 biological replicates.

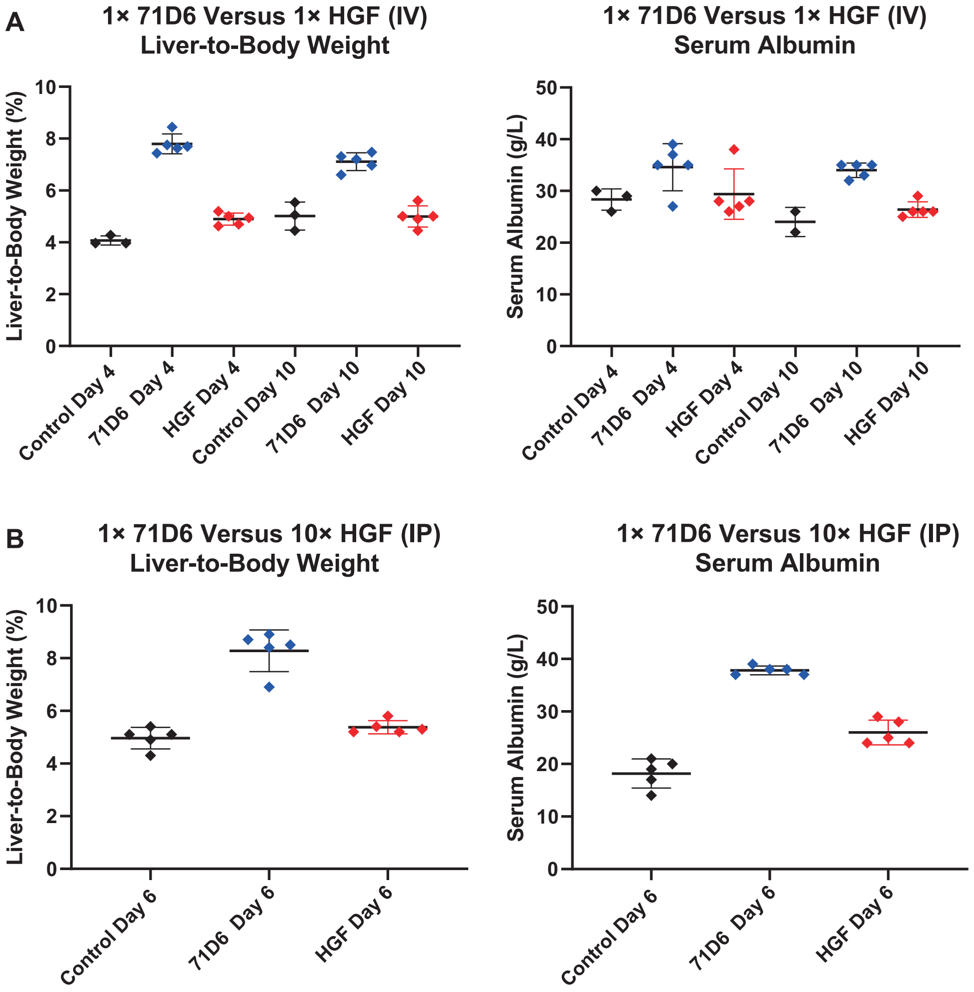

FIG. 2. 71D6 displays a potent hepatotrophic activity in mice. (A) A single 1 mg/kg bolus of 71D6 or human recombinant HGF was injected IV into adult Balb-c mice, and the liver-to-body weight and serum albumin levels were determined 4 and 8 days afterward. (B) A single 1 mg/kg bolus of 71D6 or multiple doses (10 over 5 days) of 1 mg/kg recombinant human HGF were injected IP into adult Balb-c mice. Liver-to-body weight and serum albumin levels were determined 6 days after the first injection. Black represents control group. Red represents HGF group. Blue represents 71D6 group.

mouse model of SFSS. This model reproduces the impaired regenerative capacity of the liver in patients with cirrhosis or other hepatic diseases. Mice were subjected to chronic CCl4 intoxication for 10 weeks and then randomized into 2 arms receiving either 3 mg/kg 71D6 or a control IgG1. At 3 days after randomization, all mice were subjected to 70% hepatectomy. Mouse survival was recorded up to 28 days after hepatectomy.

Satellite animals were euthanized at different time points to analyze liver regeneration, fibrosis, and inflammation. This hepatectomy model typically presents high mortality within 4 days after surgery. Remarkably, the survival rate observed in the 71D6-treated group was significantly higher than that observed in the control group ($P = 0.03$). Although only 5 of 24 mice (21%) in the control group survived for 28 days after hepatectomy, 7 of 13 71D6-treated mice (54%) were alive at the end of the experiment (Fig. 3A). As shown in Fig. 3B, 71D6 also accelerated body weight recovery following surgery compared with controls ($P < 0.001$). Liver weight was also evaluated upon autopsy of satellite animals at various time intervals. As shown in Fig. 3C, 71D6 significantly increased the liver-to-body weight ratio at most time points analyzed (days 1 and 3, $P < 0.05$; day 7, nonsignificant; day 28, $P < 0.001$). Consistent with these findings, serum albumin levels in 71D6-treated animals increased (Fig. 3D) and showed a significant difference with the control group starting on day 7 ($P < 0.01$) and reaching a peak on day 28 ($P < 0.01$). These data indicate that 71D6 treatment promotes liver regeneration and accelerates recovery of liver function after partial hepatectomy.

SERUM 71D6 PROMOTES HEPATIC PROLIFERATION FOLLOWING HEPATECTOMY THROUGH ACTIVATION OF THE ERK SIGNALING PATHWAY

Hepatocyte proliferation following hepatectomy was assessed by staining liver sections with anti-PCNA

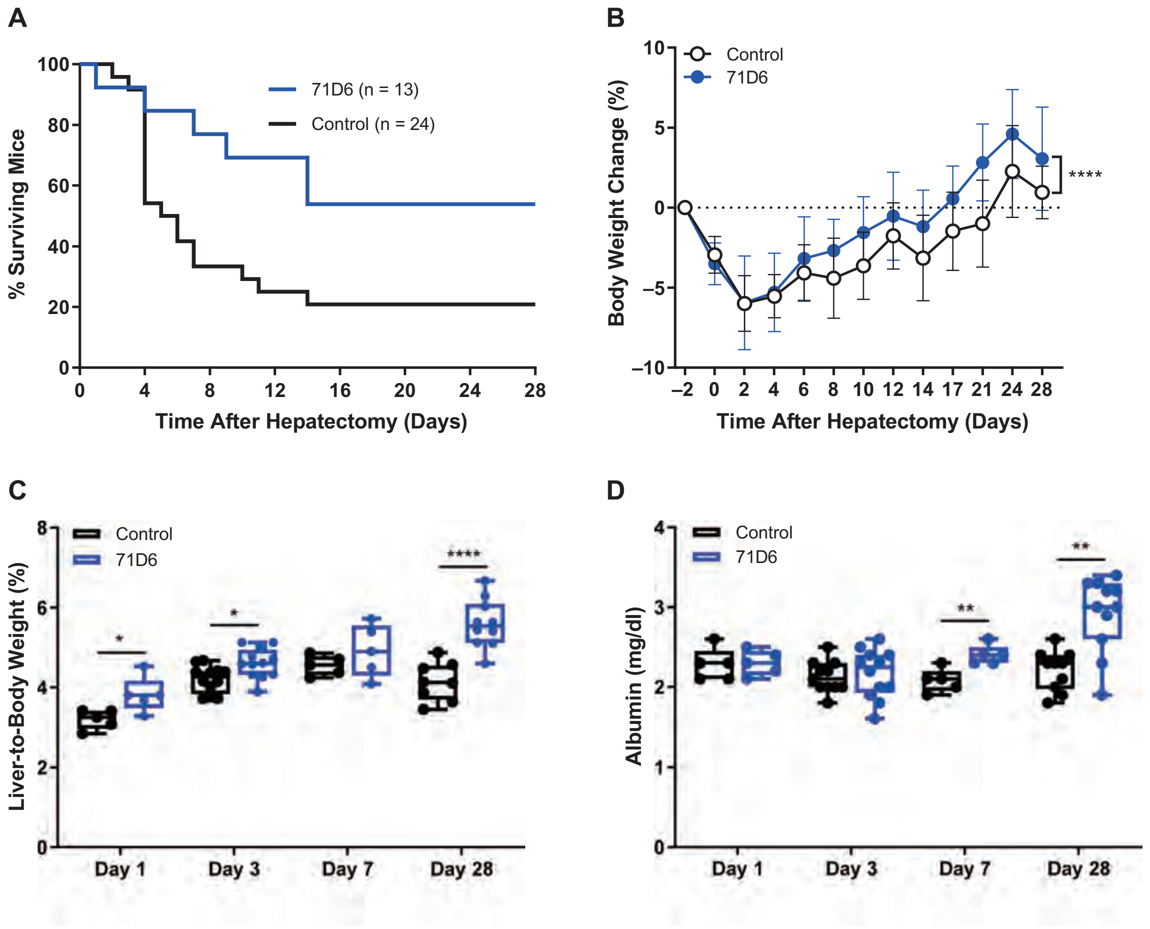

FIG. 3. 71D6 promotes liver regeneration and increases survival in mice undergoing CCl4 injury and partial hepatectomy. (A) Kaplan-Meier curve analysis of mouse survival ($P = 0.03$). (B) Body weight change over time (mean ± SD) ($P < 0.001$). (C) Liver-to-body weight over time (days 1 and 3, $P < 0.05$; day 7, nonsignificant; day 28, $P < 0.001$). (D) Serum albumin levels over time (days 1 and 3, nonsignificant; day 7, $P < 0.01$; day 28, $P < 0.01$).

antibodies. As shown in Fig. 4A, the number of PCNA-positive cells was higher in the 71D6-treated group starting at day 3 and peaking at day 28. To further characterize 71D6-induced liver proliferation, we analyzed the expression and activation of p44 ERK1 and p42 ERK2, a key event in the postinjury liver regeneration program.(15) This analysis revealed that 71D6 significantly increased the levels of phosphorylated (activated) ERK1/2 on both day 3 and day 28 following hepatectomy (Fig. 4B). Activation of ERK1/2 directly correlated with PCNA expression, suggesting that 71D6 stimulates activation of ERK1/2 in the remnant liver, resulting in accelerated hepatic regeneration. Notably, however, no ERK1/2 activation was detected in control animals despite hepatectomy typically inducing spontaneous liver regeneration within a few days. This could be attributed to, and is consistent with, the impaired regenerative capacity of a cirrhotic liver. To cast light onto the mechanism underlying this regenerative impairment, we analyzed serum HGF levels in posthepatectomy mice as well as in healthy, naïve animals. This analysis revealed that posthepatectomy mice treated with the control IgG protein displayed only a marginal increase in HGF levels compared with naïve mice (Fig. 3C). Interestingly, serum HGF levels were slightly higher in the 71D6 group, probably because of larger liver mass and/or increased hepatic function. In any case, serum HGF levels were confined to the picomolar range, whereas 71D6 levels measured in the same samples remained well above MET saturating levels for the entire duration of the study (full activation of MET is reached with 10 nM 71D6). These results explain the absence of ERK activation and the poor liver regeneration observed in the control group on one hand and justify the superior regenerative ability of the animals treated with 71D6 on the other hand.

SERUM 71D6 AMELIORATES HEPATIC FIBROSIS AFTER PARTIAL HEPATECTOMY ON CIRRHOTIC BACKGROUND

Sections of livers harvested from satellite animals were stained with H & E, PSR, and antibodies against

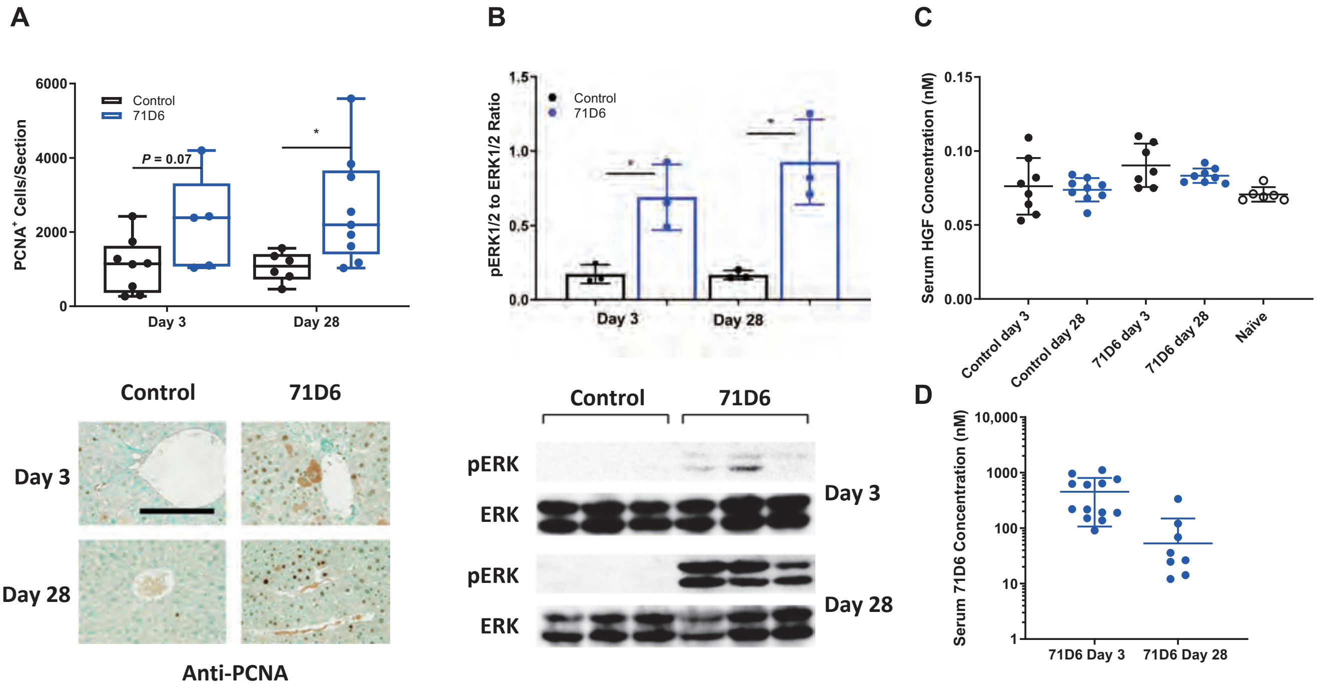

FIG. 4. 71D6 promotes hepatic proliferation following hepatectomy of cirrhotic mice through activation of the ERK signaling pathway. (A) Hepatic proliferation is expressed as the number of PCNA-positive cells per liver section analyzed. Representative images are shown below the graph. The bar is 250 μM. (B) The levels of phosphorylated and total ERK1/2 (p44/p42) were determined by Western blot analysis of liver samples. The ratio between phosphorylated ERK1/2 and total ERK1/2 was determined by densitometric analysis. (C) Serum HGF levels in mice of the control and 71D6 groups as well as in healthy, naïve animals were determined by ELISA. (D) Serum 71D6 levels in mice of the 71D6 group were determined by ELISA.

desmin or α-SMA. Liver specimens of the control group showed consistent formation of thin fibrotic septa at the portal and central areas on day 3. Although milder, fibrosis was still present at day 28. Control liver sections also displayed high density of myofibroblasts. In contrast, liver specimens of the 71D6 group showed significantly milder signs of fibrosis and a reduced presence of myofibroblasts already at day 3. Liver fibrosis was quantified and expressed as the percentage of PSR-positive area (Fig. 5A), number of desmin-positive cells (Fig. 5B), and percentage of α-SMA–positive area (Fig. 5C). To further strengthen these results, the expression of fibrosis-related genes was analyzed by quantitative RT-PCR. This analysis revealed that 71D6 significantly reduced mRNA expression of platelet-derived growth factor (*PDGF*), tissue inhibitor of metalloproteinase 3 (*TIMP3*), and transforming growth factor β1 (*TGF-β1*), which are involved in collagen deposition and activation of HSCs (Fig. 5D). Together, these results suggest that in mice subjected to CCl4 treatment and partial hepatectomy, the agonistic anti-MET antibody 71D6 effectively accelerates the regression of hepatic fibrosis by inhibiting the activation of multiple fibrogenic pathways.

SERUM 71D6 REDUCES MACROPHAGE INFILTRATION IN THE REGENERATING LIVER

Liver specimens extracted at autopsy were analyzed by immunohistochemistry using antibodies against F4/80 and CD68. The number of cells positive for F4/80 ($P < 0.05$; Fig. 6A) and CD68 ($P < 0.0001$; Fig. 6B) was significantly lower in the 71D6 group compared with the control group on day 28. Consistent with histological findings, mRNA levels of inflammatory cytokine genes (tumor necrosis factor α [*TNF-α*], interleukin 1β [*IL1β*], chemokine [C-C motif] ligand 3 [*CCL3*], and chemokine [C-C motif] ligand 5 [*CCL5*]) were significantly lower in the liver homogenates of 71D6-treated mice compared with control mice on day 28 ($P < 0.05$; Fig. 6C).

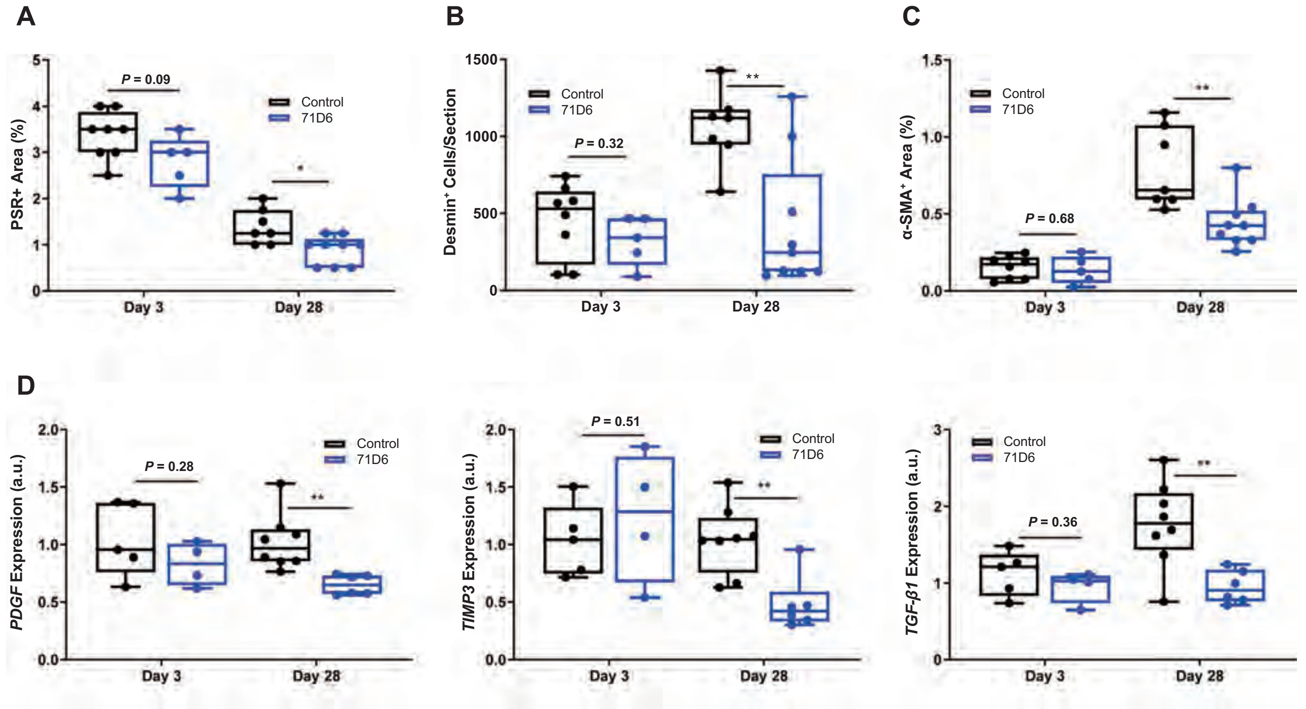

FIG. 5. 71D6 ameliorates hepatic fibrosis after partial hepatectomy on cirrhotic background. (A) Liver sections were stained with PSR. Data are expressed as percentage of PSR-positive area. (B) Liver sections were stained with anti-desmin antibodies. Data are expressed as number of desmin-positive cells per section analyzed. (C) Liver sections were stained with anti–α-SMA antibodies. Data are expressed as percentage of α-SMA–positive area. (D) Liver specimens were analyzed by RT-PCR to determine the levels of *PDGF*, *TGF-β1*, and *TIMP3* expression. Data are expressed as a.u.

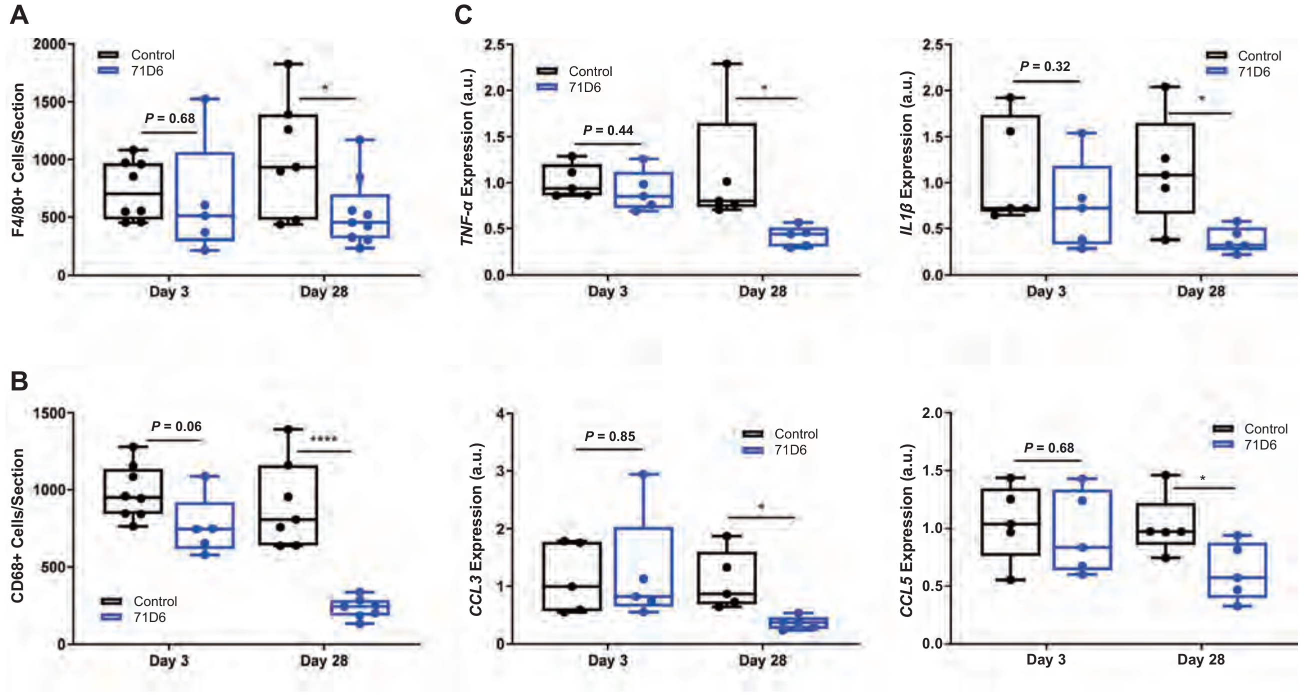

FIG. 6. 71D6 reduces macrophage infiltration in the regenerating liver. (A) Liver sections were stained with anti-F4/80 antibodies. Data are expressed as number of F4/80-positive cells per section analyzed. (B) Liver sections were stained with anti-CD68 antibodies. Data are expressed as number of CD68-positive cells per section analyzed. (C) Liver specimens were analyzed by RT-PCR to determine the levels of *TNF-α*, *IL1β*, *CCL3*, and *CCL5* expression. Data are expressed as a.u.

Discussion

Liver failure is prone to occur after liver transplantation or extended resection when the size and function of the remnant liver is unable to meet the metabolic demand of the patient. SFSS limits the use of living donor and split-liver transplants, and lifesaving large resections of tumors or nonmalignant lesions may be limited by concerns of postsurgical liver failure. Furthermore, SFSS is analogous to end-stage liver disease where the functional liver mass no longer meets metabolic demand. Therefore, there is a major need for effective therapies capable of enhancing and accelerating liver regeneration.

Most studies evaluating regenerative therapies take advantage of the 70% hepatectomy model in mice or rats. In this model, 70% of the liver, usually the median and left lateral lobes, is surgically removed. In response to this, the remnant liver enlarges until it restores normal mass and function. Although the liver has a remarkable potential for regeneration, this regenerative capacity becomes impaired with serious liver fibrosis.(16) The transition of quiescent HSCs to activated, scar-forming, myofibroblast-like cells leads to excessive extracellular matrix synthesis.(17,18) This abnormal scar formation in the liver has been shown to hold back hepatocyte proliferation. In the present study, we studied a newly developed agonistic anti-MET antibody that increased hepatocyte proliferation after partial hepatectomy in mice with CCl4-induced liver disease.

Following 70% hepatectomy, both hepatocytes and nonparenchymal cells are activated and integrate multiple signals originating from immune, hormonal, and metabolic networks to induce liver regeneration.(19) Within this process, the activation of HGF/MET signaling pathway has been demonstrated to be 1 of the essential mechanisms that lead hepatocytes into the cell cycle after hepatectomy.(20) Following resection, HGF protein levels in plasma typically rise,(21) but liver fibrosis is known to prevent this process. The lack of HGF induction on a cirrhotic background was fully confirmed in our study (Fig. 4C). To circumvent defective endogenous HGF activation, we employed the 71D6 agonistic anti-MET antibody. When bound by 71D6, the MET receptor dimerizes and becomes phosphorylated on tyrosine residues to initiate MET downstream signaling (Fig. 1).

The results presented here indicate that liver-to-body weight ratio increased very slowly in the control group, whereas it increased markedly and constantly in the 71D6-treated group (Fig. 3). Quantitative analysis of PCNA immunostaining also confirmed that the agonistic anti-MET antibody potently promotes hepatocyte proliferation (Fig. 4A). We also clarified the involvement of the ERK1/2 signaling pathway in this hepato-proliferative effect. It is known that the Ras/Raf/MEK/ERK cascade has the ability to lead to cellular responses, including proliferation. The ERK1/2 signaling pathway can also regulate the hepatocyte proliferative response during the regeneration of normal liver.(22) Our Western blot results showed that 71D6 strongly activated ERK p44/p42, closely reflecting the high levels of PCNA expression (Fig. 4B). Our results clearly show that 71D6 has the ability to mimic HGF signaling in vivo, including activation of downstream kinases and promotion of hepatocyte proliferation. However, in contrast to HGF, 71D6 is very stable in vivo (Table 2) and displays superior pharmacodynamic properties (Fig. 2). These results highlight the therapeutic potential of 71D6 in liver regeneration.

Liver fibrosis is an inadequate wound-healing response to chronic liver injury and is characterized by the excessive deposition and reduced degradation of the extracellular matrix. Excessive accumulation of extracellular matrix alters the hepatic architecture to progress to liver fibrosis, and if not prevented it may eventually lead to cirrhosis and even liver cancer. Our study provides evidence that 71D6 treatment leads to a significantly lower degree of collagen, desmin, and α-SMA compared with controls (Fig. 5A,B). This is explained by the direct inhibition of multiple fibrogenic pathways including those controlled by *PDGF*, *TIMP3*, and *TGF-β1* (Fig. 5C). These data support the hypothesis that 71D6 has the ability to antagonize TGF-β1 directly so as to reduce liver fibrosis and improve liver regeneration.(23)

Furthermore, our study showed that 71D6 also inhibited the infiltration of inflammatory cells into the liver. In fact, the number of F4/80-positive and CD68-positive cells in the 71D6 group was significantly lower than that observed in the control group (Fig. 6A,B). Consistent with these findings, qRT-PCR analysis revealed that the expressions of proinflammatory cytokines and chemokines such as TNF-α, IL1β, CCL3, and CCL5 were much lower in the liver homogenates of 71D6-treated mice compared with control animals (Fig. 6C).

Thus, not only does 71D6 overcome the inability of a cirrhotic liver to regenerate following hepatectomy, but it also achieves faster resolution of fibrosis and the effective suppression of inflammation. Together, these results suggest that activating the MET pathway via an HGF-mimetic antibody may be beneficial in patients with SFSS and possibly other types of acute and chronic liver disorders.

Acknowledgments: The authors thank Philippe Wiesel for critically reading the manuscript, Luca Rossi for in vivo work, Damiana Sattanino for assay setup, and the entire AgomAb team for continuous support.

REFERENCES

1) Riddiough GE, Christophi C, Jones RM, Muralidharan V, Perini MV. A systematic review of small for size syndrome after major hepatectomy and liver transplantation. HPB 2020;22:487-496.
2) Masuda Y, Yoshizawa K, Ohno Y, Mita A, Shimizu A, Soejima Y. Small-for-size syndrome in liver transplantation: definition, pathophysiology and management. Hepatobiliary Pancreat Dis Int 2020;19:334-341.
3) Zhong Z, Schwabe RF, Kai Y, He L, Yang L, Bunzendahl H, et al. Liver regeneration is suppressed in small-for-size liver grafts after transplantation: involvement of c-Jun N-terminal kinase, cyclin D1, and defective energy supply. Transplantation 2006;82:241-250.
4) Greenbaum LE, Ukomadu C, Tchorz JS. Clinical translation of liver regeneration therapies: a conceptual road map. Biochem Pharmacol 2020;175:113847.
5) Forbes SJ, Newsome PN. Liver regeneration—mechanisms and models to clinical application. Nat Rev Gastroenterol Hepatol 2016;13:473-485.
6) Nakamura T, Mizuno S. The discovery of hepatocyte growth factor (HGF) and its significance for cell biology, life sciences and clinical medicine. Proc Jpn Acad Ser B Phys Biol Sci 2010;86:588-610.
7) Matsumoto K, Funakoshi H, Takahashi H, Sakai K. HGF-Met pathway in regeneration and drug discovery. Biomedicines 2014;2:275-300.
8) Nakamura T, Sakai K, Nakamura T, Matsumoto K. Hepatocyte growth factor twenty years on: much more than a growth factor. J Gastroenterol Hepatol 2011;26(suppl 1):188-202.
9) Klarenbeek A, Blanchetot C, Schragel G, Sadi AS, Ongenae N, Hemrika W, et al. Combining somatic mutations present in different in vivo affinity-matured antibodies isolated from immunized *Lama glama* yields ultra-potent antibody therapeutics. Protein Eng Des Sel 2016;29:123-133.
10) Michieli P. Anti-Met antibodies and uses thereof. European patent application EP 3475302 A1 2019. https://www.lens.org/lens/patent/062-815-545-734-095.
11) Cingoz O. Motavizumab. mAbs 2009;1:439-442.
12) Ido A, Moriuchi A, Kim I, Numata M, Nagata-Tsubouchi Y, Hasuike S, et al. Pharmacokinetic study of recombinant human

hepatocyte growth factor administered in a bolus intravenously or via portal vein. Hepatol Res 2004;30:175-181.

13) Ido A, Moriuchi A, Numata M, Murayama T, Teramukai S, Marusawa H, et al. Safety and pharmacokinetics of recombinant human hepatocyte growth factor (rh-HGF) in patients with fulminant hepatitis: a phase I/II clinical trial, following preclinical studies to ensure safety. J Transl Med 2011;9:55.
14) Xue F, Takahara T, Yata Y, Minemura M, Morioka CY, Takahara S, et al. Attenuated acute liver injury in mice by naked hepatocyte growth factor gene transfer into skeletal muscle with electroporation. Gut 2002;50:558-562.
15) Tao Y, Wang M, Chen E, Tang H. Liver regeneration: analysis of the main relevant signaling molecules. Mediators Inflamm 2017;2017:4256352.
16) Chan A, Kow A, Hibi T, Di Benedetto F, Serrablo A. Liver resection in cirrhotic liver: are there any limits? Int J Surg 2020;82S:109-114.
17) Issa R, Zhou X, Trim N, Millward-Sadler H, Krane S, Benyon C, Iredale J. Mutation in collagen-1 that confers resistance to the action of collagenase results in failure of recovery from CCl4-induced liver fibrosis, persistence of activated hepatic stellate cells, and diminished hepatocyte regeneration. FASEB J 2003;17:47-49.
18) Henderson NC, Forbes SJ. Hepatic fibrogenesis: from within and outwith. Toxicology 2008;254:130-135.
19) Yagi S, Hirata M, Miyachi Y, Uemoto S. Liver regeneration after hepatectomy and partial liver transplantation. Int J Mol Sci 2020;21:8414.
20) Thorgeirsson SS. The central role of the c-Met pathway in rebuilding the liver. Gut 2012;61:1105-1106.
21) Eguchi S, Yanaga K, Okudaira S, Sugiyama N, Miyamoto S, Furui J, Kanematsu T. Changes in serum levels of hepatocyte growth factor in patients undergoing adult-to-adult living-donor liver transplantation. Transplantation 2003;76:1769-1770.
22) Chen XG, Xu CS, Liu YM. Involvement of ERK1/2 signaling in proliferation of eight liver cell types during hepatic regeneration in rats. Genet Mol Res 2013;12:665-677.
23) Fabregat I, Moreno-Càceres J, Sánchez A, Dooley S, Dewidar B, Giannelli G, ten Dijke P. TGF-β signalling and liver disease. FEBS J 2016;283:2219-2232.

A Mesenchymal-epithelial transition factor-Agonistic Antibody Accelerates Cirrhotic Liver Regeneration and Improves Mouse Survival Following Partial Hepatectomy

Kuai Ma,[1,2] Weitao Que,[1] Xin Hu,[1] Wen-Zhi Guo,[3] Er-li Gu,[2] Liang Zhong,[4] Virginia Morello,[5] Manuela Cazzanti,[5] Paolo Michieli,[5,6] Terumi Takahara,[7] and Xiao-Kang Li[1,3]

[1]Division of Transplantation Immunology, National Research Institute for Child Health and Development, Tokyo, Japan; [2]Department of Gastroenterology and Hepatology, Jing'an District Central Hospital, Jing'an Branch of Huashan Hospital, Fudan University, Shanghai, China; [3]Department of Hepatobiliary and Pancreatic Surgery, The First Affiliated Hospital of Zhengzhou University, Zhengzhou, China; [4]Department of Gastroenterology, Huashan Hospital, Fudan University, Shanghai, China; [5]AgomAb Therapeutics NV, Gent, Belgium; [6]Molecular Biotechnology Center, University of Torino Medical School, Torino, Italy; and [7]Third Department of Internal Medicine, University of Toyama, Toyama, Japan

Small-for-size syndrome (SFSS) is a common complication following partial liver transplantation and extended hepatectomy. SFSS is characterized by postoperative liver dysfunction caused by insufficient regenerative capacity and portal hyperperfusion and is more frequent in patients with preexisting liver disease. We explored the effect of the Mesenchymal-epithelial transition factor (MET)-agonistic antibody 71D6 on liver regeneration and functional recovery in a mouse model of SFSS. Male C57/BL6 mice were exposed to repeated carbon tetrachloride injections for 10 weeks and then randomized into 2 arms receiving 3 mg/kg 71D6 or a control immunoglobulin G (IgG). At 2 days after the randomization, the mice were subjected to 70% hepatectomy. Mouse survival was recorded up to 28 days after hepatectomy. Satellite animals were euthanized at different time points to analyze liver regeneration, fibrosis, and inflammation. Serum 71D6 administration significantly decreased mouse mortality consequent to insufficient regeneration of the cirrhotic liver. Analysis of liver specimens in satellite animals revealed that 71D6 promoted powerful activation of the extracellular signal-regulated kinase pathway and accelerated liver regeneration, characterized by increased liver-to-body weight, augmented mitotic index, and higher serum albumin levels. Moreover, 71D6 accelerated the resolution of hepatic fibrosis as measured by picrosirius red, desmin, and α–smooth muscle actin staining, and suppressed liver infiltration by macrophages as measured by CD68 and F4/80 staining. Analysis of gene expression by reverse-transcription polymerase chain reaction confirmed that 71D6 administration suppressed the expression of key profibrotic genes, including platelet-derived growth factor, tissue inhibitor of metalloproteinase 3, and transforming growth factor-β1, and of key proinflammatory genes, including tumor necrosis factor-α, interleukin-1β, chemokine (C-C motif) ligand 3, and chemokine (C-C motif) ligand 5. These results suggest that activating the MET pathway via an hepatocyte growth factor–mimetic antibody may be beneficial in patients with SFSS and possibly other types of acute and chronic liver disorders.

Liver Transplantation 0 1–12 2021 AASLD.
Received April 12, 2021; accepted September 10, 2021.

Small-for-size syndrome (SFSS) is a common yet underrecognized complication following partial liver transplantation and extended hepatectomy.(1) It is characterized by postoperative liver dysfunction caused by insufficient regenerative capacity and portal hyperperfusion and is more frequent in patients with preexisting liver disease.(2) Approximately one-third of liver transplant recipients who develop early graft failure qualify for SFSS. Small-for-size liver grafts show delayed and impaired regeneration(3) and have greater risks of failure

Abbreviations: agomAbs, agonistic monoclonal antibodies; α-SMA, α–smooth muscle actin; a.u., arbitrary units; CCL3, chemokine (C-C motif) ligand 3; CCl4, carbon tetrachloride; CCL5, chemokine (C-C motif) ligand 5; ELISA, enzyme-linked immunosorbent assay; ERK, including microcirculatory damage, inflammatory injury, and accelerated acute rejection, leading to liver failure with associated coagulopathy, ascites, prolonged cholestasis, and encephalopathy. Because of the persistent organ shortage, living donor liver transplantation is becoming the most viable option for patients with end-stage liver disease. Donor safety always comes first in living donor liver transplantation, and there is a growing momentum for the increased use of small-for-size grafts in association with hepato-regenerative therapies.(4,5)

Hepatocyte growth factor (HGF) is a pleiotropic cytokine of mesenchymal origin that plays a key role in organ regeneration.(6) Its high-affinity receptor, the MET tyrosine kinase, is mainly expressed by epithelial and endothelial cells, but it is also present on some immune cells as well as in various types of myofibroblasts.(7) In the liver, HGF is typically secreted by hepatic stellate cells (HSCs) and plays a key role in hepatic regeneration. Following injury, increased HGF secretion initiates a repair program that limits cell damage, ensures hepatocyte regeneration, inhibits myofibroblast hyperproliferation, and suppresses inflammation, restoring liver function.(8)

extracellular signal-regulated kinase; H & E, hematoxylin-eosin; HGF, hepatocyte growth factor; hMET, human mesenchymal-epithelial transition factor; HSCs, hepatic stellate cells; IgG, immunoglobulin G; IgG1, immunoglobulin G1; IL-1β, interleukin-1β; IP, intraperitoneally; IV, intravenously; mMET, mouse mesenchymal-epithelial transition factor; mRNA, messenger RNA; N/A, Not applicable; PCNA, proliferating cell nuclear antigen; PDGF, platelet-derived growth factor; PSR, picrosirius red; qRT-PCR, quantitative reverse-transcription polymerase chain reaction; RT-PCR, reverse-transcription polymerase chain reaction; SD, standard deviation; SFSS, small-for-size syndrome; TIMP3, tissue inhibitor of metalloproteinase 3; TNF-α, tumor necrosis factor-α.

Address reprint requests to Paolo Michieli, Ph.D., Molecular Biotechnology Center, University of Torino Medical School, Via Nizza 52, I-10126 Torino, Italy. Telephone: +39 11 670 64 99; E-mail: paolo.michieli@unito.it

Address reprint requests to Terumi Takahara, M.D., Ph.D., Third Department of Internal Medicine, University of Toyama, 2630 Sugitani, Toyama, 930-0194 Japan. Telephone: +81 76-434-502; E-mail: terutaka-tym@umin.ac.jp

Address reprint requests to Xiao-Kang Li, M.D., Ph.D., Division of Transplantation Immunology, National Research Institute for Child Health and Development, 2-10-1 Okura, Setagaya-ku, Tokyo, 157-8535 Japan. Telephone: +81-3-3416-0181; FAX: +81-3-3417-2864; E-mail: ri-k@ncchd.go.jp

This study was supported in part by the Ministry of Education, Culture, Sports, Science and Technology of Japan (Grants-in-Aid 16K11064, 24/17H04277, and 18K08558), the National Center for Child Health and Development (Grant 29-09), and Science and Technology Innovation Talents in Henan Universities (no. 19HASTIT003).

Manuela Cazzanti, Paolo Michieli, and Virginia Morello consult for, own stock in, and are employed by AgomAb Therapeutics NV.

DOI 10.1002/lt.26301

Despite the broad therapeutic potential of HGF in liver diseases, its translation to the clinic has been challenging. In fact, HGF does not display ideal drug-like properties: its very short plasma half-life (a few minutes) causes an unfavorable pharmacokinetics because of its high avidity for the extracellular matrix, it has a poor biodistribution; it needs proteolytic activation to acquire biological activity, and once activated it is unstable; lastly, its industrial manufacture is difficult and costly. To overcome the limitations of HGF and to generate a drug that could effectively promote liver regeneration in patients, we generated a series of anti-MET agonistic monoclonal antibodies ("agomAbs") that bind to MET at high affinity and determine MET activation, mimicking the biochemical and biological activity of HGF. AgomAbs combine the powerful therapeutic potential of HGF with the excellent pharmacokinetic, pharmacodynamic, and manufacturing properties of antibodies.

In this study, we explored the therapeutic potential of 71D6, a fully agonistic anti-MET antibody that cross-reacts with rodent, nonhuman primate, and human MET in a mouse model of SFSS.

Materials and Methods

SERUM 71D6 ANTIBODY GENERATION AND CHARACTERIZATION

Serum 71D6 was generated by immunization of *Llama glama* using the SIMPLE antibody platform.(9) A detailed description of its generation and characterization has been published previously.(10) Binding of 71D6 to MET and HGF-mediated and 71D6-mediated MET autophosphorylation and analysis of MET downstream signaling were performed as described.(10)

ANIMAL MODEL

Mouse procedures were authorized by the National Research Institute for Child Health and Development (permission no. A2014-010-C06). The 8-week-old male C57BL/6JJmsSLc mice (Shizuoka Laboratory Animal Center, Shizuoka, Japan) were subjected to repeated subcutaneous injection of 10% carbon tetrachloride (CCl4; Wako) dissolved in olive oil (100 μL/mouse) twice a week for 10 weeks. On the day of the last CCl4 administration, the mice were randomized into 2 arms receiving 3 mg/kg of 71D6 or a control antibody against the F glycoprotein of respiratory syncytial virus(11) (both in the mouse immunoglobulin G1 [IgG1] format). At 2 days after randomization, all of the mice were subjected to 70% hepatectomy by removal of the anterior 2 lobes and posterior left lobe. The 71D6 or control IgG were administered intraperitoneally (IP) at a dose of 3 mg/kg 2 days before hepatectomy and at days 0, 2, 4, 6, 8, 10, and 12. Mice recruited in the trial included main study animals and satellite animals. The spontaneous survival rate of the main study animals was recorded from days 0 to 28. Satellite animals (3 mice per group) were euthanized at 3, 7, and 28 days after hepatectomy. Serum and liver samples were stored at −80°C.

SERUM BIOCHEMICAL MEASUREMENTS

Serum was collected from whole-blood samples after standing for 30 minutes at 37°C and then centrifuged at 1800*g* for 25 minutes at 4°C. Serum samples were then analyzed for serum albumin concentrations using a commercially available kit (Fujifilm) and an automatic biochemical analyzer (DRI-CHEM 3500i; Fujifilm) according to the manufacturer's instructions. Serum HGF concentration was measured using the mouse/rat HGF Quantikine enzyme-linked immunosorbent assay (ELISA) kit (R&D Systems). Serum 71D6 concentration was determined by ELISA as described.(10)

HISTOPATHOLOGICAL AND IMMUNOHISTOCHEMICAL EXAMINATION

Both the liver portion extracted at the time of hepatectomy and that collected at autopsy were processed for histopathological examination. Liver tissues were fixed in 10% formalin for 48 hours, routinely processed, and sliced into sections of 4 μm in thickness. For detection of liver fibrosis, sections were stained with picrosirius red (PSR; Sigma-Aldrich), anti–α-smooth muscle actin (α-SMA) antibodies (AbCam) and anti-desmin antibodies (Boehringer). For detection of macrophage infiltration, sections were stained with antibodies against CD68 (AbCam) and F4/80 (AbCam). For detection of liver proliferation, sections were stained with anti–proliferating cell nuclear antigen (PCNA) antibodies (Dako). Sections were also stained with hematoxylin-eosin (H & E) and periodic acid–Schiff (both from Sigma-Aldrich). After staining, specimens were photographed under a microscope (Olympus). Histological and immunohistochemical results were quantified using WinRoof 7.4 software (Mitani Corporation).

TOTAL MESSENGER RNA PREPARATION AND QUANTITATIVE REVERSE-TRANSCRIPTION POLYMERASE CHAIN REACTION ANALYSIS

Total messenger RNA (mRNA) was extracted from frozen liver tissues using RNeasy Mini Kit (Qiagen). Each 0.8 μg aliquot of mRNA was reverse transcribed to complementary DNA using a Prime Script reverse-transcription (RT) reagent kit (RR037A; Takara). Quantitative reverse-transcription polymerase chain reaction (qRT-PCR) was performed using the SYBR Green system or the primer/probe set system (primer sequences are listed in Table 1) the Applied Biosystem PRISM7900 apparatus (Thermo Fisher Scientific) is a machine which is used to do RT-PCR. The PCR cycle conditions for the SYBR Green system were 95°C for 3 minutes, 45 cycles of 95°C for 3 seconds, and 60°C for 30 seconds. The PCR cycle conditions for the primer/probe set system were 50°C for 2 minutes, 95°C for 15 minutes, 40 cycles of 95°C for 30 seconds, 60°C for 1 minute, and 25°C for 2 minutes. The comparative threshold cycle (ΔΔCt) method was used for determining relative gene expression, and the results of target genes (including fibrosis-related genes and inflammation-related genes) were normalized by subtracting *18S* expression values.

IN VIVO ANALYSIS OF EXTRACELLULAR SIGNAL-REGULATED KINASE ACTIVATION

Frozen liver tissue was homogenized in radio immunoprecipitation assay buffer containing 1% protease inhibitor cocktail-1 and 1% protease inhibitor cocktail-2 (Sigma-Aldrich) followed by centrifugation in a microfuge at top speed for 30 minutes. Protein concentrations were assayed using a Protein Assay kit (Bio-Rad). Samples were separated by electrophoresis on

TABLE 1. Primers and Probes Used in This Study

Genes (PCR)	Forward (5′–3′)	Reverse (5′–3′)	Probe
TIMP3 (SYBR Green)	CACAAAGTTGCACAGTCCTG	TTTGTCGCCTCAAGCTAGA	N/A
PDGF (SYBR Green)	TACAGTTGCACTCCCAGGAAT	CTTCCAGTTGACAGTTCCGCA	N/A
TGF-β (SYBR Green)	ATCCTGTCCAAACTAAGGCTCG	ACCTCTTTAGCATAGTAGTCCGC	N/A
TNF-α (SYBR Green)	AAGCCTGTAGCCCACGTCGTA	GGCACCACTAGTTGGTTGTCTTTG	N/A
CCL5 (SYBR Green)	TGCCCTCACCATCATCCTCACT	GGCGGTTCCTTCGAGTGACA	N/A
IL-1β (SYBR Green)	ACCTTCCAGGATGAGGACATGA	AACGTCACACACCAGCAGGTTA	N/A
18S (SYBR Green)	ATGAGTCCACTTTAAATCCTTTAACGA	CTTTAATATACGCTATTGGAGCTGGAA	N/A
CCL3 (Taqman)	ACCCAGGTCTCTTTGGAGTCAGCGCA	TCCCAGCCAGGTGTCATTTTC	AGGCATTCAGTTCCAGGTCAG
18S (Taqman)	ATCCATTGGAGGGCAAGTCTGGTGC	ATGAGTCCACTTTAAATCCTTTAACGA	CTTTAATATACGCTATTGGAGGCTGGAA

NOTE: Liver-specific expression of profibrotic and proinflammatory genes determined by SYBR green PCR or Taqman PCR as indicated in the table. N/A, Not applicable.

10% polyacrylamide gels and transferred to Immobilon (Bio-Rad) polyvinylidene fluoride. After brief incubation with 5% nonfat milk to block nonspecific binding, membranes were exposed overnight at 4°C to specific phosphorylated anti-p44/p42 extracellular signal-regulated kinase (ERK) antibodies (Cell Signaling Technology). Membranes were washed and exposed to alkaline phosphatase-conjugated secondary antibodies and visualized by incubation in 5% nonfat milk. Phosphorylated p44/p42 ERK activity was quantified by laser densitometric analysis of the radiographic film using ImageJ software (National Institutes of Health, Bethesda, MD).

STATISTICAL ANALYSIS

Prism7 software (GraphPad, San Diego, CA) was used to calculate statistical significance. A 2-way analysis of variance method and Student *t* test method were used for comparisons between groups. Survival rate analysis was performed using a log-rank (Cox-Mantel) test. Data are expressed as mean ± standard deviation (SD). A value of $P < 0.05$ was considered to be statistically significant.

Results

SERUM 71D6 BINDS TO MET AT HIGH AFFINITY AND PROMOTES MET ACTIVATION, MIMICKING HGF

HGF-mimetic, agonistic anti-MET antibodies were generated by immunization of *L. glama* using the SIMPLE antibody platform.[(9)] Their biochemical and biological characterizations have been published previously.[(10)] Among these molecules, which include both partial and full agonists of MET, serum 71D6 represents the most potent fully agonistic antibody. Serum 71D6 was produced as a chimera between variable llama regions and human or mouse IgG1/λ constant regions. Serum 71D6 bound to either the human MET (hMET) or mouse MET (mMET) extracellular domain with the concentration for 50% of maximal effect in the picomolar range (Fig. 1A). Stimulation of immortalized mouse liver cells with 71D6 or HGF resulted in a similar dose-dependent activation of MET and of its downstream signaling (Fig. 1B). An overlapping pattern of MET activation and signaling was observed in MET-expressing human epithelial cells of various origin (not shown).

SYSTEMIC 71D6 ADMINISTRATION RESULTS IN BIOLOGICALLY SIGNIFICANT PLASMA LEVELS

The pharmacokinetic properties of 71D6 were tested in various mouse strains using various routes of administration. In all studies, increasing doses of the antibody were delivered as a single bolus, and antibody levels in plasma were determined at different time points using a MET-based ELISA assay. Table 2 shows the results obtained in a representative study conducted by IP injection. Serum 71D6 concentration reached a peak 8 hours after injection (65 nM at 1 mg/kg and 2638 nM at 30 mg/kg). After 2 days, plasma 71D6 levels showed only a minor deflection (38 nM at 1 mg/kg and 2466 nM at 30 mg/kg). After 8 days, all dose levels except the lowest were still detectable

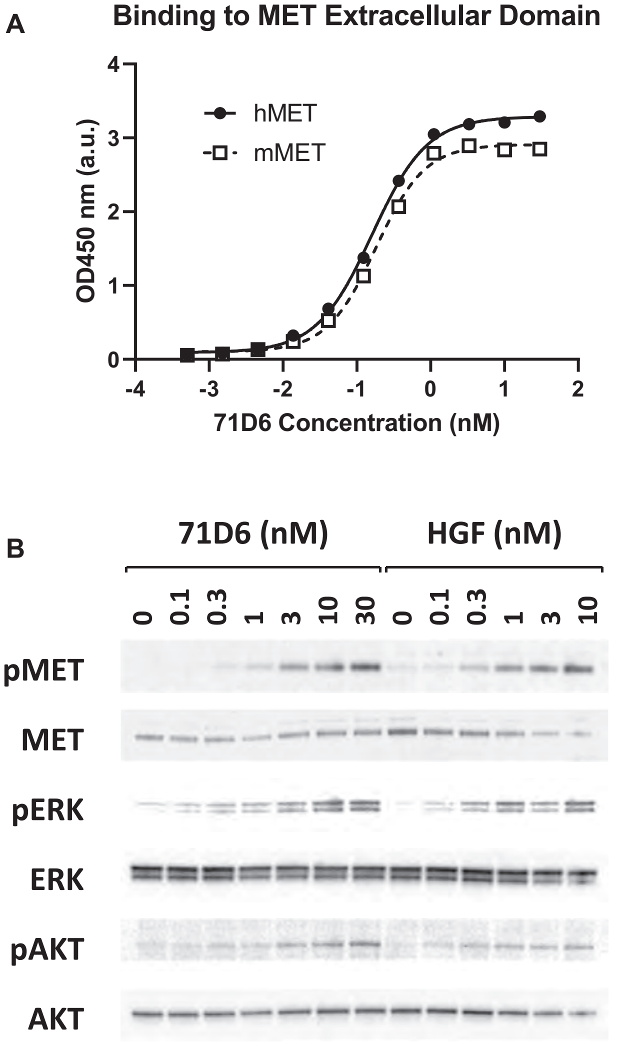

FIG. 1. 71D6 binds to MET at high affinity and elicits MET activation and downstream signaling, mimicking HGF function. (A) 71D6 binding to hMET or mMET extracellular domain was analyzed by ELISA (a.u.). (B) MET activation and downstream signaling induced by HGF or 71D6 was studied in human mouse MLP29 liver precursor cells. Cell lysates were analyzed by Western blotting using antibodies specific for the phosphorylated forms of MET, ERK, and AKT (pMET, pERK and pAKT) as well as antibodies against total MET, ERK, and AKT.

and well in the nanomolar range. Based on these data, the mean plasma half-life of 71D6 corresponded to approximately 5 days (note that recombinant HGF has a half-life of a few minutes in both rodents(12) and humans).(13) Considering that in normal, healthy mice endogenous HGF plasma levels range from 1 to 10 pM(14) and that in the MET phosphorylation assays shown in Fig. 1B both HGF and 71D6 reached saturation at about 10 nM, the concentrations reached following IP injections of 71D6 shown in Table 2 are certainly relevant from a biologic viewpoint.

SERUM 71D6 DISPLAYS A POTENT HEPATOTROPHIC ACTIVITY IN MICE

The biological effects of 71D6 administration were compared with those of recombinant HGF in vivo. In a first experiment, a single bolus of 1 mg/kg of either 71D6 or HGF was administered intravenously (IV) to adult Balb-c mice. Liver-to-body weight ratio and serum albumin levels were measured 4 and 10 days later. As shown in Fig. 2A, 71D6 administration resulted in a marked increase in liver weight both at day 4 (91%) and at day 10 (42%). In contrast, recombinant HGF administration promoted only a minor increase in liver weight (20% at day 4 and 0% at day 10). Serum albumin levels, expression of the synthetic activity of the liver, were invariably higher in the 71D6-treated mice, confirming the superior potency of the antibody. In a second experiment, we aimed at compensating the shorter half-life of HGF with more frequent administration. Because of the challenge of IV injecting the same animals multiple times, IP injection was preferred. Mice were injected IP with either a single bolus of 1 mg/kg 71D6 or with 1 mg/kg recombinant HGF every 12 hours for 5 days. Mice were euthanized at day 6 and subjected to the same analysis as noted previously. Even when administered more frequently, HGF could not match the potent hepatotrophic activity of 71D6. In fact, mice injected with a single bolus of 71D6 displayed a 70% larger liver compared with controls, whereas animals injected repeatedly with HGF showed a modest 10% increase in liver weight (Fig. 2B). Similarly, 71D6 injection resulted in 121% higher albumin levels compared with controls, whereas HGF injection increased serum albumin secretion by 52%. Therefore, 71D6 elicits a significantly more potent hepatotrophic effect in mice compared with recombinant HGF.

SERUM 71D6 PROMOTES LIVER REGENERATION AND INCREASES SURVIVAL IN MICE UNDERGOING CCl4 INJURY AND PARTIAL HEPATECTOMY

Prompted by the previous results, we evaluated the therapeutic effect of 71D6 on liver regeneration in a

TABLE 2. **Pharmacokinetic Properties of 71D6**

Dose (mg/kg)	Maximum Concentration (nM)	Day 2 Concentration (nM)	Day 8 Concentration (nM)
1	65 ± 3	38 ± 6	0 ± 0
3	271 ± 56	249 ± 70	17 ± 12
10	1265 ± 270	1062 ± 114	257 ± 27
30	2638 ± 327	2466 ± 494	446 ± 45

NOTE: 71D6 concentration in plasma was determined at different time points following IP injection of different dose levels of antibody as a single bolus. Values represent the mean ± standard deviation of at least 3 biological replicates.

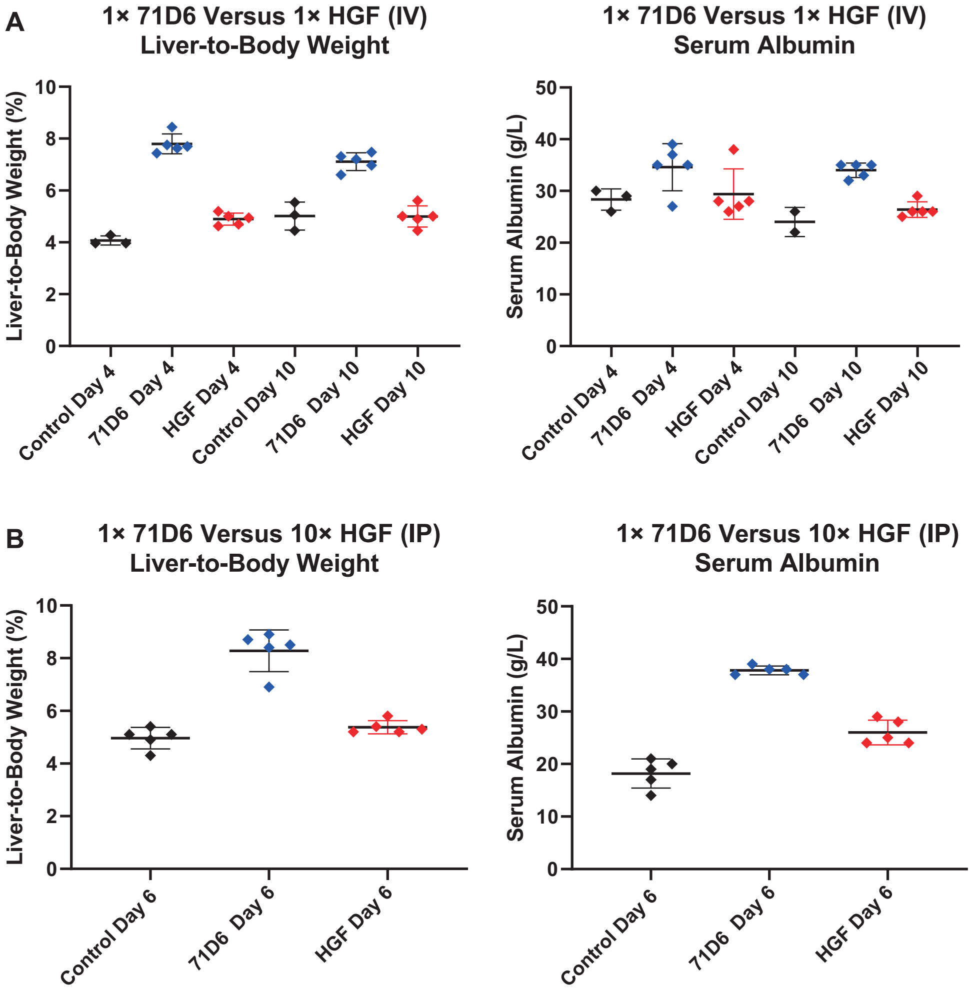

FIG. 2. 71D6 displays a potent hepatotrophic activity in mice. (A) A single 1 mg/kg bolus of 71D6 or human recombinant HGF was injected IV into adult Balb-c mice, and the liver-to-body weight and serum albumin levels were determined 4 and 8 days afterward. (B) A single 1 mg/kg bolus of 71D6 or multiple doses (10 over 5 days) of 1 mg/kg recombinant human HGF were injected IP into adult Balb-c mice. Liver-to-body weight and serum albumin levels were determined 6 days after the first injection. Black represents control group. Red represents HGF group. Blue represents 71D6 group.

mouse model of SFSS. This model reproduces the impaired regenerative capacity of the liver in patients with cirrhosis or other hepatic diseases. Mice were subjected to chronic CCl4 intoxication for 10 weeks and then randomized into 2 arms receiving either 3 mg/kg 71D6 or a control IgG1. At 3 days after randomization, all mice were subjected to 70% hepatectomy. Mouse survival was recorded up to 28 days after hepatectomy.

Satellite animals were euthanized at different time points to analyze liver regeneration, fibrosis, and inflammation. This hepatectomy model typically presents high mortality within 4 days after surgery. Remarkably, the survival rate observed in the 71D6-treated group was significantly higher than that observed in the control group ($P = 0.03$). Although only 5 of 24 mice (21%) in the control group survived for 28 days after hepatectomy, 7 of 13 71D6-treated mice (54%) were alive at the end of the experiment (Fig. 3A). As shown in Fig. 3B, 71D6 also accelerated body weight recovery following surgery compared with controls ($P < 0.001$). Liver weight was also evaluated upon autopsy of satellite animals at various time intervals. As shown in Fig. 3C, 71D6 significantly increased the liver-to-body weight ratio at most time points analyzed (days 1 and 3, $P < 0.05$; day 7, nonsignificant; day 28, $P < 0.001$). Consistent with these findings, serum albumin levels in 71D6-treated animals increased (Fig. 3D) and showed a significant difference with the control group starting on day 7 ($P < 0.01$) and reaching a peak on day 28 ($P < 0.01$). These data indicate that 71D6 treatment promotes liver regeneration and accelerates recovery of liver function after partial hepatectomy.

SERUM 71D6 PROMOTES HEPATIC PROLIFERATION FOLLOWING HEPATECTOMY THROUGH ACTIVATION OF THE ERK SIGNALING PATHWAY

Hepatocyte proliferation following hepatectomy was assessed by staining liver sections with anti-PCNA

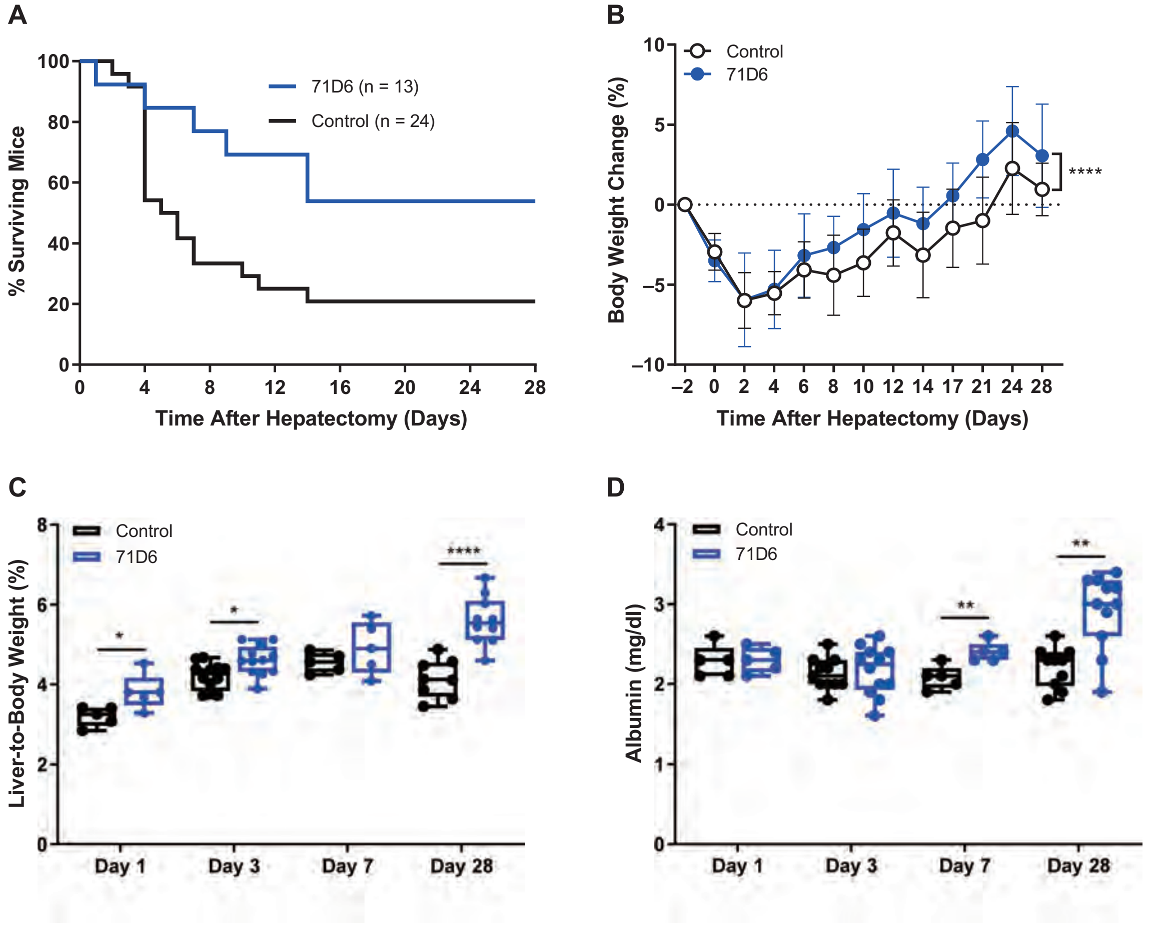

FIG. 3. 71D6 promotes liver regeneration and increases survival in mice undergoing CCl4 injury and partial hepatectomy. (A) Kaplan-Meier curve analysis of mouse survival ($P = 0.03$). (B) Body weight change over time (mean ± SD) ($P < 0.001$). (C) Liver-to-body weight over time (days 1 and 3, $P < 0.05$; day 7, nonsignificant; day 28, $P < 0.001$). (D) Serum albumin levels over time (days 1 and 3, nonsignificant; day 7, $P < 0.01$; day 28, $P < 0.01$).

antibodies. As shown in Fig. 4A, the number of PCNA-positive cells was higher in the 71D6-treated group starting at day 3 and peaking at day 28. To further characterize 71D6-induced liver proliferation, we analyzed the expression and activation of p44 ERK1 and p42 ERK2, a key event in the postinjury liver regeneration program.(15) This analysis revealed that 71D6 significantly increased the levels of phosphorylated (activated) ERK1/2 on both day 3 and day 28 following hepatectomy (Fig. 4B). Activation of ERK1/2 directly correlated with PCNA expression, suggesting that 71D6 stimulates activation of ERK1/2 in the remnant liver, resulting in accelerated hepatic regeneration. Notably, however, no ERK1/2 activation was detected in control animals despite hepatectomy typically inducing spontaneous liver regeneration within a few days. This could be attributed to, and is consistent with, the impaired regenerative capacity of a cirrhotic liver. To cast light onto the mechanism underlying this regenerative impairment, we analyzed serum HGF levels in posthepatectomy mice as well as in healthy, naïve animals. This analysis revealed that posthepatectomy mice treated with the control IgG protein displayed only a marginal increase in HGF levels compared with naïve mice (Fig. 3C). Interestingly, serum HGF levels were slightly higher in the 71D6 group, probably because of larger liver mass and/or increased hepatic function. In any case, serum HGF levels were confined to the picomolar range, whereas 71D6 levels measured in the same samples remained well above MET saturating levels for the entire duration of the study (full activation of MET is reached with 10 nM 71D6). These results explain the absence of ERK activation and the poor liver regeneration observed in the control group on one hand and justify the superior regenerative ability of the animals treated with 71D6 on the other hand.

SERUM 71D6 AMELIORATES HEPATIC FIBROSIS AFTER PARTIAL HEPATECTOMY ON CIRRHOTIC BACKGROUND

Sections of livers harvested from satellite animals were stained with H & E, PSR, and antibodies against

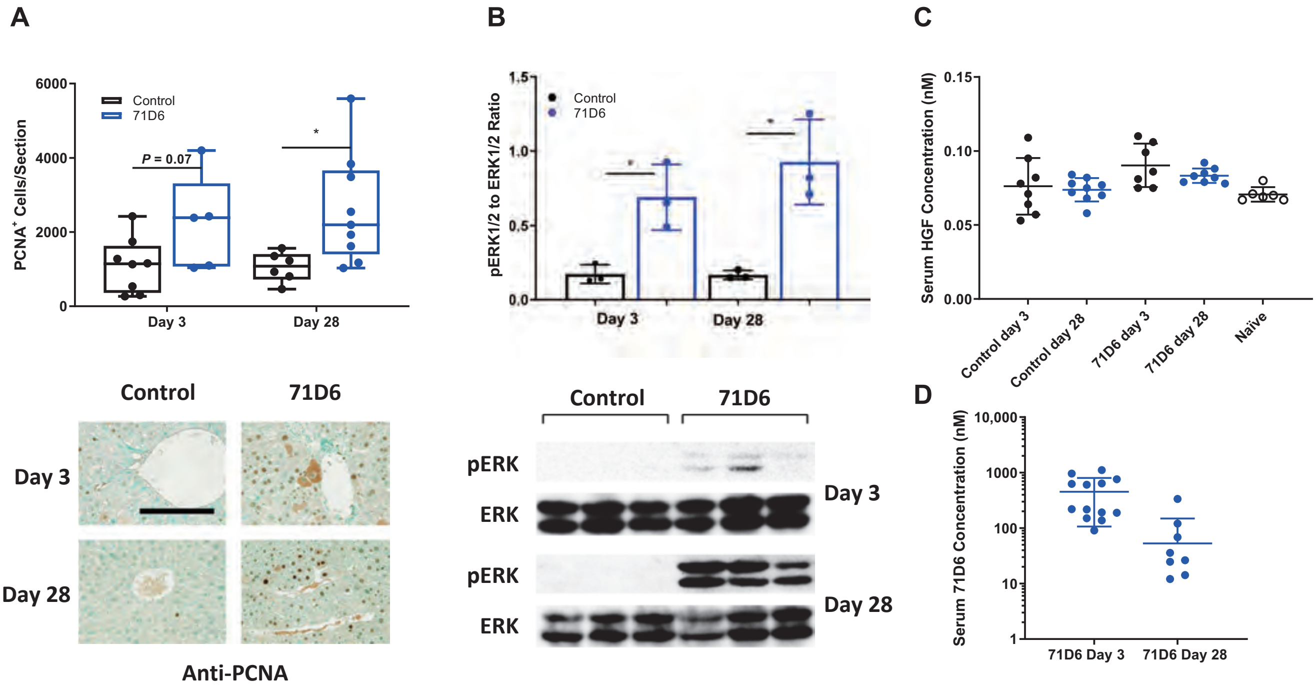

FIG. 4. 71D6 promotes hepatic proliferation following hepatectomy of cirrhotic mice through activation of the ERK signaling pathway. (A) Hepatic proliferation is expressed as the number of PCNA-positive cells per liver section analyzed. Representative images are shown below the graph. The bar is 250 μM. (B) The levels of phosphorylated and total ERK1/2 (p44/p42) were determined by Western blot analysis of liver samples. The ratio between phosphorylated ERK1/2 and total ERK1/2 was determined by densitometric analysis. (C) Serum HGF levels in mice of the control and 71D6 groups as well as in healthy, naïve animals were determined by ELISA. (D) Serum 71D6 levels in mice of the 71D6 group were determined by ELISA.

desmin or α-SMA. Liver specimens of the control group showed consistent formation of thin fibrotic septa at the portal and central areas on day 3. Although milder, fibrosis was still present at day 28. Control liver sections also displayed high density of myofibroblasts. In contrast, liver specimens of the 71D6 group showed significantly milder signs of fibrosis and a reduced presence of myofibroblasts already at day 3. Liver fibrosis was quantified and expressed as the percentage of PSR-positive area (Fig. 5A), number of desmin-positive cells (Fig. 5B), and percentage of α-SMA–positive area (Fig. 5C). To further strengthen these results, the expression of fibrosis-related genes was analyzed by quantitative RT-PCR. This analysis revealed that 71D6 significantly reduced mRNA expression of platelet-derived growth factor (*PDGF*), tissue inhibitor of metalloproteinase 3 (*TIMP3*), and transforming growth factor β1 (*TGF-β1*), which are involved in collagen deposition and activation of HSCs (Fig. 5D). Together, these results suggest that in mice subjected to CCl4 treatment and partial hepatectomy, the agonistic anti-MET antibody 71D6 effectively accelerates the regression of hepatic fibrosis by inhibiting the activation of multiple fibrogenic pathways.

SERUM 71D6 REDUCES MACROPHAGE INFILTRATION IN THE REGENERATING LIVER

Liver specimens extracted at autopsy were analyzed by immunohistochemistry using antibodies against F4/80 and CD68. The number of cells positive for F4/80 ($P < 0.05$; Fig. 6A) and CD68 ($P < 0.0001$; Fig. 6B) was significantly lower in the 71D6 group compared with the control group on day 28. Consistent with histological findings, mRNA levels of inflammatory cytokine genes (tumor necrosis factor α [*TNF-α*], interleukin 1β [*IL1β*], chemokine [C-C motif] ligand 3 [*CCL3*], and chemokine [C-C motif] ligand 5 [*CCL5*]) were significantly lower in the liver homogenates of 71D6-treated mice compared with control mice on day 28 ($P < 0.05$; Fig. 6C).

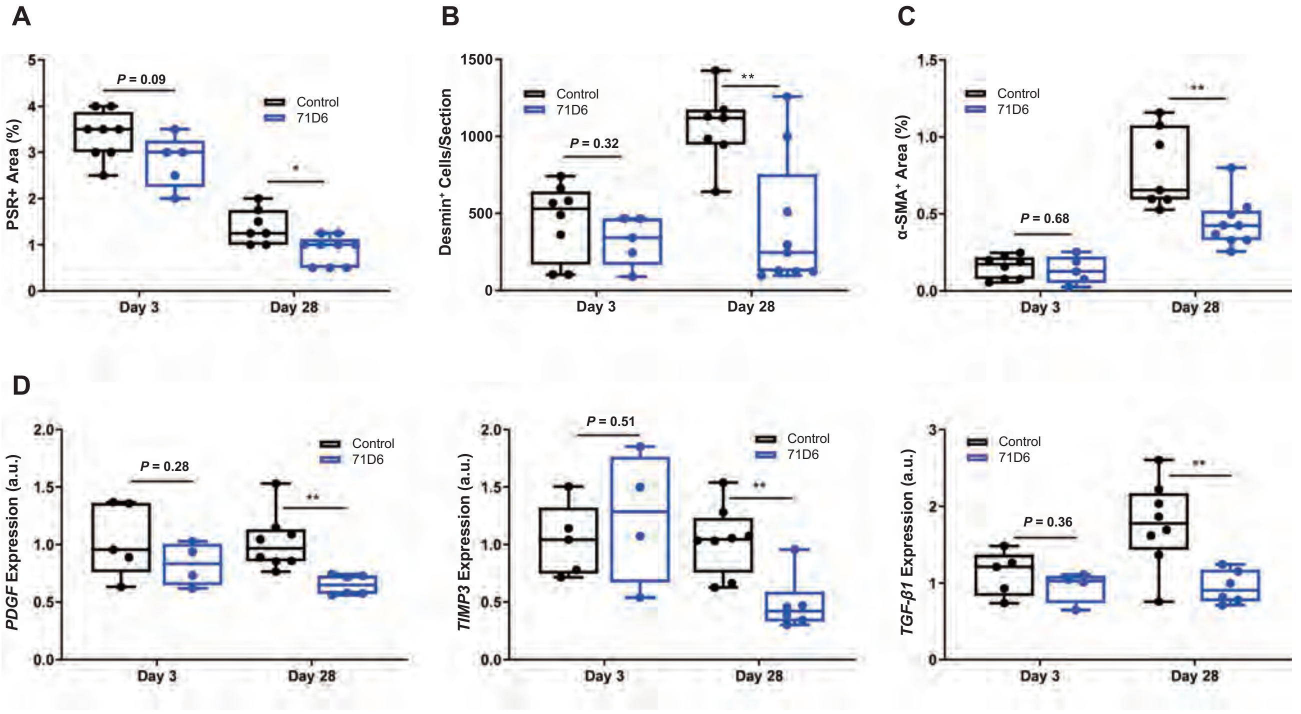

FIG. 5. 71D6 ameliorates hepatic fibrosis after partial hepatectomy on cirrhotic background. (A) Liver sections were stained with PSR. Data are expressed as percentage of PSR-positive area. (B) Liver sections were stained with anti-desmin antibodies. Data are expressed as number of desmin-positive cells per section analyzed. (C) Liver sections were stained with anti–α-SMA antibodies. Data are expressed as percentage of α-SMA–positive area. (D) Liver specimens were analyzed by RT-PCR to determine the levels of *PDGF*, *TGF-β1*, and *TIMP3* expression. Data are expressed as a.u.

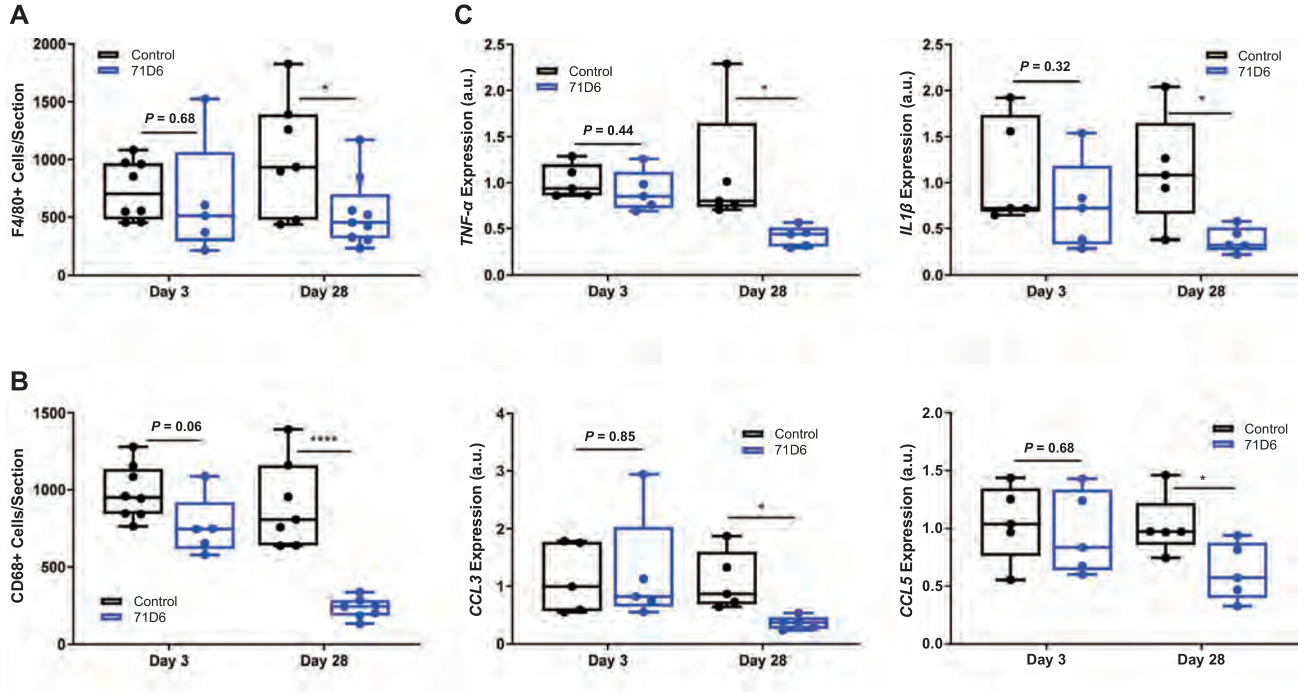

FIG. 6. 71D6 reduces macrophage infiltration in the regenerating liver. (A) Liver sections were stained with anti-F4/80 antibodies. Data are expressed as number of F4/80-positive cells per section analyzed. (B) Liver sections were stained with anti-CD68 antibodies. Data are expressed as number of CD68-positive cells per section analyzed. (C) Liver specimens were analyzed by RT-PCR to determine the levels of *TNF-α*, *IL1β*, *CCL3*, and *CCL5* expression. Data are expressed as a.u.

Discussion

Liver failure is prone to occur after liver transplantation or extended resection when the size and function of the remnant liver is unable to meet the metabolic demand of the patient. SFSS limits the use of living donor and split-liver transplants, and lifesaving large resections of tumors or nonmalignant lesions may be limited by concerns of postsurgical liver failure. Furthermore, SFSS is analogous to end-stage liver disease where the functional liver mass no longer meets metabolic demand. Therefore, there is a major need for effective therapies capable of enhancing and accelerating liver regeneration.

Most studies evaluating regenerative therapies take advantage of the 70% hepatectomy model in mice or rats. In this model, 70% of the liver, usually the median and left lateral lobes, is surgically removed. In response to this, the remnant liver enlarges until it restores normal mass and function. Although the liver has a remarkable potential for regeneration, this regenerative capacity becomes impaired with serious liver fibrosis.(16) The transition of quiescent HSCs to activated, scar-forming, myofibroblast-like cells leads to excessive extracellular matrix synthesis.(17,18) This abnormal scar formation in the liver has been shown to hold back hepatocyte proliferation. In the present study, we studied a newly developed agonistic anti-MET antibody that increased hepatocyte proliferation after partial hepatectomy in mice with CCl4-induced liver disease.

Following 70% hepatectomy, both hepatocytes and nonparenchymal cells are activated and integrate multiple signals originating from immune, hormonal, and metabolic networks to induce liver regeneration.(19) Within this process, the activation of HGF/MET signaling pathway has been demonstrated to be 1 of the essential mechanisms that lead hepatocytes into the cell cycle after hepatectomy.(20) Following resection, HGF protein levels in plasma typically rise,(21) but liver fibrosis is known to prevent this process. The lack of HGF induction on a cirrhotic background was fully confirmed in our study (Fig. 4C). To circumvent defective endogenous HGF activation, we employed the 71D6 agonistic anti-MET antibody. When bound by 71D6, the MET receptor dimerizes and becomes phosphorylated on tyrosine residues to initiate MET downstream signaling (Fig. 1).

The results presented here indicate that liver-to-body weight ratio increased very slowly in the control group, whereas it increased markedly and constantly in the 71D6-treated group (Fig. 3). Quantitative analysis of PCNA immunostaining also confirmed that the agonistic anti-MET antibody potently promotes hepatocyte proliferation (Fig. 4A). We also clarified the involvement of the ERK1/2 signaling pathway in this hepato-proliferative effect. It is known that the Ras/Raf/MEK/ERK cascade has the ability to lead to cellular responses, including proliferation. The ERK1/2 signaling pathway can also regulate the hepatocyte proliferative response during the regeneration of normal liver.(22) Our Western blot results showed that 71D6 strongly activated ERK p44/p42, closely reflecting the high levels of PCNA expression (Fig. 4B). Our results clearly show that 71D6 has the ability to mimic HGF signaling in vivo, including activation of downstream kinases and promotion of hepatocyte proliferation. However, in contrast to HGF, 71D6 is very stable in vivo (Table 2) and displays superior pharmacodynamic properties (Fig. 2). These results highlight the therapeutic potential of 71D6 in liver regeneration.

Liver fibrosis is an inadequate wound-healing response to chronic liver injury and is characterized by the excessive deposition and reduced degradation of the extracellular matrix. Excessive accumulation of extracellular matrix alters the hepatic architecture to progress to liver fibrosis, and if not prevented it may eventually lead to cirrhosis and even liver cancer. Our study provides evidence that 71D6 treatment leads to a significantly lower degree of collagen, desmin, and α-SMA compared with controls (Fig. 5A,B). This is explained by the direct inhibition of multiple fibrogenic pathways including those controlled by *PDGF*, *TIMP3*, and *TGF-β1* (Fig. 5C). These data support the hypothesis that 71D6 has the ability to antagonize TGF-β1 directly so as to reduce liver fibrosis and improve liver regeneration.(23)

Furthermore, our study showed that 71D6 also inhibited the infiltration of inflammatory cells into the liver. In fact, the number of F4/80-positive and CD68-positive cells in the 71D6 group was significantly lower than that observed in the control group (Fig. 6A,B). Consistent with these findings, qRT-PCR analysis revealed that the expressions of proinflammatory cytokines and chemokines such as TNF-α, IL1β, CCL3, and CCL5 were much lower in the liver homogenates of 71D6-treated mice compared with control animals (Fig. 6C).

Thus, not only does 71D6 overcome the inability of a cirrhotic liver to regenerate following hepatectomy, but it also achieves faster resolution of fibrosis and the effective suppression of inflammation. Together, these results suggest that activating the MET pathway via an HGF-mimetic antibody may be beneficial in patients with SFSS and possibly other types of acute and chronic liver disorders.

Acknowledgments: The authors thank Philippe Wiesel for critically reading the manuscript, Luca Rossi for in vivo work, Damiana Sattanino for assay setup, and the entire AgomAb team for continuous support.

REFERENCES

1) Riddiough GE, Christophi C, Jones RM, Muralidharan V, Perini MV. A systematic review of small for size syndrome after major hepatectomy and liver transplantation. HPB 2020;22:487-496.
2) Masuda Y, Yoshizawa K, Ohno Y, Mita A, Shimizu A, Soejima Y. Small-for-size syndrome in liver transplantation: definition, pathophysiology and management. Hepatobiliary Pancreat Dis Int 2020;19:334-341.
3) Zhong Z, Schwabe RF, Kai Y, He L, Yang L, Bunzendahl H, et al. Liver regeneration is suppressed in small-for-size liver grafts after transplantation: involvement of c-Jun N-terminal kinase, cyclin D1, and defective energy supply. Transplantation 2006;82:241-250.
4) Greenbaum LE, Ukomadu C, Tchorz JS. Clinical translation of liver regeneration therapies: a conceptual road map. Biochem Pharmacol 2020;175:113847.
5) Forbes SJ, Newsome PN. Liver regeneration—mechanisms and models to clinical application. Nat Rev Gastroenterol Hepatol 2016;13:473-485.
6) Nakamura T, Mizuno S. The discovery of hepatocyte growth factor (HGF) and its significance for cell biology, life sciences and clinical medicine. Proc Jpn Acad Ser B Phys Biol Sci 2010;86:588-610.
7) Matsumoto K, Funakoshi H, Takahashi H, Sakai K. HGF-Met pathway in regeneration and drug discovery. Biomedicines 2014;2:275-300.
8) Nakamura T, Sakai K, Nakamura T, Matsumoto K. Hepatocyte growth factor twenty years on: much more than a growth factor. J Gastroenterol Hepatol 2011;26(suppl 1):188-202.
9) Klarenbeek A, Blanchetot C, Schragel G, Sadi AS, Ongenae N, Hemrika W, et al. Combining somatic mutations present in different in vivo affinity-matured antibodies isolated from immunized *Lama glama* yields ultra-potent antibody therapeutics. Protein Eng Des Sel 2016;29:123-133.
10) Michieli P. Anti-Met antibodies and uses thereof. European patent application EP 3475302 A1 2019. https://www.lens.org/lens/patent/062-815-545-734-095.
11) Cingoz O. Motavizumab. mAbs 2009;1:439-442.
12) Ido A, Moriuchi A, Kim I, Numata M, Nagata-Tsubouchi Y, Hasuike S, et al. Pharmacokinetic study of recombinant human

hepatocyte growth factor administered in a bolus intravenously or via portal vein. Hepatol Res 2004;30:175-181.
13) Ido A, Moriuchi A, Numata M, Murayama T, Teramukai S, Marusawa H, et al. Safety and pharmacokinetics of recombinant human hepatocyte growth factor (rh-HGF) in patients with fulminant hepatitis: a phase I/II clinical trial, following preclinical studies to ensure safety. J Transl Med 2011;9:55.
14) Xue F, Takahara T, Yata Y, Minemura M, Morioka CY, Takahara S, et al. Attenuated acute liver injury in mice by naked hepatocyte growth factor gene transfer into skeletal muscle with electroporation. Gut 2002;50:558-562.
15) Tao Y, Wang M, Chen E, Tang H. Liver regeneration: analysis of the main relevant signaling molecules. Mediators Inflamm 2017;2017:4256352.
16) Chan A, Kow A, Hibi T, Di Benedetto F, Serrablo A. Liver resection in cirrhotic liver: are there any limits? Int J Surg 2020;82S:109-114.
17) Issa R, Zhou X, Trim N, Millward-Sadler H, Krane S, Benyon C, Iredale J. Mutation in collagen-1 that confers resistance to the action of collagenase results in failure of recovery from CCl4-induced liver fibrosis, persistence of activated hepatic stellate cells, and diminished hepatocyte regeneration. FASEB J 2003;17:47-49.
18) Henderson NC, Forbes SJ. Hepatic fibrogenesis: from within and outwith. Toxicology 2008;254:130-135.
19) Yagi S, Hirata M, Miyachi Y, Uemoto S. Liver regeneration after hepatectomy and partial liver transplantation. Int J Mol Sci 2020;21:8414.
20) Thorgeirsson SS. The central role of the c-Met pathway in rebuilding the liver. Gut 2012;61:1105-1106.
21) Eguchi S, Yanaga K, Okudaira S, Sugiyama N, Miyamoto S, Furui J, Kanematsu T. Changes in serum levels of hepatocyte growth factor in patients undergoing adult-to-adult living-donor liver transplantation. Transplantation 2003;76:1769-1770.
22) Chen XG, Xu CS, Liu YM. Involvement of ERK1/2 signaling in proliferation of eight liver cell types during hepatic regeneration in rats. Genet Mol Res 2013;12:665-677.
23) Fabregat I, Moreno-Càceres J, Sánchez A, Dooley S, Dewidar B, Giannelli G, ten Dijke P. TGF-β signalling and liver disease. FEBS J 2016;283:2219-2232.

www.nature.com/scientificreports

scientific reports

OPEN

Coral calcium carried hydrogen ameliorates the severity of non-alcoholic steatohepatitis induced by a choline deficient high carbohydrate fat-free diet in elderly rats

Kuai Ma[1], Xin Hu[1], Keiki Nambu[2], Daisuke Ueda[3], Naotsugu Ichimaru[4], Masayuki Fujino[1,5]✉ & Xiao-Kang Li[1]✉

Hydrogen has been reported to act as an antioxidant, anti-apoptosis and anti-inflammatory agent. Coral calcium carried hydrogen (G2-SUISO) is a safer and more convenient form of hydrogen agent than others. The mechanism underlying the hepatoprotective effects of G2-SUISO using an elderly non-alcoholic steatohepatitis (NASH) rat model was investigated. Two days after fasting, six-month-old elderly male F344/NSlc rats were given a choline deficient high carbohydrate fat-free (CDHCFF) diet from day 0 to day 3 as CDHCFF control group, and then switched to a normal diet from days 4 to 7 with or without 300 mg/kg G2-SUISO. Rats in each group were finally being sacrificed on day 3 or day 7. In the CDHCFF diet group, G2-SUISO decreased the liver weight-to-body weight ratio, the serum AST, ALT, total cholesterol levels, inflammatory infiltration, pro-inflammatory cytokine expression and lipid droplets with inhibiting lipogenic pathways by reducing sterol regulatory element-binding protein-1c, acetyl-CoA carboxylase and fatty acid synthase gene expression compared with the CDHCFF diet alone. G2-SUISO had beneficial effects of anti-apoptosis as well the down-regulation of pro-apoptotic molecules including NF-κB, caspase-3, caspase-9 and Bax. These findings suggest that G2-SUISO treatment exerts a significant hepatoprotective effect against steatosis, inflammation and apoptosis in elderly NASH rats.

Abbreviations

ACC	Acetyl-CoA carboxylase
ALT	Alanine transaminase
AST	Aspartate transaminase
Bax	Bcl-2-associated X
CCR2	C–C chemokine receptor type 2
CDHCFF	Choline deficient high carbohydrate fat-free
FAS	Fatty acid synthase
FFAs	Free fatty acids
G2-SUISO	Coral calcium carried hydrogen G2
HCC	Hepatocellular carcinoma
H_2	Hydrogen
HSCs	Hepatic stellate cells

[1]Division of Transplantation Immunology, National Research Institute for Child Health and Development, 2-10-1 Okura, Setagaya-ku, Tokyo 157-8535, Japan. [2]Acche Corporation, Tokyo, Japan. [3]Division of Hepato-Pancreato-Biliary Surgery and Transplantation, Department of Surgery, Kyoto University Graduate School of Medicine, Kyoto, Japan. [4]Department of Urology, Kinki Central Hospital, Hyogo, Japan. [5]Management Department of Biosafety, Laboratory Animal, and Pathogen Bank, National Institute of Infectious Diseases, 1-23-1, Toyama, Shinjuku-ku, Tokyo 162-8640, Japan. ✉email: mfujino-kkr@umin.ac.jp; ri-k@ncchd.go.jp

IL-6	Interleukin 6
IL-1β	Interleukin-1 beta
IFN-γ	Interferon-gamma
iNOS	Inducible nitric oxide synthase
LDs	Lipid droplets
mRNA	Messenger RNA
NASH	Non-alcoholic steatohepatitis
NAFLD	Non-alcoholic fatty liver disease
NFκB	Nuclear factor-κB
OB-R	Leptin receptor
OPN	Osteopontin
ROS	Reactive oxygen species
RT-PCR	Real time-polymerase chain reaction
SREBP-1c	Sterol regulatory element-binding protein-1c
TC	Total cholesterol
TNF-α	Tumor necrosis factor-alpha

Non-alcoholic fatty liver disease (NAFLD) is the most common chronic liver disorder associated with metabolic dysfunction and is a leading cause of cirrhosis and hepatocellular carcinoma (HCC) with a global prevalence of 25%[1]. It usually develops in the absence of excessive alcohol consumption and is associated with an unhealthy diet and lack of physical activity. Non-alcoholic steatohepatitis (NASH) is a progressive form of NAFLD, characterized by chronic inflammation and hepatocyte injury due to fat accumulation[2]. A community-based study found that fatty liver is prevalent in the elderly population, with a prevalence of over 40%[3].

Aging is a complex phenomenon characterized by the gradual decline of the tissue and organ function accompanying the irreversible age-related loss of viability. Impairment of the liver function and development of NAFLD are common among the elderly[4]. Accumulating evidence has pointed out that the process of aging itself markedly increases the prevalence of metabolic syndrome in humans, reportedly being a risk factor of NAFLD[5], as it predisposes individuals to hepatic functional and structural impairment and metabolic risk. Oxidative stress is considered the primary cause of general aging as well as diseases associated with aging, especially metabolic diseases[6]. Oxidative stress, lipotoxicity and inflammation[7] have been shown to play central roles in the development and progression of NAFLD. Furthermore, the progressively increased production of reactive oxygen species (ROS) during the aging process contributes to the accumulation of lipids, particularly cholesterol, in the liver of elderly individuals[8].

Molecular hydrogen (H_2) was previously reported to act as an antioxidant for preventive and therapeutic applications by selectively alleviating cytotoxic oxygen radicals without affecting other ROS[9]. Previous studies have reported that H_2 functions as an antioxidant, anti-apoptosis and anti-inflammatory agent in many animal models and human clinical studies[10]. Among these studies, H_2 administration can be roughly divided into inhaling H_2 gas, drinking H_2 dissolved water and injecting H_2 dissolved saline[11]. In our present study, we used coral calcium carried hydrogen (G2-SUISO), which is a safer and more convenient form of H_2 agent than others, as the source of H_2. In general, H_2 cannot be kept in supplements as-is. Coral powder was therefore selected as the material to convey H_2, and we employed a unique method to successfully immobilize H_2 on the surface of the carrier coral calcium. When the coral calcium enters the body, hydrogen is generated upon contact with moisture.

The present study investigated the potential effects of G2-SUISO with the goal of evaluating whether or not G2-SUISO could attenuate the severity of NASH induced by a choline deficient high carbohydrate fat-free (CDHCFF) diet in elderly rats.

Results

G2-SUISO attenuated CDHCFF-induced nonalcoholic steatohepatitis.

As shown in Fig. 1B and Supplementary Fig. 3A, the liver weight-to-body weight ratio in the 3d_control group was significantly higher ($p < 0.0001$) than that in the Naïve group, while this value was lower ($p < 0.01$) in the 3d_G2 group. Furthermore, the liver weight-to-body weight ratio in the 7d_G2 group was down-regulated ($p < 0.05$) compared with the 7d_control group as well. The above results suggested that CDHCFF administration resulted in liver enlargement, and going back to eating normal diet again with G2-SUISO treatment significantly attenuated this CDHCFF-induced liver enlargement.

NASH is characterized as the excessive accumulation of TC in lipid droplets (LDs) in hepatocytes, and ALT and AST activities are important biomarkers of liver damage or diseases[8]. G2-SUISO significantly reduced the serum ALT, AST and TC levels in elderly NASH rats (Fig. 1C). The serum ALT and AST levels both notably differed between the 3d_control group and 3d_G2 group ($p < 0.001$), indicating that a CDHCFF diet caused severe hepatocellular injury in rats. Compared with the 3d_control group, the serum ALT and AST levels in the 3d_G2 group were markedly decreased. In addition, the serum TC levels were higher in the 3d/7d_control group than in the 3d/7d_G2 group ($p < 0.05$ and $p < 0.05$, respectively) suggesting that G2-SUISO had notable effects of attenuating CDHCFF-induced NASH. In contrast, serum triglyceride (TG) was significantly decreased by CDHCFF diet and G2-SUISO treatment showed comparable concentrations (Supplementary Fig. 3B). Based on the HE staining of liver specimens in Fig. 1D, we observed that the normal liver showed a clear and homogeneous texture, while the CDHCFF groups developed hepatocyte steatosis, ballooning and inflammatory cell infiltration on day 3 that was relieved on day 7. Compared with the CDHCFF diet groups, hepatocyte ballooning and steatosis in rat specimens were clearly reduced in the G2-SUISO groups on days 3 and 7 (Fig. 1E, $p < 0.001$, $p < 0.001$, respectively), suggesting that G2-SUISO ameliorated hepatic steatosis in NASH rats.

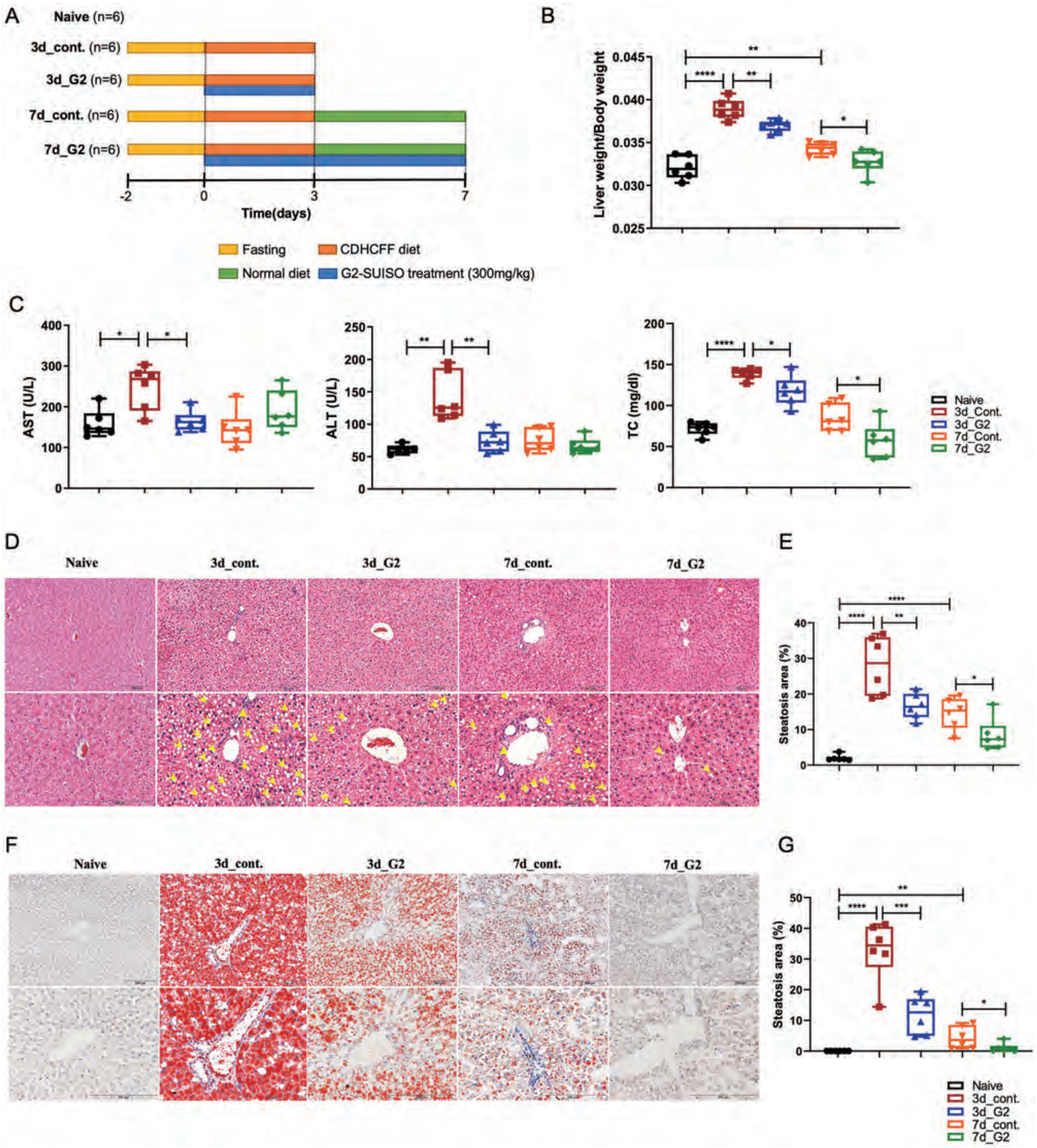

Figure 1. G2-SUISO attenuated CDHCFF-induced nonalcoholic steatohepatitis. (**A**) The experimental design and timeline of the groups was shown. (**B**) The liver weight-to-body weight ratio in the five groups is shown. (**C**) G2-SUISO treatment significantly reduced serum ALT, AST and TC levels in NASH rats. (**D**) Hematoxylin and eosin (HE) staining of liver specimens in different groups suggested that G2-SUISO improved hepatic steatosis in NAFLD rats. The yellow triangle represents the area of inflammatory cell infiltration. White vacuoles showed lipids (yellow arrow) in HE staining (magnification × 100 & × 200). (**E**) An analysis of the HE staining of fatty liver specimens is shown. Each bar represents the mean ± SD. (**F**) Liver sections of five groups were stained by Oil Red O solution. Red areas showed lipids in Oil Red O staining (magnification × 100 & × 200). (**G**) An analysis of the Oil Red O staining of fatty liver specimens is shown. Each bar represents the mean ± SD; *$p < 0.05$, **$p < 0.01$, ***$p < 0.001$, ****$p < 0.0001$.

To further explore the protective effects of G2-SUISO on reducing steatosis in elderly NASH rats, liver sections from the five groups were subjected to Oil red O staining, which was used to measure fat loading in the hepatocytes. Based on Fig. 1F, we can see that G2-SUISO decreased intracellular lipid deposition in the livers of the CDHCFF group. A histological analysis of Oil Red O staining revealed a significant increase in intracellular lipid deposition in the livers of the 3d_CDHCFF group and 7d_CDHCFF group ($p < 0.0001$ and $p < 0.01$, respectively) (Fig. 1G). Numbers of LDs were markedly reduced in the livers of G2-SUISO-treated mice on days 3 and 7 ($p < 0.001$ and $p < 0.05$, respectively).

G2-SUISO exerted protective effects against inflammation. Among cytokine-related to the progression of NASH, tumor necrosis factor-alpha (TNF-α) plays a pivotal role in the inflammatory pathogenesis of NASH[12]. As shown in Fig. 2A, hepatic mRNA expression of inflammatory cytokine-related genes, particularly TNF-α, inducible nitric oxide synthase (iNOS), osteopontin (OPN), interferon-gamma (IFN-γ), interleukin-1 beta (IL)-1β, IL-6 and C–C chemokine receptor type 2 (CCR2), were significantly higher following administration of an CDHCFF diet. In contrast, the expression of TNF-α, iNOS and CCR2 was lower in the 3d_G2 group than in the 3d_control group ($p < 0.01$, $p < 0.05$ and $p < 0.01$, respectively). The IFN-γ, OPN, IL-1β and IL-6 expression was down-regulated as well but without a significant difference. After the administration of G2-SUISO for 7 days, TNF-α and IL-1β showed notable reductions in expression ($p < 0.01$ and $p < 0.01$, respectively). The infiltration of neutrophils in liver was assessed using chloroacetate esterase staining of liver specimens. The hepatic expression of neutrophils was significantly increased in the CDHCFF diet control group compared with Naïve group on days 3 and 7 ($p < 0.05$ and $p < 0.05$, respectively) (Fig. 2B,C). Following the administration of G2-SUISO, the neutrophil numbers in NASH liver specimens were reduced on days 3 and 7 ($p < 0.05$ and $p < 0.05$, respectively), and only a few scattered inflammatory foci were observed compared with

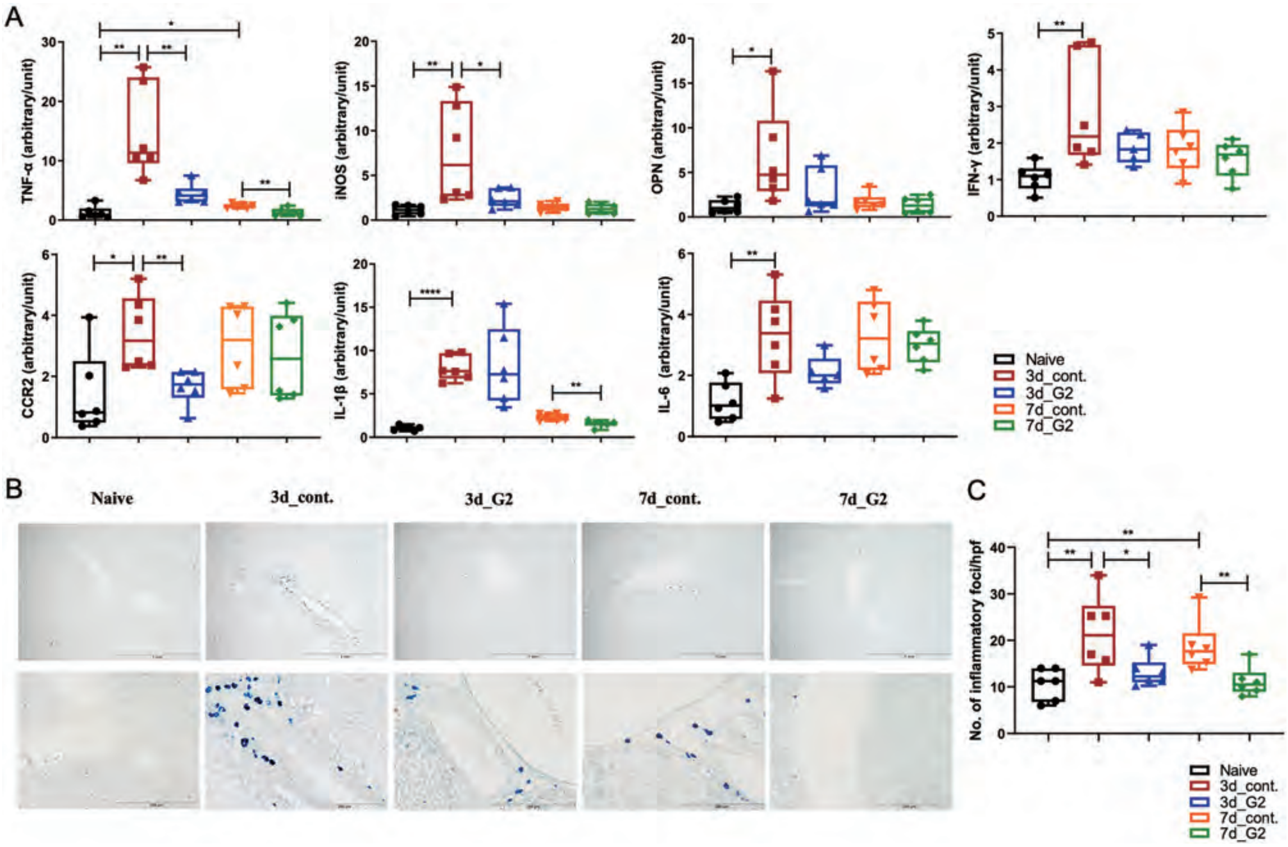

Figure 2. G2-SUISO reduced the mRNA expression of inflammatory cytokine-related genes. (**A**) Homogenates of liver tissues were analyzed by qRT-PCR, as described in the Materials and Methods. The mRNA expression of inflammatory cytokine-related genes, particularly TNF-α, iNOS and CCR2, was significantly lower in the 3d_G2 group than in the 3d_control group. The mRNA expression of inflammatory cytokine-related genes, such as IFN-γ, OPN, IL-1β and IL-6, tended to be down-regulated following G2-SUISO treatment. Values are expressed as the mean ± SD in arbitrary units; $^{*}p < 0.05$, $^{**}p < 0.01$, $^{****}p < 0.0001$. (**B**) Chloroacetate esterase staining of liver specimens with inflammatory foci in the five groups is shown (magnification × 40 & × 200). (**C**) Analysis results of chloroacetate esterase staining of fatty liver specimens are shown. A total of 4 high power fields (hpf) (× 40) were randomly selected from each liver specimens (n = 5), and the number of inflammatory foci was counted. The data are expressed as the cell number/high-power field. Each bar represents the mean ± SD; $^{*}p < 0.05$.

the control group. In addition, the infiltration of T cells and macrophages in the liver was also analyzed using CD3 and ED1 monoclonal antibody. Both expressions in the liver specimens were increased in the 3d_CDHCFF group compared to the Naïve group ($p<0.01$ and $p<0.01$, respectively), and G2-SUISO treatment decreased the infiltration of CD3- and ED1-positive cells (Supplementary Fig. 2). Taken together, these findings suggested that G2-SUISO might prevent inflammation and inflammatory cell infiltration in the NASH elderly model liver.

G2-SUISO exerted anti-apoptotic effects. Previous studies have reported that increased hepatocyte apoptosis may play an important role in controlling the development of NASH[13]. As shown in Fig. 3A, the mRNA expression of apoptosis-related molecules, particularly Bax, caspase-1, caspase-3 and NF-κB, was markedly up-regulated in the 3d_CDHCFF control group compared with Naïve group ($p<0.0001$, $p<0.001$, $p<0.0001$ and $p<0.0001$, respectively). The mRNA expression of Bax showed a significant decrease ($p<0.05$) in the 7d_G2 group, and that of caspase-1, caspase-3 and NF-κB showed decreasing trend. Furthermore, the mRNA expression of caspase-3 in the 3d_G2 group showed decreasing trend compared with the 3d_control group.

To confirm the anti-apoptosis effect of G2-SUISO, we measured the protein levels of caspase-1, caspase-3, caspase-9 and NF-κB in liver tissues in the Naïve group, 3d_control group and 3d_G2 group by Western blotting (Fig. 3B). After a densitometric analysis of the signals, we found that the expression of caspase-3, caspase-9 and NF-κB was significantly reduced by the treatment of G2-SUISO ($p<0.05$, $p<0.01$ and $p<0.05$, respectively), whereas the caspase-1 expression showed no significant difference from before treatment.

G2-SUISO reduced steatosis in CDHCFF-induced NASH. As a pathological analysis showed that G2-SUISO reduced the lipid deposition caused by an CDHCFF diet in the liver (Fig. 1C–F), the mRNA expression of fatty acid uptake- and lipid metabolism-related cytokine-related genes in the five groups, particularly leptin receptor (OB-R), fatty acid synthase (FAS) and acetylCoA carboxylase (ACC), as well as sterol regulatory element-binding protein-1c (SREBP-1c) was measured. In Fig. 4, the mRNA expression of the OB-R, ACC and FAS genes increased significantly in the 3d_CDHCFF control group compared with the Naïve group ($p<0.001$, $p<0.0001$ and $p<0.0001$, respectively). The SREBP-1c gene expression in the 3d_CDHCFF control group also showed an increasing trend but without significance. G2-SUISO markedly down-regulated the expression of OB-R compared with the 3d_CDHCFF control group ($p<0.05$) and tended to down-regulate the expression of ACC and SERBP-1c. After 7 days of G2-SUISO administration, the mRNA expression of SREBP-1c, ACC

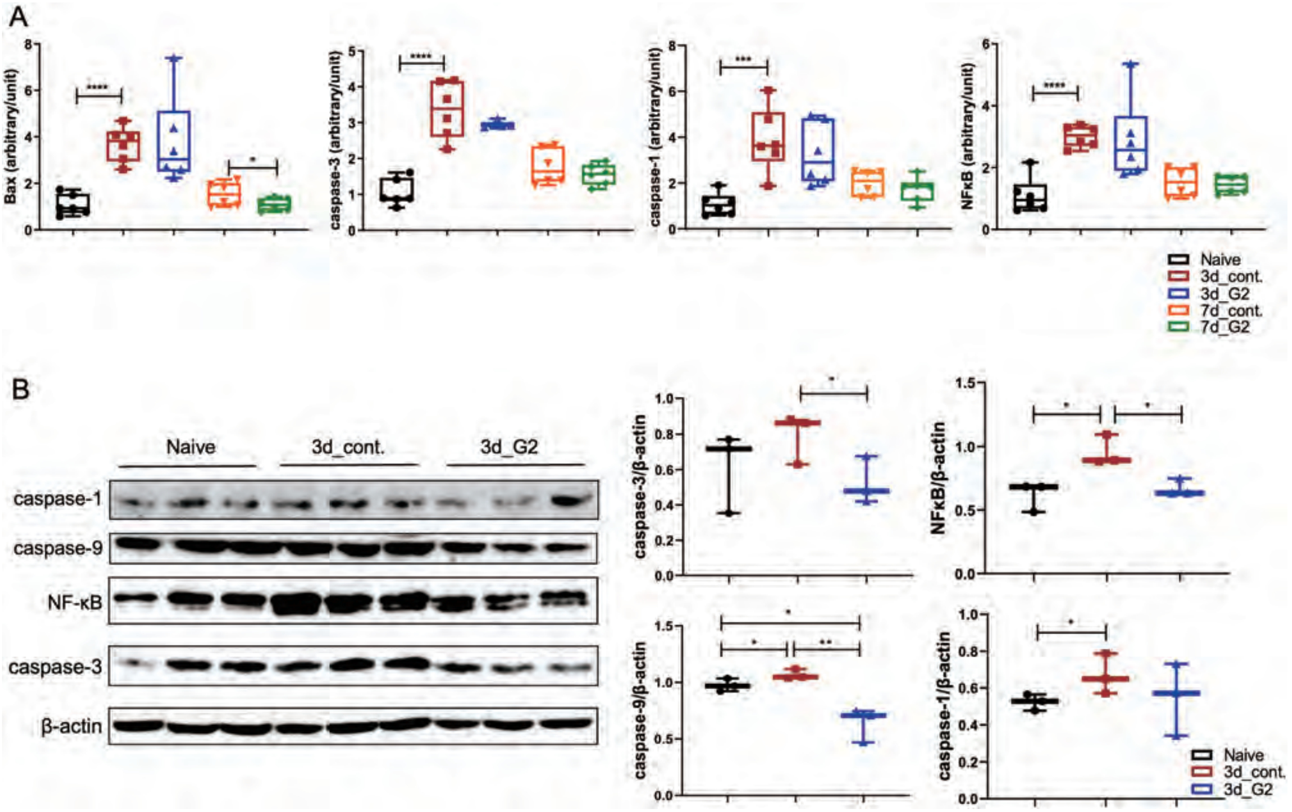

Figure 3. G2-SUISO reduced the mRNA expression of apoptotic molecules. (**A**) The mRNA expression of apoptosis-related genes in the five groups, particularly Bax, caspase-1, caspase-3 and NF-κB, is shown. (**B**) Results of a Western blot analysis of caspase-1, caspase-3, caspase-9 and NF-κB levels in the liver tissue of the Naïve group, 3d_control group and 3d_G2 group are shown. Data are expressed as the mean ± SD; $^{*}p<0.05$, $^{**}p<0.01$, $^{***}p<0.001$, $^{****}p<0.0001$.

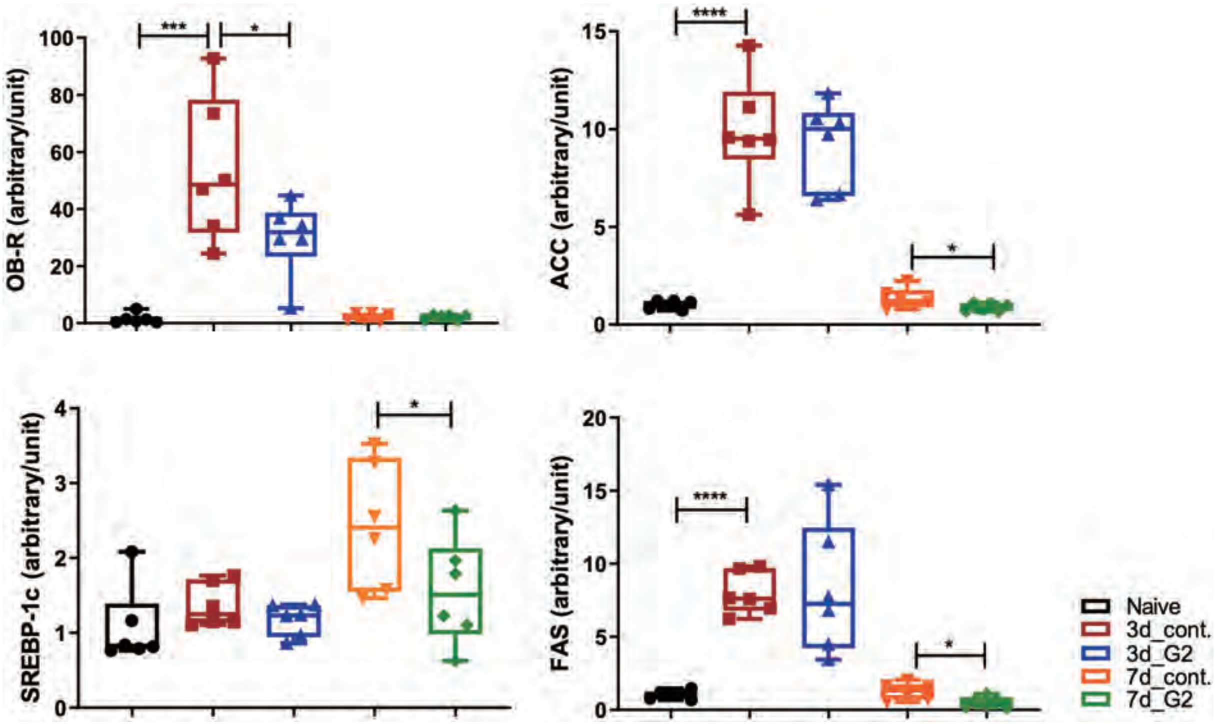

Figure 4. G2-SUISO reduced hepatocyte steatosis in CDHCFF diet-induced nonalcoholic steatohepatitis rat. The mRNA expression of fatty acid uptake- and lipid metabolism-related genes in the five groups, particularly leptin receptor (OB-R), fatty acid synthase (FAS) and acetylCoA carboxylase (ACC), as well as sterol regulatory element-binding protein-1c (SREBP-1c) are shown. Data are expressed as the mean ± SD; $^{*}p < 0.05$, $^{**}p < 0.01$, $^{***}p < 0.001$, $^{****}p < 0.0001$.

and FAS showed significant reductions ($p < 0.05$, $p < 0.05$ and $p < 0.05$, respectively). Furthermore, the mRNA expression of cholesterol metabolism genes, such as sterol regulatory element binding protein-2 (SREBP-2) or hydroxymethyl-glutaryl-CoA reductase (HMGCR) genes was increased by CDHCFF diet and G2-SUISO treatment showed the trend of decrease of the expression of these mRNA expression (Supplementary Fig. 3C).

Discussion

The prevalence of NAFLD has increased significantly in parallel with increasing rates of obesity, now being the most common cause of chronic liver disease worldwide[14]. NAFLD is reported to be a heterogeneous disease with a high prevalence in elderly patients, characterized by the accumulation of TG and fatty acids in hepatocytes[15]. Compared with younger groups, NAFLD in the elderly may carry a more substantial burden of hepatic and extrahepatic manifestations and complications[16]. Indeed, in our NASH model, aged rats showed more severe hepatitis when fed an CDHCFF diet than young rats (Supplementary Fig. 1). H_2 has been reported to act as a therapeutic antioxidant by selectively reducing cytotoxic oxygen radicals, potentially leading to therapeutic effects in a variety of diseases, such as ischemia–reperfusion injury, colitis, NASH and aging-related diseases [9,17–20]. G2-SUISO is widely used in dietary supplement products (https://acche.co.jp/supplement/items_platinum/) as a safe and effective form of antioxidant with minimal side effects. This study demonstrated the promising potential effects of G2-SUISO in a rat elderly model of NASH.

In this study, we used a CDHCFF diet, which is one of the useful methods, to generate our NASH rat model[21,22]. As expected, CDHCFF diet-fed rats exhibited increased adipose tissue weights and liver weight-to-body weight ratios compared to the Naïve group (Fig. 1). In addition, the liver pathology summarized the major features of human NASH, including steatosis, ballooning degeneration and inflammation. With this model, the hepatic lipogenic/inflammation/apoptosis gene expression and serum biochemical markers, such as AST, ALT and TC, attenuation by G2-SUISO showed convincing results for estimating the effect of the drug in our research. Oxidative stress and inflammation are the main components that contribute to the pathogenesis of NASH. It is widely acknowledged that TNF-α expression increases in cases of obesity and plays a major role in the inflammatory pathogenesis of NASH[23]. Enrichment of innate immune cells and increased inflammation are hallmarks of NASH. Increasing evidence supports that neutrophils play a key role in the onset of NASH, and histological findings from human liver biopsies suggest that enhanced infiltration of neutrophils is one of the key histological features of NASH[24,25]. Activation of the transcription factor NF-κB also results in production of key chemokines for neutrophil recruitment[26]. Steatosis is reported to lead to increased signaling of the transcription factor NF-κB, which can induce the production of pro-inflammatory mediators, such as TNF-α, IL-6 and IL-1β[27]. In addition, these pro-inflammatory cytokines contribute to the recruitment and activation of Kupffer cells to mediate inflammation in NASH. In our study, the mRNA expression of TNF-α significantly decreased following the administration of G2-SUISO to our rat NASH model (Fig. 2). The expression of other pro-inflammatory mediators, including IFN-γ, OPN, IL-1β, CCR2, iNOS and IL-6, was markedly increased under CDHCFF diet. Following G2-SUISO treatment, most of these cytokines showed a down-regulated trend, suggesting that G2-SUISO might have an anti-inflammatory effect. As shown in Fig. 3, down-regulation of NF-κB by G2-SUISO is one of the possible reason for the reduction of pro-inflammatory molecules, while the mechanism of NF-κB suppression by H_2 is still unclear[28]. Other reasons may include induction of anti-inflammatory molecules. The trend toward enhanced mRNA expression of HO-1 was observed by G2-SUISO administration (data not shown) and several studies demonstrated that HO-1 inhibit NF-κB[29–31].

Previous studies have reported that cell death, including apoptosis, seems to play a vital role in the progression of NASH[13]. Apoptotic hepatocytes stimulate immune cells and hepatic stellate cells (HSCs) to progress to NASH and fibrosis through the production of inflammasomes and cytokines. NF-κB is a master regulator of inflammation and cell death in the development of various liver diseases, such as NAFLD, hepatocellular injury, liver fibrosis and HCC[32]. The activation of NF-κB in Kupffer cells or infiltrating monocytes is pro-inflammatory and induces the expression of death ligands, such as TNF-α[33]. Caspases are related to the induction of apoptosis, which is a mode of cell death regulated by homeostasis, supporting the coordinated demolition and clearance of aging and damaged cells[34]. Bax belongs to the Bcl-2 protein family, and its pro-apoptotic function has been confirmed in many studies[35]. The expression of these pro-apoptotic molecules was significantly up-regulated in the CDHCFF diet control group on day 3 (Fig. 3). The administration of G2-SUISO then down-regulated the pro-apoptosis molecules, such as NF-κB and caspases, on day 3 according to our Western blot analyses. These findings suggest that G2-SUISO may prevent apoptosis in the NASH model liver by inhibiting the expression of pro-apoptotic molecules.

In the present study, G2-SUISO attenuated lipid accumulation in CDHCFF-induced NASH in elderly rats. The reverse alterations in the hepatic lipid accumulation can be explained by the effects of G2-SUISO on lipid metabolism. Previous studies have shown that the excessive hepatic accumulation of TG and FFAs induces hepatic steatosis[36,37]. The present study demonstrated that treatment with G2-SUISO ameliorated the lipid accumulation in the liver of CDHCFF diet rats via the modulation of lipid metabolism-related molecules. The hepatic uptake of fatty acids is thought to occur via several mechanisms, including a transporter-mediated mechanism. In patients with NAFLD, the hepatic expression of fatty acid synthesis genes and fatty acid oxidation-related genes is up-regulated. ACC catalyzes the production of malonyl-CoA and is a major building block for de novo lipogenesis, promoting the oxidation of FFAs[38]. SREBP-1c is a transcription factor that is a major regulator of FAS and other lipogenic proteins and is essential for the utilization and storage of glucose carbon[39]. It regulates the onset of the lipogenic program and is able to bind to the promoters of several lipogenesis enzyme genes and induce their expression[40]. The activity of the SREBP-1c/FAS pathway was previously shown to be markedly elevated and to contribute to the progression of hepatic steatosis in NASH mice[41]. Our present findings showed that G2-SUISO significantly down-regulated SREBP-1c, FAS and ACC expression (Fig. 4), indicating that G2-SUISO protects NASH rats from the SREBP-1c/FAS pathway. In this study, serum TG remained reduced after 2 days of fasting and feeding the CDHCFF diet, with comparable concentrations with/without G2-SUISO (Supplementary Fig. 3B). Previous study demonstrated that serum TG concentration was decreased after 2 days fasting but gradually increase after refeeding[21]. The reason why serum triglyceride levels are not increased by the CDHCFF diet is still unclear, but one possible reason may be due to the use of rats of different species and ages in this study.

As shown in Fig. 5, hepatic FFAs in the liver were increased after feeding an CDHCFF diet and accounted for the majority of the lipid accumulation, which can trigger NASH[42,43]. Excessive consumption and dietary abnormalities (such as consuming an CDHCFF diet after fasting) is related to oxidative stress in various tissues, including vessels, adipose tissues and the liver, and is consequent to disease development. Normally, oxidative stress, such as ROS, is continuously generated within cells but is counterbalanced by the antioxidant system to defend the body from cellular or tissue damage[44]. In the progression of aging and lipogenesis, an imbalance of oxidant synthesis and antioxidants is the major contributor to the pathogenesis of NASH, leading to liver injury and hepatocyte deterioration[45].

Antioxidants have been suggested to be beneficial for health promotion and disease prevention. Chemiluminescence emission in vitro has been used to verify that H_2 can scavenge ROS markedly[46]. Our results confirmed that the administration of G2-SUISO, a proven safe and convenient antioxidant, improved NASH in our elderly rat model, probably due to its antioxidant activity. Hepatic and general serum marker levels including the liver weight-to-body weight ratio, AST and ALT were all improved, while FFA uptake-related, inflammatory and pro-apoptosis molecules were suppressed in the NASH liver by administration of G2-SUISO. The beneficial effects of G2-SUISO against hepatic steatosis in NASH elderly rats may be exerted through the inhibition of lipogenesis pathways by reducing SREBP-1c, ACC and FAS expression, thereby causing a reduction in the hepatic fat accumulation and a significant decrease in TC levels in serum. Overall, these results indicate that G2-SUISO represents a simple and novel therapeutic strategy for NASH and NAFLD. Previous studies also showed that H_2 therapy is a very promising treatment of liver diseases and the rational use of it has already solved many problems clinically[47]. However, the current clinical delivery method of H_2 is not very convenient, and G2-SUISO can be made into capsules to solve this problem and facilitate H_2 administration.

Methods

Manufacturing method of G2-SUISO. The original method of coral calcium carried hydrogen was described previously[48,49]. The coral powder containing calcium carbonate was sealed into a pressure vessel, and gas with a concentration of 100% (vol) H_2 was circulated at a rate of 5 L/min at a temperature of 800 °C and pressure of 0.8 MPa, treated at a high temperature for 1 h. At 300 °C and 0.8 MPa, H_2 gas concentration of 100% (vol)

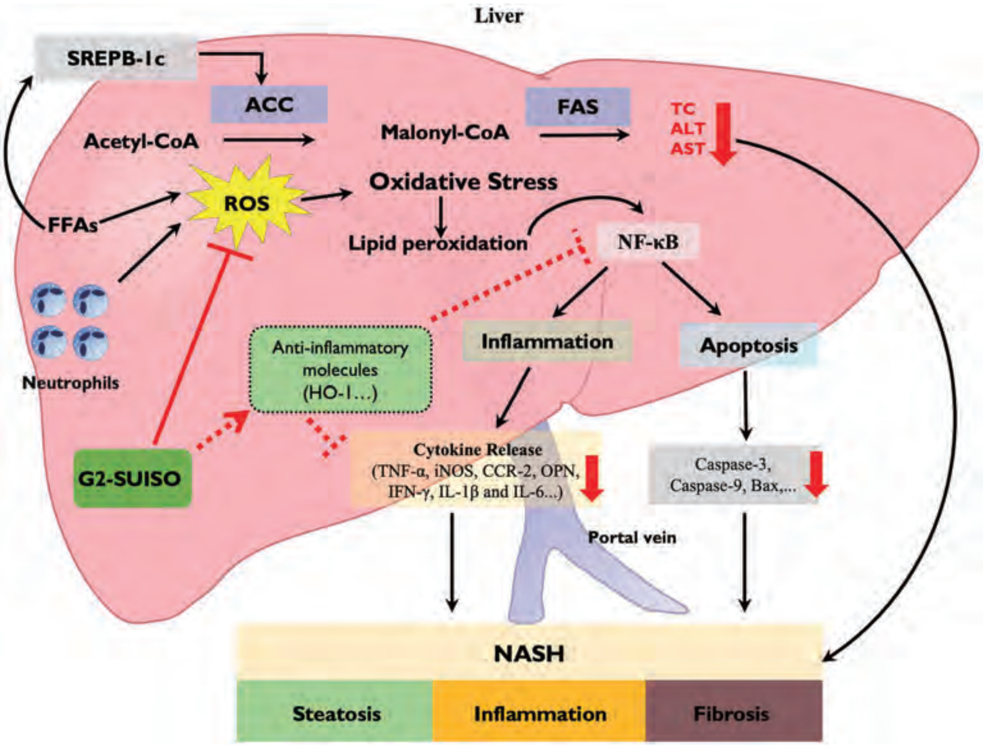

Figure 5. Schematic hypothesis of the mechanisms underlying the effects of G2-SUISO for treating nonalcoholic steatohepatitis. The beneficial effect of G2-SUISO against hepatic steatosis in NASH elderly rats may occur through the inhibition of lipogenesis pathways by reducing SREBP-1c, ACC and FAS gene expression, thereby causing a reduction in the hepatic fat accumulation and a significant decrease in total cholesterol (TC) levels in serum. The administration of G2-SUISO can decrease lipid peroxidation and pro-inflammatory cytokines, such as TNF-α, iNOS, CCR-2, IFN-γ, OPN, IL-1β and IL-6, which modulate liver damage in CDHCFF diet-fed rats. G2-SUISO might also up-regulated anti-inflammatory molecules, such as HO-1, which suppressed NF-κB and inflammatory cytokine expression. G2-SUISO is therefore able to reduce the activities of AST and ALT in the serum of NASH elderly rats. Furthermore, G2-SUISO was found to exert anti-apoptotic effects as well by down-regulating pro-apoptotic molecules, such as caspase-9, caspase-3 and Bax via down-regulation of NF-κB. Overall, this study provides evidence for the beneficial effects of G2-SUISO in reversing the progression of NASH in elderly rats.

was circulated at a speed of 5 L/min and treated at a low temperature for 4 h. Finally, hydrogen powder with an average particle size of about 10 µm was obtained by grinding.

Animal model. Six-month-old elderly male F344/NSlc rats (450–500 g) were purchased from Shizuoka Laboratory Animal Center (Shizuoka, Japan) and housed in a feeding room with automatically controlled light and temperature according to the guidelines of the Institutional Animal Care and Use Committee. All animal procedures were authorized by the National Research Institute for Child Health and Development (Permission No. A2020-004-C01-M01).

An acute NASH model was originally developed in 1997[21] and is currently used in the field of fatty liver research with minor modification[22,50–52]. As early as three days after starting the CDHCFF diet, rats may develop hepatic inflammation. In our study, acute NASH in a rat model was induced by fasting for two days followed by feeding a CDHCFF diet for three days. Rats in the present study were randomized into five groups as shown in Fig. 1A and as follows: (1) Naïve group (n = 6): rats received a normal diet and were gavaged with distilled water; (2) CDHCFF control group on day 3 (3d_cont.) (n = 6): rats were fed an CDHCFF diet from days 0 to 3 and then sacrificed on day 3; (3) CDHCFF + G2-SUISO-treated group on day 3 (3d_G2) (n = 6): rats had NASH induced, were gavaged with 300 mg/kg G2-SUISO from days 0 to 3, and then were sacrificed on day 3; (4) CDHCFF control group on day 7 (7d_cont.) (n = 6): rats were fed an CDHCFF diet from days 0 to 3, switched to a normal diet from days 4 to 7, and then were sacrificed on day 7; (5) CDHCFF + G2-SUISO-treated group on day 7 (7d_G2) (n = 6): rats were fed an CDHCFF diet from days 0 to 3 and then switched to a normal diet from days 4 to 7. At the same time, rats were gavaged with 300 mg/kg G2-SUISO from days 0 to 7 before finally being sacrificed on day 7. At sacrifice, blood was collected, the liver weight-to-body weight ratio was measured, and the entire liver was removed for further analyses.

Serum biochemical analyses. Serum was collected from whole-blood samples after standing for 30 min at 37 °C and centrifuged at 3000 g for 20 min at 4 °C. The samples were then measured for the AST, ALT, TC and TG concentrations with a commercially available kit (Fujifilm, Tokyo, Japan) and an automatic biochemical analyzer (DRI-CHEM 3500i; Fujifilm) according to the manufacturer's instructions.

Histology and histopathological analyses. Liver tissues were cut and fixed in 10% formaldehyde solution for 48 h and embedded in paraffin for histological analysis. Sections of liver 4-μm-thick were prepared and subjected to staining with hematoxylin and eosin (HE) (Muto Pure Chemicals, Tokyo, Japan) for morphological analyses to evaluate hepatocyte steatosis, ballooning and inflammatory cell infiltration. For another assessment of inflammatory cell infiltration, the quantification of neutrophils in liver specimens was stained using the Naphthol AS-D Chloroacetate Esterase Staining Kit (Muto Pure Chemicals). Slides were then examined by light microscopy (OLYMPUS, Tokyo, Japan) in a blind fashion to assess the inflammation state. Histological results were quantified using the WinRoof 7.4 software program (Mitani Corporation, Tokyo, Japan) as described previously[53].

Oil Red O staining. The frozen liver samples with optimal cutting temperature were cryo-sectioned at 5 μm with a cryostat and then stained with Oil Red O working solution (Muto Pure Chemicals) for TG and FFA staining to evaluate hepatocyte steatosis[54]. Results were quantified using the WinRoof 7.4 software program (Mitani Corporation) as well.

Immunohistochemical examinations. Immunohistochemical staining was performed on frozen sections using mouse anti-rat ED1 monoclonal antibody (Bio-Rad, Hercules, CA, USA) and Purified mouse anti-rat CD3 monoclonal antibody (BD Biosciences, San Diego, CA) as described previously[55].

Total mRNA preparation and quantitative reverse transcription polymerase chain reaction (qRT-PCR). Total mRNA was extracted from liver tissues using an RNeasy Mini Kit (Qiagen, Valencia, CA, USA). Each 0.8-μg aliquot of mRNA was reverse-transcribed to cDNA using a Prime Script RT reagent Kit (RR037A; Takara, Shiga, Japan). qRT-PCR was performed by the SYBR® Green system using an Applied Biosystem PRISM7900 apparatus (Thermo Fisher Scientific, Waltham, MA, USA). The PCR cycle conditions for the SYBR® Green system were 50 °C for 2 min, 95 °C for 2 min, 45 cycles of 95 °C for 15 s and 60 °C for 60 s. The comparative cycle threshold (CT) method was used to determine the relative gene expression. The results of target genes (Table 1) were normalized by subtracting the CT value of 18S expression. The fold change was calculated by a comparative CT method as described previously[56].

Genes	**Forward (5′–3′)**	**Reverse (5′–3′)**	
SYBR green PCR system			
IFN-γ	GAAAGCCTAGAAAGTCTGAAGAAC	GCACCGACTCCTTTTCCGCTTCCT	
IL-6	TGATGGATGCTTCCAAACTG	GAGCATTGGAAGTTGGGGTA	
IL-1β	CACCTTCTTTTCCTTCATCTTTG	GTCGTTGCTTGTCTCTCCTTGTA	
CCR2	TTCTGGGCTCACTATGCTGC	AAGGGCCACAAGTATGCTGA	
Bax	CCAGGACGCATCCACCAAGAAGC	TGCCACACGGAAGAAGACCTCTCG	
Caspase-1	GTGTTGCAGATAATGAGGGC	AAGGTCCTGAGGGCAAAGAG	
Caspase-3	GGACCTGTGGACCTGAAAAA	GCATGCCATATCATCGTCAG	
Bcl-2	GGATGACTTCTCTCGTCGCTACCGT	ATCCCTGAAGAGTTCCTCCACCAC	
NFκB	GCATGCCATATCATCGTCAG	TGCTTCTCTCCCCAGGAATA	
OB-R	TGCCTTGGAGGACTATGGGT	AGCCCCCTTCAAAGACGAAG	
ACC	GCCTCTTCCTGACAAACGAG	TCCATACGCCTGAAACATGA	
SREBP-1c	TGGATTGCACATTTGAAGACAT	GCTCCTCTTTGATTCCAGGC	
FAS	CAGCTGTCAGTGTAAAGAAACATGTC	AGCTCACGTGCAGTTTAATTGTG	
HMGCR	CCCAGCCTACAAACTGGAAA	CCATTGGCACCTGGTACTCT	
SREBP-2	AGACTTGGTCATGGGGACAG	GGGGAGACATCAGAAGGACA	
18S	ATGAGTCCACTTTAAATCCTTTAACGA	CTTTAATATACGCTATTGGAGCTGGAA	
Genes	**Forward (5′–3′)**	**Reverse (5′–3′)**	**Probe**
Taqman probe PCR			
TNF-α	AATGGGCTCCCTCTCATCAGT	ACGGGCTTGTCACTCGAGTT	CCAGACCCTCACACTCAGATCATCTTCTCA
iNOS	GGACATTAACAACAACGTGGAGAA	AACCATTTTGATGCTTGTGACTCTT	TGCTATTCCCAGCCCAACAACACAGG
OPN	CAAAGTCCAGGAGTTTCCCTGTT	CTCTTCATGCGGGAGGTGA	TGATGAACAGTATCCCGATGCCACAGAT
18S	ATCCATTGGAGGGCAAGTCTGGTGC	ATGAGTCCACTTTAAATCCTTTAACGA	CTTTAATATACGCTATTGGAGGCTGGAA

Table 1. Primer sequences and probes used in this study.

Western blot analyses. Western blot analysis was performed as described previously[20]. In brief, frozen liver tissues in the five groups were homogenized in RIPA buffer containing 1% protease inhibitor cocktail-1 and 1% protease inhibitor cocktail-2 (Sigma-Aldrich, St. Louis, MO, USA) followed by centrifugation in a microfuge at top speed for 30 min. Protein concentrations were assayed using a Bio-Rad Protein Assay (Bio-Rad). Samples were separated by electrophoresis on 10% polyacrylamide gels and transferred to Immobilon-PVDF (Bio-Rad). The membranes corresponding to the molecule of interest were cut out prior to hybridization with the antibody. After brief incubation with 5% non-fat milk to block non-specific binding, membranes were exposed overnight at 4 °C to specific caspase-1, caspase-3, caspase-9 and nuclear factor-κB (NF-κB). Protein expression was quantified by a laser densitometric analysis of the radiographic film using the ImageJ software program (NIH, Bethesda, MD, USA). The protein normalization was performed using β-actin as internal loading control.

Statistical analyses. The GraphPad Prism 9 software program (GraphPad, San Diego, CA, USA) was used to calculate statistical significance. Student's *t*-test was used for unpaired data. Data are expressed as the mean ± standard deviation (SD). A value of $p<0.05$ was considered to be statistically significant (*$p<0.05$; **$p<0.01$; ***$p<0.001$; ****$p<0.0001$).

Data availability

The datasets that support the findings of this study are available from the corresponding author on reasonable request.

Received: 27 March 2023; Accepted: 16 July 2023

References

1. Powell, E. E., Wong, V. W. & Rinella, M. Non-alcoholic fatty liver disease. *Lancet* **397**, 2212–2224. https://doi.org/10.1016/S0140-6736(20)32511-3 (2021).
2. Fraile, J. M., Palliyil, S., Barelle, C., Porter, A. J. & Kovaleva, M. Non-alcoholic steatohepatitis (NASH)—a review of a crowded clinical landscape, driven by a complex disease. *Drug Des. Dev. Ther.* **15**, 3997–4009. https://doi.org/10.2147/DDDT.S315724 (2021).
3. Chen, T. P., Lai, M., Lin, W. Y., Huang, K. C. & Yang, K. C. Metabolic profiles and fibrosis of nonalcoholic fatty liver disease in the elderly: A community-based study. *J. Gastroenterol. Hepatol.* **35**, 1636–1643. https://doi.org/10.1111/jgh.15073 (2020).
4. Yang, J. *et al.* Oxidative stress and non-alcoholic fatty liver disease: Effects of omega-3 fatty acid supplementation. *Nutrients* https://doi.org/10.3390/nu11040872 (2019).
5. Sheedfar, F., Di Biase, S., Koonen, D. & Vinciguerra, M. Liver diseases and aging: Friends or foes?. *Aging Cell* **12**, 950–954. https://doi.org/10.1111/acel.12128 (2013).
6. Finkel, T. & Holbrook, N. J. Oxidants, oxidative stress and the biology of ageing. *Nature* **408**, 239–247. https://doi.org/10.1038/35041687 (2000).
7. Chen, Z., Tian, R., She, Z., Cai, J. & Li, H. Role of oxidative stress in the pathogenesis of nonalcoholic fatty liver disease. *Free Radic. Biol. Med.* **152**, 116–141. https://doi.org/10.1016/j.freeradbiomed.2020.02.025 (2020).
8. Gao, Y. *et al.* Exercise and dietary intervention ameliorate high-fat diet-induced NAFLD and liver aging by inducing lipophagy. *Redox Biol.* **36**, 101635. https://doi.org/10.1016/j.redox.2020.101635 (2020).
9. Ohsawa, I. *et al.* Hydrogen acts as a therapeutic antioxidant by selectively reducing cytotoxic oxygen radicals. *Nat. Med.* **13**, 688–694. https://doi.org/10.1038/nm1577 (2007).
10. Hu, Q. *et al.* Molecular hydrogen: A potential radioprotective agent. *Biomed. Pharmacother.* **130**, 110589. https://doi.org/10.1016/j.biopha.2020.110589 (2020).
11. Iketani, M. & Ohsawa, I. Molecular hydrogen as a neuroprotective agent. *Curr. Neuropharmacol.* **15**, 324–331. https://doi.org/10.2174/1570159x14666160607205417 (2017).
12. Wigg, A. J. *et al.* The role of small intestinal bacterial overgrowth, intestinal permeability, endotoxaemia, and tumour necrosis factor alpha in the pathogenesis of non-alcoholic steatohepatitis. *Gut* **48**, 206–211. https://doi.org/10.1136/gut.48.2.206 (2001).
13. Kanda, T. *et al.* Apoptosis and non-alcoholic fatty liver diseases. *World J. Gastroenterol.* **24**, 2661–2672. https://doi.org/10.3748/wjg.v24.i25.2661 (2018).
14. Wang, X. J. & Malhi, H. Nonalcoholic fatty liver disease. *Ann. Intern. Med.* **169**, ITC65–ITC80. https://doi.org/10.7326/AITC201811060 (2018).
15. Noureddin, M. *et al.* Clinical and histological determinants of nonalcoholic steatohepatitis and advanced fibrosis in elderly patients. *Hepatology* **58**, 1644–1654. https://doi.org/10.1002/hep.26465 (2013).
16. Bertolotti, M. *et al.* Nonalcoholic fatty liver disease and aging: epidemiology to management. *World J. Gastroenterol.* **20**, 14185–14204. https://doi.org/10.3748/wjg.v20.i39.14185 (2014).
17. Nie, C. *et al.* Hydrogen gas inhalation alleviates myocardial ischemia-reperfusion injury by the inhibition of oxidative stress and NLRP3-mediated pyroptosis in rats. *Life Sci.* **272**, 119248. https://doi.org/10.1016/j.lfs.2021.119248 (2021).
18. Fu, Z., Zhang, J. & Zhang, Y. Role of molecular hydrogen in ageing and ageing-related diseases. *Oxid. Med. Cell Longev.* **2022**, 2249749. https://doi.org/10.1155/2022/2249749 (2022).
19. LeBaron, T. W. *et al.* Molecular hydrogen is comparable to sulfasalazine as a treatment for DSS-induced colitis in mice. *EXCLI J.* **20**, 1106–1117. https://doi.org/10.17179/excli2021-3762 (2021).
20. Li, S. W. *et al.* Hydrogen-rich water protects against liver injury in nonalcoholic steatohepatitis through HO-1 enhancement via IL-10 and Sirt 1 signaling. *Am. J. Physiol. Gastrointest. Liver Physiol.* **320**, G450–G463. https://doi.org/10.1152/ajpgi.00158.2020 (2021).
21. Delzenne, N. M., Hernaux, N. A. & Taper, H. S. A new model of acute liver steatosis induced in rats by fasting followed by refeeding a high carbohydrate-fat free diet. Biochemical and morphological analysis. *J. Hepatol.* **26**, 880–885. https://doi.org/10.1016/s0168-8278(97)80256-5 (1997).
22. Nagai, K. *et al.* Impact of venous-systemic oxygen persufflation with nitric oxide gas on steatotic grafts after partial orthotopic liver transplantation in rats. *Transplantation* **95**, 78–84. https://doi.org/10.1097/TP.0b013e318277e2d1 (2013).
23. Machado, M. V. & Diehl, A. M. Pathogenesis of nonalcoholic steatohepatitis. *Gastroenterology* **150**, 1769–1777. https://doi.org/10.1053/j.gastro.2016.02.066 (2016).
24. Cho, Y. & Szabo, G. Two faces of neutrophils in liver disease development and progression. *Hepatology* **74**, 503–512. https://doi.org/10.1002/hep.31680 (2021).
25. Wu, L. *et al.* The role of neutrophils in innate immunity-driven nonalcoholic steatohepatitis: Lessons learned and future promise. *Hepatol. Int.* **14**, 652–666. https://doi.org/10.1007/s12072-020-10081-7 (2020).

26. Ishida, Y. *et al.* Opposite roles of neutrophils and macrophages in the pathogenesis of acetaminophen-induced acute liver injury. *Eur. J. Immunol.* **36**, 1028–1038. https://doi.org/10.1002/eji.200535261 (2006).
27. Cobbina, E. & Akhlaghi, F. Non-alcoholic fatty liver disease (NAFLD)—pathogenesis, classification, and effect on drug metabolizing enzymes and transporters. *Drug Metab. Rev.* **49**, 197–211. https://doi.org/10.1080/03602532.2017.1293683 (2017).
28. Russell, G., Nenov, A., Kisher, H. & Hancock, J. T. Molecular hydrogen as medicine: An assessment of administration methods. *Hydrogen* **2**, 444–460 (2021).
29. Yang, H. *et al.* Heme oxygenase-1 inhibits the proliferation of hepatic stellate cells by activating PPARγ and suppressing NF-κB. *Comput. Math. Methods Med.* **2022**, 8920861. https://doi.org/10.1155/2022/8920861 (2022).
30. Bellezza, I. *et al.* Inhibition of NF-κB nuclear translocation via HO-1 activation underlies α-tocopheryl succinate toxicity. *J. Nutr. Biochem.* **23**, 1583–1591. https://doi.org/10.1016/j.jnutbio.2011.10.012 (2012).
31. Gao, W. *et al.* Dissecting the crosstalk between Nrf2 and NF-κB response pathways in drug-induced toxicity. *Front. Cell Dev. Biol.* https://doi.org/10.3389/fcell.2021.809952 (2022).
32. Luedde, T. & Schwabe, R. F. NF-kappaB in the liver–linking injury, fibrosis and hepatocellular carcinoma. *Nat. Rev. Gastroenterol. Hepatol.* **8**, 108–118. https://doi.org/10.1038/nrgastro.2010.213 (2011).
33. Ricchi, M. *et al.* Differential effect of oleic and palmitic acid on lipid accumulation and apoptosis in cultured hepatocytes. *J. Gastroenterol. Hepatol.* **24**, 830–840. https://doi.org/10.1111/j.1440-1746.2008.05733.x (2009).
34. Van Opdenbosch, N. & Lamkanfi, M. Caspases in cell death, inflammation, and disease. *Immunity* **50**, 1352–1364. https://doi.org/10.1016/j.immuni.2019.05.020 (2019).
35. Guo, M. *et al.* Bax functions as coelomocyte apoptosis regulator in the sea cucumber *Apostichopus japonicus*. *Dev. Comp. Immunol.* **102**, 103490. https://doi.org/10.1016/j.dci.2019.103490 (2020).
36. Choi, S. S. & Diehl, A. M. Hepatic triglyceride synthesis and nonalcoholic fatty liver disease. *Curr. Opin. Lipidol.* **19**, 295–300. https://doi.org/10.1097/MOL.0b013e3282ff5e55 (2008).
37. Ong, K. T., Mashek, M. T., Bu, S. Y., Greenberg, A. S. & Mashek, D. G. Adipose triglyceride lipase is a major hepatic lipase that regulates triacylglycerol turnover and fatty acid signaling and partitioning. *Hepatology* **53**, 116–126. https://doi.org/10.1002/hep.24006 (2011).
38. Fang, K. *et al.* Diosgenin ameliorates palmitic acid-induced lipid accumulation via AMPK/ACC/CPT-1A and SREBP-1c/FAS signaling pathways in LO2 cells. *BMC Complement Altern. Med.* **19**, 255. https://doi.org/10.1186/s12906-019-2671-9 (2019).
39. Moon, Y. S. & Ali, S. Possible mechanisms for the equilibrium of ACC and role of ACC deaminase-producing bacteria. *Appl. Microbiol. Biotechnol.* **106**, 877–887. https://doi.org/10.1007/s00253-022-11772-x (2022).
40. Stoeckman, A. K. & Towle, H. C. The role of SREBP-1c in nutritional regulation of lipogenic enzyme gene expression. *J. Biol. Chem.* **277**, 27029–27035. https://doi.org/10.1074/jbc.M202638200 (2002).
41. An, J. P. *et al.* Anti-hepatic steatosis activity of Sicyos angulatus extract in high-fat diet-fed mice and chemical profiling study using UHPLC-qTOF-MS/MS spectrometry. *Phytomedicine* **63**, 152999. https://doi.org/10.1016/j.phymed.2019.152999 (2019).
42. Puri, P. *et al.* A lipidomic analysis of nonalcoholic fatty liver disease. *Hepatology* **46**, 1081–1090. https://doi.org/10.1002/hep.21763 (2007).
43. Bechmann, L. P. *et al.* The interaction of hepatic lipid and glucose metabolism in liver diseases. *J. Hepatol.* **56**, 952–964. https://doi.org/10.1016/j.jhep.2011.08.025 (2012).
44. Vona, R., Gambardella, L., Cittadini, C., Straface, E. & Pietraforte, D. Biomarkers of oxidative stress in metabolic syndrome and associated diseases. *Oxid. Med. Cell Longev.* **2019**, 8267234. https://doi.org/10.1155/2019/8267234 (2019).
45. Oseini, A. M. & Sanyal, A. J. Therapies in non-alcoholic steatohepatitis (NASH). *Liver Int.* **37**(Suppl 1), 97–103. https://doi.org/10.1111/liv.13302 (2017).
46. Deenin, W., Malakul, W., Boonsong, T., Phoungpetchara, I. & Tunsophon, S. Papaya improves non-alcoholic fatty liver disease in obese rats by attenuating oxidative stress, inflammation and lipogenic gene expression. *World J. Hepatol.* **13**, 315–327. https://doi.org/10.4254/wjh.v13.i3.315 (2021).
47. Shi, J., Duncan, B. & Kuang, X. Hydrogen treatment: A novel option in liver diseases. *Clin. Med. (Lond.)* **21**, e223–e227. https://doi.org/10.7861/clinmed.2020-0370 (2021).
48. Okuda, R. *et al.* Evaluation of released amount of hydrogen after high pressure hydrogen loading in carbonate. *Results Eng.* **4**, 100047. https://doi.org/10.1016/j.rineng.2019.100047 (2019).
49. Li, H. *et al.* Hydrogen adsorption and desorption characteristics of heat-treated calcium carbonate derived from Akoya-Pearl-Oyster nacre. *J. Environ. Chem. Eng.* **8**, 103983. https://doi.org/10.1016/j.jece.2020.103983 (2020).
50. Minor, T., Akbar, S., Tolba, R. & Dombrowski, F. Cold preservation of fatty liver grafts: prevention of functional and ultrastructural impairments by venous oxygen persufflation. *J. Hepatol.* **32**, 105–111. https://doi.org/10.1016/s0168-8278(00)80196-8 (2000).
51. Miyachi, Y. *et al.* Etiology of liver steatosis influences the severity of ischemia/reperfusion injury and survival after liver transplantation in rats. *Liver Transpl.* **26**, 1504–1515. https://doi.org/10.1002/lt.25814 (2020).
52. Okamura, Y. *et al.* Impact of subnormothermic machine perfusion preservation in severely steatotic rat livers: A detailed assessment in an isolated setting. *Am. J. Transpl.* **17**, 1204–1215. https://doi.org/10.1111/ajt.14110 (2017).
53. Liu, C. *et al.* 5-ALA/SFC attenuated binge alcohol-induced gut leakiness and inflammatory liver disease in HIV transgenic rats. *Alcohol Clin. Exp. Res.* **43**, 1651–1661. https://doi.org/10.1111/acer.14117 (2019).
54. Li, S. *et al.* Astaxanthin prevents ischemia-reperfusion injury of the steatotic liver in mice. *PLoS ONE* **12**, e0187810. https://doi.org/10.1371/journal.pone.0187810 (2017).
55. Kawasaki, M. *et al.* Inducible liver injury in the transgenic rat by expressing liver-specific suicide gene. *Biochem. Biophys. Res. Commun.* **311**, 920–928. https://doi.org/10.1016/j.bbrc.2003.10.085 (2003).
56. Zhao, J. *et al.* Monotherapy with anti-CD70 antibody causes long-term mouse cardiac allograft acceptance with induction of tolerogenic dendritic cells. *Front. Immunol.* **11**, 555996. https://doi.org/10.3389/fimmu.2020.555996 (2020).

Acknowledgements

This study was supported by research grants from the Grant of Ministry of Education, Culture, Sports, Science and Technology of Japan (Grants-in-Aid 21K08634) and a Grant from the National Center for Child Health and Development (31-02).

Author contributions

X.K.L. conceptualized the study and all authors contributed to the study design. Data collection was conducted by K.M. The preparation of the research materials and data analysis were conducted by K.M., M.F., and X.K.L. Results and interpretations of the study data were discussed by all authors. The first draft of the manuscript was written by K.M., and all authors commented on earlier versions of the manuscript. All authors read and approved the final manuscript.

Competing interests

The authors declare no competing interests.

Additional information

Supplementary Information The online version contains supplementary material available at https://doi.org/10.1038/s41598-023-38856-6.

Correspondence and requests for materials should be addressed to M.F. or X.-K.L.

Reprints and permissions information is available at www.nature.com/reprints.

日中笹川医学奨学金制度＜学位取得コース＞評価書
課程博士：指導教官

第 44 期　　研究者番号：G4410　　　　作成日　：2024 年 3 月 10 日

氏　名	徐　勇	XU YONG	性別	M	生年月日　1990/05/04

所属機関（役職）	長崎大学大学院医歯薬学総合研究科（大学院生）	
研究先（指導教官）	長崎大学原爆後障害医療研究所幹細胞生物学研究分野(原研幹細胞)(李 桃生　教授)	
研究テーマ	ニカラベンによる間葉系幹細胞の放射線損傷の軽減 Nicaraven for attenuating the radiation-induced damage of Mesenchymal stem(stromal) cells	
専攻種別	□論文博士	☑課程博士

研究者評価（指導教官記入欄）

成績状況	優　良	取得単位数 早期卒業修了(既に学位取得)
学生本人が行った研究の概要	胸部の放射線がん治療に伴う肺傷害のメカニズムを解明し、新たな予防・治療の開発である。また、人工呼吸管理について、酸素吸入や換気量が肺傷害に与える影響を動物実験で調べている。	
総合評価	【良かった点】 ものごとを真摯に取り組み、研究も順調に進み、既に研究成果を出し、これまでに第一著者として論文３本を国際学術誌に採択・掲載された。昨年１０月に、早期終了し医学博士の学位を取得した。 【改善すべき点】 特になし 【今後の展望】 既に学位を取得され、中国で就職した。	
学位取得見込	昨年１０月に、早期卒業修了し、博士学位を取得された	

評価者（指導教官名）　　李桃生

日中笹川医学奨学金制度＜学位取得コース)＞報告書
研究者用

第44期　　研究者番号：　G4410　　作成日：2024年3月　10　日

氏名	徐 勇	XU YONG	性別	M	生年月日　1990/05/04
所属機関(役職)	長崎大学大学院医歯薬学総合研究科（大学院生）				
研究先（指導教官）	長崎大学原爆後障害医療研究所幹細胞生物学研究分野（原研幹細胞）（李 桃生　教授）				
研究テーマ	ニカラベンによる基質細胞の放射線損傷の軽減 Nicaraven attenuates radiation-induced injury of stromal cells in lungs				
専攻種別	論文博士	□	課程博士	☑	

1．研究概要(1)

1)目的(Goal)

i. To investigate whether nicaraven can attenuate radiation-induced injury of lung stromal cells (LSCs).

ii.To understand the relevant molecular mechanisms on nicaraven for attenuating radiation-induced injury of LSCs.

2)戦略(Approach)

C57BL/6 mice (9-week old) were exposed to 6 Gy X-ray thoracic radiation per day for 5 days (cumulative dose of 30 Gy) and nicaraven (50 mg/kg) or saline was injected intraperitoneally in 5 min after each radiation exposure. At 6 day (acute phase) or 14 days (subacute phase), we collected lung tissues and cultured as “explants” to grow LSCs, and further evaluated the quality and quantity of LSCs.

3)材料と方法(Materials and methods)

1. Ex vivo expansion of LSCs from mouse lung tissue ″explants″.
   MSCs were expanded using a method as previously desrcibed (Figure 1B).
2. Detection of characterization of LSCs.
   IF stainging was performed to detect the expression levels of CD90,CD105,Pro-SPC,F4/80 in LSCs.
3. Evaluation of DNA damage of LSCs.
   To evaluate the DNA damage of LSCs,the expression levels of γ-H2AX and CD90 were estimated by immunostaining.
4. Evaluation of paracrine mechanisms of LSCs.
   ELISA was used to detect the growth factors of HGF,VEGF,SDF-1a and inflammatory factors of IL-1β CCL2, TNF-1a in conditioned medium from the supernatents of one passaged LSCs.

4)実験結果(Results)

4.1 Nicaraven attenuates radiation-induced changes on the number and phenotype of LSCs

We sacrificed mice and took lung tissue for experiments at the acute and subacute phases (Figure 1A). Our data showed that the irradiated lungs produced a significantly lower number of LSCs compared to healthy lungs after culture at the acute and subacute phases, which was significantly mitigated by nicaraven administration. To examine whether ionizing radiation would change the phenotypic characterization of LSCs. Of the acute phase, compared to the CON group, these LSCs in the IR group expressed significantly lower Pro-SPC, CD90, and CD105 ($p<0.01$; Figure 2D); but higher F4/80 ($p<0.01$; Figure 2D). However, LSCs in the IR+N group significantly expressed higher Pro-SPC, CD90, CD105 ($p<0.01$; Figure 2D), and lower F4/80 ($p<0.01$; Figure 2D) than that of the IR group. Of the subacute phase, LSCs in the IR group also showed lower expression of Pro-SPC, CD90, CD105 ($p<0.01$; Figure 2D), but higher expression of F4/80 ($p<0.01$; Figure 2D) than that of the CON group. However, LSCs in the IR+N group expressed significantly higher Pro-SPC, CD90, and CD105 ($p<0.01$; Figure 2D) but lower F4/80 ($p<0.01$; Figure 2D) compared to the IR group.

4.2 Nicaraven significantly attenuates radiation-induced changes in the factors production of LSCs

We examined the levels of related cytokines in the conditioned medium. Compared with these LSCs from the healthy lungs, LSCs from the irradiated lungs produced significantly less HGF, VEGF, and SDF-1α in the conditioned medium ($p<0.01$). However, all these changes of HGF, VEGF, and SDF-1α released by LSCs from the irradiated lungs were significantly mitigated by nicaraven administration at the acute and subacute phases ($p<0.01$). We detected the contents of IL-1β, TNF-α, and CCL2 in the conditioned medium. Compared with the healthy controls, the contents of IL-1β and TNF-α released by LSCs from irradiated lungs were significantly increased in the conditioned medium ($p<0.01$), which were partially mitigated by nicaraven administration at the acute phase. Similarly, LSCs from irradiated lungs at the subacute phase produced more IL-1β, TNF-α, and CCL2 in the conditioned medium ($p<0.01$) but significantly attenuated by nicaraven administration ($p<0.01$).

4.3 Nicaraven significantly attenuates radiation-induced DNA damage of CD90-positive LSCs

Immunofluorescence staining was performed to detect the formation of γ-H2AX foci in LSCs (Figure 4A). Quantitative data showed that the percentage of γ-H2AX-positive LSCs was not significantly changed in the IR group than the CON group. However, the percentage of γ-H2AX-positive LSCs was significantly higher in the IR+N group compared to the IR group at the acute and subacute phases ($p<0.05$; Figure 4B). We further detected the formation of γ-H2AX foci in CD90-positive LSCs. Quantitative data indicated that the percentage of γ-H2AX foci in CD90-positive LSCs was significantly higher in the IR group compared to the CON group, at either the acute phase ($p<0.01$; Figure 4C) or the subacute phase ($p<0.01$; Figure 4C). Interestingly, the percentage of CD90-positive LSCs with γ-H2AX foci was significantly lower in the IR+N group compared to the IR group, at either the acute ($p<0.01$; Figure 4C) and subacute ($p<0.01$; Figure 4C) phases. These results indicated that nicaraven administration significantly reduced radiation-induced DNA damage of CD90-positive LSCs.

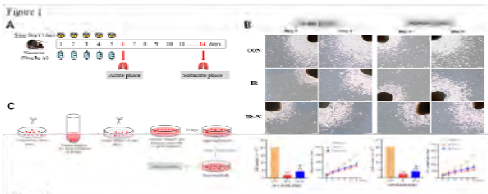
Figure 1

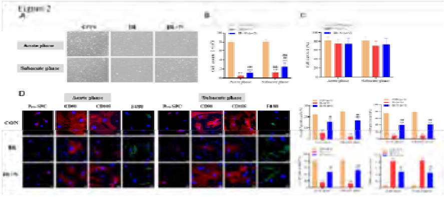
Figure 2

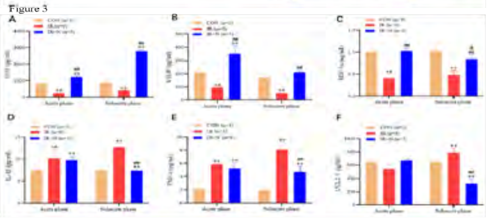
Figure 3

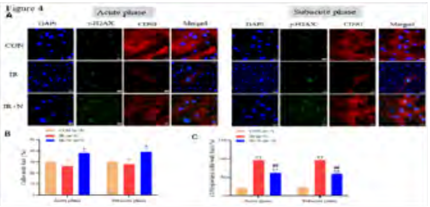
Figure 4

5）考察（Discussion）

The use of radiation therapy to treat cancer inevitably involves exposure of normal tissues. Which can damage tissue homeostasis. Mesenchymal stromal cells (MSCs) residing in the lung are highly susceptible to radiation and are known to play critical roles in tissue homeostasis. In this study, we tried to primarily MSCs from lung tissues "explants" and then investigated whether nicaraven can attenuate the radiation-induced injury of MSCs, mainly focusing the quantity and quality of MSCs after nicaraven administrations. Our data indicated that nicaraven administration significantly restored the outgrowth of MSCs and their altered phenotypes caused by radiation exposure, clearly attenuated the radiation-induced DNA damage of MSCs. Besides these, nicaraven administration significantly increased the production of HGF,VEGF, SDF-1a, IL-6 and decreased the levels of TNF-a, CCL2 in the conditioned medium, suggesting the effectiveness of nicaraven for attenuating radiation-induced injury of MSCs.

High ionizing radiation induces directly DNA double-strand breaks and triggers the release of ROS. The level of ROS overwhelms can cause DNA damage. Nicaraven has been well recognized on radical-specific scavenging properties and can attenuate radiation-induced DNA damage of lung tissue cells. we herein found that nicaraven can attenuate DNA damage of lung cells, especially the CD90-positive mesenchymal stromal cells.

Repair of damaged tissues is a fundamental biological mechanism that allows the ordered replacement of dead or damaged cells after injury. Over the last few decades, advances have been reported in the use of mesenchymal stromal cells (MSCs) for lung tissue repair and regeneration. MSCs are highly metabolically active and their secretome gives rise to the same effects commonly described for the cells themselves. MSCs not only replace damaged lung epithelial cells but also promote tissue repair through the secretion of chemokines, cytokines, growth factors and paracrine molecules.

Indeed, there are some limitations in this study. First, we only investigated the radiation-induced injury in lung stromal cells, a mixed cell population, because all types of stromal cells could be outgrew naturally from lung tissue "explants". Secondly, we were interested to detect the quality of CD90- or CD105-positive resident mesenchymal stem cells, but it is technically difficult for us to get enough pure CD90- or CD105-positive cells from the lungs of mice for experiments, especially the irradiated lungs.

6）参考文献（References）

1. Henry E, Cores J, Hensley MT, Anthony S et.al. Adult Lung Spheroid Cells Contain Progenitor Cells and Mediate Regeneration in Rodents With Bleomycin-Induced Pulmonary Fibrosis. Stem Cells Transl Med. 2015 Nov;4(11):1265-74.
2. Sveiven SN, Nordgren TM. Lung-resident mesenchymal stromal cells are tissue-specific regulators of lung homeostasis. Am J Physiol Lung Cell Mol Physiol. 2020 Aug 1;319(2):L197-L210.
3. Wynn TA. Integrating mechanisms of pulmonary fibrosis. J Exp Med. 2011 Jul 4;208(7):1339-50.
4. Chen Y, Liu X, Tong Z. Mesenchymal Stem Cells in Radiation-Induced Pulmonary Fibrosis: Future Prospects. Cells. 2022 Dec 20;12(1):6.
5. Wang LK, Wu TJ, Hong JH et.al. Radiation Induces Pulmonary Fibrosis by Promoting the Fibrogenic Differentiation of Alveolar Stem Cells. Stem Cells Int. 2020 Sep 29;2020:6312053.
6. Zanoni M, Cortesi M, Zamagni A et.al. The Role of Mesenchymal Stem Cells in Radiation-Induced Lung Fibrosis. Int J Mol Sci. 2019 Aug 8;20(16):3876.

2. 執筆論文 Publication of thesis ※記載した論文を添付してください。Attach all of the papers listed below.

論文名 1 Title	Hyperoxia but not high tidal volume contributes to ventilator-induced lung injury in healthy mice				
掲載誌名 Published journal	BMC Pulmonary medicine				
	2023 年 9 月	23(1) 巻(号)	154 頁 〜 頁	言語 Language	English
第1著者名 First author	Yong Xu	第2著者名 Second author	Yu Li	第3著者名 Third author	Da Zhai
その他著者名 Other authors	Reiko Sekiya; Chen Yan; Keiichi Jingu; Tao-Sheng Li				
論文名 2 Title	Optimization on the dose and time of nicaraven administration for mitigating the side effects of radiotherapy in a preclinical tumor-bearing mouse model				
掲載誌名 Published journal	Therapeutic Advances in Respiratory Disease				
	2022 年 12 月	16 巻(号)	頁 〜 頁	言語 Language	English
第1著者名 First author	Yong Xu	第2著者名 Second author	Lina Abdelghany	第3著者名 Third author	Reiko Sekiya
その他著者名 Other authors	Da Zhai; Keiichi Jingu; Tao-Sheng Li				
論文名 3 Title	Nicaraven mitigates radiation-induced lung injury by downregulating the NF-κB and TGF-β/Smad pathways to suppress the inflammatory response				
掲載誌名 Published journal	Journal of Radiation Research				
	2022 年 3 月	63(2) 巻(号)	158 頁 〜 167 頁	言語 Language	English
第1著者名 First author	Yong Xu	第2著者名 Second author	Da Zhai	第3著者名 Third author	Shinji Goto
その他著者名 Other authors	Xu Zhang; Keiichi Jingu; Tao-Sheng Li				
論文名 4 Title	Nicaraven Exerts a Limited Effect on Radiation-Induced Inhibition of Tumor Growth in a Subcutaneous Murine Tumor Model				
掲載誌名 Published journal	Radiation Research				
	2023 年 10 月	200(4) 巻(号)	382 頁 〜 388 頁	言語 Language	English
第1著者名 First author	Lina Abdelghany	第2著者名 Second author	Yong Xu	第3著者名 Third author	Reiko Sekiya
その他著者名 Other authors	Chen Yan; Keiichi Jingu; Tao-Sheng Li				
論文名 5 Title	Hydrostatic pressure stabilizes HIF-1α expression in cancer cells to protect against oxidative damage during metastasis				
掲載誌名 Published journal	Oncology Reports				
	2021 年 10 月	46(4) 巻(号)	211 頁 〜 頁	言語 Language	English
第1著者名 First author	Da Zhai	第2著者名 Second author	Yong Xu	第3著者名 Third author	Lina Abdelghany
その他著者名 Other authors	Xu Zhang; Jingyan Liang; Shuohua Zhang; Changying Guo; Tao-Sheng Li				
論文名 6 Title	Ex Vivo Hydrostatic Pressure Loading of Atrial Tissues Activates Profibrotic Transcription via TGF-β Signal Pathway				
掲載誌名 Published journal	International Heart Journal				
	2022 年 3 月	63(2) 巻(号)	367 頁 〜 374 頁	言語 Language	English
第1著者名 First author	Xu Zhang	第2著者名 Second author	Yousuf Yassouf	第3著者名 Third author	Kai Huang
その他著者名 Other authors	Yong Xu, Zi-Sheng Huang, Da Zhai, Reiko Sekiya, Ke-Xiang Liu, Tao-Sheng Li				

3. 学会発表 Conference presentation ※筆頭演者として総会・国際学会を含む主な学会で発表したものを記載してください

※Describe your presentation as the principal presenter in major academic meetings including general meetings or international meetin

学会名 Conference	The radiation Disaster Medical Science 5th International Symposium		
演 題 Topic	Nicaraven for attenuating radiation-induced lung injury		
開催日 date	2021 年 2 月 17 日	開催地 venue	Online
形式 method	□ 口頭発表 Oral ☑ ポスター発表 Poster	言語 Language	□ 日本語 ☑ 英語 □ 中国語
共同演者名 Co-presenter	None		
学会名 Conference	日本放射线影响学会第65回大会		
演 題 Topic	Nicaraven attenuates radiation-induced lung injury by suppressing inflammatory response.		
開催日 date	2022 年 9 月 17 日	開催地 venue	大阪公立大学
形式 method	□ 口頭発表 Oral ☑ ポスター発表 Poster	言語 Language	□ 日本語 ☑ 英語 □ 中国語
共同演者名 Co-presenter	None		
学会名 Conference			
演 題 Topic			
開催日 date	年 月 日	開催地 venue	
形式 method	□ 口頭発表 Oral □ ポスター発表 Poster	言語 Language	□ 日本語 □ 英語 □ 中国語
共同演者名 Co-presenter			
学会名 Conference			
演 題 Topic			
開催日 date	年 月 日	開催地 venue	
形式 method	□ 口頭発表 Oral □ ポスター発表 Poster	言語 Language	□ 日本語 □ 英語 □ 中国語
共同演者名 Co-presenter			

4. 受賞(研究業績) Award (Research achievement)

名 称 Award name				
	国名 Country		受賞年 Year of award	年 月
名 称 Award name				
	国名 Country		受賞年 Year of award	年 月

5. 本研究テーマに関わる他の研究助成金受給 Other research grants concerned with your resarch theme

受給実績 Receipt record	□ 有　□ 無
助成機関名称 Funding agency	
助成金名称 Grant name	
受給期間 Supported period	年　月 ～　年　月
受給額 Amount received	円
受給実績 Receipt record	□ 有　□ 無
助成機関名称 Funding agency	
助成金名称 Grant name	
受給期間 Supported period	年　月 ～　年　月
受給額 Amount received	円

6. 他の奨学金受給 Another awarded scholarship

受給実績 Receipt record	■ 有　□ 無
助成機関名称 Funding agency	Nagasaki University
奨学金名称 Scholarship name	Maeda Saeko Memorial Scholarship
受給期間 Supported period	2021 年 4 月 ～ 2022 年 4 月
受給額 Amount received	600,000 円

7. 研究活動に関する報道発表 Press release concerned with your research activities

※記載した記事を添付してください。Attach a copy of the article described below

報道発表 Press release	□ 有　□ 無	発表年月日 Date of release	
発表機関 Released medium			
発表形式 Release method	・新聞　・雑誌　・Web site　・記者発表　・その他（　　　　）		
発表タイトル Released title			

8. 本研究テーマに関する特許出願予定 Patent application concerned with your research theme

出願予定 Scheduled	□ 有　□ 無	出願国 Application	
出願内容（概要） Application contents			

9. その他 Others

指導責任者（記名）　李　桃生

Xu *et al. BMC Pulmonary Medicine* (2023) 23:354
https://doi.org/10.1186/s12890-023-02626-x

BMC Pulmonary Medicine

RESEARCH **Open Access**

Hyperoxia but not high tidal volume contributes to ventilator-induced lung injury in healthy mice

Yong Xu[1,2], Yu Li[3], Da Zhai[1,2], Chen Yan[1,2], Jingyan Liang[4], Taiga Ichinomiya[5], Tetsuya Hara[5], Chiaki Inadomi[5*] and Tao-Sheng Li[1,2*]

Abstract

Background Mechanical ventilation is a supportive therapy used to maintain respiratory function in several clinical and surgical cases but is always accompanied by lung injury risk due to improper treatment. We investigated how tidal volume and oxygen delivery would contribute independently or synergistically to ventilator-induced lung injury (VILI).

Methods Under general anesthesia and tracheal intubation, healthy female C57BL/6 N mice (9 weeks old) were randomly ventilated for 2 h by standard (7 ml/kg) or high (14 ml/kg) tidal volume at positive end-expiratory pressure (PEEP) of 2 cmH_2O, with room air, 50% O_2 (moderate hyperoxia), or 100% O_2 (severe hyperoxia); respectively. Mice were sacrificed 4 h after mechanical ventilation, and lung tissues were collected for experimental assessments on lung injury.

Results Compared with the healthy control, severe hyperoxia ventilation by either standard or high tidal volume resulted in significantly higher wet-to-dry lung weight ratio and higher levels of IL-1β and 8-OHdG in the lungs. However, moderate hyperoxia ventilation, even by high tidal volume did not significantly increase the levels of IL-1β and 8-OHdG in the lungs. Western blot analysis showed that the expression of RhoA, ROCK1, MLC2, and p-MLC2 was not significantly induced in the ventilated lungs, even by high tidal volume at 2 cmH_2O PEEP.

Conclusion Severe hyperoxia ventilation causes inflammatory response and oxidative damage in mechanically ventilated lungs, while high tidal volume ventilation at a reasonable PEEP possibly does not cause VILI.

Keywords Mechanical ventilation, Tidal volume, Oxidative damage, Inflammatory response, Mechanotransduction

---

*Correspondence:
Chiaki Inadomi
inadomic@nagasaki-u.ac.jp
Tao-Sheng Li
litaoshe@nagasaki-u.ac.jp
[1] Department of Stem Cell Biology, Atomic Bomb Disease Institute, Nagasaki University, 1-12-4 Sakamoto, Nagasaki 852-8523, Japan
[2] Department of Stem Cell Biology, Nagasaki University Graduate School of Biomedical Sciences, 1-12-4 Sakamoto, Nagasaki 852-8523, Japan
[3] Department of Anesthesiology, The Second Affiliated Hospital of Nanchang University, Nanchang City 330006, Jiangxi Province, China
[4] Institute of Translational Medicine, Medical College, Yangzhou University, Yangzhou 225000, Jiangsu, P.R. China
[5] Department of Anesthesiology and Intensive Care Medicine, Nagasaki University Graduate School of Biomedical Sciences, 1-7-1 Sakamoto, Nagasaki 852-8501, Japan

Introduction

Every year over 800,000 critically ill patients require mechanical ventilation in the United States [1]. Although mechanical ventilation provides essential life support, can also induce or aggravate lung injury by causing ventilator-induced lung injury (VILI) [2]. Mechanical ventilation strategies for reducing VILI in patients with apparent pulmonary diseases are well known: low tidal volume to limit overdistention, optimal oxygen level to prevent hyperoxia, and high positive end-expiratory pressure (PEEP) to prevent injury from low lung volume (atelectrauma) and alveolar collapse [3–5]. Mechanical ventilation is also often applied to patients with shock [6, 7], general anesthesia cases [8], respiratory arrest [9], and so on. Previous studies have attempted to optimize tidal volume and oxygen level to alleviate VILI in patients without apparent pulmonary diseases [3, 10–12]. However, the optimal mechanical ventilation strategy for cases without apparent pulmonary diseases is still uncertain.

Excessive high tidal volume ventilation can result in oxidative stress-induced damage, recruitment of neutrophils, and local release of inflammatory mediators in lungs [13, 14]. VILI involves direct tissue damage due to high mechanical stretch and indirect tissue damage by transducing mechanical stress to activate specific intracellular pathways involved in "mechanotransduction" in lung cells. Previous studies have demonstrated the critical role of mechanotransduction signaling pathways, mainly including Rho-associated protein kinase (ROCK) signaling pathway in VILI. Rho GTPases are signaling G proteins that are distributed across the lower surface of the cell and regulate cytoskeletal dynamics by controlling actin polymerization and myosin II-mediated contraction [15, 16].

Oxygen administration is important for preventing or correcting hypoxemia. Exposure to hyperoxia is a recognized cause of lung injury, producing histopathologic changes similar to those seen in VILI, including oxidative stress and inflammatory response [17–19]. Oxidative damage is mediated by reactive oxygen species (free radicals) derived directly from molecular oxygen. The accumulation of free hydroxyl radicals and peroxynitrite results in the oxidation of proteins and peroxidation of membrane lipids and nucleic acids [20, 21]. Despite the near-ubiquitous concomitant use of mechanical ventilation and oxygen delivery, little is known about the independent and synergistic effects of tidal volume and oxygen delivery on VILI underlying healthy lungs.

In this study, we purposed to investigate how tidal volume and oxygen delivery would independently or synergistically contribute to VILI, mainly focusing on the inflammatory response and oxidative damage in the lungs.

Materials and methods

Animals

Nine weeks old female C57BL/6 N mice (19-22 g, CLEA, Japan) were used for the study. Mice were housed in a pathogen-free room with a controlled environment under a 12-h light-dark cycle and maintained on laboratory chow, with free access to food and water as previously described [22]. This study was approved by the Institutional Animal Care and Use Committee of Nagasaki University (No.1608251335-12). All animal procedures were performed in accordance with institutional and national guidelines.

Mechanical ventilation protocol

Mice were anesthetized with intraperitoneal injection of domitor (0.75 mg/kg), midazolam (4 mg/kg), vetorphale (5 mg/kg), and then orotracheally intubated with a 20 g intravenous indwelling catheter and attached to a mini ventilator (MiniVent Type 845, Harvard Apparatus, USA). Mice were randomized to be ventilated by standard tidal volume (7 ml/kg) [23, 24] or high tidal volume (14 ml/kg); respectively with room air (21% O_2), 50% O_2 ($FIO_2 = 0.5$, moderate hyperoxia), or 100% O_2 ($FIO_2 = 1.0$, severe hyperoxia) for 2 h (Fig. 1A). The ventilation rate was 120 breaths/min. We used 2 cmH_2O PEEP in the official experiments, but high tidal volume ventilation with room air (21% O_2) at 10 cm and 20 cmH_2O PEEP were also tested for inducing lung injury. Non-ventilated mice under general anesthesia with spontaneous breathing were used as controls and were kept on spontaneous breathing for 6 h before being sacrificed. Body temperature was maintained using a 37 °C heating pad.

Tissue sampling

Mice were sacrificed at 4 h after mechanical ventilation (Fig. 1A). After flushing with PBS via right ventricle to remove the blood, the lungs were extracted and weighed. The left lobe was fixed with 4% paraformaldehyde for paraffin sections. The right superior lobe was used for measuring the wet-to-dry lung weight ratio. The other lobes of the right lung tissue samples were stored under −80˚C, and used for other experimental analyses.

Lung wet-to-dry weight ratio

The wet-to-dry lung weight ratio is widely used as a parameter for the assessment of pulmonary edema. The freshly extracted lung tissue sample of the right superior lobe was weighed and recorded as the wet weight. After the incubation in an oven at 80 °C for 24 h, the dried tissue sample was weighed and recorded as dry weight. The wet-to-dry lung weight ratio was calculated.

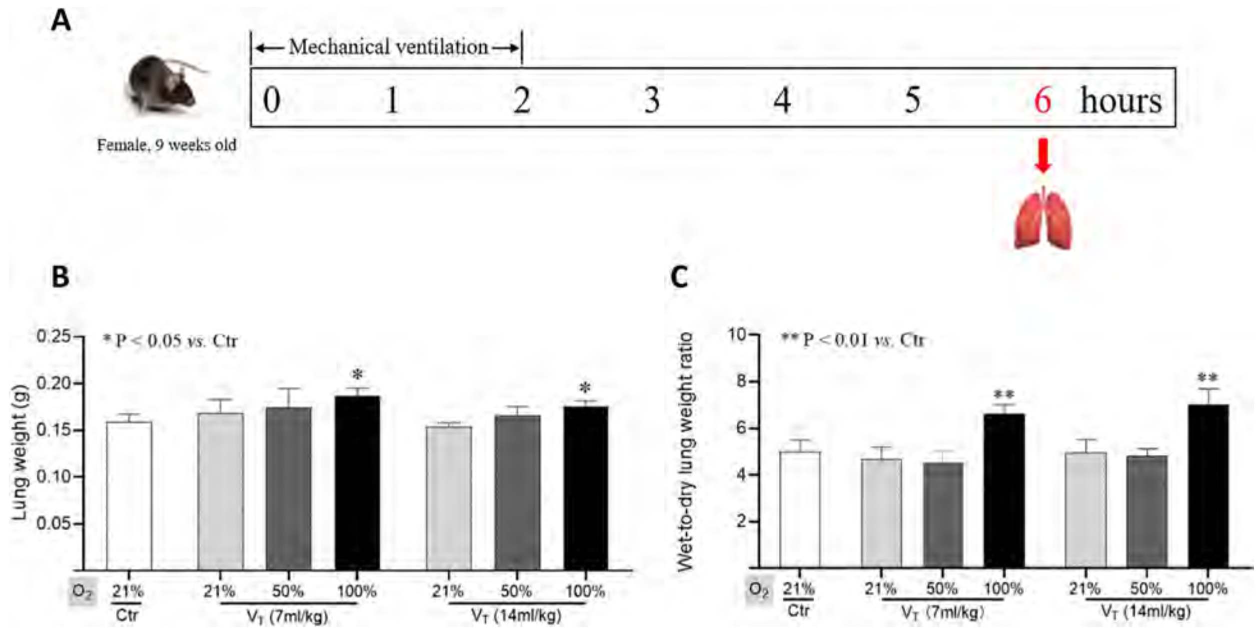

Fig. 1 Lung weight and wet-to-dry lung weight ratio. **A**. Schematic diagram about the experimental timeline. Lung weight (**B**) and wet-to-dry lung weight ratio (**C**) are shown. Data are represented as the means ± SD, *n* = 3 ~ 5 in each group. $*p < 0.05$, $**p < 0.01$ vs. Ctr group. V_T: tidal volume

Immunohistochemical analysis

The oxidative injury of the lungs was detected by immunohistochemical analysis as previously described [22]. Briefly, paraffin sections of 5-μm-thick were deparaffinized and rehydrated. After antigen retrieval and blocking, sections were incubated with anti-mouse 8-OHdG antibody (1:100 dilution, Santa Cruz) overnight at 4℃, and followed by the appropriate fluorescent-conjugated secondary antibodies at 25 °C for 60 min. The nuclei were stained with 4, 6-diamidino-2-phenylindole (DAPI) (1:1000 dilution, Life technologies). The positive staining was examined under fluorescence microscope (FV10CW3, OLYMPUS). The percentage of 8-OHdG-positive cells was calculated from 12 randomly selected fields of view (6 fields/slide in 2 slides) and used for statistical analysis.

ELISA

To evaluate the inflammatory response, ELISA kits (R&D Systems) were used to detect the contents of transforming growth factor β1 (TGF-β1) and interleukin-1beta (IL-1β) in lung tissue lysates as previously described [25]. Briefly, the lung tissues were homogenized using Multi-beads shocker® and added to the T-PER reagent (Thermo Fisher Scientific) consisting of proteinase and dephosphorylation inhibitors (Thermo Fisher Scientific). Lung tissue lysates (100 μg protein) were added to each well and measured following the manufacturer's instructions. The optical density was measured at 450 nm using a microplate reader (Multiskan Fc, Thermo Fisher Scientific).

RT-qPCR analysis

RT-qPCR was performed to evaluate the gene expression of *Rhoa, Rock1, Rock2, Tgfb1* and *Actb*. Briefly, total RNA was isolated from the lung tissues using Quick-RNATMMicroPrep Kit (Zymo Research, Irvine, CA, USA). RNA concentration and purity were measured by a NanoDrop2000 spectrophotometer (Thermo-Fisher Scientific, Wal-tham, MA, USA) and 1.25 μg RNA was reverse-transcribed using the SuperScript™ VILO™ cDNA Synthesis Kit (Thermo-Fisher Scientific). Quantitative PCR was carried out with the SYBR Green real-time PCR Master Mix (Toyobo, Osaka, Japan). The reactions were performed on a CFX96TM real-time PCR System (Bio-Rad). The gene expression was normalized by housekeeping gene *Actb*. Primers were the following: *Rhoa* (Forward: 5'- TGCTTGCTCATA GTCTTCA-3', Reverse:5'-CCAACTCTACCTGCTTCC -3'); *Rock1* (Forward: 5'- AGC TTT TGTTGG CAA TCA GC -3', Reverse:5'- ACT TTC CTGCAA GCT TTT ATC CA -3'); *Rock2* (Forward: 5'- CAGTCC CTG GGT AGT TCA GC -3', Reverse:5'- GCCTGG CAT ATA CTCCATC-3'); *Tgfb1* (Forward:5'-ATTCCTGGCGT TACCTTG-3', Reverse:5'-CTGTATTCCGTCTCCTTG G-3'); *Actb* (Forward:5'-GCACCACACCTTCTACAA -3', Reverse:5'-TACGACCAGAGGCATACA-3').

Western blot

Western blot was performed as previously described [22]. Total proteins (30 ug) from lung tissue were separated by SDS-PAGE gels and then transferred to 0.22-μm PVDF membranes (Bio-Rad). After blocking, the membranes were incubated with primary antibodies against RhoA (1:1000 dilution; cat. no. 2117s; CST), ROCK1 (1:1000 dilution; ab156284; Abcam), MLC2 (1:1000 dilution; cat. no. 3672s; CST), p-MLC2 (1:1000 dilution; cat. no. 3671s; CST), 8-OHdG (1:500 dilution; sc-393,871; Santa Cruz), or α-Tubulin (1:1000 dilution; cat. no. 3873 S; CST) overnight at 4˚C, respectively; followed by the appropriate horseradish peroxidase-conjugated secondary antibodies (Dako). The expression was visualized using an enhanced chemiluminescence detection kit (Thermo Scientific). Semiquantitative analysis was done using ImageQuant LAS 4000 mini (GE Healthcare Life Sciences). Additional file 1 is the original WB image in the manuscript.

Statistical analysis

Statistical analysis was performed as previously described [25]. All the values were presented as the mean ± SD. For comparison of multiple sets of data, one-way analysis of variance (ANOVA) followed by Tukey's test (Dr. SPSS II, Chicago, IL) was used for statistical analyses. All analyses were carried out with the SPSS19.0 statistical software (IBM SPSS Co., USA). A p-value less than 0.05 was accepted as significant.

Results

Mechanical ventilation with severe hyperoxia at 2 cmH$_2$O PEEP significantly induces lung injury

All mice survived in the official experiments (Fig. 1A). Our data showed that lung weight in severe hyperoxia ventilation with standard or high tidal volume were increased significantly ($p < 0.05$ vs. control; Fig. 1B). Similarly, severe hyperoxia ventilation significantly increased the wet-to-dry lung weight ratio, regardless of standard or high tidal volume ($p < 0.01$ vs. control; Fig. 1C).

ELISA was performed to detect the levels of IL-1β and TGF-β1. IL-1β level in the lungs was significantly increased by severe hyperoxia ventilation with either standard or high tidal volume ($p < 0.05$ or $p < 0.01$ vs. control; Fig. 2A). However, moderate hyperoxia ventilation, even by high tidal volume for 2 h did not significantly increase the IL-1β level in lungs (Fig. 2A). Consistent with previous study [26], TGF-β1 level was not significantly changed in the ventilated lungs compared with the control (Fig. 2B).

Oxidative stress can damage macromolecules such as DNA, lipids, and proteins, and 8-OHdG is a marker of oxidative damage to DNA and RNA [27]. Immunohistochemical analysis of lung tissues showed that severe hyperoxia, not moderate hyperoxia ventilation with high or standard tidal volume significantly increased the expression of 8-OHdG in the lungs ($p < 0.01$ vs. control; Fig. 3A). Moreover, Western blot also confirmed the enhancement of 8-OHdG in the ventilated lungs with severe hyperoxia ($p < 0.01$ vs. control; Fig. 3B).

Relatively high tidal volume ventilation at 2 cmH$_2$O PEEP does not clearly induce lung injury

Previous studies have reported that excessive high tidal volume (> 25 ml/kg) ventilation can independently lead to lung injury [4, 28]. In this study, a relatively high tidal volume (14 ml/kg, double of standard) ventilation at 2 cmH$_2$O PEEP for 2 h did not significantly increase the wet-to-dry lung weights ratio, as well as the levels of IL-1β and 8-OHdG in the lungs (Figs. 2 and 3). This suggests inconspicuous damage in the lungs.

We further tried to evaluate whether high tidal volume ventilation induced the activation of mechanotransduction signaling in the lungs. Western blot analysis showed that the expression of RhoA, ROCK1,

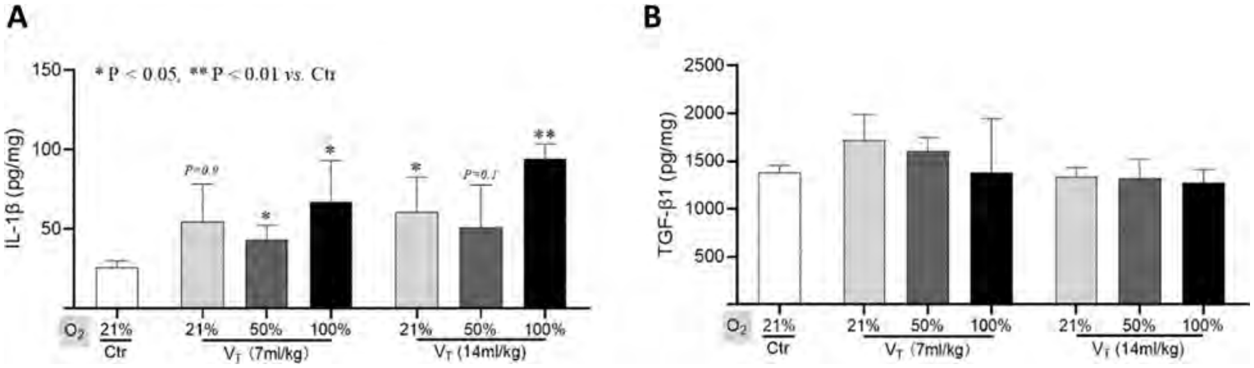

Fig. 2 The levels of IL-1β and TGF-β1 in lung tissues. ELISA data on the levels of IL-1β (**A**) and TGF-β1 (**B**) in lungs are shown. Data are represented as the means ± SD, n = 3 ~ 5 in each group. *$p < 0.05$, **$p < 0.01$ vs. Ctr group. V$_T$: tidal volume

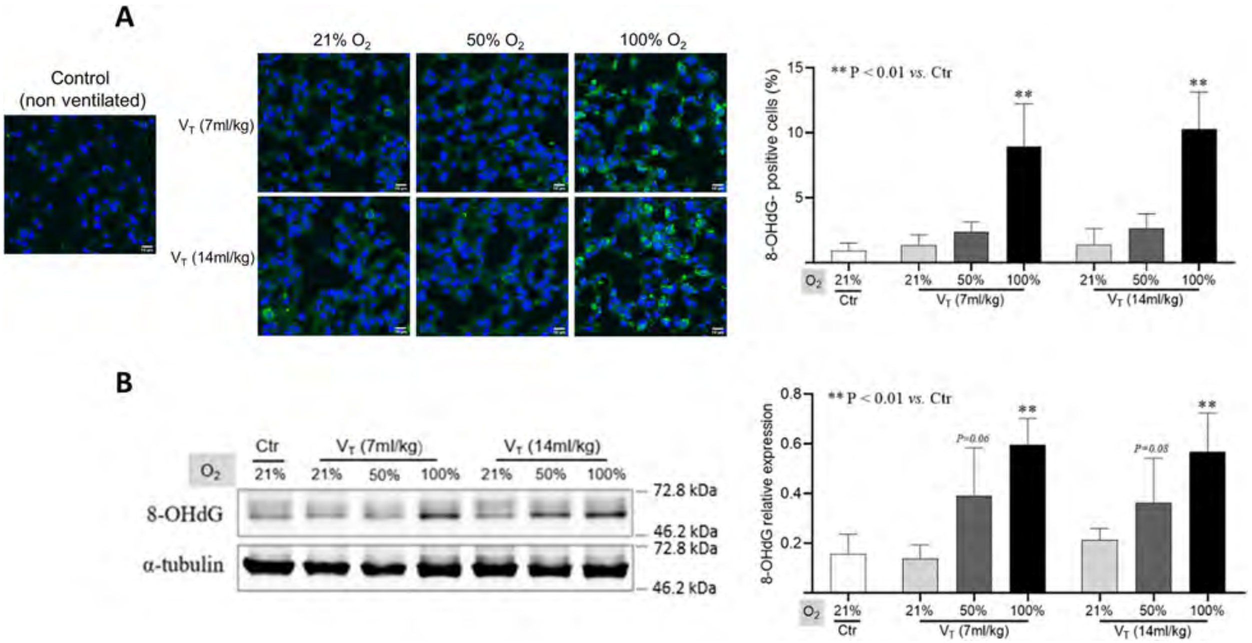

Fig. 3 The expression of 8-OHdG in lung tissues. **A** Representative confocal images (left) and quantitative data (right) of 8-OHdG-positive cells in lung tissues. **B** Representative blots (left) and quantitative data (right) on the expression of 8-OHdG in lungs. Data are normalized to α-tubulin and represented as the means ± SD, *n* = 3 ~ 5 in each group. $^{**}p < 0.01$ vs. Ctr group. V_T: tidal volume. Additional file 1 is the original WB image in the manuscript

MLC2, and p-MLC2 was not significantly increased in the ventilated lungs even by high tidal volume at 2 cmH_2O PEEP (Fig. 4). RT-qPCR analysis also confirmed that the expression of *Rhoa*, *Rock1*, *Rock2*, and *Tgfb1* was not significantly enhanced in the ventilated lungs (Fig. 5).

Maintaining some amount of PEEP is essential for patients receiving mechanical ventilation [29]. Because our data showed a non-injurious setting for high tidal volume ventilation at 2 cmH_2O PEEP, we then tested whether VILI would be detectable clearly at higher PEEP. Mice were assigned to be ventilated with high tidal volume (14 ml/kg) with room air at 10 or 20 cmH_2O PEEP for 2 h. All mice survived well during mechanical ventilation, but one mouse died at 1 h after mechanical ventilation at 20 cmH_2O PEEP. Our data showed that high tidal volume ventilation at 10 or 20 cmH_2O PEEP resulted in higher wet-to-dry lung weight ratio and enhanced the expression of IL-1β, TGF-β1, and 8-OHdG in the lungs (Supplementary Fig. 1). However, the expression of *Rhoa*,

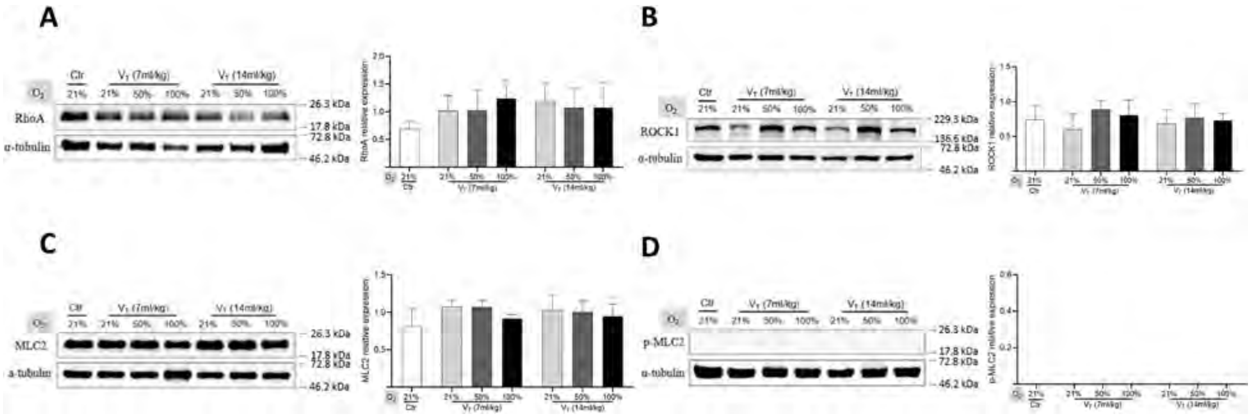

Fig. 4 Western blot analysis on the expression of RhoA, ROCK1, MLC2, and p-MLC2 in lungs. Representative blots (left) and quantitative data (right) on the expression of RhoA (**A**), ROCK1 (**B**), MLC2 (**C**), and p-MLC2 (**D**). Data are normalized to α-tubulin and represented as the means ± SD, *n* = 3 ~ 5 in each group. V_T: tidal volume. Additional file 1 is the original WB image in the manuscript

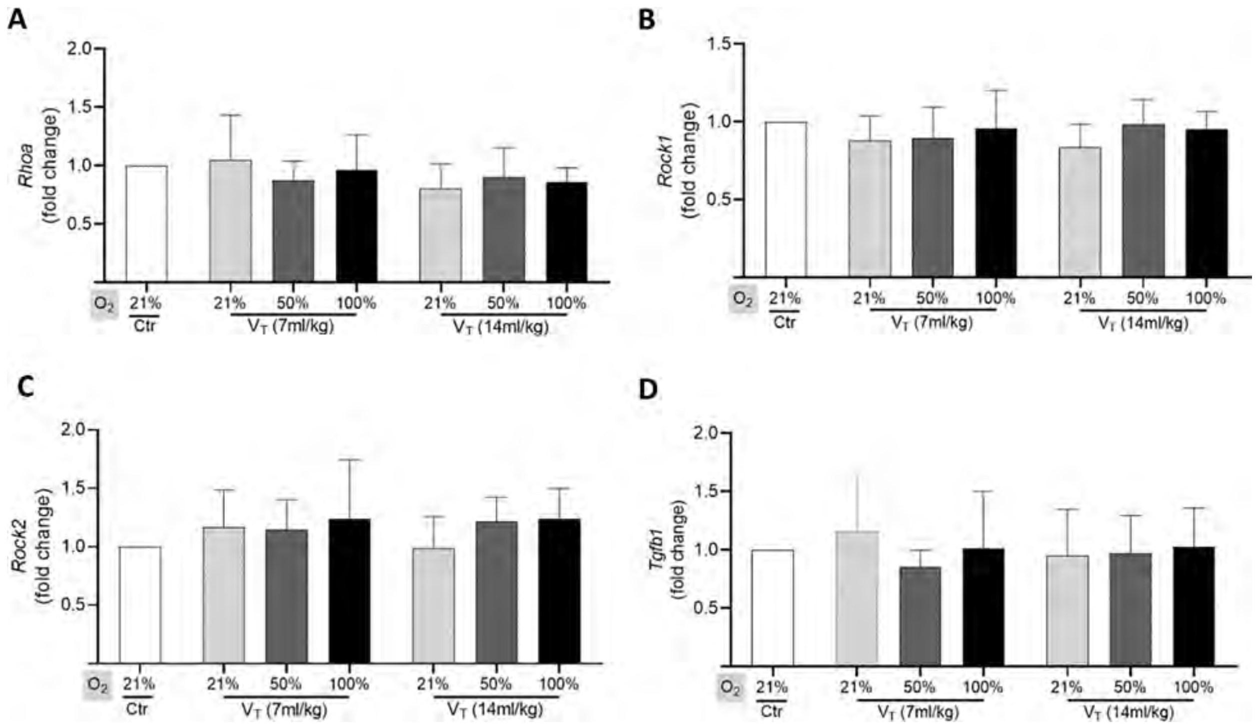

Fig. 5 RT-PCR analysis on the expression of *Rhoa, Rock1, Rock2,* and *Tgfb1* in lungs. Quantitative RT-PCR data shows the relative expression of *Rhoa* (**A**), *Rock1* (**B**), *Rock2* (**C**), and *Tgfb1* (**D**) in lungs. Data are represented as the means ± SD, $n = 3 \sim 5$ in each group. V_T: tidal volume

Rock1, and *Rock2* in the lungs kept stable or even slightly decreased at 4 h after high tidal volume ventilation at 10 or 20 cmH_2O PEEP (Supplementary Fig. 2).

Discussion

Mechanical ventilation-associated lung injury is a common clinical complication in critically ill patients. Unequivocal evidence suggests that excessive mechanical ventilation and hyperoxia have the potential to aggravate and precipitate lung injury in patients without apparent pulmonary diseases [3, 10–12]. In this study, we also found that severe hyperoxia ventilation clearly induced lung injury. In contrast, lung injury was not clearly detectable with moderate hyperoxia ventilation with a relatively high tidal volume at 2 cmH_2O PEEP.

The levels of oxygen commonly used clinically, ranging from 50 to 100% in one atmosphere, are potentially toxic, and these patients risk exacerbation of underlying lung injury. Previous studies have demonstrated that hyperoxia augments lung injury from excessive high tidal volume ventilation in rabbits [30], in rats [31], and in ex vivo mouse lungs [32]. Although the tolerances to oxygen toxicity may be a little different between mice and human beings, healthy mice are still commonly used for experimental investigation of VILI. In this study, severe hyperoxia (100% O_2) ventilation for 2 h significantly increased the wet-to-dry lung weight ratio, as well as IL-1β and 8-OHdG levels in the lungs, suggesting VILI. However, moderate hyperoxia (50% O_2) ventilation did not significantly induce lung injury, even with high tidal volume. Moreover, we did not detect significant changes in TGF-β1 expression. We speculated that mechanical ventilation with relative high tidal volume (14 ml/kg) at 2 cmH_2O PEEP for 2 h might not able to activate the TGF-β signaling pathway [26].

According to previous studies [28, 30], excessive high tidal volume (> 25ml/kg) ventilation is associated with the increased release of inflammatory cytokines and exacerbated oxidative damage. As this study is purposed to investigate VILI in patients without apparent pulmonary diseases, we only tested a relatively high tidal volume (14 ml/kg, double of standard). Based on the levels of IL-1β, TGF-β1 and 8-OHdG in the lungs, high tidal volume ventilation with air or moderate hyperoxia at 2 cmH_2O PEEP for 2 h did not clearly induce serious injuries to the lungs. As shown in the supplemental data, to confirm that the negative data would not be a technical problem of assessment, we used several mice to test high tidal volume ventilation with room air at very high PEEP. Our data showed that high tidal volume ventilation with room air at very high PEEP (> 10 cmH_2O) increased the levels of IL-1β, TGF-β1, and 8-OHdG in lungs, indicating VILI. Therefore, short-term ventilation with high tidal volume (14 ml/kg) at a low/physiological level of PEEP will be harmless.

In conditions of excessive mechanical overdistension, animal models have shown different signaling pathways involved in the induction of lung injury through mechanical transduction, including RhoA/ROCK signaling, and the MLC phosphorylation of downstream targets of ROCK [15, 16]. Although a relatively high tidal volume (14 ml/kg) ventilation did not cause obvious lung injury in our study, we were still interested to know about the activation of the mechanotransduction signalings in the lungs. Unexpectedly, the expression of RhoA, ROCK1, MLC2, and p-MLC2 was not significantly changed in the lungs ventilated with a relatively high tidal volume at 2 cmH_2O PEEP. Furthermore, the expression of *Rhoa*, *Rock1*, and *Rock2* in the lungs even slightly decreased at 4 h after high tidal volume ventilation at 10 or 20 cmH_2O PEEP, although lung injuries were clearly detectable. Several reasons can be considered about the "inactivation" of mechanotransduction signalings in lungs in our study. Firstly, it is difficult to detect changes in the expression of RhoA, ROCK, and MLC2 in lungs [33, 34]. Secondly, we collected the lung tissues at 4 h after mechanical ventilation administration, which might be not a suitable time window for sensitive detection about the changes of p-MLC2 according to previous reports [35, 36]. Thirdly, the anesthetic midazolam we used is a common central muscle relaxant, which might interfere with the activation of mechanotransduction signaling.

There are some limitations in our study. Firstly, it is necessary to include experimental groups of spontaneous breathing with high F_{IO2} for validating the oxygen toxicity to the lungs. Secondly, as this study was originally designed to investigate the synergistic effect of high tidal volume and hyperoxia in VILI, we only evaluated the inflammatory response by IL-1β and TGF-β levels. Thirdly, we were also not able to include more reliable parameters on VILI defination, such as respiratory mechanics and histological findings.

Conclusions

Severe hyperoxia ventilation causes inflammatory response and oxidative damage in mechanically ventilated lungs, while high tidal volume ventilation at a reasonable PEEP possibly does not cause VILI.

Supplementary Information

The online version contains supplementary material available at https://doi.org/10.1186/s12890-023-02626-x.

Additional file 1.

Acknowledgements

Not applicable.

Authors' contributions

TSL and CI contributed to the conception and design of the study. YX performed the experiments and acquired the data. TSL, YX, YL, DZ, CY, JYL, TI, TH, and CI analyzed and interpreted the data. YX drafted the manuscript and prepared figures. TSL, YX, YL, and DZ critically revised the manuscript for important intellectual content. TSL and CI confirmed the authenticity of all the raw data. All authors read and approved the final version of the manuscript.

Funding

Not applicable.

Availability of data and materials

The datasets used and/or analyzed during the current study are available from the corresponding author on reasonable request.

Declarations

Ethics approval and consent to participate

The animal experiments were approved by the Institutional Animal Care and Use Committee of Nagasaki University (approval no.1608251335-12). We confirmed that all experiments were performed in accordance with relevant guidelines and regulations. And we ensured that manuscript reporting adhered to the ARRIVE guidelines (https://arriveguidelines.org) for the reporting of animal experiments.

Consent for publication

Not applicable.

Competing interests

The authors declare no competing interests.

Received: 28 May 2023 Accepted: 31 August 2023

References

1. Supinski GS, Callahan LA. Diaphragm weakness in mechanically ventilated critically ill patients. Crit Care. 2013;17(3):R120.
2. Henderson WR, Chen L, Amato MBP, Brochard LJ. Fifty years of Research in ARDS. Respiratory mechanics in Acute Respiratory Distress Syndrome. Am J Respir Crit Care Med. 2017;196(7):822–33.
3. Gajic O, Dara SI, Mendez JL, Adesanya AO, Festic E, Caples SM, Rana R, St Sauver JL, Lymp JF, Afessa B, Hubmayr RD. Ventilator-associated lung injury in patients without acute lung injury at the onset of mechanical ventilation. Crit Care Med. 2004;32(9):1817–24.
4. Slutsky AS, Ranieri VM. Ventilator-induced lung injury. N Engl J Med. 2013;369(22):2126–36.
5. Futier E, Constantin JM, Paugam-Burtz C, Pascal J, Eurin M, Neuschwander A, Marret E, Beaussier M, Gutton C, Lefrant JY, Allaouchiche B, Verzilli D, Leone M, De Jong A, Bazin JE, Pereira B, Jaber S, IMPROVE Study Group. A trial of intraoperative low-tidal-volume ventilation in abdominal surgery. N Engl J Med. 2013;369(5):428–37.
6. Alviar CL, Rico-Mesa JS, Morrow DA, Thiele H, Miller PE, Maselli DJ, van Diepen S. Positive pressure ventilation in cardiogenic shock: review of the evidence and practical advice for patients with mechanical circulatory support. Can J Cardiol. 2020;36(2):300–12.

7. Jouffroy R, Saade A, Pegat-Toquet A, Philippe P, Carli P, Vivien B. Prehospital mechanical ventilation in septic shock patients. Am J Emerg Med. 2019;37(10):1860–3.
8. Guay J, Ochroch EA, Kopp S. Intraoperative use of low volume ventilation to decrease postoperative mortality, mechanical ventilation, lengths of stay and lung injury in adults without acute lung injury. Cochrane Database Syst Rev. 2018;7(7):CD011151.
9. Khoury A, De Luca A, Sall FS, Pazart L, Capellier G. Ventilation feedback device for manual ventilation in simulated respiratory arrest: a crossover manikin study. Scand J Trauma Resusc Emerg Med. 2019;27(1):93.
10. Serpa Neto A, Cardoso SO, Manetta JA, Pereira VG, Espósito DC, Pasqualucci Mde O, Damasceno MC, Schultz MJ. Association between use of lung-protective ventilation with lower tidal volumes and clinical outcomes among patients without acute respiratory distress syndrome: a meta-analysis. JAMA. 2012;308(16):1651–9.
11. Determann RM, Royakkers A, Wolthuis EK, Vlaar AP, Choi G, Paulus F, Hofstra JJ, de Graaff MJ, Korevaar JC, Schultz MJ. Ventilation with lower tidal volumes as compared with conventional tidal volumes for patients without acute lung injury: a preventive randomized controlled trial. Crit Care. 2010;14(1):R1.
12. Wongsurakiat P, Pierson DJ, Rubenfeld GD. Changing pattern of ventilator settings in patients without acute lung injury: changes over 11 years in a single institution. Chest. 2004;126(4):1281–91.
13. Chapman KE, Sinclair SE, Zhuang D, Hassid A, Desai LP, Waters CM. Cyclic mechanical strain increases reactive oxygen species production in pulmonary epithelial cells. Am J Physiol Lung Cell Mol Physiol. 2005;289(5):L834–41.
14. Davidovich N, DiPaolo BC, Lawrence GG, Chhour P, Yehya N, Margulies SS. Cyclic stretch-induced oxidative stress increases pulmonary alveolar epithelial permeability. Am J Respir Cell Mol Biol. 2013;49(1):156–64.
15. Marchioni A, Tonelli R, Cerri S, Castaniere I, Andrisani D, Gozzi F, Bruzzi G, Manicardi L, Moretti A, Demurtas J, Baroncini S, Andreani A, Cappiello GF, Busani S, Fantini R, Tabbì L, Samarelli AV, Clini E. Pulmonary Stretch and Lung Mechanotransduction: implications for progression in the fibrotic lung. Int J Mol Sci. 2021;22(12):6443.
16. Tschumperlin DJ, Ligresti G, Hilscher MB, Shah VH. Mechanosensing and fibrosis. J Clin Invest. 2018;128(1):74–84.
17. Matute-Bello G, Frevert CW, Martin TR. Animal models of acute lung injury. Am J Physiol Lung Cell Mol Physiol. 2008;295(3):L379–99.
18. Choi WI, Quinn DA, Park KM, Moufarrej RK, Jafari B, Syrkina O, Bonventre JV, Hales CA. Systemic microvascular leak in an in vivo rat model of ventilator-induced lung injury. Am J Respir Crit Care Med. 2003;167(12):1627–32.
19. Held HD, Boettcher S, Hamann L, Uhlig S. Ventilation-induced chemokine and cytokine release is associated with activation of nuclear factor-kappab and is blocked by steroids. Am J Respir Crit Care Med. 2001;163(3 Pt 1):711–6.
20. Nakane M. Biological effects of the oxygen molecule in critically ill patients. J Intensive Care. 2020;8(1):95.
21. Auten RL, Davis JM. Oxygen toxicity and reactive oxygen species: the devil is in the details. Pediatr Res. 2009;66(2):121–7.
22. Xu Y, Zhai D, Goto S, Zhang X, Jingu K, Li TS. Nicaraven mitigates radiation-induced lung injury by downregulating the NF-κB and TGF-β/Smad pathways to suppress the inflammatory response. J Radiat Res. 2022;63(2):158–65.
23. Dreyfuss D, Soler P, Saumon G. Mechanical ventilation-induced pulmonary edema. Interaction with previous lung alterations. Am J Respir Crit Care Med. 1995;151(5):1568–75.
24. Wolthuis EK, Vlaar AP, Choi G, Roelofs JJ, Juffermans NP, Schultz MJ. Mechanical ventilation using non-injurious ventilation settings causes lung injury in the absence of pre-existing lung injury in healthy mice. Crit Care. 2009;13(1):R1.
25. Yan C, Luo L, Urata Y, Goto S, Li TS. Nicaraven reduces cancer metastasis to irradiated lungs by decreasing CCL8 and macrophage recruitment. Cancer Lett. 2018;418:204–10.
26. Cabrera-Benítez NE, Parotto M, Post M, Han B, Spieth PM, Cheng WE, Valladares F, Villar J, Liu M, Sato M, Zhang H, Slutsky AS. Mechanical stress induces lung fibrosis by epithelial-mesenchymal transition. Crit Care Med. 2012;40(2):510–7.
27. Helbock HJ, Beckman KB, Ames BN. 8-Hydroxydeoxyguanosine and 8-hydroxyguanine as biomarkers of oxidative DNA damage. Methods Enzymol. 1999;300:156–66.
28. Amatullah H, Maron-Gutierrez T, Shan Y, Gupta S, Tsoporis JN, Varkouhi AK, Teixeira Monteiro AP, He X, Yin J, Marshall JC, Rocco PRM, Zhang H, Kuebler WM, Dos Santos CC. Protective function of DJ-1/PARK7 in lipopolysaccharide and ventilator-induced acute lung injury. Redox Biol. 2021;38:101796.
29. Mercat A, Richard JC, Vielle B, Jaber S, Osman D, Diehl JL, Lefrant JY, Prat G, Richecoeur J, Nieszkowska A, Gervais C, Baudot J, Bouadma L, Brochard L. Expiratory pressure (Express) Study Group. Positive end-expiratory pressure setting in adults with acute lung injury and acute respiratory distress syndrome: a randomized controlled trial. JAMA. 2008;299(6):646–55.
30. Sinclair SE, Altemeier WA, Matute-Bello G, Chi EY. Augmented lung injury due to interaction between hyperoxia and mechanical ventilation. Crit Care Med. 2004;32(12):2496–501.
31. Cooper JA Jr, Fuller JM, McMinn KM, Culbreth RR. Modulation of monocyte chemotactic protein-1 production by hyperoxia: importance of RNA stability in control of cytokine production. Am J Respir Cell Mol Biol. 1998;18(4):521–5.
32. Bailey TC, Martin EL, Zhao L, Veldhuizen RA. High oxygen concentrations predispose mouse lungs to the deleterious effects of high stretch ventilation. J Appl Physiol (1985). 2003;94(3):975–82.
33. Gawlak G, Tian Y, O'Donnell JJ 3rd, Tian X, Birukova AA, Birukov KG. Paxillin mediates stretch-induced rho signaling and endothelial permeability via assembly of paxillin-p42/44MAPK-GEF-H1 complex. FASEB J. 2014;28(7):3249–60.
34. Zhang Y, Jiang L, Huang T, Lu D, Song Y, Wang L, Gao J. Mechanosensitive cation channel Piezo1 contributes to ventilator-induced lung injury by activating RhoA/ROCK1 in rats. Respir Res. 2021;22(1):250.
35. Bárány K, Ledvora RF, Mougios V, Bárány M. Stretch-induced myosin light chain phosphorylation and stretch-release-induced tension development in arterial smooth muscle. J Biol Chem. 1985;260(11):7126–30.
36. Lee E, Liu Z, Nguyen N, Nairn AC, Chang AN. Myosin light chain phosphatase catalytic subunit dephosphorylates cardiac myosin via mechanisms dependent and independent of the MYPT regulatory subunits. J Biol Chem. 2022;298(9):102296.

Publisher's Note

THERAPEUTIC ADVANCES in
Respiratory Disease

Original Research

Optimization on the dose and time of nicaraven administration for mitigating the side effects of radiotherapy in a preclinical tumor-bearing mouse model

Ther Adv Respir Dis

2022, Vol. 16: 1–10

DOI: 10.1177/17534666221137277

Yong Xu, Lina Abdelghany, Reiko Sekiya, Da Zhai, Keiichi Jingu and Tao-Sheng Li

Abstract

Objective: Radiation-induced lung injury (RILI) is one of the serious complications of radiotherapy. We have recently demonstrated that nicaraven can effectively mitigate RILI in healthy mice. Here, we further tried to optimize the dose and time of nicaraven administration for alleviating the side effects of radiotherapy in tumor-bearing mice.

Methods and results: A subcutaneous tumor model was established in the back of the chest in C57BL/6N mice by injecting Lewis lung cancer cells. Therapeutic thoracic irradiations were done, and placebo or different doses of nicaraven (20, 50, 100 mg/kg) were administrated intraperitoneally pre-irradiation (at almost 5–10 min before irradiation) or post-irradiation (within 5 min after irradiation). Mice that received radiotherapy and nicaraven were sacrificed on the 30th day, but control mice were sacrificed on the 15th day. Serum and lung tissues were collected for evaluation. Nicaraven significantly decreased the level of CCL8, but did not clearly change the levels of 8-OHdG, TGF-β, IL-1β, and IL-6 in serum. Besides these, nicaraven effectively decreased the levels of TGF-β, IL-1β, and SOD2 in the lungs, especially by post-irradiation administration with the dose of 20 mg/kg. Although there was no significant difference, the expression of SOD1, 53BP1, and caspase 3 was detected lower in the lungs of mice received nicaraven post-irradiation than that of pre-irradiation.

Conclusion: According to our data, the administration of nicaraven at a relatively low dose soon after radiotherapy will be recommended for attenuating the side effects of radiotherapy.

Keywords: DNA damage, fibrosis, inflammatory response, lung injury, radiation

Received: 2 April 2022; revised manuscript accepted: 20 October 2022.

Introduction

Radiotherapy is an essential tool for the treatment of intrathoracic malignancies, including lung, breast, and esophageal cancers.[1,2] Exposure of healthy tissues to radiation and the toxicity it causes often limits its effectiveness and decreases the survival benefit of radiotherapy. Beyond the systemic side effects, radiation-induced lung injury (RILI) is a serious obstacle to patients receiving radiotherapy for thoracic malignant tumors.[3,4] RILI occurs in 5–20% of lung cancer patients receiving radiotherapy, which may lead to the discontinuation of treatment. However, there are still no effective drugs and protective strategies to prevent radiation side effects in cancer patients undergoing radiotherapy.

It is well known that ionizing radiation induces directly DNA double-strand breaks and triggers the release of ROS.[5] The level of ROS overwhelms can cause oxidative damage to DNA, lipids, and proteins.[6] Although radiotherapy is a local therapy, it has systemic effects mainly influencing immune and inflammation processes.[7] Moreover, it has been demonstrated that radiation-induced injuries to tissue cells can promote

Correspondence to:
Tao-Sheng Li
Department of Stem Cell Biology, Atomic Bomb Disease Institute, Nagasaki University, 1-12-4 Sakamoto, Nagasaki 852-8523, Japan.

Department of Stem Cell Biology, Graduate School of Biomedical Sciences, Nagasaki University, Nagasaki, Japan
litaoshe@nagasaki-u.ac.jp

Yong Xu
Lina Abdelghany
Da Zhai
Department of Stem Cell Biology, Atomic Bomb Disease Institute, Nagasaki University, Nagasaki, Japan

Department of Stem Cell Biology, Graduate School of Biomedical Sciences, Nagasaki University, Nagasaki, Japan

Reiko Sekiya
Department of Stem Cell Biology, Atomic Bomb Disease Institute, Nagasaki University, Nagasaki, Japan

Keiichi Jingu
Department of Radiation Oncology, Graduate School of Medicine, Tohoku University, Sendai, Japan

the release of a multitude of inflammatory cytokines and chemokines, which indirectly contribute to the consequent damage to cells and tissues and eventually culminate in fibrotic changes.[8–10] Therefore, the scavenging of ROS and the suppression of the inflammatory response are thought to be potential pharmacological interventions for mitigating the side effects of radiotherapy.

Many past studies have challenged to develop radioprotective agents. Thiol-synthetic compounds, such as amifostine has been approved to use clinically for protecting against radiation injury, however, amifostine has the disadvantages of toxicity and limited route of administration in the clinic.[11] Nitrogen oxides, such as Tempol, have also been tested as a radioprotectant, but its application is limited due to problems on producing hypotension and increasing heart rate.[12] Some natural antioxidants, such as vitamin E and selenium have also shown radioprotective effects, but the benefit of antioxidants for cancer radiotherapy is asked to be further confirmed because of the probable effect on radiosensitivity of cancer cells.[12,13] Therefore, there is still required to develop an ideal agent for mitigating the side effects of radiotherapy for cancer patients.

Nicaraven, a chemically synthesized hydroxyl radical-specific scavenger,[14] has previously been reported to protect against radiation-induced cell death.[14,15] Nicaraven can also reduce the radiation-induced recruitment of macrophages and neutrophils into irradiated lungs.[16] Moreover, we have recently demonstrated that nicaraven can also effectively protect against RILI by suppressing the inflammatory response.[17] To further develop for clinical application, we herein aim to optimize the dose and time of nicaraven administration for attenuating the side effects of radiotherapy.

Using a preclinical tumor-bearing mice model, we administered different doses of nicaraven, before or soon after thoracic irradiations. We then evaluated the systemic side effects and RILI, mainly by focusing on oxidative stress and inflammatory responses. According to our experimental data, the administration of nicaraven at a relatively low dose soon after radiotherapy will be recommended for attenuating the side effects of radiotherapy.

Materials and methods

Cancer cells and animals

Mouse Lewis lung cancer (LLC) cells were used for the experiments. The cells were maintained in DMEM (FUJIFILM Wako Pure Chemical Corporation), supplemented with 10% fetal bovine serum (Cytiva) and 1% penicillin/streptomycin (Gibco; Thermo Fisher Scientific, Inc.), and cultured at 37°C in a humidified incubator with 5% CO2.

Male C57BL/6N mice (8 weeks old) were used for the study. Mice were housed in a pathogen-free room with a controlled environment under a 12-h light-dark cycle and maintained on laboratory chow, with free access to food and water. This study was approved by the Institutional Animal Care and Use Committee of Nagasaki University (No.1608251335-12). All animal procedures were performed in accordance with institutional and national guidelines.

Tumor-bearing mouse model, radiotherapy, and nicaraven administration

To match the pathological status of cancer patients, we used a preclinical tumor-bearing model for the experiment. Briefly, mice were subcutaneously inoculated with 5×10^5 LLC cells/0.1 ml of saline in the back of the chest. At 10 days after cancer cell inoculation, mice had randomly received radiotherapy and nicaraven administration as indicated in Figure 1(a). Considering the common clinical radiotherapy regimen for lung cancer and breast cancer,[18,19] thoracic irradiations (including the heart and lungs) were delivered to mice at a dosage rate of 1.0084 Gy/min (200 kV, 15 mA, 5 mm Al filtration, ISOVOLT TITAN320, General Electric Company, United States). Mice were intraperitoneally injected with 0 (placebo), 20, 50, 100 mg/kg nicaraven pre-irradiation (almost 5–10 min before irradiation) or post-irradiation (within 5 min after irradiation), respectively. Six mice without irradiation exposure were used as control ($n = 6$, Control group).

We measured the body weights of mice every other day. Mice that received radiotherapy and nicaraven were sacrificed on the 30th day, but the control mice were sacrificed on the 15th day. To collect serum, we took the blood from the inferior vena cava of mice under general anesthesia before sacrifice. Lung tissues were then excised and weighed. The collected serum and lung tissue samples were stored under −80°C, and used for experimental evaluations as follows.

ELISA

We measured the concentrations of 8-oxo-29-deoxyguanosine (8-OHdG), a marker of DNA oxidation in serum using an ELISA kit (Nikken SEIL Corporation, Shizuoka, Japan) according to the manufacturer's instructions. The mean values of duplicate assays with each sample were used for the statistical analyses.

ELISA kits (R&D Systems) were used to detect the contents of transforming growth factor β (TGF-β), interleukin-1beta (IL-1β), interleukin-6 (IL-6), C-C Motif Chemokine Ligand 8 (CCL8) in serum and lung tissues according to the manufacturer's instructions. Briefly, the lung tissues were homogenized using Multi-beads shocker® and added to the T-PER reagent (Thermo Fisher Scientific) consisting of proteinase and dephosphorylation inhibitors (Thermo Fisher Scientific). Then, lung lysates and serum were added to each well and measured per the manufacturer's instructions. The optical density of each well was measured at 450 nm using a microplate reader (Multiskan Fc, Thermo Fisher Scientific).

Western blot

Western blot was performed as previously described.[20] Briefly, total protein from the lung tissues was separated by SDS-PAGE gels and then transferred to 0.22-μm PVDF membranes (Bio-Rad). After blocking, the membranes were incubated with primary antibodies against SOD1 (1:500 dilution; cat. no. sc11407; Santa Cruz), SOD2 (1:500 dilution; cat. no. sc30080; Santa Cruz), β-actin (1:1,000 dilution; cat. no. 8457S; CST), 53BP1 (1:1,000 dilution; cat. no. ab36823; Abcam), caspase 3 (1:1,000 dilution; cat. no. 9662; CST), α-SMA (1:1,000 dilution; cat. no. 19245S; CST), collagen Ⅰ (1:1,000 dilution; cat. no. ab34710; Abcam), or α-Tubulin (1:1,000 dilution; cat. no. 3873S; CST) overnight at 4°C, respectively, followed by the appropriate horseradish peroxidase-conjugated secondary antibodies (Dako). The expression was visualized using an enhanced chemiluminescence detection kit (Thermo Scientific). Semiquantitative analysis was done using ImageQuant LAS 4000 mini (GE Healthcare Life Sciences).

Statistical analysis

All the values were presented as the mean ± SD. For comparison of multiple sets of data, one-way analysis of variance (ANOVA) followed by Tukey's test (Dr. SPSS II, Chicago, IL) was used for statistical analyses. All analyses were carried out with the SPSS19.0 statistical software (IBM SPSS Co., USA). A *p*-value less than 0.05 was accepted as significant.

Results

Nicaraven for mitigating the systemic side effects of radiotherapy is not very clearly detectable in tumor-bearing mice under our experimental treatment regimens

Mice had well tolerated the therapeutic regimens, but two mice in the post-irradiation administration with the dose of 20 mL/kg group died on the 9th and 10th days, and one mouse in the placebo group died on the 19th day during the follow-period (Figure 1(a)). Thoracic irradiation was delivered to mice using lead shielding sheets, and we found the death of mice at the next morning after radiation exposure. Radiation exposure to the brain stem may happen even only 1-mm positioning error. As a single 6 Gy exposure to the brain stem can kill some mice,[21] we speculated the death of mice should be an error exposure to the brain due to some positioning or shadowing problems of mice during thoracic exposure. The body weights of mice in all groups were decreased temporarily during radiotherapy, but tended to increase a few days after the stopping of irradiation exposures (Figure 1(b)). There was no significant difference on the body weight changes of mice among groups. Compared with the control mice, the lung weights were slightly increased in mice received placebo treatment after radiotherapy. However, the lung weights showed significantly lower in mice received nicaraven post-irradiation than that of placebo treatment ($p < 0.05$, Figure 1(c)).

ELISA was performed to detect the levels of 8-OHdG, TGF-β, IL-1β, IL-6, CCL8 in serum. The level of 8-OHdG in serum was not significantly different among groups (Figure 2(a)). However, the serum level of 8-OHdG was

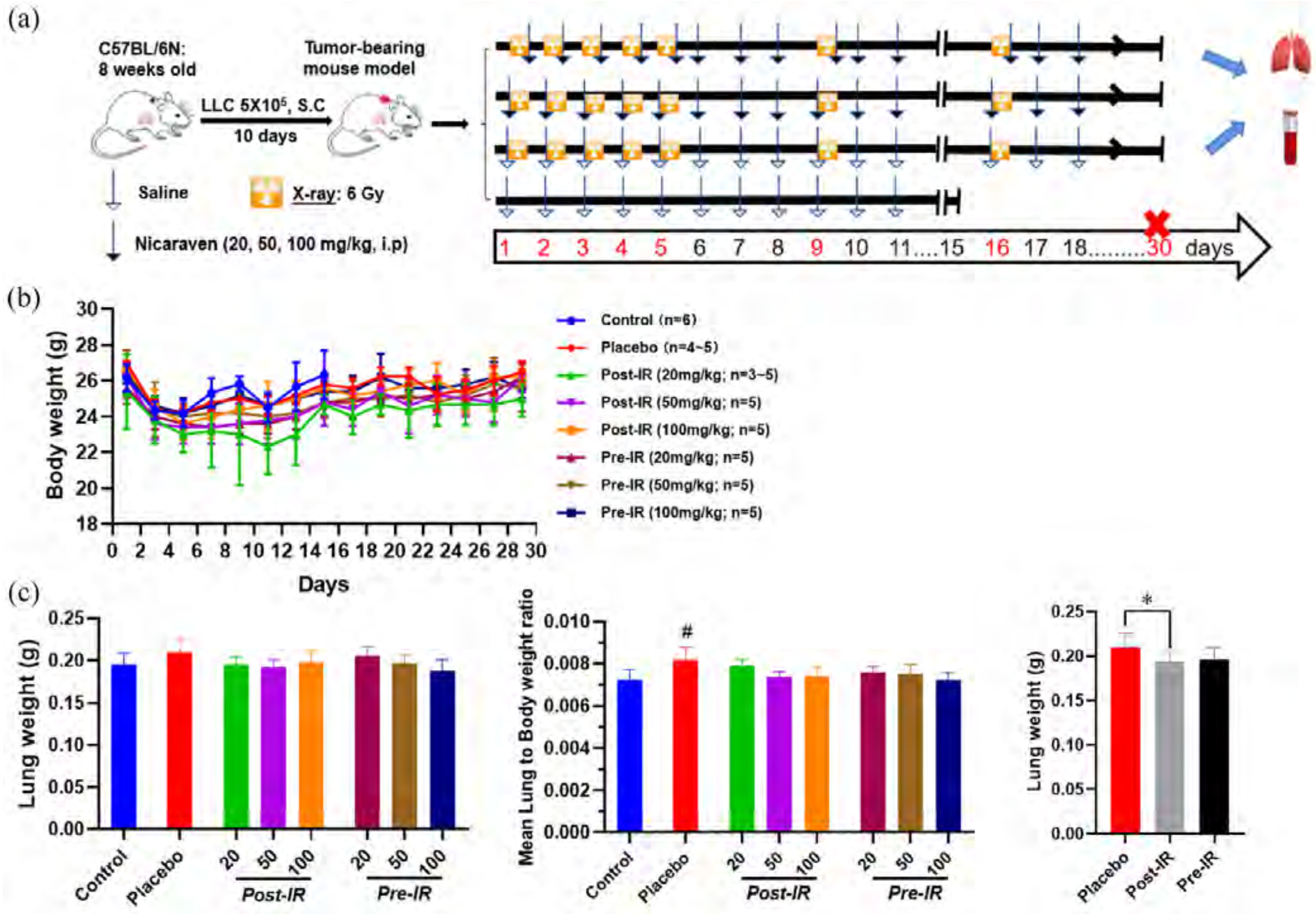

Figure 1. Changes of body weight and lung weight in mice. (a) Schematic diagram about the experimental timeline and protocol. (b) Quantitative data on the changes of body weights through 30 days. (c) Quantitative data on the changes of lung weight and lung to body weight ratio in mice. Data are represented as the means ± SD, $n=3\sim6$ in per group. $^{\#}p<0.05$ *versus* Control group, $^{*}p<0.05$ *versus* Placebo group. IR, irradiation; Post-IR, post-irradiation; Pre-IR, pre-irradiation.

detected significantly lower in mice received nicaraven post-irradiation than that of pre-irradiation ($p<0.05$, Figure 2(a)). Our results also showed that the administration of nicaraven with any dose before or after irradiation did not clearly change the levels of TGF-β, IL-1β, IL-6 in serum. However, the level of CCL8 in serum was significantly lower in mice received nicaraven either post-irradiation or pre-irradiation when compared with mice received placebo treatment ($p<0.05$, Figure 2(e)).

The administration of nicaraven at a relatively low dose after radiotherapy shows partial attenuation of RILI in a preclinical tumor-bearing mouse model

To evaluate the inflammatory responses in lungs, ELISA analysis indicated that the TGF-β level in lungs was slightly increased in mice received placebo treatment after thoracic radiation, but was effectively attenuated by post-irradiation administration with 20 mg/kg nicaraven ($p<0.05$, Figure 3(a)). Similarly, the IL-1β level in the lungs was also increased in mice that received placebo treatment after thoracic radiation, but significantly decreased by post-irradiation administration with 20 or 50 mg/kg nicaraven ($p<0.05$, Figure 3(b)). Strangely, it seems that post-irradiation administration with relatively lower doses of nicaraven more effectively alleviates the enhancement of TGF-β and IL-1β in lung tissues. However, the levels of IL-6 and CCL8 in the lungs were not significantly different among all groups (Figure 3(c), (d)).

The expression of SOD1 in lungs was detected higher by Western blot in the placebo group than

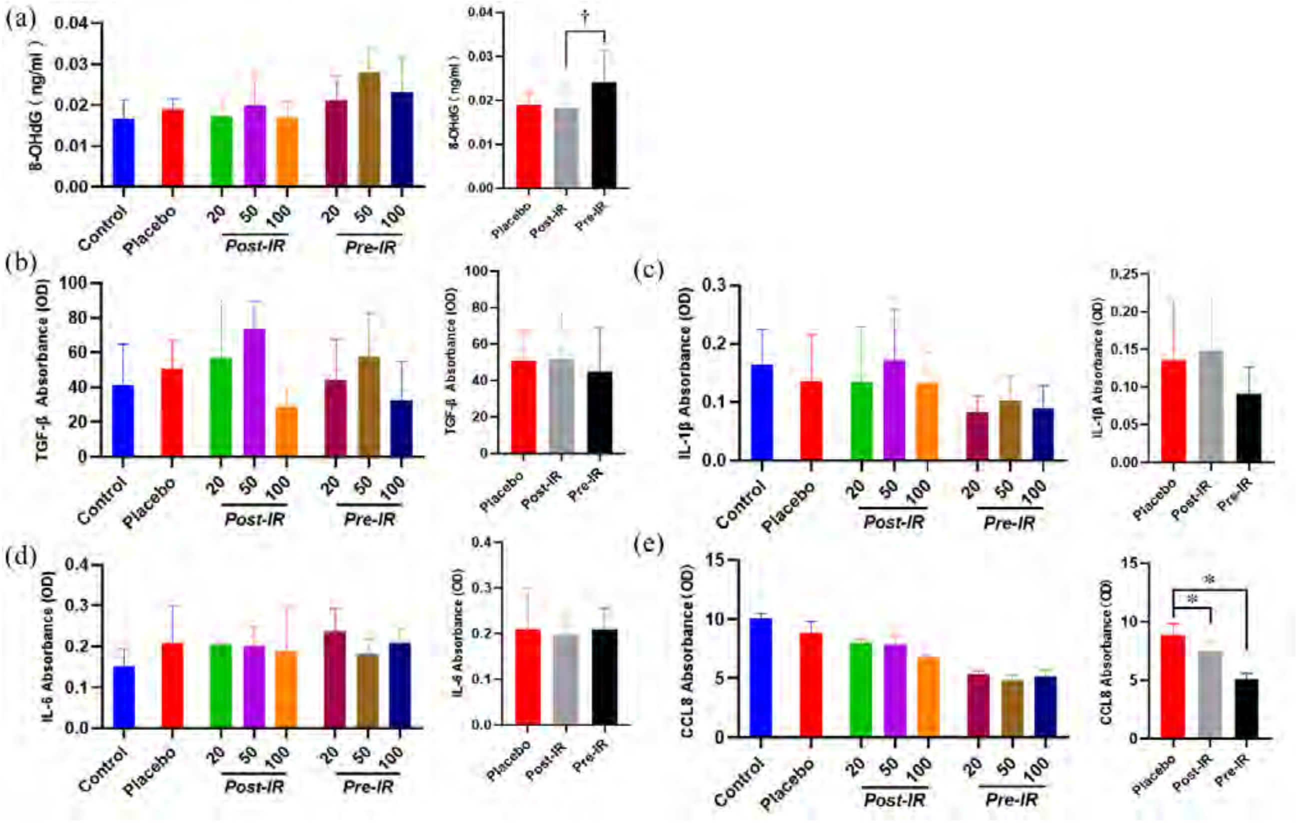

Figure 2. The effect of nicaraven on levels of 8-OHdG and inflammatory factors in serum.
Quantitative data on the levels of 8-OHdG (a), TGF-β (b), IL-1β (c), IL-6 (d), CCL8 (e). Data are represented as the means ± SD, *n*=3~6 in per group. $^*p < 0.05$ *versus* Placebo group, $^†p < 0.05$ *versus* post-IR group.
IR: irradiation; Post-IR: post-irradiation; Pre-IR: pre-irradiation.

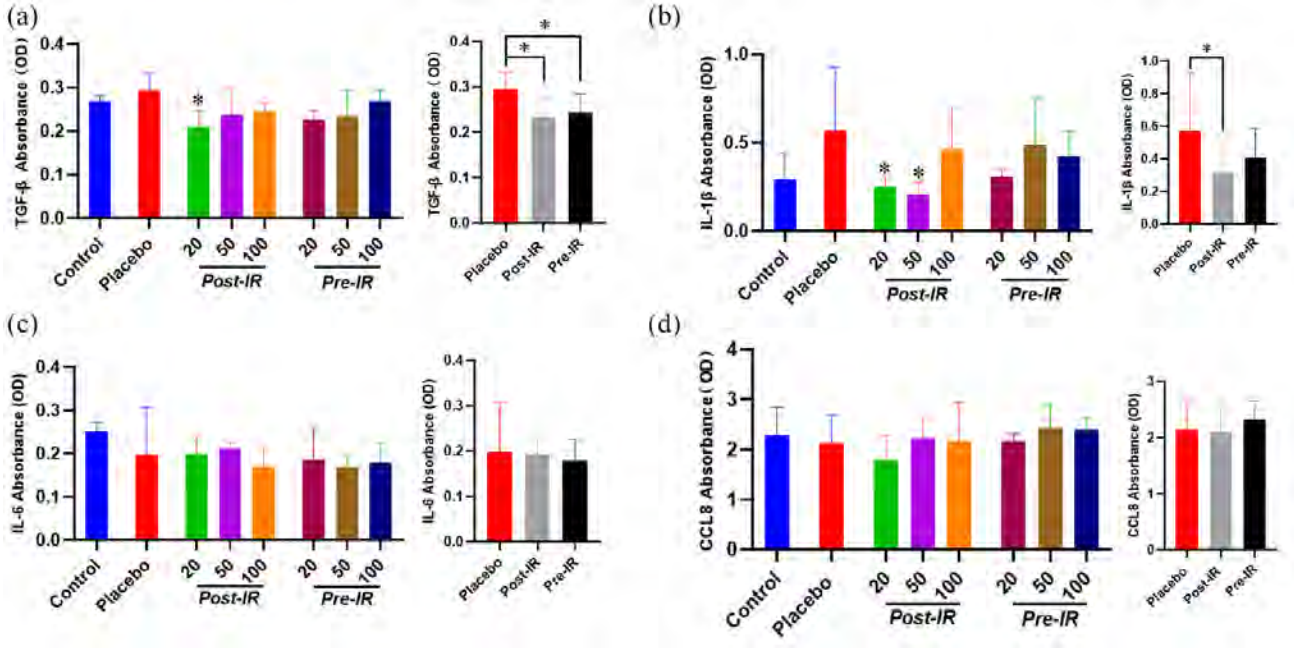

Figure 3. ELISA analysis on the inflammatory response in irradiated lungs. Quantitative data on the levels of TGF-β (a), IL-1β (b), IL-6 (c), CCL8 (d) in irradiated lung tissues were shown. Data are represented as the means ± SD, *n*=3~6 in per group. $^*p < 0.05$ *versus* Placebo group.
IR: irradiation; Post-IR: post-irradiation; Pre-IR: pre-irradiation.

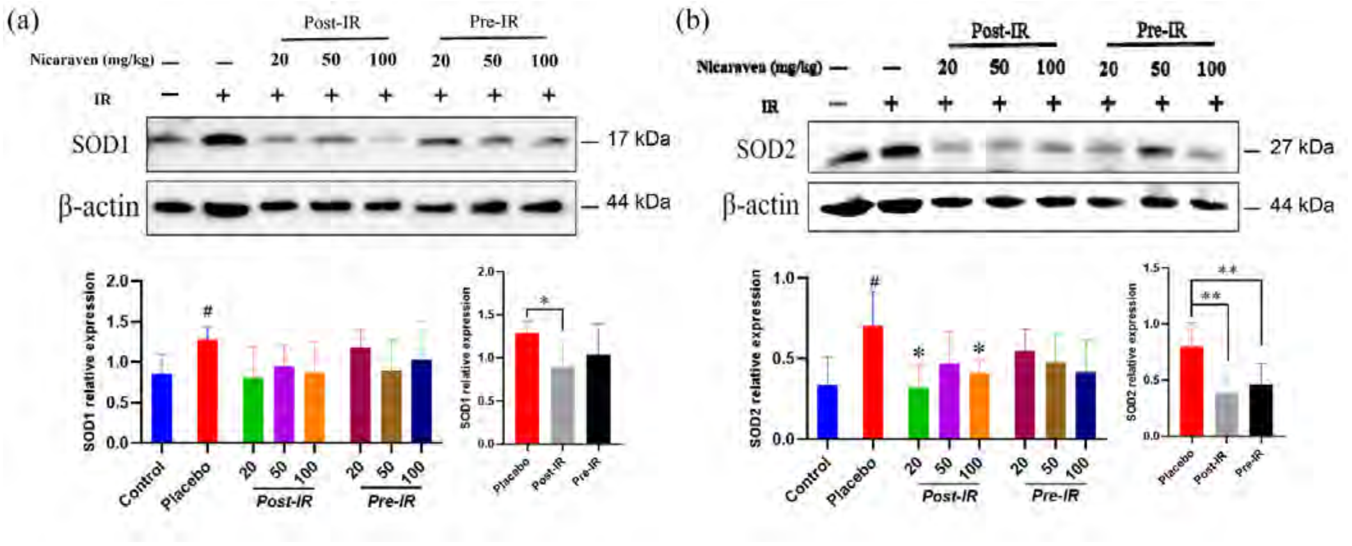

Figure 4. Nicaraven on attenuating oxidative response in irradiated lungs. Representative blots (up), and quantitative data (down) on the expression of SOD1 (a), SOD2 (b). Data are represented as the means ± SD, $n = 3 \sim 6$ in per group. $^{\#}p < 0.05$ *versus* Control group, $^{*}p < 0.05$, $^{**}p < 0.01$ *versus* Placebo group.
IR: irradiation; Post-IR: post-irradiation; Pre-IR: pre-irradiation.

the control group ($p < 0.05$, Figure 4(a)). Although there was no significant difference among all groups (Figure 4(a)), the increased expression of SOD1 in the lungs was effectively attenuated by post-irradiation administration ($p < 0.05$, Figure 4(a)). The expression of SOD2 was also significantly increased in the placebo group, but the increased expression of SOD2 was clearly decreased by post-irradiation administration with 20 or 100 mg/kg nicaraven ($p < 0.05$, Figure 4(b)). The enhanced expression of SOD2 in the lungs was effectively decreased by either post-irradiation or pre-irradiation administration ($p < 0.01$, Figure 4(b)).

We also measured the expression of 53BP1, a marker for DNA damage in lungs by Western blot. Post-irradiation administration of nicaraven showed to slightly decrease the 53BP1 expression in lungs (Figure 5(a)). Caspase 3 has been considered a key effector in inducing cell apoptosis. Compared with the control group without irradiation, Western blot analysis showed a significant enhancement on the expression of caspase 3 in lungs of mice from the placebo group ($p < 0.05$, Figure 5(b)), but the enhanced expression of caspase 3 in irradiated lungs was effectively attenuated only by post-irradiation administration of nicaraven ($p < 0.05$, Figure 5(b)).

We finally investigated the expression of α-SMA and collagen Ⅰ, the common markers of fibrosis in lungs. Compared with the control group, Western blot analysis showed higher expression of α-SMA and collagen Ⅰ in lungs of mice from the placebo group (Figure 6). Although there was no significant difference among groups, the enhanced expression of α-SMA and collagen Ⅰ in irradiated lungs was partially attenuated in mice that received post-irradiation administration of nicaraven (Figure 6).

Discussion

Radiotherapy for cancer is known to accompany side effects, which may lead to the discontinuation of treatment and decrease the quality of life of patients.[22] In this study, we investigated the optimal dose and time of nicaraven administration for attenuating the side effects of radiotherapy in tumor-bearing mice. We could not clearly detect significant changes on body weight and the levels of inflammatory cytokines in serum. However, nicaraven administration, especially with a relatively lower dose at the time soon after thoracic irradiations partially decreased the levels of TGF-β, IL-1β, SOD1, SOD2, and caspase 3 in lungs, suggesting the effectiveness of nicaraven for attenuating the side effects of radiotherapy.

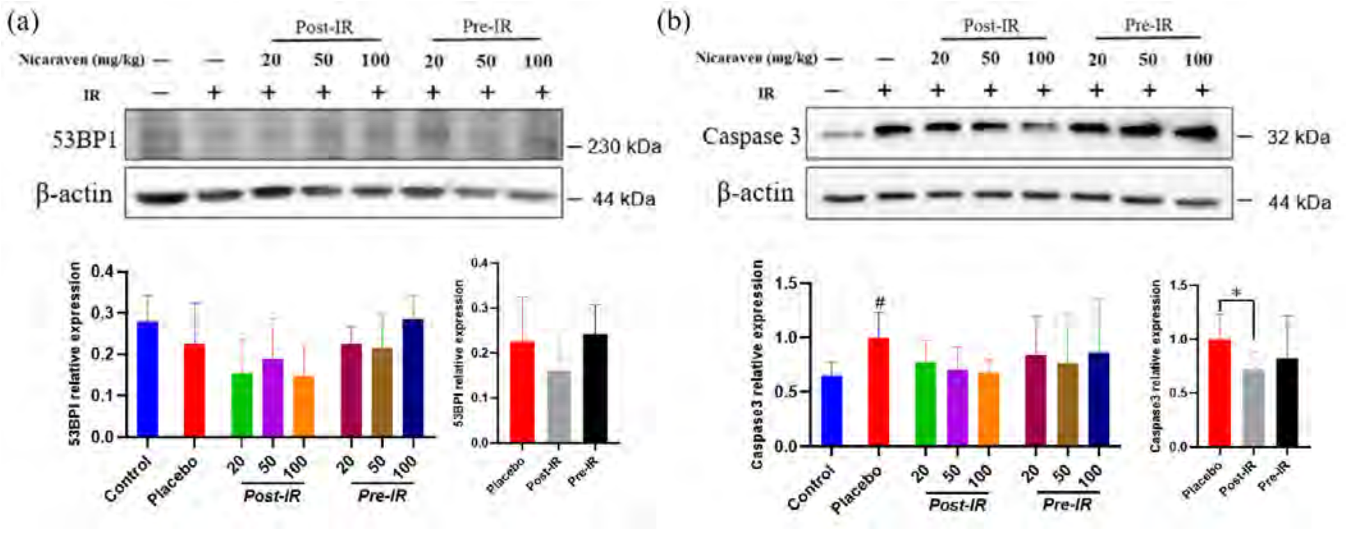

Figure 5. Western blot analysis on the expression of the DNA damage and cell apoptosis in irradiated lungs. Representative blots (up) and quantitative data (down) on the expression of 53BP1 (a), caspase 3 (b). Data are normalized to β-actin. Data are represented as the means ± SD, $n = 3\text{~}6$ in per group. $^{\#}p < 0.05$ *versus* Control group, $^{*}p < 0.05$ *versus* Placebo group.
IR: irradiation; Post-IR: post-irradiation; Pre-IR: pre-irradiation.

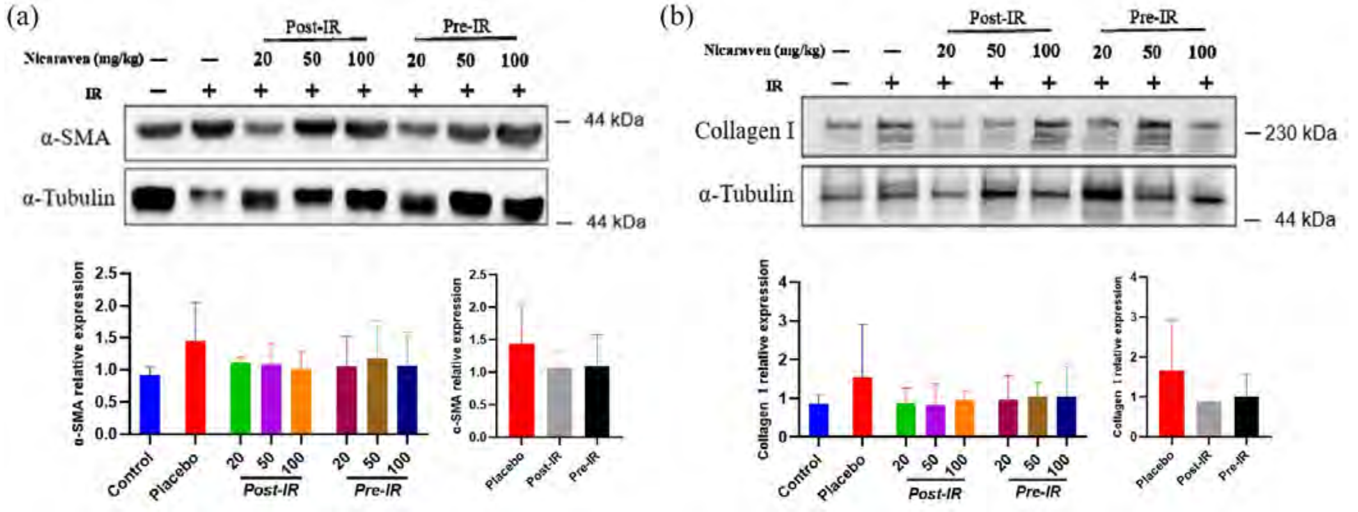

Figure 6. The fibrotic changes in irradiated lungs.
Representative blots (up) and quantitative data (down) on the expression of α-SMA (a), collagen Ⅰ (b) were shown. Data are normalized to α-Tubulin. Data are represented as the means ± SD, $n = 3\text{~}6$ in per group.
IR: irradiation; Post-IR: post-irradiation; Pre-IR: pre-irradiation.

Nicaraven has been well recognized on radical-specific scavenging property.[14] The 8-OHdG, an oxidized nucleoside of DNA has been frequently used as a marker for detecting oxidative stress.[23] However, consistent with our previous study,[24] nicaraven administration did not effectively decrease the level of 8-OHdG in serum in this study.

Radiation exposure results in the release of pro-inflammatory cytokines and chemokines.[8–10] Radiation-induced systemic and local inflammatory responses can be detected in the blood by an increased level of circulatory cytokines and the activation of immune cells.[7,25] However, we found that nicaraven administration did not significantly change the levels of TGF-β, IL-1β, and IL-6 in serum. Several reasons can be considered for it. First, the sample number in each group was too small to detect a statistical significance. Second, the initial sizes of tumors were widely varied among animals and groups, which also resulted in large variations in measuring data. Third, we collected lungs and serum at 14 days after the last irradiation, which will be not a suitable time window for sensitive detection about the changes of 8-OHdG and inflammatory factors in serum. Otherwise, tumor-secreted factors might also be considered to affect the levels of cytokines and chemokines in serum,[26] but we did not find significant correlations between tumor weights and the levels of systemic inflammatory factors (data not shown).

Increasing evidence has shown that the release of a multitude of cytokines in response to radiation exposure can contribute to the damage to the cells/tissues.[22] Previous studies have demonstrated that RILI could be alleviated by blocking pro-inflammatory factors.[27,28] In this study, we observed that nicaraven partially attenuated the enhanced expression of TGF-β and IL-1β in the lungs, especially by post-irradiation administration with relatively low doses. We have not yet found a clear reason why post-irradiation administration with relatively lower doses of nicaraven even more effectively alleviates the enhancement of TGF-β and IL-1β in the irradiated lungs. Previous studies have well documented the harmless of nicaraven at the dose of 100 mg/kg in mice.[29] As VEGF level may increase in tumor-bearing mice, it is a possibility that a high dose of nicaraven increases the permeability of alveolar capillaries and cause edema of lungs in these tumor-bearing mice.

SOD1 and SOD2 are antioxidant enzymes, but their expression generally increases in response to oxidative stresses and various types of injuries.[6] Nicaraven partially attenuated the enhanced expression of SOD1 and SOD2 in irradiated lungs, especially by post-irradiation administration. Radiation can directly lead to cell death and apoptosis.[4,17] Nicaraven also partially decreased the expression of 53BP1 and caspase 3 in irradiated lungs, especially by post-irradiation administration. The main manifestations of the late stage of RILI are fibroblast proliferation and collagen deposition.[25] Post-irradiation administration of nicaraven partially decreased the expression of α-SMA and collagen Ⅰ in irradiated lungs.

This study has several limitations. First, we did not perform histopathological analysis on lungs. Second, we only used male mice for the experiment, but gender difference may affect radiation-induced outcomes.[30,31] Third, we could not provide data on the 8-OHdG level in lungs because of our technical mistake. Otherwise, due to the small sample size and large individual variation, there was no statistically significance on the expression of α-SMA and collagen I in lungs among groups. Although we have already planned a phase I-II clinical trial in esophageal cancer patients who receiving radiotherapy, the benefit of nicaraven administration will be needed to be further confirmed before clinical application for cancer radiotherapy.

According to our experimental evaluations in a preclinical tumor-bearing mouse model, nicaraven seems to effectively attenuate the side effects of radiotherapy. As nicaraven has a very limited effect on the growth of established tumors,[16] nicaraven may be useful for mitigating the side effects of radiotherapy in cancer patients, and post-irradiation administration with a relatively low dose will be highly recommended.

Declarations

Ethics approval and consent to participate

The animal experiments were approved by the Institutional Animal Care and Use Committee of Nagasaki University (Approval no.1608251335-12) and all animal procedures were performed in accordance with institutional and national guidelines.

Consent for publication

The authors give their consent for publication.

Author contributions

Yong Xu: Data curation; Investigation; Methodology; Writing – original draft; Writing – review & editing.

Lina Abdelghany: Data curation; Investigation; Writing – review & editing.

Reiko Sekiya: Data curation; Investigation.

Da Zhai: Data curation; Writing – review & editing.

Keiichi Jingu: Conceptualization.

Tao-Sheng Li: Conceptualization; Data curation; Investigation; Methodology; Resources; Supervision; Writing – review & editing.

Acknowledgements

None.

Funding

The authors disclosed receipt of the following financial support for the research, authorship, and/or publication of this article: This study was mainly supported by the Japan Agency for Medical Research and Development (JP20lm0203081), a Grant-in-Aid from the Ministry of Education, Science, Sports, Culture and Technology, Japan. The funder played no role in the study design, data collection, and analysis, decision to publish, or manuscript preparation.

Competing interests

The authors declared no potential conflicts of interest with respect to the research, authorship, and/or publication of this article.

Availability of data and materials

The datasets used and/or analyzed during the current study are available from the corresponding author on reasonable request.

ORCID iD

Tao-Sheng Li https://orcid.org/0000-0002-7653-8873

References

1. Giuranno L, Ient J, De Ruysscher D, *et al.* Radiation-induced lung injury (RILI). *Front Oncol* 2019; 9: 877.
2. Kim H, Park SH, Han SY, *et al.* LXA4-FPR2 signaling regulates radiation-induced pulmonary fibrosis via crosstalk with TGF-β/Smad signaling. *Cell Death Dis* 2020; 11: 653.
3. Bickelhaupt S, Erbel C, Timke C, *et al.* Effects of CTGF blockade on attenuation and reversal of radiation-induced pulmonary fibrosis. *J Natl Cancer Inst* 2017; 109: 8.
4. McBride WH and Schaue D. Radiation-induced tissue damage and response. *J Pathol* 2020; 250: 647–655.
5. Huang L, Snyder AR and Morgan WF. Radiation-induced genomic instability and its implications for radiation carcinogenesis. *Oncogene* 2003; 22: 5848–5854.
6. Nakane M. Biological effects of the oxygen molecule in critically ill patients. *J Intensive Care* 2020; 8: 95.
7. Formenti SC and Demaria S. Systemic effects of local radiotherapy. *Lancet Oncol* 2009; 10: 718–726.
8. Jin H, Yoo Y, Kim Y, *et al.* Radiation-induced lung fibrosis: preclinical animal models and therapeutic strategies. *Cancers (Basel)* 2020; 12: 1561.
9. Kainthola A, Haritwal T, Tiwari M, *et al.* Immunological aspect of radiation-induced pneumonitis, current treatment strategies, and future prospects. *Front Immunol* 2017; 8: 506.
10. Im J, Lawrence J, Seelig D, *et al.* FoxM1-dependent RAD51 and BRCA2 signaling protects idiopathic pulmonary fibrosis fibroblasts from radiation-induced cell death. *Cell Death Dis* 2018; 9: 584.
11. Weiss JF and Landauer MR. History and development of radiation-protective agents. *Int J Radiat Biol* 2009; 85: 539–573.
12. Hahn SM, Krishna MC, DeLuca AM, *et al.* Evaluation of the hydroxylamine Tempol-H as an in vivo radioprotector. *Free Radic Biol Med* 2000; 28: 953–958.
13. Hosseinimehr SJ. Trends in the development of radioprotective agents. *Drug Discov Today* 2007; 12: 794–805.
14. Akimoto T. Quantitative analysis of the kinetic constant of the reaction of N, N -propylenedinicotinamide with the hydroxyl radical using dimethyl sulfoxide and deduction of its structure in chloroform. *Chem Pharm Bull (Tokyo)* 2000; 48: 467–476.
15. Watanabe M, Akiyama N, Sekine H, *et al.* Inhibition of poly (ADP-ribose) polymerase as a protective effect of nicaraven in ionizing radiation- and ara-C-induced cell death. *Anticancer Res* 2006; 26(5A): 3421–3427.
16. Yan C, Luo L, Urata Y, *et al.* Nicaraven reduces cancer metastasis to irradiated lungs by decreasing CCL8 and macrophage recruitment. *Cancer Lett* 2018; 418: 204–210.
17. Xu Y, Zhai D, Goto S, *et al.* Nicaraven mitigates radiation-induced lung injury by downregulating the NF-κB and TGF-β/Smad pathways to suppress the inflammatory response. *J Radiat Res* 2022; 2022; rrab112.
18. Kepka L and Socha J. Dose and fractionation schedules in radiotherapy for non-small cell lung cancer. *Transl Lung Cancer Res* 2021; 10: 1969–1982.
19. Shah BA, Xiao J, Oh C, *et al.* Five-fraction prone accelerated partial breast irradiation: long-term

oncologic, dosimetric, and cosmetic outcome. *Pract Radiat Oncol* 2022; 12: 106–112.

20. Doi H, Kitajima Y, Luo L, *et al*. Potency of umbilical cord blood- and Wharton's jelly-derived mesenchymal stem cells for scarless wound healing. *Sci Rep* 2016; 6: 18844.
21. Yang L, Yang J, Li G, *et al*. Pathophysiological responses in rat and mouse models of radiation-induced brain injury. *Mol Neurobiol* 2017; 54: 1022–1032.
22. Hanania AN, Mainwaring W, Ghebre YT, *et al*. Radiation-induced lung injury: assessment and management. *Chest* 2019; 156: 150–162.
23. Valavanidis A, Vlachogianni T and Fiotakis C. 8-hydroxy-2 -deoxyguanosine (8-OHdG): a critical biomarker of oxidative stress and carcinogenesis. *J Environ Sci Health C Environ Carcinog Ecotoxicol Rev* 2009; 27: 120–139.
24. Kawakatsu M, Urata Y, Imai R, *et al*. Nicaraven attenuates radiation-induced injury in hematopoietic stem/progenitor cells in mice. *PLoS ONE* 2013; 8: e60023.
25. Mavragani IV, Laskaratou DA, Frey B, *et al*. Key mechanisms involved in ionizing radiation-induced systemic effects. A current review. *Toxicol Res (Camb)* 2015; 5: 12–33.
26. Singh M, Tian XJ, Donnenberg VS, *et al*. Targeting the temporal dynamics of hypoxia-induced tumor-secreted factors halts tumor migration. *Cancer Res* 2019; 79: 2962–2977.
27. Li W, Lu L, Liu B, *et al*. Effects of phycocyanin on pulmonary and gut microbiota in a radiation-induced pulmonary fibrosis model. *Biomed Pharmacother* 2020; 132: 110826.
28. Chen B, Na F, Yang H, *et al*. Ethyl pyruvate alleviates radiation-induced lung injury in mice. *Biomed Pharmacother* 2017; 92: 468–478.
29. Zhang X, Moriwaki T, Kawabata T, *et al*. Nicaraven attenuates postoperative systemic inflammatory responses-induced tumor metastasis. *Ann Surg Oncol* 2020; 27: 1068–1074.
30. Özdemir BC, Csajka C, Dotto GP, *et al*. Sex differences in efficacy and toxicity of systemic treatments: an undervalued issue in the era of precision oncology. *J Clin Oncol* 2018; 36: 2680–2683.
31. Narendran N, Luzhna L and Kovalchuk O. Sex difference of radiation response in occupational and accidental exposure. *Front Genet* 2019; 10: 260.

Journal of Radiation Research, Vol. 63, No. 2, 2022, pp. 158–165
https://doi.org/10.1093/jrr/rrab112
Advance Access Publication: 6 January 2022

Nicaraven mitigates radiation-induced lung injury by downregulating the NF-κB and TGF-β/Smad pathways to suppress the inflammatory response

Yong Xu[1,2], Da Zhai[1,2], Shinji Goto[1,2], Xu Zhang[1,2], Keiichi Jingu[3] and Tao-Sheng Li[1,2,*]

[1]Department of Stem Cell Biology, Atomic Bomb Disease Institute, Nagasaki University, Nagasaki 852-8523, Japan
[2]Department of Stem Cell Biology, Nagasaki University Graduate School of Biomedical Sciences, 1-12-4 Sakamoto, Nagasaki 852-8523, Japan
[3]Department of Radiation Oncology, Graduate School of Medicine, Tohoku University, Sendai 980-8574, Japan.
*Corresponding author: Department of Stem Cell Biology, Atomic Bomb Disease Institute, Nagasaki University, 1-12-4 Sakamoto, Nagasaki 852-8523, Japan. Tel: +81-95-819-7099; Fax: +81-95-819-7100, E-mail: litaoshe@nagasaki-u.ac.jp

(Received 23 June 2021; revised 16 August 2021; editorial decision 29 October 2021)

ABSTRACT

Radiation-induced lung injury (RILI) is commonly observed in patients receiving radiotherapy, and clinical prevention and treatment remain difficult. We investigated the effect and mechanism of nicaraven for mitigating RILI. C57BL/6 N mice (12-week-old) were treated daily with 6 Gy X-ray thoracic radiation for 5 days in sequences (cumulative dose of 30 Gy), and nicaraven (50 mg/kg) or placebo was injected intraperitoneally in 10 min after each radiation exposure. Mice were sacrificed and lung tissues were collected for experimental assessments at the next day (acute phase) or 100 days (chronic phase) after the last radiation exposure. Of the acute phase, immunohistochemical analysis of lung tissues showed that radiation significantly induced DNA damage of the lung cells, increased the number of Sca-1$^+$ stem cells, and induced the recruitment of CD11c$^+$, F4/80$^+$ and CD206$^+$ inflammatory cells. However, all these changes in the irradiated lungs were effectively mitigated by nicaraven administration. Western blot analysis showed that nicaraven administration effectively attenuated the radiation-induced upregulation of NF-κB, TGF-β, and pSmad2 in lungs. Of the chronic phase, nicaraven administration effectively attenuated the radiation-induced enhancement of α-SMA expression and collagen deposition in lungs. In conclusion we find that nicaraven can effectively mitigate RILI by downregulating NF-κB and TGF-β/pSmad2 pathways to suppress the inflammatory response in the irradiated lungs.

Keywords: radiation; DNA damage; lung injury; inflammatory response

INTRODUCTION

Radiotherapy is used for cancer treatment, but exposure to high doses of ionizing radiation also damages the normal tissue cells [1, 2]. Radiation-induced lung injury (RILI), including acute pneumonitis and chronic pulmonary fibrosis, is frequently observed in patients receiving thoracic radiotherapy. It is estimated that RILI occurs in 13–37% of lung cancer patients undergoing curative radiotherapy, which may limit the dose of radiotherapy and affect the quality of life [3]. Currently, the pathogenesis of RILI has not yet been fully understood, and there is no effective drug in the clinic.

It is known that high dose ionizing radiation leads to DNA double-strand breaks [4]. DNA damage contributes to oxidative stress, vascular damage, and inflammation. Pneumonitis develops within hours or days after high dose irradiation exposure, and is accompanied by an increased capillary permeability and the accumulation of inflammatory cells in lungs [5–7]. The recruited inflammatory cells secret profibrotic cytokines to activate the resident fibroblasts, which finally leads to an excessive collagen production and deposition in the interstitial space of lungs [8–10].

NF-κB (nuclear factor kappa B) is an important regulator of inflammatory response. The NF-κB signaling pathway is known to be activated following radiation exposure [11]. TGF-β/Smad signaling pathway also deeply involves in RILI [12, 13]. Thoracic irradiation causes a continuous increase of TGF-β_1 in plasma, which is a predictor of radiation pneumonitis after radiotherapy [14]. The activation of TGF-β induces the conversion of fibroblasts into myofibroblasts, the elevated

---

expression of α-smooth muscle actin (α-SMA), and the synthesis of extracellular matrix proteins such as collagen [15, 16]. Therefore, targeting these pathways can be a potential strategy for mitigating RILI.

Nicaraven, a hydroxyl free radical scavenger [17], has previously been demonstrated to protect against the radiation-induced cell death [18, 19]. We have also recently found that the administration of nicaraven to mice soon after high dose γ-ray exposure attenuates the radiation-induced injury of hematopoietic stem/progenitor cells, which is more likely associated with anti-inflammatory effect rather than radical scavenging [20, 21]. Moreover, nicaraven can reduce the radiation-induced recruitment of macrophages and neutrophils into lungs [22]. Therefore, we speculate that nicaraven may effectively mitigate RILI, at least partly by inhibiting inflammatory response through NF-κB and TGF-β/Smad signaling pathways [23].

By exposing the lungs of adult mice to 30 Gy X-ray, we investigated the effect and mechanism of nicaraven for mitigating RILI. Our results showed that nicaraven administration significantly reduced the DNA damage of lung tissue (stem) cells, inhibited the radiation-induced recruitment of CD11c$^+$, F4/80$^+$ and CD206$^+$ inflammatory cells in lungs at the acute phase, and also mitigated the radiation-induced enhancement of α-SMA and partly decreased the fibrotic area in the irradiated lungs at the chronic phase.

MATERIALS AND METHODS

Animals

Male C57BL/6 N mice (12-week-old; CLEA, Japan) were used for study. Mice were housed in pathogen-free room with a controlled environment under a 12 h light–dark cycle, with free access to food and water. This study was approved by the Institutional Animal Care and Use Committee of Nagasaki University (No.1608251335-12). All animal procedures were performed in accordance with institutional and national guidelines.

Thoracic radiation exposure and nicaraven administration

The RILI model was established as previously described [24]. Briefly, mice were treated daily with 6 Gy X-ray thoracic radiation for 5 days in sequences (cumulative dose of 30 Gy) at a dose rate of 1.0084 Gy/min (200 kV, 15 mA, 5 mm Al filtration, ISOVOLT TITAN320, General Electric Company, United States) (Supplementary Fig. 1A). Nicaraven (50 mg/kg; n = 6, IR + N group) or placebo (n = 6, IR group) was injected intraperitoneally to mice within 10 min after each radiation exposure, and we continued the daily injections for 5 additional days after the last radiation exposure (Supplementary Fig. 1A). Age-matched mice without radiation exposure were used as control (n = 6, CON group). The body weights of mice were recorded once a week. We sacrificed the mice the next day (Acute phase) or the 100th day (Chronic phase) after the last exposure (Supplementary Fig. 1A). At the end of follow-up, mice were euthanized under general anesthesia by severing the aorta to remove the blood. Lung tissues were excised and weighed, and then collected for experimental evaluations as follows.

Immunohistochemical analysis

The DNA damage in lung tissue (stem) cells was detected by immunohistochemical analysis. Briefly, lungs were fixed in 4% paraformaldehyde, and paraffin sections of 6-μm-thick were deparaffinized and rehydrated. After antigen retrieval and blocking, sections were incubated with rabbit anti-mouse γ-H2AX antibody (1:400 dilution, Abcam) and rat anti-mouse Sca-1 antibody (1:200 dilution, Abcam) overnight at 4°C, and followed by the appropriate fluorescent-conjugated secondary antibodies at 25°C for 60 min. The nuclei were stained with 4, 6-diamidino-2-phenylindole (DAPI) (1:1000 diution, Life technologies). The positive staining was examined under fluorescence microscope (FV10CW3, OLYMPUS).

The recruitment of inflammatory cells was detected by immunostaining with mouse anti-mouse CD11c antibody (1:150 dilution, Abcam), rat anti-mouse F4/80 antibody (1:100 dilution, Abcam), goat anti-mouse CD206 antibody (1:200 dilution, R&D Systems) overnight at 4°C, and followed by the appropriate Alexa fluorescent-conjugated secondary antibodies (1:400 dilution, Invitrogen), respectively. The nuclei were stained with DAPI. The positive staining was examined under fluorescence microscope (FV10CW3, OLYMPUS).

For quantitative analysis, we counted the positively stained cells in 12 images from two separated independent sections of each lung tissue sample. The number of positively stained cells in each lung tissue sample was normalized by the number of nuclei, and the average value per field (image) from each lung tissue sample was used for statistical analysis.

Masson's trichrome staining

To detect the fibrotic change in lungs, Masson's trichrome staining was performed according to the manufacturer's protocol (Sigma-Aldrich, St. Louis, MO, USA). The stained sections were mounted and then imaged using a microscope (Biorevo BZ-9000; Keyence Japan, Osaka, Japan). The fibrotic area was quantified by measuring the positively stained area using the Image-Pro Plus software (version 5.1.2, Media Cybernetics Inc, Carlsbad, CA, USA), and expressed as a percentage of the total area. The average value from 12 images randomly selected from two separated slides for each lung tissue sample was used for statistical analysis.

Western blot

Western blot was performed as previously described [25]. Briefly, lung tissue sample was homogenized using Multi-beads shocker® and added to the T-PER reagent (Thermo Fisher Scientific) consisting of proteinase and dephosphorylation inhibitors (Thermo Fisher Scientific). Total tissue protein purified from lungs were separated by SDS-PAGE gels and then transferred to 0.22-μm PVDF membranes (Bio-Rad). After blocking, the membranes were incubated with primary antibodies against NF-kB p65 (1:500 dilution, Abcam), IκBα (1:1000 dilution, CST), TGF-β (1:1000 dilution, Abcam), pSmad2 (1:1000 dilution, Abcam), α-Tubulin (1:1000 dilution, CST), or GAPDH (1:1000 dilution, Abcam), respectively; and followed by the appropriate horseradish peroxidase-conjugated secondary antibodies (Dako). The expression was visualized using an enhanced chemiluminescence detection kit (Thermo Scientific).

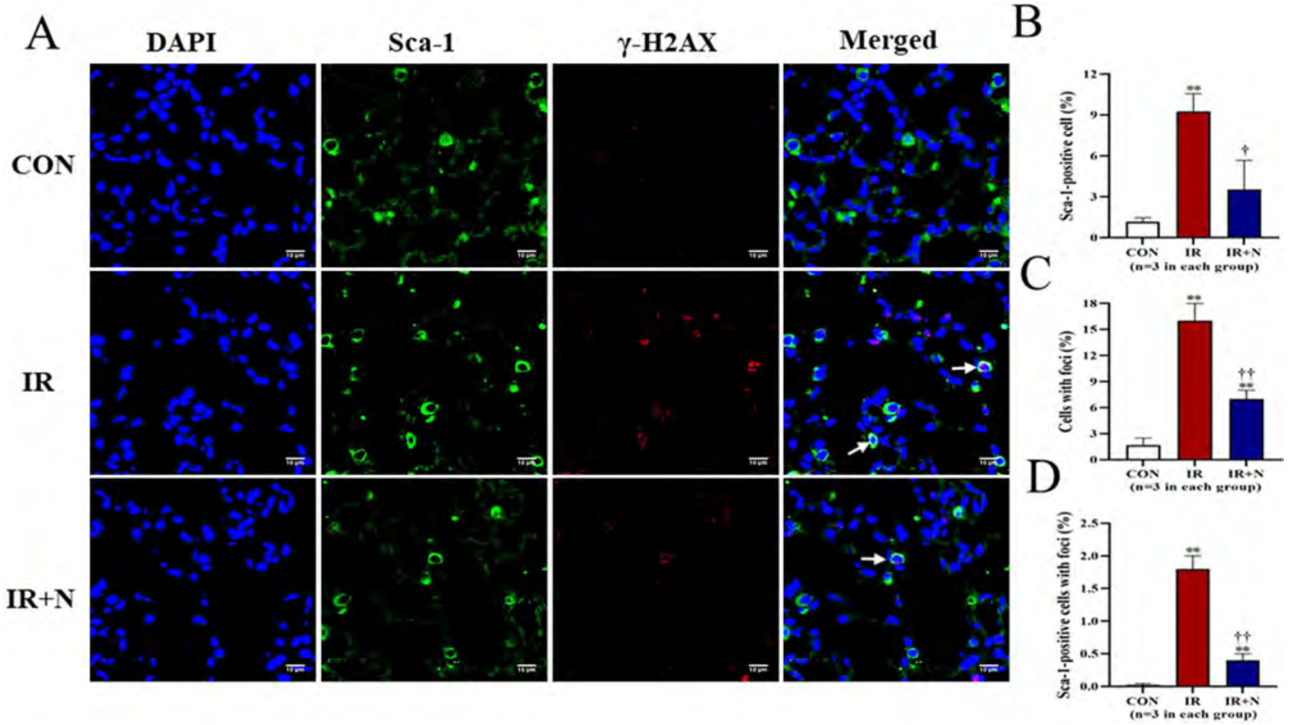

Fig. 1. The DNA damage of lung tissue cells at the acute phase after treatments. (A) Representative confocal images show the expression of Sca-1 and γ-H2AX in lung tissue cells. Quantitative data on the number of Sca-1^+ stem cells (B), the total cells with γ-H2AX foci formation (C), and the Sca-1^+ stem cells with γ-H2AX foci formation (D, Arrows) are shown. Scale bars: 10 μm. The nuclei were stained with DAPI. Data are represented as means ± SD. $**p < 0.01$ vs CON group, $\dagger p < 0.05$, $\dagger\dagger p < 0.01$ vs IR group. CON: Control, IR: Radiation, IR + N: Radiation+Nicaraven.

Semiquantitative analysis was done using ImageQuant LAS 4000 mini (GE Healthcare Life Sciences).

Statistical analysis

All the values were presented as mean ± SD. For comparison of multiple sets of data, one-way analysis of variance (ANOVA) followed by Tukey's test (Dr. SPSS II, Chicago, IL) was used. For comparison of two sets of data, an unpaired two-tailed *t*-test was used. All analysis was carried out with the SPSS19.0 statistical software (IBM SPSS Co., USA). A p-value less than 0.05 was accepted as significant.

RESULTS

Nicaraven significantly reduced the radiation-induced DNA damage of lung tissue (stem) cells at the acute phase.

All mice survived after treatments and during the follow-up period. The body weights of the mice were decreased temporarily soon after radiation exposure, but tended to increase approximately 10 days after radiation exposure. Although the body weights of mice between IR group and IR + N group were not significantly different, they were significantly lower than the age-matched non-irradiated mice in the CON group ($p < 0.05$, Supplementary Fig. 1B). Moreover, the lung weights of mice were not significantly different among all groups at either the acute phase or the chronic phase (Supplementary Fig. 1C).

Immunohistochemistry was performed to evaluate the expression of Sca-1 and γ-H2AX in lung tissue cells at the acute phase (Fig. 1A). Compared to CON group, the number of Sca-1^+ stem cells was significantly increased in the IR group (9.27 ± 1.30% vs 1.17 ± 0.29%, $p < 0.01$; Fig. 1B). However, the increased number of Sca-1^+ stem cells in irradiated lungs was significantly attenuated by nicaraven administration (3.53 ± 2.15%, $p < 0.05$ vs IR group; Fig. 1B).

The formation of γ-H2AX foci in nuclei of lung tissue cells was dramatically increased in the IR group, but was mildly changed in the IR + N group (Fig. 1A). Quantitative data also indicated that the percentage of γ-H2AX-positive cells was significantly less in the IR + N group than the IR group (16.27 ± 2.05% vs 7.13 ± 0.91%, $p < 0.01$; Fig. 1C). Moreover, we tried to evaluate the formation of γ-H2AX foci in Sca-1^+ stem cells. Interestingly, the number of Sca-1^+ stem cells with γ-H2AX foci was more effectively decreased in the IR + N group compared to the IR group (1.93 ± 0.51% vs 0.35 ± 0.19%, $p < 0.01$; Fig. 1D). These results indicate that nicaraven administration can reduce the radiation-induced DNA damage in lung tissue cells, especially in these Sca-1^+ stem cells.

Nicaraven effectively decreased the radiation-induced recruitment of inflammatory cells into lungs.

According to our previous studies [20, 21], nicaraven protects tissue (stem) cells against radiation injury by inhibiting

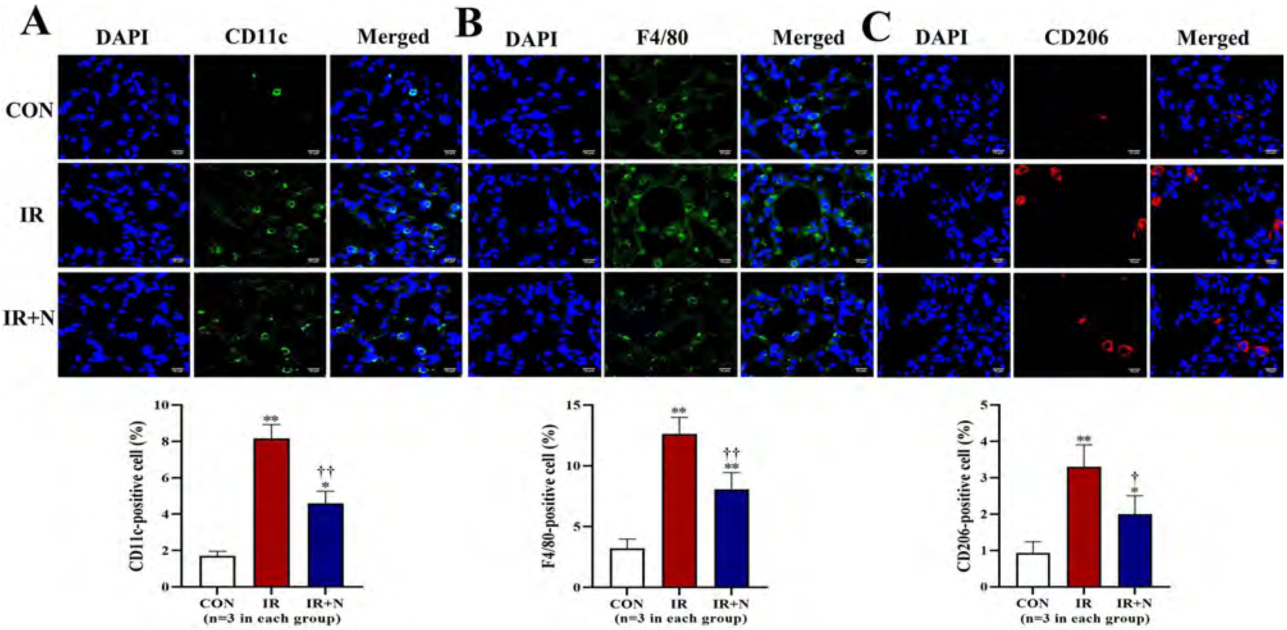

Fig. 2. Immunohistochemical detection of inflammatory cells in lungs at the acute phase after treatments. Representative confocal images (upper) and quantitative data (lower) show the CD11c$^+$ cells (A), F4/80$^+$ cells (B), and CD206$^+$ cells (C) in lungs. Scale bars: 10 μm. The nuclei were stained with DAPI. Data are represented as means ± SD. $*p < 0.05$, $**p < 0.01$ vs CON group, $\dagger p < 0.05$, $\dagger\dagger p < 0.01$ vs IR group. CON: Control, IR: Radiation, IR + N: Radiation+Nicaraven.

inflammatory response. Therefore, immunohistochemical analysis was performed to detect the inflammatory cells in lungs. The number of CD11c + monocytes and F4/80+ macrophages was significantly higher in the IR group than the CON group ($p < 0.01$, Fig. 2A and B). However, nicaraven administration significantly reduced the recruitment of CD11c + monocytes (8.23 ± 0.75% vs 4.61 ± 0.65%, $p < 0.01$; Fig. 2A) and F4/80+ macrophages (12.63 ± 1.36% vs 8.07 ± 1.38%, $p < 0.01$; Fig. 2B) into irradiated lungs. Similarly, the number of M2 macrophages (CD206+) was also significantly higher in irradiated lungs than that of non-irradiated lungs ($p < 0.01$, Fig. 2C). Interestingly, nicaraven administration significantly decreased the CD206$^+$ macrophages in irradiated lungs (3.3 ± 0.61% vs 2.1 ± 0.53%, $p < 0.05$; Fig. 2C).

Nicaraven significantly attenuated the radiation-induced upregulation of NF-κB and TGF-β in lungs

To further understand the molecular mechanism of nicaraven on mitigating RILI, we investigated the expression of NF-κB and IκBα (inhibitor of NF-κB) in lungs at the acute phase. Compared to the CON group, the IR group showed a significant enhancement on the expression of NF-κB ($p < 0.05$, Fig. 3A). However, the enhanced expression of NF-κB in irradiated lungs was effectively attenuated by nicaraven administration ($p = 0.09$, Fig. 3A). In contrast, the expression of total IκBα was significantly decreased in irradiated lungs ($p < 0.01$ vs CON group, Fig. 3B), which was effectively attenuated by nicaraven administration ($p < 0.01$ vs IR group, Fig. 3B). We also investigated the expression of TGF-β and pSmad2 in irradiated lungs at the acute phase (Fig. 3C and D). The irradiated lungs showed a significant upregulation of TGF-β and pSmad2 ($p < 0.05$ vs CON group, Fig. 3C and D), but was effectively attenuated by nicaraven administration ($p < 0.05$ vs IR group, Fig. 3C and D).

Nicaraven clearly attenuated the radiation-induced enhancement of α-SMA and partially reduced the fibrotic area in irradiated lungs at the chronic phase

We further investigated the expression of α-SMA and collagen deposition in irradiated lungs at the chronic phase. Western blot indicated an enhanced expression of α-SMA in the irradiated lungs ($p < 0.05$ vs CON group, Fig. 4A), but the enhanced expression of α-SMA in irradiated lungs was completely attenuated by nicaraven administration (Fig. 4A). Similarly, Masson's trichrome staining showed that the fibrotic area in lungs was significantly higher in the IR group than the CON group ($p < 0.05$, Fig. 4B). However, nicaraven administration tended to only partially reduce the fibrotic area in irradiated lungs (6.24 ± 0.64% vs 5.14 ± 0.51%, $p = 0.08$; Fig. 4B).

DISCUSSION

This study was proposed to investigate the potential effect and underlying mechanism of nicaraven on mitigating RILI. Our experimental data revealed that nicaraven administration not only reduced the DNA damage (γ-H2AX foci formation) of lung tissue (stem) cells, but also inhibited the recruitment of macrophages and neutrophils into irradiated lungs at the acute phase. Nicaraven administration also significantly attenuated the radiation-induced enhancement of TGF-β and NF-κB, and partially reduced the fibrotic area in irradiated lungs at the chronic phase.

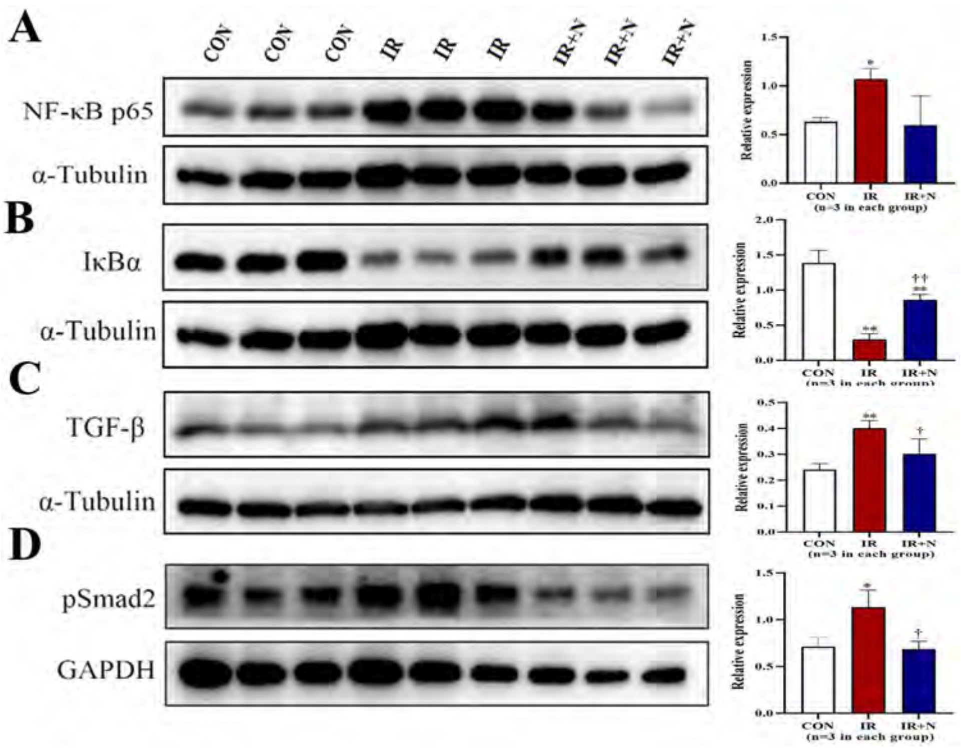

Fig. 3. Western blot analysis on the expression of NF-κB, IκBα, TGF-β, and pSmad2 in lungs. Representative blots (left) and quantitative data (right) on the expression of NF-κB p65 (A), IκBα (B), TGF-β (C), pSmad2 (D) in lungs are shown. Data are normalized to α-Tubulin or GAPDH, and represented as means ± SD. $*p < 0.05$, $**p < 0.01$ vs CON group, $\dagger p < 0.05$, $\dagger\dagger p < 0.01$ vs IR group. CON: Control, IR: Radiation, IR + N: Radiation+Nicaraven.

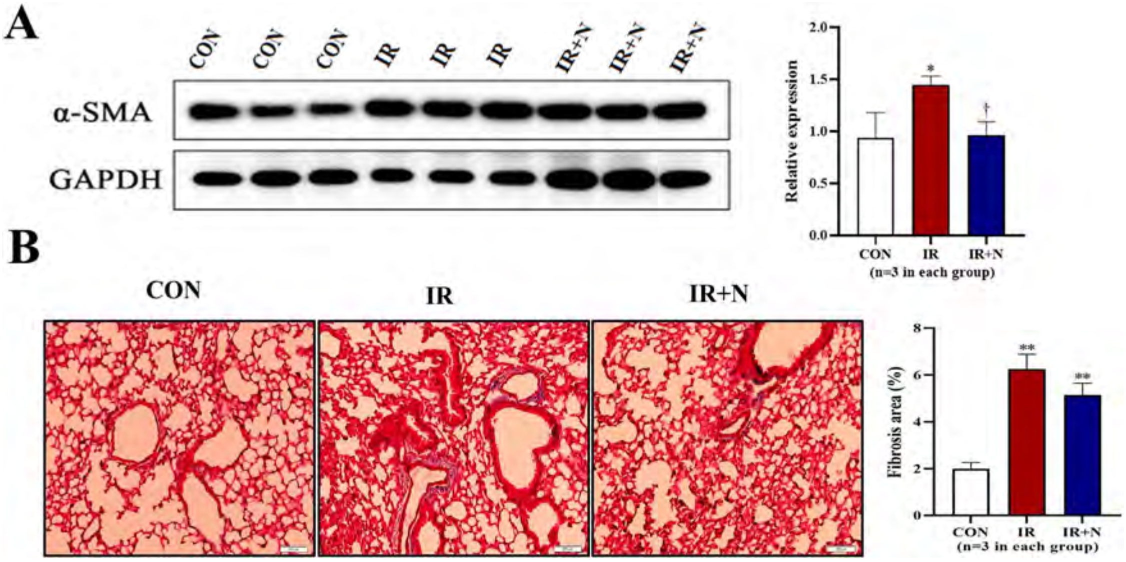

Fig. 4. The fibrotic changes in lungs at the chronic phase after treatments. (A) Representative blots (left) and quantitative data (right) on the expression of α-SMA in lungs are shown. (B) Representative images (left) and quantitative data (right) of Masson's trichrome staining on the fibrotic area in lungs are shown. Scale bars: 200 μm. Data are represented as means ± SD. $*p < 0.05$, $**p < 0.01$ vs CON group, $\dagger p < 0.05$ vs IR group. CON: Control, IR: Radiation, IR + N: Radiation+Nicaraven.

Nicaraven is known as a powerful radical scavenger that effectively protects various tissues and organs against injuries, particularly for ischemia–reperfusion injury in the brain [26–28]. Considering the well-recognized antioxidative property and the potential anti-inflammatory effect of nicaraven, we evaluated the probable role of nicaraven on mitigating RILI.

The exposure to high levels of ionizing radiation leads to DNA double-strand breaks, which elicit cell death or stochastic change [4]. Stem cells are known to play critical role in tissue homeostasis, while ionizing radiation exposure can disrupt the tissue homeostasis. Alveolar epithelium is composed of two cell types: Type I cells account for 95% of the gas exchange surface area, and type II cells can transform into type I cells and have the ability to repair alveoli. Sca-1-positive cells are identified as a population of alveolar type II cells with progenitor cell properties [29]. It has also been demonstrated that the proliferation of Sca-1-positive cells increases during the alveolar epithelial repair phase [29, 30]. In this study, the number of Sca-1-positive cells were exactly increased in irradiated lungs at the acute phase, suggesting the probable role of Sca-1-positive cells for repairing the injured lungs after high dose irradiation. Nicaraven administration showed to reduce the DNA damage of lung tissue cells, especially in these Sca-1-positive cells at the acute phase, which indirectly indicates the protective effect of nicaraven on RILI.

Various chemokines/cytokines are known to be increased in organs/tissues exposed to high dose irradiation, which in turn induces the recruitment of inflammatory cells at the acute phase. The recruited inflammatory cells play a key role in the pathogenesis of RILI [31, 32], because inflammatory cascade is known to promote fibroblast proliferation and collagen deposition [33]. In responding to high dose radiation exposure, the recruitment of monocytes/immune cells ($CD11c^+$) into lung tissue plays critical pathophysiological role on RILI. Among the recruited monocytes/immune cells, macrophages ($F4/80^+$) represent an important profibrogenic initiator/mediator, but M2 macrophages ($CD206^+$) are thought to be an anti-inflammatory phenotype of macrophages. In this study, we found that the recruitment of monocytes/immune cells, including the M2 macrophages was significantly increased in the irradiated lungs. Consistent with previous reports [22, 34], the administration of nicaraven inhibited significantly the recruitment of monocytes into the irradiated lungs. It will be better to understand the precise role of especial subpopulation of inflammatory cells, such as the M2 macrophages in lungs using genetically modified animals. However, the purpose of this study was designed to examine the potency of nicaraven for attenuating RILI through an anti-inflammatory mechanism, we used a wild-type mice rather than the genetically modified mice for experiments.

TGF-β is one of the most critical master regulators on promoting acute inflammation and chronic fibrosis in lungs [12–16]. Previous studies have demonstrated that radiation exposure activates TGF-β/Smad signaling pathway to initiate the inflammatory response, induce the proliferation and activation of fibroblasts, and enhance the synthesis of matrix proteins [35, 36]. Therefore, the inhibition of TGF-β/Smad signaling pathway may effectively mitigate RILI. In this study, nicaraven administration exactly downregulated the expression of TGF-β and pSmad2 in irradiated lungs at the acute phase.

NF-κB has emerged as a ubiquitous factor involved in the regulation of numerous critical processes, including immune [37], inflammation response [38], cell apoptosis [39], and cell proliferation [40]. While in an inactivated state, NF-κB is located in the cytosol complexed with the inhibitory protein IκBα. Radiation exposure can activate NF-κB signaling pathway. Radiation exposure activates the kinase IKK, which in turn phosphorylates IκBα and results in ubiquitin-dependent degradation [11, 38, 40]. Dysregulation of NF-κB signaling can lead to inflammation, autoimmune disease and cancer [41]. In this study, nicaraven administration effectively downregulated the expression of NF-κB, suggesting the involvement of NF-κB pathway in the protective effect of nicaraven to RILI.

Generally, although nicaraven administration only tended to partially reduce the fibrotic area in the irradiated lungs, many other parameters, such as the expression of α-SMA was more sensitively and clearly changed. As the activated fibroblasts (α-SMA$^+$) are generally thought to be the predominant source of collagen-producing cells, the inhibition on α-SMA expression in irradiated lungs by nicaraven administration suggested the probable benefit of nicaraven for attenuating the development of fibrotic change in irradiated lungs at the chronic phase. In summary, nicaraven administration effectively protected the RILI, likely by suppressing inflammatory response through the NF-κB and TGF-β/Smad signaling pathways. Nicaraven could be a potential drug for mitigating RILI.

SUPPLEMENTARY DATA

Supplementary data is available at *RADRES Journal* online.

ACKNOWLEDGEMENTS

This study was supported by the Agency for Medical Research and Development under Grant Number JP20lm0203081. The funder played no role in study design, data collection and analysis, decision to publish, or manuscript preparation.

CONFLICT OF INTEREST

The authors indicate no potential conflicts of interest.

REFERENCES

1. Bentzen SM. Preventing or reducing late side effects of radiation therapy: radiobiology meets molecular pathology. *Nat Rev Cancer* 2006;6:702–13.
2. McBride WH, Schaue D. Radiation-induced tissue damage and response. *J Pathol* 2020;250:647–55.
3. Rodrigues G, Lock M, D'Souza D et al. Prediction of radiation pneumonitis by dose volume histogram parameters in lung cancer–a systematic review. *Radiother Oncol* 2004;71:127–38.
4. Huang L, Snyder AR, Morgan WF. Radiation-induced genomic instability and its implications for radiation carcinogenesis. *Oncogene* 2003;22:5848–54.
5. Hanania AN, Mainwaring W, Ghebre YT et al. Radiation-induced lung injury: assessment and management. *Chest* 2019;156:150–62.

6. Giuranno L, Ient J, De Ruysscher D et al. Radiation-induced lung injury (RILI). *Front Oncol* 2019;9:877.
7. Kim H, Park SH, Han SY et al. LXA4-FPR2 signaling regulates radiation-induced pulmonary fibrosis via crosstalk with TGF-β/Smad signaling. *Cell Death Dis* 2020;11:653.
8. Jin H, Yoo Y, Kim Y et al. Radiation-induced lung fibrosis: preclinical animal models and therapeutic strategies. *Cancers (Basel)* 2020;12:1561.
9. Kainthola A, Haritwal T, Tiwari M et al. Immunological aspect of radiation-induced pneumonitis, current treatment strategies, and future prospects. *Front Immunol* 2017;8:506.
10. Im J, Lawrence J, Seelig D et al. FoxM1-dependent RAD51 and BRCA2 signaling protects idiopathic pulmonary fibrosis fibroblasts from radiation-induced cell death. *Cell Death Dis* 2018;9:584.
11. Devary Y, Rosette C, DiDonato JA et al. NF-kappa B activation by ultraviolet light not dependent on a nuclear signal. *Science* 1993;261:1442–5.
12. Madani I, De Ruyck K, Goeminne H et al. Predicting risk of radiation-induced lung injury. *J Thorac Oncol* 2007;2:864–74.
13. Fleckenstein K, Gauter-Fleckenstein B, Jackson IL et al. Using biological markers to predict risk of radiation injury. *Semin Radiat Oncol* 2007;17:89–98.
14. Anscher MS, Kong FM, Andrews K et al. Plasma transforming growth factor beta1 as a predictor of radiation pneumonitis. *Int J Radiat Oncol Biol Phys* 1998;41:1029–35.
15. Singh V, Torricelli AA, Nayeb-Hashemi N et al. Mouse strain variation in SMA(+) myofibroblast development after corneal injury. *Exp Eye Res* 2013;115:27–30.
16. Tatler AL, Jenkins G. TGF-β activation and lung fibrosis. *Proc Am Thorac Soc* 2012;9:130–6.
17. Akimoto T. Quantitative analysis of the kinetic constant of the reaction of N,N'-propylenedini-cotinamide with the hydroxyl radical using dimethyl sulfoxide and deduction of its structure in chloroform. *Chem Pharm Bull(Tokyo)* 2000;48:467–76.
18. Mori Y, Takashima H, Seo H et al. Experimental studies on Nicaraven as radioprotector–free radical scavenging effect and the inhibition of the cellular injury. *Nihon Igaku Hoshasen Gakkai Zasshi* 1993;53:704–12.
19. Watanabe M, Akiyama N, Sekine H et al. Inhibition of poly (ADP-ribose) polymerase as a protective effect of nicaraven in ionizing radiation- and ara-C-induced cell death. *Anticancer Res* 2006;26:3421–7.
20. Zingarelli B, Scott GS, Hake P et al. Effects of nicaraven on nitric oxide-related pathways and in shock and inflammation. *Shock* 2000;13:126–34.
21. Masana Y, Yoshimine T, Fujita T et al. Reaction of microglial cells and macrophages after cortical incision in rats: effect of a synthesized free radical scavenger, (+/−)-N,N'-propylenedinicotinamide (AVS). *Neurosci Res* 1995;23: 217–21.
22. Yan C, Luo L, Urata Y et al. Nicaraven reduces cancer metastasis to irradiated lungs by decreasing CCL8 and macrophage recruitment. *Cancer Lett* 2018;418:204–10.
23. Lin H, Wu X, Yang Y et al. Nicaraven inhibits TNFα-induced endothelial activation and infla-mmation through suppressing NF-κB signaling pathway. *Can J Physiol Pharmacol* 2021;99:803–11.
24. Citrin DE, Shankavaram U, Horton JA et al. Role of type II pneumocyte senescence in radiation-induced lung fibrosis. *J Natl Cancer Inst* 2013;105:1474–84.
25. Doi H, Kitajima Y, Luo L et al. Potency of umbilical cord blood- and Wharton's jelly-derived mesenchymal stem cells for scarless wound healing. *Sci Rep* 2016;6:18844.
26. Asano T, Johshita H, Koide T et al. Amelioration of ischaemic cerebral oedema by a free radical scavenger, AVS: 1,2-bis(nicotinamido)-propane. An experimental study using a regional ischaemia model in cats. *Neurol Res* 1984;6:163–8.
27. Asano T, Takakura K, Sano K et al. Effects of a hydroxyl radical scavenger on delayed ischemic neurological deficits following aneurysmal subarachnoid hemorrhage: results of a multicenter, placebo-controlled double-blind trial. *J Neurosurg* 1996;84:792–803.
28. Imperatore C, Germanò A, d'Avella D et al. Effects of the radical scavenger AVS on behavioral and BBB changes after experimental subarachnoid hemorrhage. *Life Sci* 2000;66:779–90.
29. Liu Y, Kumar VS, Zhang W et al. Activation of type II cells into regenerative stem cell antigen-1(+) cells during alveolar repair. *Am J Respir Cell Mol Biol* 2015;53:113–24.
30. Liu Y, Sadikot RT, Adami GR et al. FoxM1 mediates the progenitor function of type II epithelial cells in repairing alveolar injury induced by Pseudomonas aeruginosa. *J Exp Med* 2011;208:1473–84.
31. Johnston CJ, Williams JP, Elder A et al. Inflammatory cell recruitment following thoracic irradiation. *Exp Lung Res* 2004;30:369–82.
32. Meziani L, Deutsch E, Mondini M. Macrophages in radiation injury: a new therapeutic target. *Onco Targets Ther* 2018;7:e1494488.
33. Boothe DL, Coplowitz S, Greenwood E et al. Transforming growth factor β-1 (TGF-β1) is a serum biomarker of radiation induced fibrosis in patients treated with intracavitary accelerated partial breast irradiation: preliminary results of a prospective study. *Int J Radiat Oncol Biol Phys* 2013;87:1030–6.
34. Zhang X, Moriwaki T, Kawabata T et al. Nicaraven attenuates postoperative systemic Inflam-matory responses-induced tumor metastasis. *Ann Surg Oncol* 2020;27:1068–74.
35. Meng XM, Nikolic-Paterson DJ, Lan HY. TGF-β: the master regulator of fibrosis. *Nat Rev Nephrol* 2016;12:325–38.
36. Samarakoon R, Overstreet JM, Higgins PJ. TGF-β signaling in tissue fibrosis: redox controls, target genes and therapeutic opportunities. *Cell Signal* 2013;25:264–8.
37. Baeuerle PA, Henkel T. Function and activation of NF-kappa B in the immune system. *Annu Rev Immunol* 1994;12:141–79.
38. Barnes PJ, Karin M. Nuclear factor-kappaB: a pivotal transcription factor in chronic inflammatory diseases. *N Engl J Med* 1997;336:1066–71.
39. Bours V, Bonizzi G, Bentires-Alj M et al. NF-kappaB activation in response to toxical and therapeutical agents: role in inflammation and cancer treatment. *Toxicology* 2000;153: 27–38.

40. Karin M, Cao Y, Greten FR et al. NF-kappaB in cancer: from innocent bystander to major culprit. *Nat Rev Cancer* 2002;2: 301–10.

41. Yu H, Lin L, Zhang Z et al. Targeting NF-κB pathway for the therapy of diseases: mechanism and clinical study. *Signal Transduct Target Ther* 2020;5:209.

Nicaraven Exerts a Limited Effect on Radiation-Induced Inhibition of Tumor Growth in a Subcutaneous Murine Tumor Model

Authors: Abdelghany, Lina, Xu, Yong, Sekiya, Reiko, Yan, Chen, Jingu, Keiichi, et al.

Source: Radiation Research, 200(4) : 382-388

Published By: Radiation Research Society

URL: https://doi.org/10.1667/RADE-22-00212.1

RADIATION RESEARCH **200**, 382–388 (2023)
0033-7587/23 $15.00

DOI: 10.1667/RADE-22-00212.1

Nicaraven Exerts a Limited Effect on Radiation-Induced Inhibition of Tumor Growth in a Subcutaneous Murine Tumor Model

Lina Abdelghany,[a,b] Yong Xu,[a,b] Reiko Sekiya,[a,b] Chen Yan,[a,b] Keiichi Jingu,[c] Tao-Sheng Li[a,b,1]

[a] Department of Stem Cell Biology, Atomic Bomb Disease Institute, Nagasaki University, 1-12-4 Sakamoto, Nagasaki 852-8523, Japan; [b] Department of Stem Cell Biology, Nagasaki University Graduate School of Biomedical Sciences, 1-12-4 Sakamoto, Nagasaki 852-8523, Japan; [c] Department of Radiation Oncology, Graduate School of Medicine, Tohoku University, Sendai, Japan

---

Abdelghany L, Xu Y, Sekiya R, Yan C, Jingu K, Li T-S. Nicaraven Exerts a Limited Effect on Radiation-Induced Inhibition of Tumor Growth in a Subcutaneous Murine Tumor Model. Radiat Res. 200, 382–388 (2023).

Nicaraven selectively protects normal tissue from radiation-induced injury. To further develop the clinical application of nicaraven for mitigating the side effects of cancer radiotherapy, we investigated the potential effect of nicaraven administration in radiation-induced inhibition of tumor growth. A subcutaneous tumor model was established in mice by the injection of Lewis lung cancer cells at the back of the chest. X-ray radiation was delivered to the thoracic area and different doses of nicaraven (0, 20, 50, 100 mg/kg) were administrated intraperitoneally pre- or post-irradiation. The tumor size was measured every other day. Mice were euthanized on day 30, and the tumor weight and the levels of cytokines in tumor tissue were measured. Pre- or post-irradiation administration of nicaraven up to a dose of 100 mg/kg did not significantly diminish the radiation-induced inhibition of tumor growth, but post-irradiation administration of 20 and 50 mg/kg nicaraven resulted in relatively lower tumor weight. The levels of IL-1β, IL-6, IL-10, MCP-1, MIP-2a, TGF-β_1, VEGF, p53, p21, cyclin D1 and caspase-3 in tumor tissue did not change by nicaraven administration and were not significantly associated with the tumor weights. According to our experimental data, nicaraven will not significantly diminish the radiation-induced inhibition of tumor growth, even with pre-irradiation administration at a high dose.

INTRODUCTION

For many years, radiotherapy has played a momentous role in cancer treatment with curative intent or as an adjuvant modality with chemotherapy or surgery (*1*). Additionally, radiotherapy is used as a palliative remedy to relieve symptoms in non-malignant and malignant disorders (*2*). However, many patients experience radiation-induced adverse effects due to radiation exposure to the surrounding normal tissue (*3*).

Two main mechanisms cause radiation-induced tissue toxicity: direct DNA damage and the generation of reactive oxygen species (ROS) (*4*). Furthermore, water molecule ionization produces ROS and nitrogen species that make up 60% of the total damage imposed (*5*). ROS also provokes inflammation and immune responses, a serious and common complication after exposure to radiation (*6*). Although some traditional agents have a protective effect on the surrounding normal tissue, they may diminish the radiosensitivity of cancer cells (*7*). Development of a new agent that selectively protects the normal tissue from radiation-induced injury is needed for clinical application in cancer patients who are receiving radiotherapy.

Nicaraven, a small molecule, originally recognized as a free radical scavenger that is well known to protect normal tissue from ischemia-reperfusion injury (*8*). We have recently found the protective effect of nicaraven on normal tissue against radiation injury, which is more likely associated with an anti-inflammatory effect rather than the free radical scavenging effect (*9–11*). We have further confirmed that nicaraven shows a very limited effect on the growth of established tumors in mice (*12*, *13*). Due to the selective radioprotection to normal tissue, nicaraven would be beneficial for cancer patients who are receiving radiotherapy.

Using a tumor-bearing mice model, we administered different doses of nicaraven pre-or post-irradiation. We monitored the tumor growth every other day and measured the levels of inflammatory cytokines/chemokines in tumor tissue. According to our data, nicaraven will not significantly diminish the radiation-induced inhibition of tumor growth.

MATERIALS AND METHODS

Cell Line

The Lewis lung carcinoma cells were grown in DMEM (FUJIFILM Wako) supplemented with 10% fetal bovine serum (Gibco) and 1% streptomycin/penicillin (Gibco), at 37°C in a 5% CO_2 incubator. Cells with almost 80% confluent were harvested for the establishment of a tumor model in mice.

---

[1] Tao-Sheng Li, MD, PhD., Department of Stem Cell Biology, Atomic Bomb Disease Institute, Nagasaki University, 1-12-4 Sakamoto, Nagasaki 852-8523, Japan; email: litaoshe@nagasaki-u.ac.jp.

Mouse Tumor Model

We used 8-week-old male C57BL/6N mice (CLEA Japan Inc., Tokyo, Japan) for the experiment. To establish a tumor model, 5×10^5 cancer cells in 0.1 mL saline solution were injected subcutaneously into the interscapular fat pad of each mouse, at the back of the chest. This study was approved by the Institutional Animal Care and Use Committee of our University (No. 1608251335-12). All experimental procedures were performed by institutional and national guidelines.

Irradiation and Nicaraven Administration Regimens

At 10 days after cancer cell injection, a total of 41 mice were randomly divided into 8 groups, and different treatments were performed as illustrated in Fig. 1A.

For irradiations, general anesthesia was induced in tumor-bearing mice by intraperitoneal injection with an anesthesia cocktail. Thoracic irradiations were delivered to mice by shielding them with a specially designed lead apparatus, which allows a regional delivery of radiation to the tumor nodule in the back of the chest. X-ray radiation was delivered (200 kV, 15 mA, 5 mm aluminum filtration, ISOVOLT TITAN320, General Electric Company), at a dose rate of 1.0084 Gy/min.

Mice were intraperitoneally injected with 20, 50, or 100 mg/kg nicaraven pre-irradiation (about 5 min before exposure) or post-irradiation (within 5 minutes after exposure) ($n = 5$ in each group). For placebo control, mice received radiation treatment but were given saline injection only (placebo group, $n = 5$). In addition, we also included a control group ($n = 6$), in which the mice received neither radiation nor nicaraven administration. The tumor size was monitored by measuring the tumor dimensions using Vernier calipers every other day. Tumor volumes were calculated as: volume (mm^3) = length × width^2/2.

Enzyme-linked Immunosorbent Assay (ELISA)

The tumor tissues were collected after mice euthanasia, and tumor weight was measured. The levels of cytokines/chemokines (IL-1β, IL-6, IL-10, MCP-1, MIP-2a, TGF-β_1, and VEGF) were measured by commercial ELISA kits (R&D Systems) according to the instructions of the manufacturer. The tumor tissues were homogenized in a T-PER reagent containing proteinase and phosphatase inhibitors (Thermo Fisher Scientific) using Multi-beads shocker®. The optical density of each well was measured at 450 nm using a microplate reader (iMark™ Microplate Reader; Bio-Rad Laboratories).

Western Blotting

The tissue lysates were heated at 95°C for 5 min, then loaded on an SDS-PAGE gel and transferred to PVDF membrane (Bio-Rad Laboratories). Membranes were probed with primary antibodies against p53 (1:1,000 dilution; cat. no. 2524s; Cell Signaling Technology), p21 (1:1000 dilution; cat. no. 37543; Cell Signaling Technology), caspase 3 (1:1,000 dilution; cat. no. 14220; Cell Signaling Technology), cyclin D1 (1:1000 dilution; cat. no. 2978; Cell Signaling Technology), and β-actin (1:1,000 dilution; cat. no. HRP-66009; Proteintech), at 4°C overnight or 25°C for 1 h. Followed by horseradish peroxidase-conjugated anti-rabbit secondary antibody (Cell Signaling Technology) for 1 h at 25°C, the expression was visualized using an ECL detection kit (SuperSignal West Femto, ThermoFisher Scientific). The blots were detected using ImageQuant LAS 4000 Mini biomolecular imager (Cytiva) and analyzed by ImageJ 2.1.0 software (National Institutes of Health).

Statistical Analysis

Results are expressed as means ± SD. Statistical differences among groups were determined using a one-way analysis of variance (ANOVA) followed by Dunnett's multiple comparison test. Correlations between cytokine levels and tumor weights were assessed using Pearson's correlation analysis (GraphPad Prism 8.0 software).

RESULTS

Neither Pre-Irradiation nor Post-Irradiation Administration of Nicaraven up to 100 mg/kg Diminishes the Radiation-Induced Inhibition of Tumor Growth

As shown in Fig. 1 on the therapeutic regimens, different treatments were started when a subcutaneous tumor nodule was formed in the back of the chest of mice. As the standard regimen of radiation treatment (*14*), daily 6 Gy thoracic irradiation was delivered to mice for 5 consecutive days. The tumor nodule grew quickly in non-irradiated controls, and we terminated the follow-up on day 15 for mice of the control group due to the large tumor nodules (Fig. 1A). According to the measured tumor size (Fig. 1B), tumor growth was almost stopped after the daily 6 Gy irradiation for 5 days. As the size of the tumor nodule did not decrease after the first round of radiotherapy, we decided to deliver an additional 6 Gy thoracic irradiation on day 9. The tumor size was still slowly increasing during the follow-up. To further confirm that nicaraven administration would not diminish the radiotherapy-induced inhibition of tumor growth, another 6 Gy thoracic irradiation was delivered to mice again on day 16 (Fig. 1A). We finally terminated the follow-up for all groups on day 30.

The radiation-induced inhibition of tumor growth during the follow-up period was almost not affected by nicaraven administration with different doses given either pre- or post-irradiation (Fig. 1B). Compared to the placebo, the mean change of the tumor volume was slightly decreased only by the post-irradiation administration with 20 and 50 mg/kg nicaraven.

At the endpoint of follow-up, we euthanized the mice and extracted the tumor tissues (Fig. 1C). The tumor sizes varied largely even in the same group, and the tumor weight was much higher in the control group without radiation treatment than in other groups that received radiation. Interestingly, the tumor weight was not significantly different among all groups that received thoracic irradiation, whether the mice were given placebo treatment or nicaraven administration with different doses at different timing (Fig. 1D). Moreover, a simple and direct comparison between pre- or post-irradiation groups also showed that the radiation-induced inhibition of tumor growth was not significantly affected by the timing of nicaraven administration (Fig. 1E).

Nicaraven Administration did not Significantly Change the Levels of IL-1β, IL-6, IL-10, MCP-1, MIP-2a, TGF-β_1, VEGF, p53, p21, Caspase-3 and Cyclin D1 in the Tumors

Previous studies have demonstrated the anti-inflammatory effect of nicaraven (*11*, *15*). Therefore, we measured the levels of IL-1β, IL-6, IL-10, MCP-1, MIP-2a, and TGF-β_1 in tumor tissue by ELISA. As shown in Fig. 2, the levels of IL-1β, MCP-1, MIP-2a, and TGF-β_1 in tumors were not significantly different among all groups, although the level of IL-6 was slightly decreased in 20 and 50 mg/kg pre-irradiation compared to placebo (Fig. 2B). Furthermore, IL-10 was

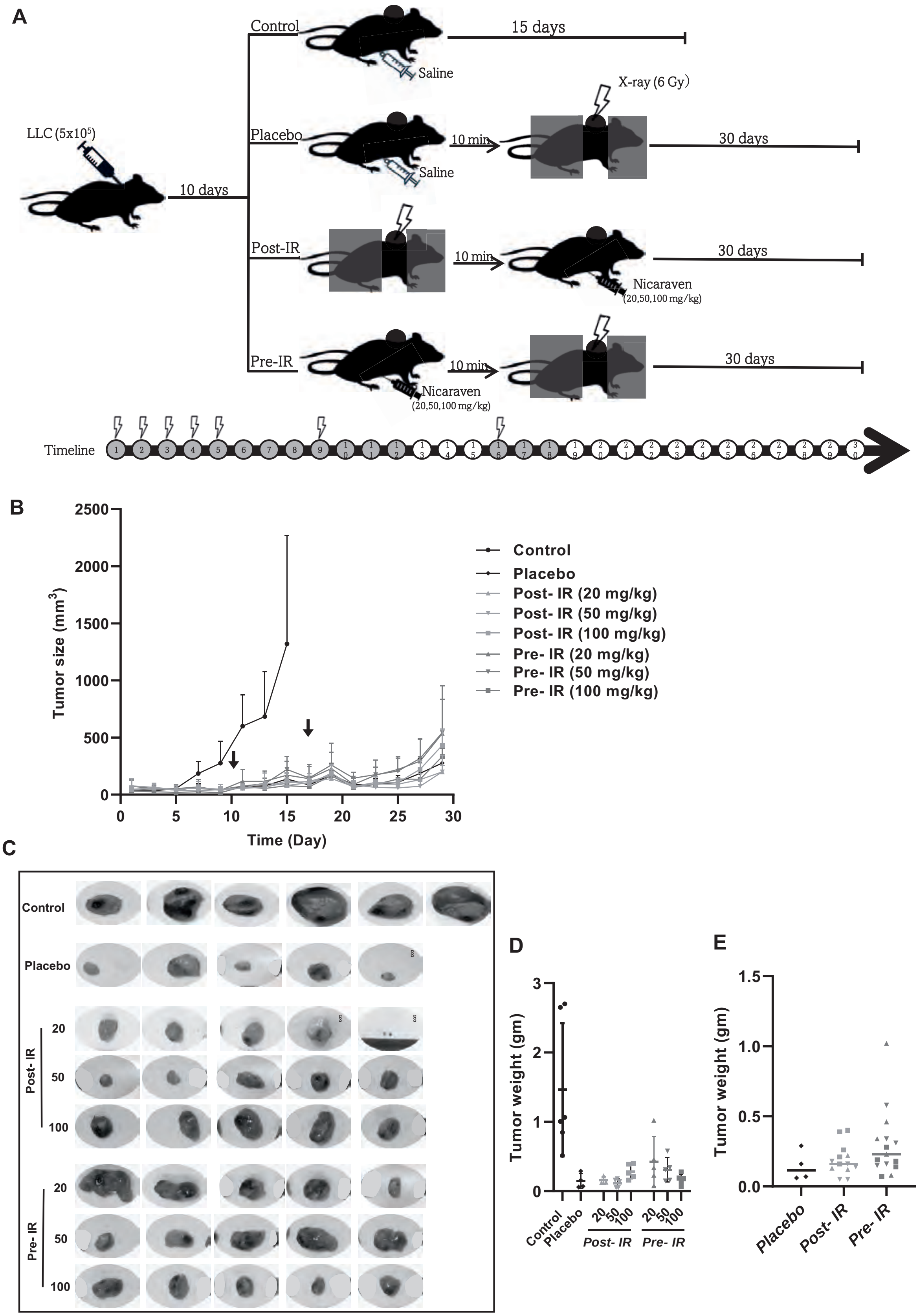

FIG. 1. Changes in tumor size and weight in mice. Panel A: Schematic diagram of the experimental timeline and therapeutic regimens. Panel B: Quantitative data on the changes in tumor size. Panels C–E: The excised tumors and tumor weight at the endpoint are shown. Data are represented as the means ± SD, n = 3–5 per group. IR: irradiation; Post-IR: post-irradiation; Pre-IR: pre-irradiation. §: mouse death during the follow-up.

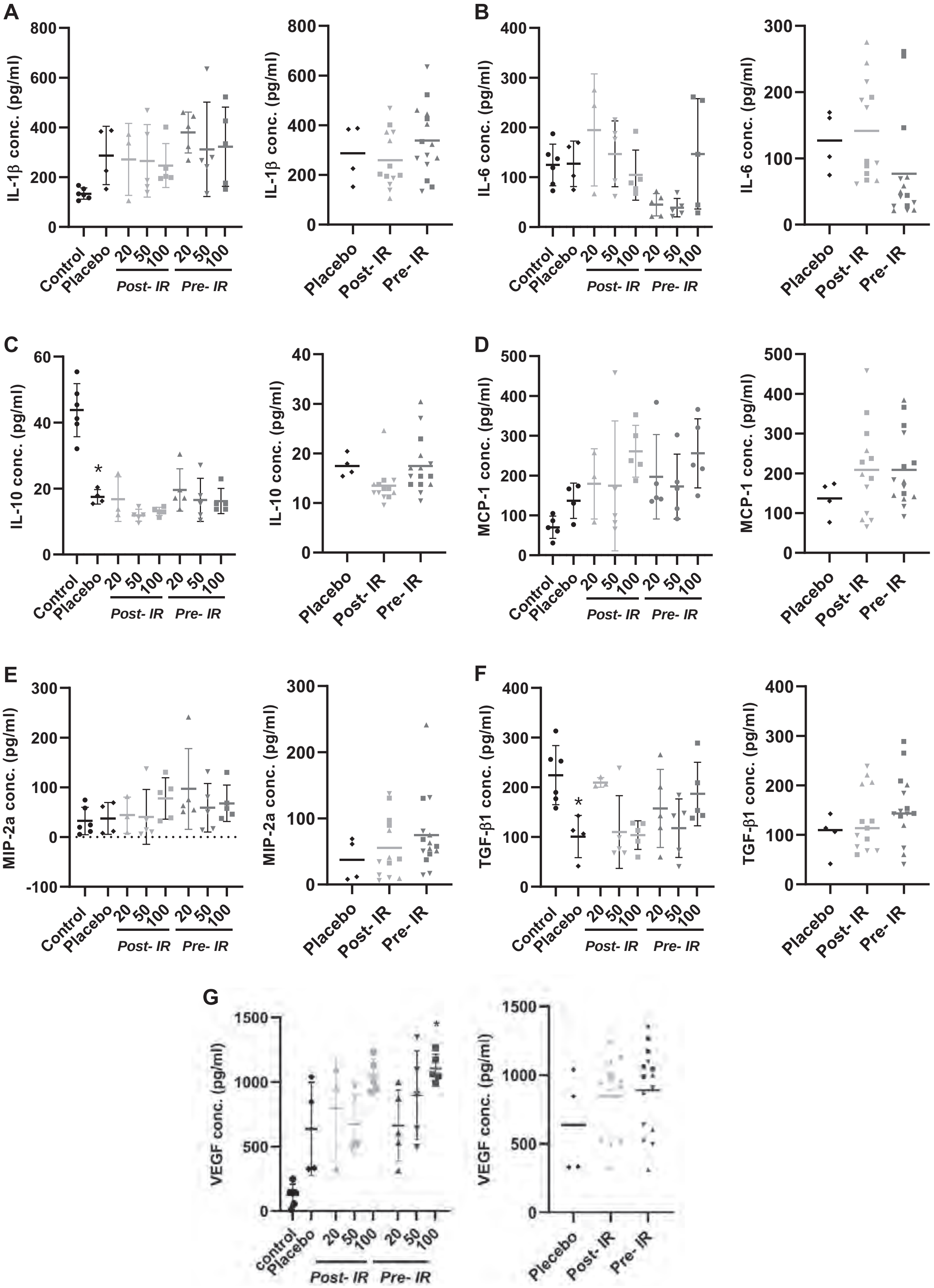

FIG. 2. ELISA analysis on the inflammatory cytokines in the tumors. Quantitative data on the levels of IL-1β (panel A), IL-6 (panel B), IL-10 (panel C), MCP-1 (panel D), MIP-2a (panel E), TGF-β_1 (panel F), and VEGF (panel G) in the excised tumor tissue samples are shown. Data are represented as the means ± SD, n = 3–5 per group. IR: irradiation; Post-IR: post-irradiation; Pre-IR: pre- irradiation.

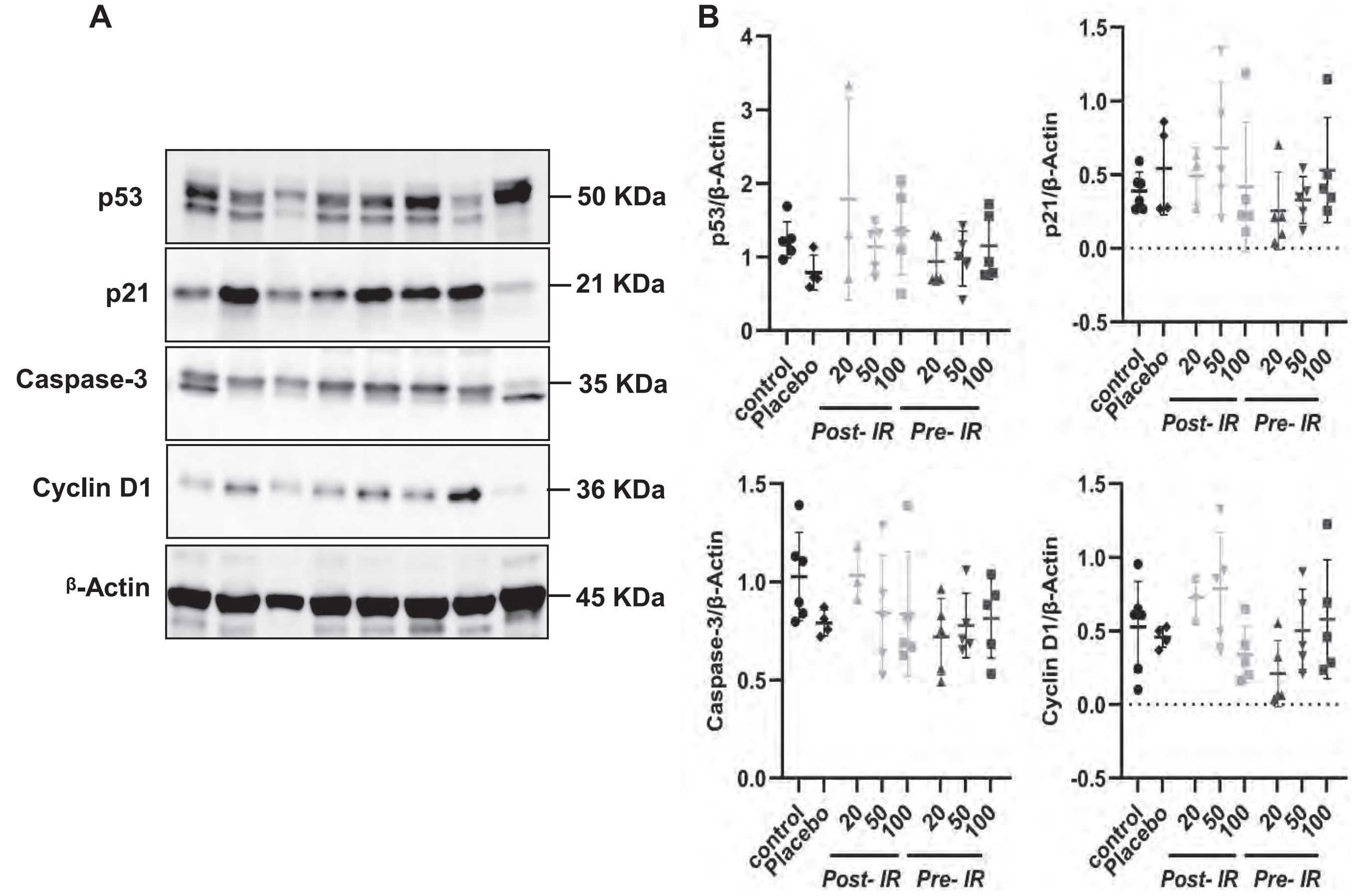

FIG. 3. Western blot for detecting the expression of the apoptotic markers. Representative images (panel A) and semi-quantification data (panel B) show the expression of p53, p21, caspase-3 and cyclin D1 in the tumor extracts.

slightly decreased by post-irradiation nicaraven administration at the doses of 50 and 100 mg/kg (Fig. 2C). Otherwise, the levels of IL-1β, IL-6, IL-10, MCP-1, MIP-2a, and TGF-β_1 in the tumors were not significantly correlated with the tumor weights (Supplementary Table S1;[2] https://doi.org/10.1667/RADE-22-00212.1.S1). We also measured the VEGF level in tumors and did not find significant difference among all groups (Fig. 2G).

To further evaluate the apoptosis, we measured the expression of p53, p21, caspase-3 and cyclin D1 in tumors by Western blot. Nicaraven administration did not significantly change the expression of p53, p21, caspase-3 and cyclin D1 in tumors (Fig. 3).

DISCUSSION

Radiotherapy for many types of malignant tumors has proven satisfactory in inhibiting tumor growth (*16–18*). To obtain better outcomes of radiotherapy, it is still asked to reduce the early and late side effects, as well as to increase tumor response (*19*, *20*). Multiple approaches, such as the use of radio-protectors (pre-radiotherapy) or radio-mitigators (during or immediately post-radiotherapy) have been tested clinically to reduce the side effects of radiotherapy (*21–29*). However, there is still no clear evidence of how the approaches affect the sensitivity of cancer cells to radiation.

The side effect of cancer patients receiving radiotherapy is dependent on several parameters, such as the tumor location (*30*), the dose, and irradiated volume (*31*). Therefore, radiation-induced toxicity to normal tissue should be evaluated in tumor-bearing models using clinically relevant combination-treatment schedules and surrogate endpoints (*32*). However, most studies in animals have delivered single dose irradiation rather than clinically relevant fractionated irradiation (*33*). In this study, we established a tumor on the back of the chest of the mice. To design a clinically relevant radiation treatment regimen, thoracic radiation treatment was delivered to the tumor-baring mice in 5 fractions (6 Gy/day for 5 days) for a cycle of standard treatment at first and were given two additional doses of 6 Gy thoracic irradiation according to the status of tumor growth. Our data showed that nicaraven administration with different doses either pre-or post-irradiation did not diminish the radiation-induced inhibition of tumor growth.

---

[2] Editor's note. The online version of this article (DOI: https://doi.org/10.1667/RADE-22-00212.1) contains supplementary information that is available to all authorized users.

Exposure to radiation generates ROS that provokes DNA damage and death to both the cancer cells and the surrounding normal tissue (*34*). Hence, some free radical scavenging radio-protectors greatly decrease the effect of radiation in inhibiting tumor growth (*20*). Nicaraven is originally known as a free radical scavenger (*35*); however, our past studies have demonstrated that nicaraven barely changes the ROS levels on different types of cells (*10*). Therefore, it is not surprising to us the minimal effect that nicaraven has in radiation-induced inhibition of tumor growth as shown in our study.

It has been reported that hypo-fractionated radiation converts "cold" tumors to "hot" inflammatory tumors by releasing pro-inflammatory factors (*36*). Since nicaraven has shown an anti-inflammatory effect (*11*, *15*), we measured the levels of several cytokines/chemokines in the tumors. We found that the levels of IL-1β, IL-6, IL-10, MCP-1, MIP-2a, TGF-β_1, VEGF, p53, p21, caspase-3 and cyclin D1 in tumor tissues did not significantly change by nicaraven administration and radiotherapy. The pharmacokinetics of nicaraven have been carefully conducted by Chugai Pharmaceutical Co., Ltd. Nicaraven shows a quick (few minutes) adequate whole-body distribution after injection and a short half-life (1.2–1.4 h) in murine. As we collected the tumor tissues almost 2 weeks after the last nicaraven administration, it would not be the optimal time window for detection.

In summary, it seems that nicaraven has a very limited effect on the sensitivity of radiotherapy to established tumors. According to the results from this experimental study, post-irradiation administration of nicaraven at low doses will be recommended. However, randomized controlled trials are needed to further confirm the benefit of nicaraven administration for cancer patients who are receiving radiotherapy.

SUPPLEMENTARY TABLES

Correlations between the levels of cytokines in tumor tissues and the tumor weights at the endpoint.

ACKNOWLEDGMENTS

This study was supported by Japan Agency for Medical Research and Development, a Grant-in-Aid from the Ministry of Education, Science, Sports, Culture and Technology, Japan. All data are included in the paper and/or the Supplementary Material.

Received: November 28, 2022; accepted: August 3, 2023; published online: September 13, 2023

REFERENCES

1. Bradley JD, Paulus R, Komaki R, Masters G, Blumenschein G, Schild S, et al. Standard-dose versus high-dose conformal radiotherapy with concurrent and consolidation carboplatin plus paclitaxel with or without cetuximab for patients with stage IIIA or IIIB non-small-cell lung cancer (RTOG 0617): a randomised, two-by-two phase 3 study. The Lancet Oncology. 2015 Feb; 16(2):187–99.
2. Seegenschmiedt MH, Micke O, Muecke R; German Cooperative Group on Radiotherapy for Non-malignant Diseases (GCG-BD). Radiotherapy for non-malignant disorders: state of the art and update of the evidence-based practice guidelines. The British journal of radiology. 2015 Jul; 88(1051):20150080.
3. Trott KR, Herrmann T, Kasper M. Target cells in radiation pneumopathy. International journal of radiation oncology. 2004 Feb; 58(2):463–9.
4. Jack CI, Cottier B, Jackson MJ, Cassapi L, Fraser WD, Hind CR. Indicators of free radical activity in patients developing radiation pneumonitis. International journal of radiation oncology.1996 Jan; 34(1):149–54.
5. Terasaki Y, Ohsawa I, Terasaki M, Takahashi M, Kunugi S, Dedong K, et al. Hydrogen therapy attenuates irradiation-induced lung damage by reducing oxidative stress. American journal of physiology Lung cellular and molecular physiology. 2011 Oct; 301(4): 415-26.
6. Kim SR, Kim DI, Kim SH, Lee H, Lee KS, Cho SH, et al. NLRP3 inflammasome activation by mitochondrial ROS in bronchial epithelial cells is required for allergic inflammation. Cell Death & Disease. 2014 Oct; 5(10):e1498.
7. Giuranno L, Ient J, De Ruysscher D, Vooijs MA. Radiation-Induced Lung Injury (RILI). Frontiers in Oncology. 2019 Sep; 9(6):1–16.
8. Alam Mohd S, Ku K, Hashimoto M, Nosaka S, Saitoh Y, Yamauchi M, et al. Hydroxyl radical scavenging effect of nicaraven in myocardial and coronary endothelial preservation and reperfusion injury. Cardiovascular Research. 1997 Mar; 33(3):686–92.
9. Ali H, Galal O, Urata Y, Goto S, Guo C, Luo L, et al. The potential benefits of nicaraven to protect against radiation-induced injury in hematopoietic stem/progenitor cells with relative low dose exposures. Biochemical and Biophysical Research Communications. 2014 Sep; 452(3):548–53.
10. Kawakatsu M, Urata Y, Imai R, Goto S, Ono Y, Nishida N, et al. Nicaraven Attenuates Radiation-Induced Injury in Hematopoietic Stem/Progenitor Cells in Mice. PloS one 2013 Mar; 8(3):1–7.
11. Yan C, Luo L, Urata Y, Goto S, Li TS. Nicaraven reduces cancer metastasis to irradiated lungs by decreasing CCL8 and macrophage recruitment. Cancer Letters. 2018 Apr; 418:204–10.
12. Yan C, Luo L, Urata Y, Goto S, Guo C, Li TS. Nicaraven, a Potential Radioprotective Agent, has Very Limited Effects on the Survival of Cancer Cells and the Growth of Established Tumors. Radiation research. 2017 Feb; 3 45:339–45.
13. Abdelghany L, Zhang X, Kawabata T, Goto S, El-Mahdy N, Jingu K, et al. Nicaraven prevents the fast growth of inflamed tumors by an anti-inflammatory mechanism. Medical oncology. 2021 Nov; 39(1):7.
14. Qu MX, Murrell DH, Millman B, Palma DA, Louie A V. Dose Escalation in 5-Fraction Palliative Thoracic Radiotherapy: A Feasibility and Safety Planning Study. International Journal of Radiation Oncology. 2019 Sep; 105(1):E586–7.
15. Lin H, Wu X, Yang Y, Wang Z, Huang W, Wang LF, et al. Nicaraven inhibits TNFα-induced endothelial activation and inflammation through suppressing NF-κB signaling pathway. Canadian journal of physiology and pharmacology. 2021 Aug; 99(8):803-811.
16. Vinod SK, Hau E. Radiotherapy treatment for lung cancer: Current status and future directions. Respirology. 2020 Nov; 25 Suppl 2: S61–71.
17. Vordermark D. Radiotherapy of Cervical Cancer. Oncology research and treatment. 2016; 39(9):516–20.
18. Hennequin C, Barillot I, Azria D, Belkacémi Y, Bollet M, Chauvet B, et al. [Radiotherapy of breast cancer]. Cancer radiotherapie. 2016 Sep; 20 Supp l:S139-46.
19. Farhood B, Goradel NH, Mortezaee K, Khanlarkhani N, Salehi E, Nashtaei MS, et al. Melatonin as an adjuvant in radiotherapy for radioprotection and radiosensitization. Clinical & translational oncology. 2019 Mar; 21(3):268–79.

20. Zakeri K, Narayanan D, Vikram B, Evans G, Coleman CN, Prasanna PGS. Decreasing the Toxicity of Radiation Therapy: Radioprotectors and Radiomitigators Being Developed by the National Cancer Institute Through Small Business Innovation Research Contracts. International journal of radiation oncology. 2019 May; 104(1):188–96.

21. Arroyo-Hernández M, Maldonado F, Lozano-Ruiz F, Muñoz-Montaño W, Nuñez-Baez M, Arrieta O. Radiation-induced lung injury: current evidence. BMC Pulmonary Medicine. 2021 Jan; 21(1):1–12.

22. Antonadou D, Coliarakis N, Synodinou M, Athanassiou H, Kouveli A, Verigos C, et al. Randomized phase III trial of radiation treatment +/- amifostine in patients with advanced-stage lung cancer. International journal of radiation oncology. 2001 Nov; 51(4):915–22.

23. Para AE, Bezjak A, Yeung IWT, Van Dyk J, Hill RP. Effects of genistein following fractionated lung irradiation in mice. Radiotherapy and oncology. 2009 Sep; 92(3):500–10.

24. Vujaskovic Z, Batinic-Haberle I, Rabbani ZN, fu Feng Q, Kang SK, Spasojevic I, et al. A small molecular weight catalytic metalloporphyrin antioxidant with superoxide dismutase (SOD) mimetic properties protects lungs from radiation-induced injury. Free radical biology & medicine. 2002 Sep; 33(6):857–63.

25. Rübe CE, Wilfert F, Uthe D, Schmid KW, Knoop R, Willich N, et al. Modulation of radiation-induced tumour necrosis factor alpha (TNF-alpha) expression in the lung tissue by pentoxifylline. Radiotherapy and oncology. 2002 Aug; 64(2):177–87.

26. Sun Y, Du YJ, Zhao H, Zhang GX, Sun N, Li XJ. Protective effects of ulinastatin and methylprednisolone against radiation-induced lung injury in mice. Journal of radiation research. 2016 Sep; 57(5):505–11.

27. Bao P, Gao W, Li S, Zhang L, Qu S, Wu C, et al. Effect of pretreatment with high-dose ulinastatin in preventing radiation-induced pulmonary injury in rats. European journal of pharmacology. 2009 Jan; 603(1–3):114–9.

28. Prasanna PGS, Stone HB, Wong RS, Capala J, Bernhard EJ, Vikram B, et al. Normal tissue protection for improving radiotherapy: Where are the Gaps? Translational cancer research. 2012 Jun; 1(1):35–48.

29. Tsai JR, Liu PL, Chen YH, Chou SH, Cheng YJ, Hwang JJ, et al. Curcumin Inhibits Non-Small Cell Lung Cancer Cells Metastasis through the Adiponectin/NF-κb/MMPs Signaling Pathway. PloS one. 2015; 10(12):e0144462.

30. Vogelius IR, Bentzen SM. A literature-based meta-analysis of clinical risk factors for development of radiation induced pneumonitis. Acta oncologica. 2012 Nov; 51(8):975–83.

31. Leprieur EG, Fernandez D, Chatellier G, Klotz S, Giraud P, Durdux C. Acute radiation pneumonitis after conformational radiotherapy for non small cell lung cancer: clinical, dosimetric, and associated-treatment risk factors. Journal of cancer research and therapeutics. 2013 Jul- Sep; 9(3):447–51.

32. Dabjan MB, Buck CM, Jackson IL, Vujaskovic Z, Marples B, Down JD. A survey of changing trends in modelling radiation lung injury in mice: bringing out the good, the bad, and the uncertain. Laboratory investigation; a journal of technical methods and pathology. 2016 Sep; 96(9):936–49.

33. Paun A, Haston CK. Genomic and genome-wide association of susceptibility to radiation-induced fibrotic lung disease in mice. Radiotherapy and oncology. 2012 Dec; 105(3):350–7.

34. Lee SY, Jeong EK, Ju MK, Jeon HM, Kim MY, Kim CH, et al. Induction of metastasis, cancer stem cell phenotype, and oncogenic metabolism in cancer cells by ionizing radiation. Molecular cancer. 2017 Jan; 16(1):10.

35. Watanabe M, Akiyama N, Sekine H, Mori M, Manome Y. Inhibition of poly (ADP-ribose) polymerase as a protective effect of nicaraven in ionizing radiation- and ara-C-induced cell death. Anticancer Research. 2006 Sep- Oct; 26(5 A):3421–7.

36. Formenti SC, Rudqvist NP, Golden E, Cooper B, Wennerberg E, Lhuillier C, et al. Radiotherapy induces responses of lung cancer to CTLA-4 blockade. Nature medicine. 2018 Dec; 24(12):1845–51.

ONCOLOGY REPORTS 46: 211, 2021

Hydrostatic pressure stabilizes HIF-1α expression in cancer cells to protect against oxidative damage during metastasis

DA ZHAI[1,2], YONG XU[1,2], LINA ABDELGHANY[1,2,3], XU ZHANG[1,2], JINGYAN LIANG[4],
SHOUHUA ZHANG[5], CHANGYING GUO[6] and TAO-SHENG LI[1,2]

[1]Department of Stem Cell Biology, Atomic Bomb Disease Institute, Nagasaki University; [2]Department of Stem Cell Biology, Nagasaki University Graduate School of Biomedical Sciences, Nagasaki 852-8523, Japan; [3]Department of Pharmacology and Toxicology, Faculty of Pharmacy, Tanta University, Tanta 31527, Egypt; [4]Institute of Translational Medicine, Medical College, Yangzhou University, Yangzhou, Jiangsu 225000; [5]Department of General Surgery, Jiangxi Provincial Children's Hospital; [6]Department of Thoracic Surgery, Jiangxi Cancer Hospital, Nanchang, Jiangxi 330000, P.R. China

Received November 6, 2020; Accepted April 23, 2021

DOI: 10.3892/or.2021.8162

Abstract. The tissue microenvironment is known to play a pivotal role in cancer metastasis. Interstitial fluid hydrostatic pressure generally increases along with the rapid growth of malignant tumors. The aim of the present study was to investigate the role and relevant mechanism of elevated hydrostatic pressure in promoting the metastasis of cancer cells. Using a commercial device, Lewis lung cancer (LLC) cells were exposed to 50 mmHg hydrostatic pressure (HP) for 24 h. The survival time and morphology of the cells did not notably change; however, the results from a PCR array revealed the upregulation of numerous metastasis-promoting genes (*Hgf, Cdh11* and *Ephb2*) and the downregulation of metastasis suppressing genes (*Kiss1, Syk* and *Htatip2*). In addition, compared with that in the control, the cells which had undergone exposure to 50 mmHg HP showed significantly higher protein expression level of HIF-1α and the antioxidant enzymes, SOD1 and SOD2, as well as improved tolerance to oxidative stress ($P<0.05$ vs. control). Following an intravenous injection of the LLC cells into healthy mice, to induce lung metastasis, it was found that the exposure of the LLC cells to 50 mmHg HP for 24 h, prior to injection into the mice, resulted in higher cell survival/retention in the lungs 24 h later and also resulted in more metastatic tumor lesions 4 weeks later ($P<0.05$ vs. control). Further investigation is required to confirm the molecular mechanism; however, the results from the present study suggested that elevated interstitial fluid HP in malignant tumors may promote the metastasis of cancer cells by stabilizing HIF-1α expression to defend against oxidative damage.

Introduction

Metastasis occurs in ~90% of malignant tumors and is the leading cause of cancer-associated mortality in patients with cancer worldwide (1,2). A number of biological factors and multiple signaling pathways, such as epithelial-mesenchymal transition, resistance to apoptosis and angiogenesis have been associated with the complex processes of metastasis (3); however, a novel approach for effectively controlling tumor metastasis is still required.

Metastasis is defined as cancer cells leaving the original tumor mass and disseminating to other parts of the body via the bloodstream or lymphatic system. Therefore, the metastatic process represents a multi-step event (3). For example, remote hematogenous metastasis requires the cancer cells to successfully pass through the following steps: i) Transendothelial migration into the vessel (known as intravasation); ii) survival in the circulatory system; iii) attachment to the vessel wall and transendothelial migration out of the vessel (known as extravasation) and iv) eventually live and propagate at the distal site (4,5). All of these steps are accompanied with a change in the surrounding microenvironment, with various biomechanical forces and oxidative stress (6); therefore, metastasis can be a stressful and inefficient event to the cancer cell (7).

Biomechanical forces have been demonstrated to play critical roles in regulating cell migration and proliferation (8,9). With the rapid advancement of mechanobiology in recent years, it has become a hot topic for understanding how biomechanical forces mediate malignant tumor progression (2,8). Beyond the mechanical stress during metastatic processes, it is also well-known that elevated interstitial fluid hydrostatic pressure (HP) occurs in solid tumors (10,11). Higher interstitial fluid HP in tumor mass has been demonstrated to be associated with a worse prognosis in patients with head and neck cancer (12). Furthermore, the exposure of cancer cells to 20 mmHg HP has been demonstrated to accelerate cell motility (8). However, it is not clear whether and how the elevation of interstitial fluid HP in tumor mass promotes the metastasis of cancer cells.

Correspondence to: Professor Tao-Sheng Li, Department of Stem Cell Biology, Atomic Bomb Disease Institute, Nagasaki University, 1-12-4 Sakamoto, Nagasaki 852-8523, Japan
E-mail: litaoshe@nagasaki-u.ac.jp

Key words: hydrostatic pressure, HIF-1α, metastasis, oxidative stress, adhesion

Notably, it has recently been reported that cyclical mechanical force can induce the stabilization of HIF-1α and upregulate the protein expression level of CXCL2 in monocytes (13). HIF-1α is well-known as a master upstream regulator of oxidative stress, metabolism and DNA repair of cells (14-16). Therefore, we hypothesized that elevated interstitial fluid HP in a rapid growing malignant tumor may stabilize HIF-1α to promote the metastasis of cancer cells.

In the present study, mouse Lewis lung carcinoma (LLC) cells were exposed to 50 mmHg HP for 24 h, then the role of HP on the metastatic property of these cells was investigated using both *in vitro* and *in vivo* experiments.

Materials and methods

Cells and animals. The LLC cells (LL/2) were used for the experiments. The cells were maintained in DMEM (FUJIFILM Wako Pure Chemical Corporation), supplemented with 10% fetal bovine serum (Cytiva) and 1% penicillin/streptomycin (Gibco; Thermo Fisher Scientific, Inc.), and cultured at 37˚C in a humidified incubator with 5% CO_2.

A total of 19, male C57BL/6 mice (10-12 weeks old; weight, 23-25 g; CLEA Japan, Inc.) were used for the *in vivo* study. The mice were kept in specific, pathogen-free conditions and were allowed free access to food and water under a controlled temperature (24±1˚C) with 55% humidity in a 12-h light/dark cycle. The animal experiments were approved by the Institutional Animal Care and Use Committee of Nagasaki University (approval no. 1608251335-11). All the animal procedures were performed in accordance with institutional and national guidelines. At the end of the experiments, the mice were administered with general anesthesia using an intraperitoneal injection of mixed anesthetics (0.75 mg/kg medetomidine, 4 mg/kg midazolam and 5 mg/kg butorphanol) and sacrificed by severing the abdominal aorta for blood removal. The removal of vital organs (lung tissue) was used as confirmation of the death of the mice following sacrifice.

HP stimulation. HP was induced in the LLC cells using a pneumatic pressurizing system (Strex. Inc.). Briefly, the LLC cells were seeded in 60 mm diameter Petri dishes (1×10^5 cells/dish) and cultured for 36 h to form an adherent monolayer. The culture dishes were then randomly selected to move into a sealed chamber in which 50 mmHg HP was stably applied using the pneumatic pressurizing system and kept for 24 h (HP group). The culture dishes without HP exposure were used as the control (CON group).

Cell morphology observation and cell count. Cell morphology was observed under a light microscope (1X71S8F-3; Olympus Corporation) at x200 magnification, 24 h following HP exposure. Then, the cells were collected as a single cell suspension to measure the total cell number using a TC20™ Automated Cell Counter (Bio-Rad Laboratories, Inc.).

Reverse transcription (RT)^2 Profiler™ PCR array. To investigate the mRNA expression level of genes associated with metastasis, RNA was isolated from the cells using a Quick-RNA™ MicroPrep kit (Zymo Research Corp.). The concentration of RNA was measured using a NanoDrop® 2000 spectrophotometer (Thermo Fisher Scientific, Inc.). Then, 1 µg RNA was used to generate cDNA using the RT^2 First Strand kit (Qiagen Corporation), at 25˚C for 10 min, 42˚C for 60 min, then 85˚V for 5 min. Mouse Tumor Metastasis RT^2 Profiler™ PCR array (cat. no. 330231; Qiagen Corporation) was used with a RT^2 SYBR-Green Master mix, according to the manufacturer's instructions and a Roche LightCycler 480 machine (Roche Diagnostics). The array contained a total of 84 genes associated with metastasis. The genes included in the assay were also defined by biological function by the manufacturer. The fold change in expression to the control was calculated using a web-based data analysis program (https://geneglobe.qiagen.com/jp/analyze). Among the 5 available housekeeping genes (*Actb, B2m, Gapdh, Gusb* and *Hsp90ab1*) in the array, *Actb, Gusb* and *Hsp90ab1* were automatically selected as the optimal set of internal control for normalization.

Adhesion assay. To evaluate the adhesion ability, the cells from both the HP and CON groups were harvested as single cell suspensions. Freshly harvested cells (5×10^4 cells in 5 ml DMEM) were seeded onto a 25-cm^2 Collagen I-coated Flask (Thermo Fisher Scientific, Inc.). Following incubation for 60 min, the unattached cells were gently removed by washing with PBS twice. The number of adherent cells was counted under a light microscope at x200 magnification. The average cell count from >20 randomly selected fields was used for statistical analysis.

Western blot analysis. The protein expression level of HIF-1α, SOD1 and SOD2 was evaluated using western blot analysis, as previously described (17). Total protein from the cells was extracted using 1X RIPA buffer (FUJIFILM Wako Pure Chemical Corporation) and the concentration was detected using a BCA assay. A total of 30 µg protein from each sample was separated using 10-12% SDS-PAGE, then transferred to 0.2-µm PVDF membranes (Bio-Rad Laboratories, Inc.). After blocking with 5% skimmed milk for 1 h at room temperature, the membranes were incubated with primary antibodies against HIF-1α (1:250 dilution; cat. no. ab1; room temperature for 2 h; Abcam), SOD1 (1:500 dilution; cat. no. sc11407; overnight at 4˚C; Santa Cruz Biotechnology, Inc.), SOD2 (1:500 dilution; cat. no. sc30080; overnight at 4˚C; Santa Cruz Biotechnology, Inc.) and β-actin (1:1,000 dilution; cat. no. 8457S; overnight at 4˚C; Cell Signaling Technology, Inc.), followed by incubation with horseradish peroxidase-conjugated secondary antibodies (rabbit anti-mouse, 1:1,000 dilution; cat. no. P026002; goat anti-rabbit, 1:1,000 dilution; cat. no. P044801) (both from Dako; Agilent Technologies, Inc.) at room temperature for 1 h. The expression level was visualized using an enhanced chemiluminescence detection kit (Thermo Fisher Scientific, Inc.). Semi-quantitative analysis was done using ImageQuant LAS 4000 mini detection system (v1.0; GE Healthcare Life Sciences).

Evaluation of oxidative stress tolerance. To evaluate oxidative stress tolerance, the cells from both groups were treated with 0, 20 or 50 µM hydrogen peroxide (H_2O_2) in PBS at 37˚C for 2 h. The apoptotic cells were stained with Annexin V-FITC, while the necrotic cells were labelled with PI using an

Annexin V-FITC Apoptosis Detection Kit (Abcam). The cells without staining were used as negative control. Quantitative flow cytometry analysis was performed using a FACSVerse™ flow cytometer and analyzed using BD FACSuite Software (v1.2 Suite 1.0.2) (both from BD Biosciences).

In addition, intracellular reactive oxygen species (ROS) was detected in the cells. Briefly, the cells from both groups were treated with 0, 20 or 50 μM H_2O_2 in PBS at 37˚C for 1 h, then incubated with 10 μM general oxidative stress indicator (CM-H2DCFDA; Invitrogen; Thermo Fisher Scientific, Inc.) for another 30 min in the dark. Cells without staining were used as a negative control. The accumulation of intracellular ROS was measured by fluorescence intensity using a FACSVerse™ flow cytometer (BD Biosciences) and analyzed using BD FACSuite Software (v1.2 Suite 1.0.2) (both from BD Biosciences).

Experimental lung cancer metastasis model. To evaluate the metastatic potency, experimental lung cancer metastasis was induced in mice using an intravenous injection of LLC cells ($5x10^5$ cells in 0.5 ml saline) from the HP (n=6) and the CON (n=7) groups. A total of 4 weeks after the cells were injected into the mice, all the mice were sacrificed as aforementioned. Removal of lung tissue was used for both confirmation of mice death and experimental evaluation. Excised lung tissue was weighed and the number of tumor lesions on the lung surface was counted. For the mice that spontaneously died during the 4-week follow-up period, the date of death was recorded and the lung tissue samples were collected for evaluation. Statistical analysis of the overall survival rate of the mice was also determined.

Immunohistochemical staining. The cell proliferation and microvessel density in the metastatic lesions of the lungs was detected using immunohistochemistry staining. The lungs were fixed in 4% paraformaldehyde for 24 h, at 4˚C, and paraffin-embedded sections (6-μm thick) were deparaffinized and rehydrated (xylene, 2x3 min washes; xylene 1:1 with 100% ethanol, 3 min; 100% ethanol, 2x3 min washes; 95% ethanol, 3 min; 70% ethanol, 3 min; 50% ethanol, 3 min; running cold tap water to rinse). After blocking with 1% BSA in PBS (Sigma-Aldrich; Merck KGaA), the sections were incubated with rabbit anti-mouse Ki67 antibody (cat. no. ab16667; 1:100 dilution;) and rabbit anti-mouse CD31 antibody (cat. no. ab28394; 1:150 dilution) (both from Abcam) overnight at 4˚C, followed by incubation with the Alexa fluorescent 546-conjugated goat anti rabbit IgG(H+L) secondary antibody (cat. no. A11013; 1:350 dilution; Invitrogen; Thermo Fisher Scientific, Inc.) at room temperature for 1 h. Nuclei were stained with 4, 6-diamidino-2-phenylin-dole (DAPI; cat. no. D21490; Thermo Fisher Scientific, Inc.) at room temperature for 5 min. Positive staining was examined under a fluorescent microscope (FV10C-W3; Olympus Corporation). The percentage of Ki67-positive cells was calculated from 10 randomly selected fields of view (5 fields/slide in 2 slides) and used for statistical analysis. The CD31-positive stained structures were counted as microvessels and the average number of microvessels counted from 10 randomly selected fields of view (5 fields/slide in 2 slides) was used for statistical analysis.

PKH26 red fluorescent cell labeling. To evaluate the survival/retention of the LLC cells in the lungs of the mice, the cells were labelled with a PKH26 Red Fluorescent Cell Linker kit (Sigma-Aldrich; Merck KGaA). Briefly, the cells were incubated with 2 μM PKH26 dye for 5 min at room temperature, as the manufacturer's recommendations. Then, the mice were intravenously injected with the PKH26-labelled cells ($1x10^6$ cells in 0.5 ml saline) from the HP (n=3) and the CON (n=3) groups. The mice were sacrificed 24 h following the injection and the lung tissue samples were collected. Cryosections (8-μm thick) of the lung tissues were used for the direct detection of PKH26-labelled LLC cells under a fluorescent microscope (FV10C-W3; Olympus Corporation).

Statistical analysis. The data are presented as the mean ± SD. Statistical significance between two groups was determined using an unpaired t-test (SPSS; v20.0; IBM Corp.). The survival of the mice was analyzed using a Kaplan-Meier curve and statistical significance was determined using the log-rank test (GraphPad Prism; v8.0.1; GraphPad Software, Inc.). P<0.05 was used to indicate a statistically significant difference.

Results

Exposure of the LLC cells to 50 mmHg HP altered the mRNA expression level of numerous genes associated with metastasis. Firstly, the mRNA expression level of genes associated with metastasis was analyzed between the HP and CON groups. The RT^2 Profiler™ PCR array revealed that numerous genes were up- or downregulated, with a >1.3-fold difference in the HP group compared with that in the CON group (Table SI). The top 10 up- or downregulated genes are shown in Fig. 1A. Within the top 10 upregulated genes, the upregulation of several adhesion molecules was found, including *Cdh1, Cdh11* and *Fn1* (Fig. 1B). In addition, the upregulation of numerous metastasis-promoting genes, such as *Hgf, Cdh11* and *Ephb2,* was also found. Within the top 10 downregulated genes, metastasis suppressors, including *Kiss1, Syk* and *Htatip2,* were frequently detected (Fig. 1B). The overall change in the gene expression profile indicated the potential role of HP in enhancing metastatic properties of the LLC cells.

HP exposure enhances the adhesion property of the LLC cells. The exposure of the LLC cells to 50 mmHg HP for 24 h did not induce notable morphological changes (Fig. 2A). The total number of harvested cells was also comparable between the groups (P=0.70; Fig. 2A), indicating a limited effect of 50 mmHg HP exposure on cell growth.

As the PCR array data indicated the upregulation of numerous adhesion molecules, the adhesion property of the cells was investigated. It was found that the exposure to 50 mmHg HP significantly increased the number of adherent cells on a collagen I-coated flask (P<0.05; Fig. 2B).

HP exposure increases the protein expression level of HIF-1α and antioxidant enzymes in the LLC cells. HIF-1α, a master regulator of the cellular adaptive response to hypoxia, is known to play critical roles in metabolic reprogramming (16) and metastasis (14) in cancer cells. Western blot analysis showed

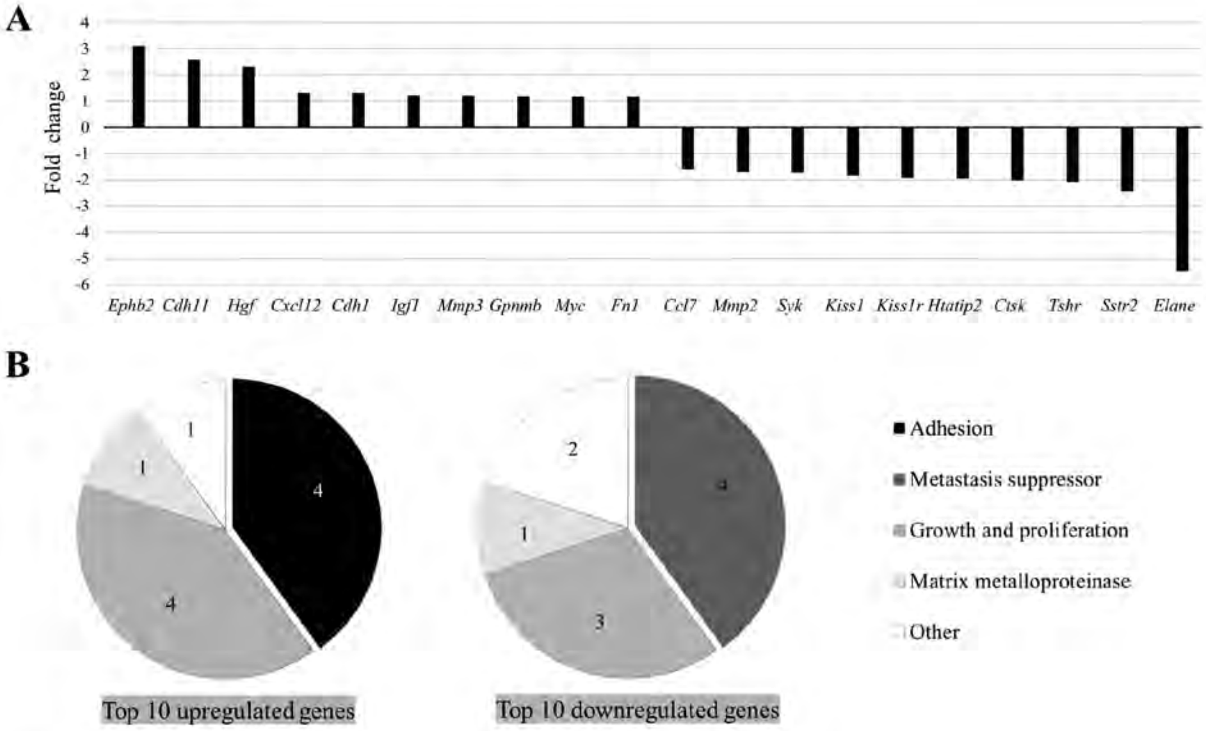

Figure 1. Change in the mRNA expression level of genes in the Lewis lung cancer cells following treatment with or without 50 mmHg HP for 24 h. The mRNA expression level of metastasis-related genes was measured using a reverse transcription[2] Profiler™ PCR array. The data are presented as the fold change in the cells with HP compared with that in the CON. The top 10 up- and downregulated genes are according to the (A) fold change and (B) the biological functional categories of the genes. HP, hydrostatic pressure exposure; CON, control.

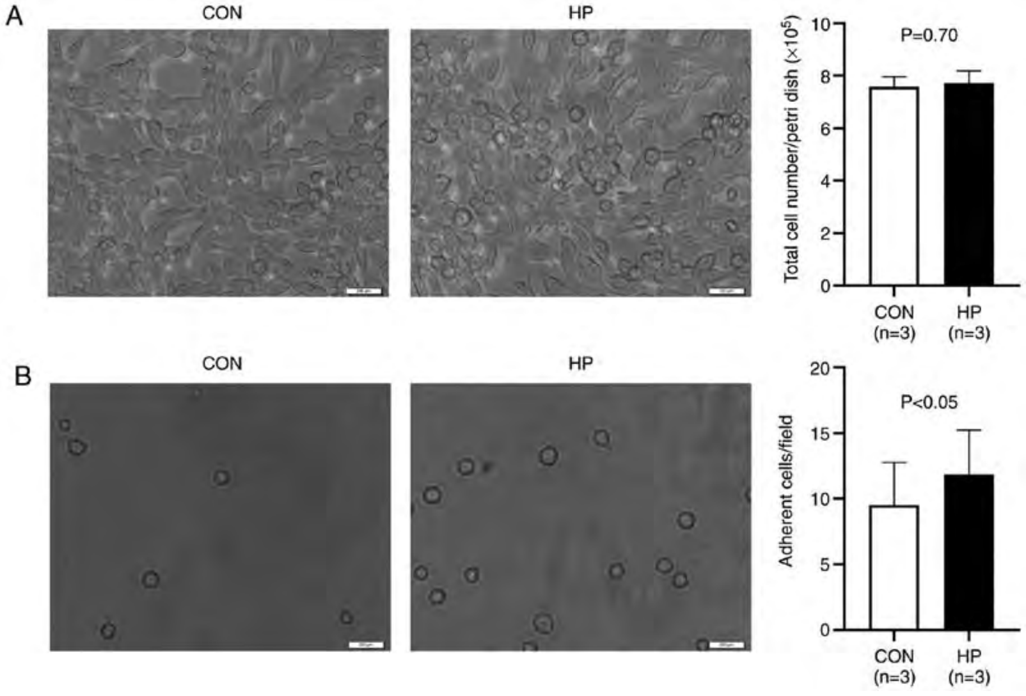

Figure 2. Survival and adhesion property of the Lewis lung cancer cells following treatment with or without 50 mmHg HP for 24 h. (A) Representative images of cell morphology under a phase-contrast microscope (left) and quantitative analysis of the total number of surviving cells per petri dish (right). (B) Representative images (left) and quantitative data (right) of the adherent cells in collagen I-coated flasks. Scale bar, 200 μm. The data are presented as the mean ± SD from 3 independent experiments. HP, hydrostatic pressure exposure; CON, control.

that the protein expression level of HIF-1α was significantly increased in cells exposed to 50 mmHg HP for 24 h ($P<0.01$; Fig. 3A).

The protein expression level of the antioxidant enzymes, SOD1 and SOD2, which are HIF-1α downstream signals (18,19), was also investigated. As expected, the exposure

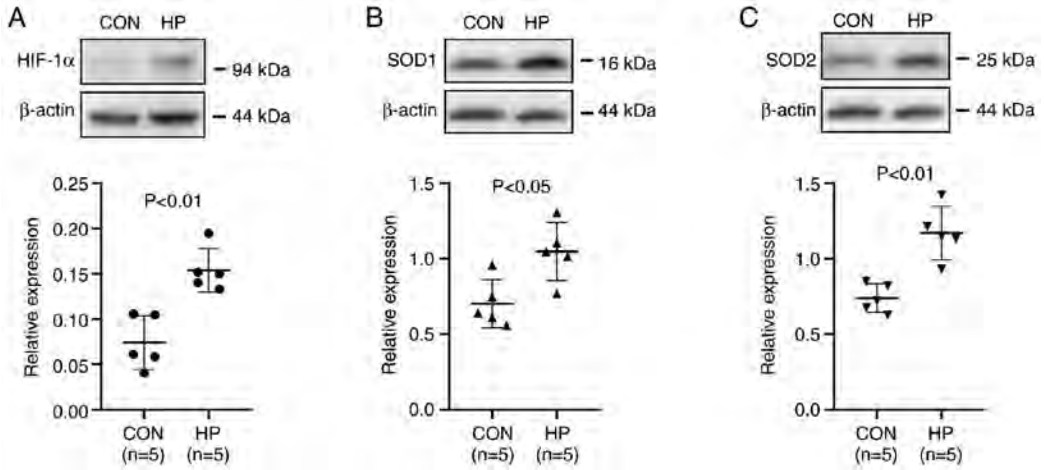

Figure 3. Protein expression level of HIF-1α, SOD1 and SOD2 is increased following exposure of the LLC cells to 50 mmHg HP for 24 h. Representative blots and semi-quantitative analysis of the protein expression level of (A) HIF-1α, (B) SOD1 and (C) SOD2 in the LLC cells following treatment with or without 50 mmHg HP for 24 h. The data are presented as the mean ± SD from 5 independent experiments. HP, hydrostatic pressure; CON, control; LLC, Lewis lung cancer.

of the cells to 50 mmHg HP for 24 h also significantly upregulated the protein expression level of SOD1 and SOD2 ($P<0.05$; Fig. 3B and C).

HP exposure induces the tolerance of the LLC cells to oxidative stress. In addition, the oxidative stress tolerance of the cells was investigated *in vitro*. Cell necrosis, under 20 or 50 μM H_2O_2 treatment was significantly reduced in the LLC cells pretreated with 50 mmHg for 24 h ($P<0.05$; Fig. 4A); however, the percentage of apoptotic cells was not significantly different between the 2 groups treated with 20 or 50 μM H_2O_2 ($P=0.26$ and $P=0.45$, respectively; Fig. 4A).

The intracellular ROS level at the baseline (without H_2O_2 stimulation) was detected at comparable levels between the HP and CON groups (Fig. 4B). Unexpectedly, 1-h stimulation with 20 or 50 μM H_2O_2 notably decreased the ROS accumulation in the LLC cells without pretreatment with 50 mmHg HP compared with that at baseline (Fig. 4B). By contrast, after 1-h stimulation with 20 μM H_2O_2, the ROS accumulation was slightly increased in the LLC cells pretreated with 50 mmHg HP compared with that at baseline. We hypothesized that the less intracellular ROS accumulation in the LLC cells without HP exposure was due to the severe cell damage or cell death, rather than the resistance to oxidative stress.

HP exposure promotes the metastasis of the LLC cells to the lungs. To evaluate the metastatic potency *in vivo*, the LLC cells were intravenously injected into healthy adult mice. Compared with that in the mice that received LLC cells without HP exposure, significantly worse survival was observed in the mice that received LLC cells pretreated with 50 mmHg HP ($P<0.05$; Fig. 5A). All the mice were killed 4 weeks following the injection of the cells and the maximum percentage body weight loss observed was 9.3%. There were significantly more metastatic tumor lesions in the lungs of the mice in the HP group compared with that in the CON group ($P<0.05$; Fig. 5B and C). The weight of the lung tissue was also significantly higher in the HP group compared with that in the CON group ($P<0.05$; Fig. 5D). These data suggested that HP exposure promoted the metastasis of the LLC cells to the lungs.

To further understand the mechanism involved, the LLC cells were labelled with PKH26 before intravenous injection into the mice, then the survival/retention of the cells in the lungs was analyzed 24 h later. As expected, more LLC cells (or cell clusters) were detected in the lungs from mice in the HP group compared with that in the CON group (Fig. 6A), suggesting an improved survival/retention of the LLC cells by pretreatment with 50 mmHg HP.

Cell proliferation and neovascularization in the metastatic lesions was also analyzed using immunostaining. The percentage of Ki67-positive cells was not significantly different between the HP and CON groups ($P=0.20$; Fig. 6B). However, the density of the CD31-positive microvessels in the metastatic lesions was significantly higher in the HP group compared with that in the CON group ($P<0.05$; Fig. 6C).

Discussion

Various mechanical forces within the microenvironment of the tumor mass have been reported to play critical roles in the progression of malignant tumors (2). Owing to the hyper-permeability of immature capillaries, the elevation of the interstitial fluid HP could be commonly induced by the presence of excess fluid accumulation within malignant tumors (20,21). A previous study has reported that HP may drive breast cancer cells toward a more invasive phenotype (9); however, the precise role and relevant mechanism of the mechanical forces in mediating metastasis is still not well understood.

To investigate the role of HP on the metastatic property of cancer cells, the LLC cells were exposed to 50 mmHg HP to mimic the *in vivo* tumor microenvironment, then the mRNA expression level of genes associated with tumor metastasis was analyzed. A PCR array indicated noticeable changes, including the upregulation of metastasis promotors (*Hgf, Cdh11* and *Ephb2*) and the downregulation of metastasis suppressors (*Kiss1, Syk and Htatip2*) in the LLC cells following exposure to 50 mmHg HP for 24 h. The most upregulated gene, *Ephb2*, has been demonstrated to modulate the metastatic phenotype (22) and induce angiogenesis (23). The most downregulated gene, *Elane*, has been demonstrated to modulate

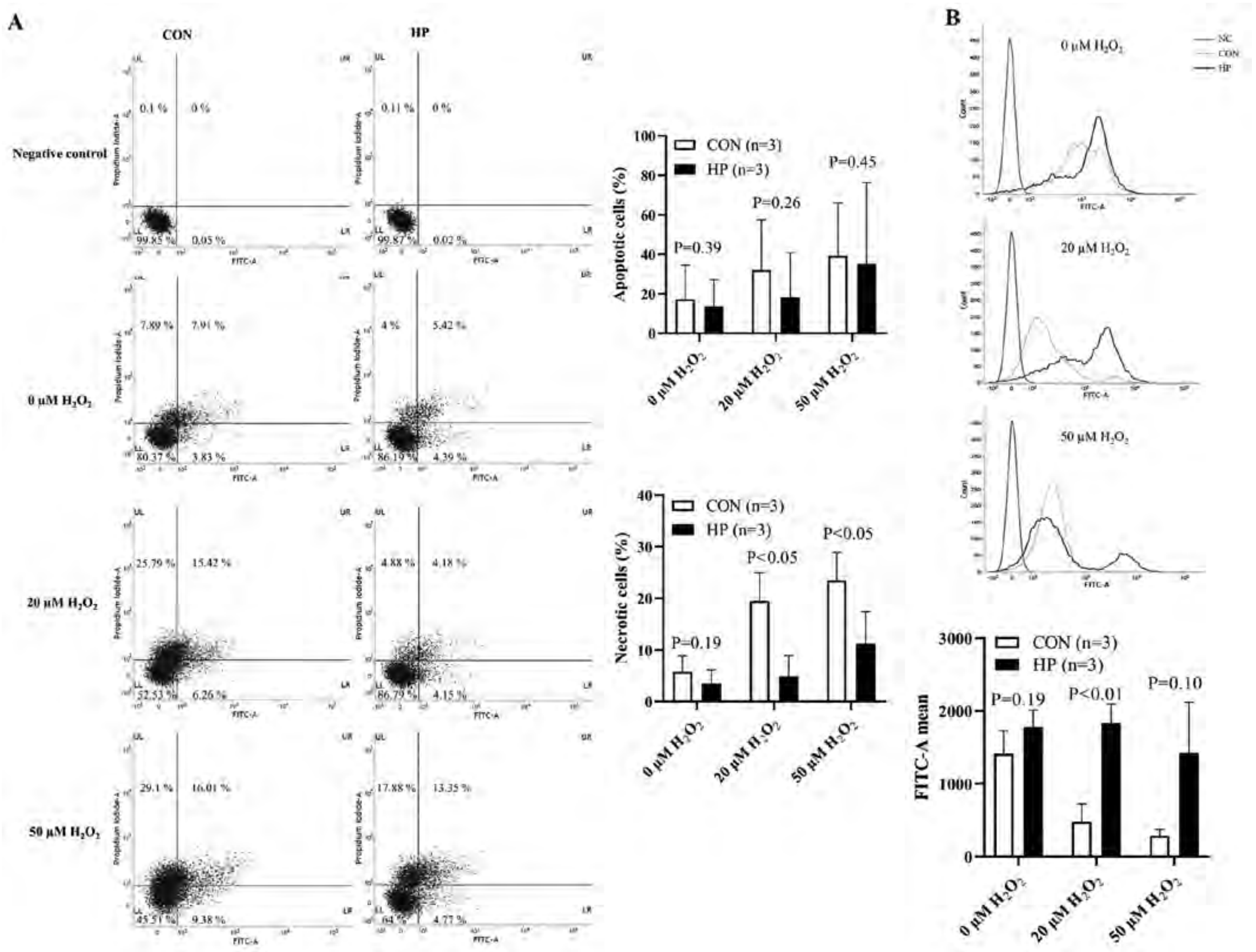

Figure 4. Tolerance of the LLC cells to oxidative stress. The LLC cells were treated with or without 50 mmHg HP and with 0, 20 and 50 μM H_2O_2. The apoptotic/necrotic cells and intracellular ROS was subsequently detected using flow cytometry. (A) Representative flow cytometry plots (left) and quantitative data (right) of the number of apoptotic and necrotic cells. (B) Representative histograms (upper) and quantitative data (lower) of the mean intensity of the intracellular ROS levels. The data are presented as the mean ± SD from three independent experiments. HP, hydrostatic pressure; CON, control; LLC, Lewis lung cancer; ROS, reactive oxygen species; H_2O_2, hydrogen peroxide.

neutrophil expression, inflammation and repair (24). Using an experimental lung metastasis model in mice, it was further confirmed that the LLC cells pretreated with 50 mmHg HP developed a significantly higher number of tumor metastasis lesions in the lungs. These data suggested that an elevated interstitial fluid HP in a rapidly growing malignant tumor may enhance the metastatic property of cancer cells.

Additional experiments were performed to further understand how HP enhanced the metastatic property of the LLC cells from different aspects, according to the multi-step processes of hematogenous metastasis. It is well-known that cancer cells enter the circulation system and are exposed to hyperoxic arterial blood for hematogenous metastasis (6). Accumulating evidence suggests that oxidative stress kills most of the circulating cancer cells, resulting in a very poor efficiency of metastasis (6,7). Therefore, oxidative stress tolerance is essential for the successful metastasis of cancer cells. HIF-1α is well-known as an important mediator of metabolism reprogramming of cancer cells by regulating antioxidant enzymes and antioxidant properties (25). Notably, it has been recently demonstrated that cyclic mechanical force stabilizes HIF-1α by reducing protein degradation (13). Consistently, the results from the present study showed the upregulation of HIF-1α protein expression level in the LLC cells following exposure to 50 mmHg HP for 24 h. In addition, the protein expression level of the antioxidant enzymes, SOD1 and SOD2, the direct downstream targets of HIF-1α (18,19), were also significantly increased in cells exposed to 50 mmHg HP. This could contribute to enhancing antioxidant capacity of cancer cells for remote hematogenous metastasis. Consistent with the upregulation of various adhesion molecules, the exposure to 50 mmHg HP also enhanced the adhesion property of the LLC cells, as shown by the results of the *in vitro* adhesion and the *in vivo* cell tracking assays.

HIFs are heterodimeric proteins composed of HIF-α and HIF-1β subunits. HIF-1α is an O_2-regulated subunit, while HIF-1β is a constitutively expressed subunit (26). The protein expression level of HIF-1α has been reported to be overexpressed in numerous malignant tumors, including lung, prostate, breast and colon carcinomas (27,28). It has been demonstrated that the enhanced protein expression level of HIF-1α was associated with poor prognosis in patients with breast, oropharyngeal and prostate cancer (29-31). As a master regulator of cellular response

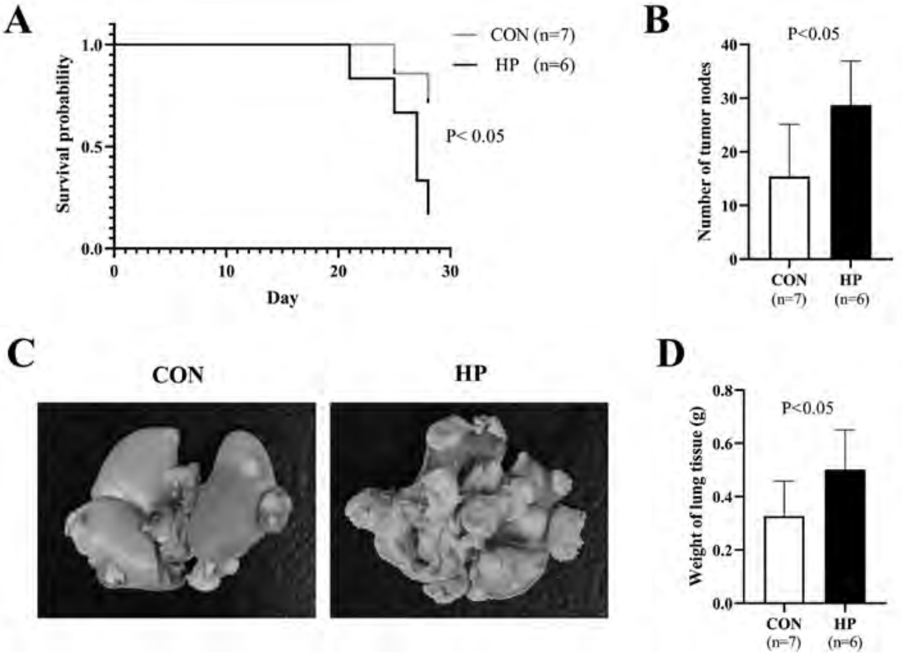

Figure 5. Experimental lung metastasis model in healthy adult mice. The Lewis lung cancer cells were treated with or without 50 mmHg HP and were intravenously injected into the mice, then lung metastasis was evaluated 4 weeks later. (A) Kaplan-Meier curves show the survival probability of the mice. (B) Quantitative data and (C) representative images of tumor metastasis lesions on the surface of lungs. (D) The weight of lung tissues. The data are presented as the mean ± SD. HP, hydrostatic pressure; CON, control.

to hypoxia, HIF-1 can induce the transcription of several genes involved in angiogenesis, cell proliferation and cell metabolism (15,32). One of the most popularly recognized downstream genes of HIF-1 is vascular endothelial growth factor (VEGF), which is known to induce angiogenesis for the rapid growth of malignant tumors (33). VEGF, originally named as vascular permeability factor, was first identified as a tumor-secreted factor, which increases vascular permeability and promotes the accumulation of ascite fluid (21). Considering the hyper-permeability of microvessels in the tumor (34), it is reasonable to hypothesize that an excess accumulation of exudate in the interstitial space contributes, at least in part, to the increase of the interstitial fluid HP in the tumor mass. As a result, elevated HP may stabilize HIF-1α, which thereby induces VEGF and antioxidant enzymes to accelerate the growth and metastasis of malignant tumors.

There is a caution in Cellosaurus that the LLC cells (LL/2) could be identical to 3LL cells. It is reported that LL/2 cell line could be identical to 3LL cell line because both of them are from mouse Lewis lung carcinoma and show the same biological characteristics. Therefore, this will not affect the conclusion of the present study.

A total of 4 weeks after the cells were injected into the mice was used as the humane endpoint, based on clinical signs (reduced intake and activity) and pathophysiological changes (weight loss >20%). During the follow-up for 4 weeks, the progression of tumor metastasis in the lungs of the mice was not directly monitored; however, it was indirectly monitored by observing the clinical signs (intake and activity) and pathophysiological changes (weight loss) of mice.

For the 7 mice that died spontaneously, prior to the end of the 4-week follow-up time in the lung metastasis mice model, it was confirmed that the 7 mice did not die from lung metastasis-induced respiratory failure or systemic cachexia. We hypothesized that the cause of spontaneous death may be due to another cause, based on the following: i) There were no signs of severe clinical symptoms in the 7 mice following daily monitoring; ii) based on the assessment of the exercised lungs, there were fewer metastatic lesions in the lungs of the 7 mice; iii) according to the examination of the 7 mice after sacrifice, there was no serious bleeding, inflammation or purulent secretions in the body, no notable signs of metastasis or organ necrosis was found in the chest cavity or in any of the other organs and no obvious occurrence of cachexia was found.

The present study has several limitations. First, a single cell line was used and the cells were only exposed to 50 mmHg HP for all the experiments. This is due to the following reasons: i) The present study was designed to examine whether an elevated HP could promote the metastasis of cancer cells; ii) the C57BL/6 mice were used for *in vivo* experiments and the LLC cell line is the most reproducible syngeneic model for evaluating lung metastasis to date (35); iii) interstitial fluid pressure in solid malignant tumors could be elevated to ~30 mmHg HP (12,36) and iv) the exposure of the LLC cells to 50 mmHg HP altered the mRNA expression level of genes associated with metastasis; however, higher pressure (100 mmHg) induced cell death and cell debris production (data not shown). Therefore, further experiments are required to exposure different cancer cell lines with different HPs. Second, the PCR array was not repeated due to a limited budget. In addition, the fold-change result may also have greater variations if P>0.05; therefore, it is important to have a sufficient number of biological replicates to validate the array data. However, a mixture of RNA samples was used from three independent experiments to generate the cDNA for a single PCR array in each group. Therefore, the PCR array data was expressed as the average level in 3 samples from each group. Third, further interventional experiments, such as the interference of the HIF-1α signaling

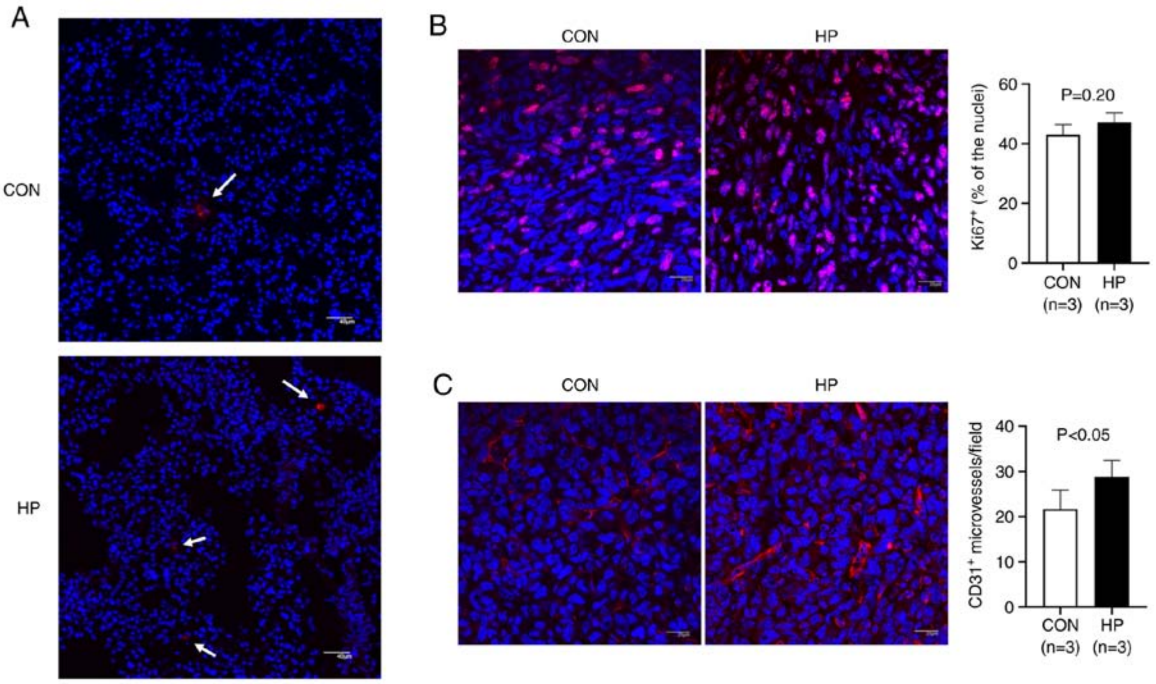

Figure 6. Survival/retention of the LLC cells and immunostaining analysis of proliferating cells and microvessels in the metastatic lesions. The LLC cells were treated with or without 50 mmHg HP, then intravenously injected into the mice. (A) Representative confocal microscopy images of the survival/retention of the PKH26-labelled cells or cell clusters (arrows) in the lungs, 24 h following injection. Scale bar, 40 μm. (B) Representative images (left) and quantitative data (right) of the Ki67-positive proliferative cells in the metastatic lesions in lungs. Scale bar, 20 μm. (C) Representative images (left) and quantitative data (right) of the CD31-positive microvessels in the metastatic lesions in the lungs. Scale bar, 20 μm. The nuclei were stained with DAPI. The data are presented as the mean ± SD. HP, hydrostatic pressure; CON, control; LLC, Lewis lung cancer.

pathway was not performed, as silencing HIF-1α alone would change cell biological properties. Furthermore, multiple factors, including the increase in mRNA expression level of HIF-1α and adhesion molecules could be involved in the HP-induced cancer cell metastasis; therefore, a genetic intervention approach to directly confirm the role of HIF-1α was not performed in the present study. Forth, Annexin V-positive apoptotic cells were only analyzed using flow cytometry and the expression level of other apoptotic proteins, such as the caspase family, can also be used to indicate apoptosis. In addition, a colony-forming assay was not included, as the potential role of HP in cancer cell metastasis, rather than tumorigenesis and tumor growth was the aim of the present study.

From the results in the present study, an elevated HP in rapidly growing malignant tumors may enhance the metastatic potency of cancer cells via complex mechanisms, including the increase in the mRNA expression level of adhesion molecules to improve cell adhesion and the stabilization of HIF-1α to induce the expression of antioxidant enzymes to defend against oxidative damage during metastasis (Fig. 7). It is critical to elucidate the comprehensive molecular mechanisms underlying the stabilization of HIF-1α by HP in further investigations.

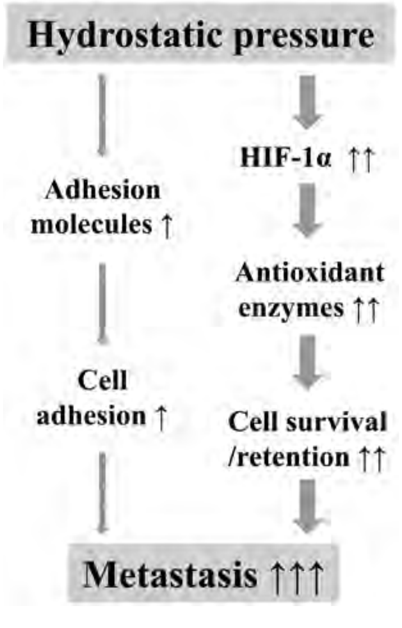

Figure 7. Schematic diagram of hydrostatic pressure induced metastasis of cancer cells. An elevated hydrostatic pressure in malignant tumors may enhance the metastatic potency of cancer cells by i) increasing the mRNA expression level of adhesion molecules to improve cell adhesion, and ii) stabilizing HIF-1α to induce the expression of antioxidant enzymes to protect against oxidative damage.

Acknowledgements

Not applicable.

Funding

This study was supported in part by a Grant-in-Aid from the Ministry of Education, Science, Sports, Culture and Technology, Japan (grant no. 17H04265), the Collaborative Research Program of the Atomic-bomb Disease Institute of Nagasaki University and the Japan China Sasakawa Medical Fellowship.

Availability of data and materials

The datasets used and/or analyzed during the current study are available from the corresponding author on reasonable request.

Author's contributions

All the authors contributed to the conception and design of the study. DZ, YX and LA performed the experiments and acquired the data. TSL, DZ, YX, LA and XZ analyzed and interpreted the data. DZ and SZ drafted the manuscript. TSL, JL and CG critically revised the manuscript for important intellectual content. TSL and DZ confirmed the authenticity of all the raw data. All authors read and approved the final version of the manuscript.

Ethics approval and consent to participate

The animal experiments were approved by the Institutional Animal Care and Use Committee of Nagasaki University (approval no. 1608251335-11) and all animal procedures were performed in accordance with institutional and national guidelines.

Patient consent for publication

Not applicable.

Competing interests

The authors declare that they have no competing interests.

References

1. Brabletz T, Lyden D, Steeg PS and Werb Z: Roadblocks to translational advances on metastasis research. Nat Med 19: 1104-1109, 2013.
2. Bregenzer ME, Horst EN, Mehta P, Novak CM, Repetto T and Mehta G: The role of cancer stem cells and mechanical forces in ovarian cancer metastasis. Cancers 11: 1008, 2019.
3. Eccles SA and Welch DR: Metastasis: Recent discoveries and novel treatment strategies. Lancet 369: 1742-1757, 2007.
4. Fidler IJ: The pathogenesis of cancer metastasis: The 'seed and soil' hypothesis revisited. Nat Rev Cancer 3: 453-458, 2003.
5. Zijl FV, Krupitza G and Mikulits W: Initial steps of metastasis: Cell invasion and endothelial transmigration. Mutat Res 728: 23-34, 2011.
6. Piskounova E, Agathocleous M, Murphy MM, Hu Z, Huddlestun SE, Zhao Z, Leitch AM, Johnson TM, DeBerardinis RJ and Morrison SJ: Oxidative stress inhibits distant metastasis by human melanoma cells. Nature 527: 186-191, 2015.
7. Vanharanta S and Massague J: Origins of metastatic traits. Cancer Cell 24: 410-421, 2013.
8. Kao YC, Jheng JR, Pan HJ, Liao WY, Lee CH and Kuo PL: Elevated hydrostatic pressure enhances the motility and enlarges the size of the lung cancer cells through aquaporin upregulation mediated by caveolin-1 and ERK1/2 signaling. Oncogene 36: 863-874, 2017.
9. Tse JM, Cheng G, Tyrrell JA, Wilcox-Adelman SA, Boucher Y, Jain RK and Munn LL: Mechanical compression drives cancer cells toward invasive phenotype. Proc Natl Acad Sci USA 109: 911-916, 2012.
10. Less JR, Posner MC, Boucher Y, Borochovitz D, Wolmark N and Jain RK: Interstitial hypertension in human breast and colorectal tumors. Cancer Res 52: 6371-6374, 1992.
11. Nathan SS, DiResta GR, Casas-Ganem JE, Hoang BH, Sowers R, Yang R, Huvos AG, Gorlick R and Healey JH: Elevated physiologic tumor pressure promotes proliferation and chemosensitivity in human osteosarcoma. Clin Cancer Res 11: 2389-2397, 2005.
12. Gutmann R, Leunig M, Feyh J, Goetz AE, Messmer K, Kastenbauer E and Jain RK: Interstitial hypertension in head and neck tumors in patients: Correlation with tumor size. Cancer Res 52: 1993-1995, 1992.
13. Solis AG, Bielecki P, Steach HR, Sharma L, Harman CC, Yun S, de Zoete MR, Warnock JN, To SDF, York AG, *et al*: Mechanosensation of cyclical force by PIEZO1 is essential for innate immunity. Nature 573: 69-74, 2019.
14. Rankin EB, Nam JM and Giaccia AJ: Hypoxia: Signaling the metastatic cascade. Trends Cancer 2: 295-304, 2016.
15. Semenza GL: Hypoxia-inducible factors in physiology and medicine. Cell 148: 399-408, 2012.
16. Semenza GL: Regulation of cancer cell metabolism by hypoxia-inducible factor 1. Semin Cancer Biol 19: 12-16, 2009.
17. Urata Y, Goto S, Luo L, Doi H, Kitajima Y, Masuda S, Ono Y and Li TS: Enhanced Nox1 expression and oxidative stress resistance in c-kit-positive hematopoietic stem/progenitor cells. Biochem Biophys Res Commun 454: 376-380, 2014.
18. Hu XQ, Song R and Zhang L: Effect of oxidative stress on the estrogen-NOS-NO-KCa channel pathway in uteroplacental dysfunction: Its implication in pregnancy complications. Oxid Med Cell Longev 2019: 9194269, 2019.
19. Novak S, Drenjancevic I, Vukovic R, Kellermayer Z, Cosic A, Tolusic Levak M, Balogh P, Culo F and Mihalj M: Anti-inflammatory effects of hyperbaric oxygenation during DSS-induced colitis in BALB/c mice include changes in gene expression of HIF-1α, proinflammatory cytokines, and antioxidative enzymes. Mediators Inflamm 2016: 7141430, 2016.
20. Jain RK, Martin JD and Stylianopoulos T: The role of mechanical forces in tumor growth and therapy. Annu Rev Biomed Eng 16: 321-346, 2014.
21. Senger DR, Galli SJ, Dvorak AM, Perruzzi CA, Harvey VS and Dvorak HF: Tumor cells secrete a vascular permeability factor that promotes accumulation of ascites fluid. Science 219: 983-985, 1983.
22. Liu YL, Horning AM, Lieberman B, Kim M, Lin CK, Hung CN, Chou CW, Wang CM, Lin CL, Kirma NB, *et al*: Spatial EGFR dynamics and metastatic phenotypes modulated by upregulated EphB2 and Src pathways in advanced prostate cancer. Cancers (Basel) 11: 1910, 2019.
23. Sato S, Vasaikar S, Eskaros A, Kim Y, Lewis JS, Zhang B, Zijlstra A and Weaver AM: EPHB2 carried on small extracellular vesicles induces tumor angiogenesis via activation of ephrin reverse signaling. JCI Insight 4: e132447, 2019.
24. Makaryan V, Zeidler C, Bolyard AA, Skokowa J, Rodger E, Kelley ML, Boxer LA, Bonilla MA, Newburger PE, Shimamura A, *et al*: The diversity of mutations and clinical outcomes for ELANE-associated neutropenia. Curr Opin Hematol 22: 3-11, 2015.
25. Nakashima R, Goto Y, Koyasu S, Kobayashi M, Morinibu A, Yoshimura M, Hiraoka M, Hammond EM and Harada H: UCHL1-HIF-1 axis-mediated antioxidant property of cancer cells as a therapeutic target for radiosensitization. Sci Rep 7: 6879, 2017.
26. Semenza GL: Pharmacologic targeting of hypoxia-inducible factors. Annu Rev Pharmacol Toxicol 59: 379-403, 2019.
27. Zhong H, De Marzo AM, Laughner E, Lim M, Hilton DA, Zagzag D, Buechler P, Isaacs WB, Semenza GL and Simons JW: Overexpression of hypoxia-inducible factor 1alpha in common human cancers and their metastases. Cancer Res 59: 5830-5835, 1999.
28. Talks KL, Turley H, Gatter KC, Maxwell PH, Pugh CW, Ratcliffe PJ and Harris AL: The expression and distribution of the hypoxia-inducible factors HIF-1alpha and HIF-2alpha in normal human tissues, cancers, and tumor-associated macrophages. Am J Pathol 157: 411-421, 2000.
29. Generali D, Berruti A, Brizzi MP, Campo L, Bonardi S, Wigfield S, Bersiga A, Allevi G, Milani M, Aguggini S, *et al*: Hypoxia-inducible factor-1alpha expression predicts a poor response to primary chemoendocrine therapy and disease-free survival in primary human breast cancer. Clin Cancer Res 12: 4562-4568, 2006.
30. Aebersold DM, Burri P, Beer KT, Laissue J, Djonov V, Greiner RH and Semenza GL: Expression of hypoxia-inducible factor-1alpha: A novel predictive and prognostic parameter in the radiotherapy of oropharyngeal cancer. Cancer Res 61: 2911-2916, 2001.
31. Nanni S, Benvenuti V, Grasselli A, Priolo C, Aiello A, Mattiussi S, Colussi C, Lirangi V, Illi B, D'Eletto M, *et al*: Endothelial NOS, estrogen receptor beta, and HIFs cooperate in the activation of a prognostic transcriptional pattern in aggressive human prostate cancer. J Clin Invest 119: 1093-1108, 2009.

32. Semenza GL: Defining the role of hypoxia-inducible factor 1 in cancer biology and therapeutics. Oncogene 29: 625-634, 2010.
33. Apte RS, Chen DS and Ferrara N: VEGF in signaling and disease: Beyond discovery and development. Cell 176: 1248-1264, 2019.
34. Dvorak HF: Vascular permeability factor/vascular endothelial growth factor: A critical cytokine in tumor angiogenesis and a potential target for diagnosis and therapy. J Clin Oncol 20: 4368-4380, 2002.
35. Kellar A, Egan C and Morris D: Preclinical murine models for lung cancer: Clinical trial applications. Biomed Res Int 2015: 621324, 2015.
36. Mori T, Koga T, Shibata H, Ikeda K, Shiraishi K, Suzuki M and Iyama K: Interstitial fluid pressure correlates clinicopathological factors of lung cancer. Ann Thorac Cardiovasc Surg 21: 201-208, 2015.

EXPERIMENTAL STUDY

Ex Vivo Hydrostatic Pressure Loading of Atrial Tissues Activates Profibrotic Transcription via TGF-β Signal Pathway

Xu Zhang,[1,2] Mhd, Yousuf Yassouf,[1,2], Kai Huang,[1,2], Yong Xu,[1,2], Zi-Sheng Huang,[1,2], Da Zhai,[1,2],
Reiko Sekiya,[1,2], Ke-Xiang Liu,[3] MD and Tao-Sheng Li,[1,2] MD

Summary

Excessive mechanical stress causes fibrosis-related atrial arrhythmia. Herein, we tried to investigate the mechanism of atrial fibrogenesis in response to mechanical stress by *ex vivo* approach. We collected atrial tissues from mice and then cultured them as "explants" under atmospheric pressure (AP group) or 50 mmHg hydrostatic pressure loading (HP group) conditions. Pathway-specific PCR array analysis on the expression of fibrosis-related genes indicated that the loading of atrial tissues to 50 mmHg for 24 hours extensively upregulated a series of profibrotic genes. qRT-PCR data also showed that loading atrial tissues to 50 mmHg enhanced *Rhoa, Rock2*, and *Thbs1* expression at different time points. Interestingly, the enhanced expression of *Thbs1* at 1 hour declined at 6-24 hours and then increased again at 72 hours. In contrast, an enhanced expression of *Tgfb1* was observed at 72 hours. In contrast, daily loading to 50 mmHg for 3 hours significantly accelerated the outgrowth of mesenchymal stem-like stromal cells from atrial tissues; however, we did not observe significant phenotypic changes in these outgrowing cells. Our *ex vivo* experimental data clearly show the induction of profibrotic transcription of atrial tissues by HP loading, which confirms the common pathological feature of atrial fibrosis following pressure overload.

(Int Heart J 2022; 63: 367-374)

Key words: Mechanical stress, Mechanotransduction, Fibrogenesis, Arrhythmia

Atrial arrhythmia, such as atrial fibrillation (AF), whose treatment remains thorny, is the most common rhythm disturbance encountered in the clinical setting.[1)] The most common pathogenesis of AF is atrial fibrosis. Many studies already reported that excessive mechanical stresses play critical role in atrial fibrosis development.[2-4)] Although various profibrotic signals, especially the transforming growth factor-β (TGF-β), can induce interstitial fibrogenesis, the question remains to further clarify the molecular and cellular mechanisms of atrial fibrosis in response to mechanical stresses.

Mechanotransduction, the process of cells that sense the mechanical force from the microenvironment through mechanosensing receptors and then translate mechanical stress into biochemical signals, plays vital roles in tissue cell homeostasis and pathology, such as fibrogenesis.[5)] TGF-β signaling pathway is the core in mechanotransduction of cardiac fibrosis. Additionally, as an essential signal isoform, TGF-β_1 induces the expression of profibrotic genes through the canonical signaling pathway with activation of Smad2/3, or through noncanonical signaling pathways with activation of RhoA and its downstream kinase ROCK.[6)] As a multicomponent target, RhoA/ROCK signaling is known to involve in cardiac fibrosis.[7)] Thrombospondin-1 (TSP-1), another member of the TGF-β superfamily, can also be excessively induced in response to various stresses or tissue damage.[8)]

Mechanical stresses modulate many aspects of cell function, such as proliferation and differentiation, from single cells to pattern formation in whole organisms.[9)] Stromal cells within the defined tissues/organs are known to be the key player of fibrogenesis. Using a mouse unilateral ureteral obstruction model, we recently demonstrated that renal stromal cells shift to profibrogenic phenotype.[10)] Thus, we reasonably speculate the fibrotic phenotypic shifting of atrial stromal cells in response to excessive mechanical stresses, but direct experimental evidence is needed.

By *ex vivo* loading mouse atrial tissues to 50 mmHg HP, a kind of mechanical compressive stresses, we investigated the dynamic changes on the expression of fibrosis-related genes and the biological properties of stromal

---

From the [1]Department of Stem Cell Biology, Nagasaki University Graduate School of Biomedical Sciences, Nagasaki, Japan, [2]Department of Stem Cell Biology, Atomic Bomb Disease Institute, Nagasaki University, Nagasaki, Japan and [3]Department of Cardiovascular Surgery, The Second Hospital of Jilin University, Jilin, China.

This study was mainly supported by a Grant-in-Aid for the Ministry of Education, Science, Sports, Culture and Technology of Japan and the Collaborative Research Program of the Atomic Bomb Disease Institute of Nagasaki University.

Address for correspondence: Tao-Sheng Li, MD, Department of Stem Cell Biology, Atomic Bomb Disease Institute, Nagasaki University, 1-12-4 Sakamoto, Nagasaki, Nagasaki 852-8523, Japan. E-mail: litaoshe@nagasaki-u.ac.jp

Received for publication August 10, 2021. Revised and accepted November 8, 2021.

doi: 10.1536/ihj.21-481

cells.

Methods

Experimental animals: C57BL/6 male mice (9-12 weeks old, CLEA, Japan) were used in this study. All experiments were approved by the Institutional Animal Care and Use Committee of Nagasaki University (No.1608251335-9), and animal procedures were performed following institutional and national guidelines.

***Ex vivo* culture of atrial tissues as "explants":** The *ex vivo* culture of atrial tissues as "explants" was performed as described previously,[11] with a few modifications. Briefly, mice were administered general anesthesia by an intraperitoneal injection of mixed anesthetic (0.75 mg/kg medetomidine, 4 mg/kg midazolam, 5 mg/kg butorphanol). Next, atrial tissues were collected into 6-cm dishes with 2 mL PBS and then minced into small fragments (almost 1 mm × 1 mm) using a surgical knife under zoom stereomicroscope (Olympus SZ61). Then, the minced tissue fragments were moved onto 6-cm culture dishes coated with 15 ug/mL fibronectin (CORNING) for culturing as "explants." We used Iscove's Modified Dulbecco's Medium with the supplement of 10% fetal bovine serum (HyClone, Thermo Scientific), 1% penicillin/streptomycin (Wako), and all culture was performed at 37°C in a humidified incubator under 5% CO_2 and 95% air.

Hydrostatic pressure loading: We loaded the atrial "explants" to 50 mmHg hydrostatic pressure (HP group), by using a set of commercial devices (STREX, Inc.). Of which, gas from the incubator flowed continuously into a closed container to keep the HP at 50 mmHg while maintaining the same temperature, humidity, and CO_2 level as the incubator. As a control, the atrial "explants" were kept in a common CO_2 incubator with AP.

Mouse fibrotic pathway-specific PCR array analysis: To compare the expression of fibrosis-related genes between HP and AP groups, we mixed an equal amount of RNA from three independent mice atrial tissue samples of each group for PCR array analysis. Briefly, total RNA was purified by using Quick-RNA™ Microprep Kit (ZYMO RESEARCH). The RNA concentration was determined using a NanoDrop 2000 spectrophotometer (Thermo Fisher Scientific), and 1 ug of RNA was used to generate cDNA using the RT^2 First Strand Kit (Qiagen). The mouse fibrosis RT^2 Profiler PCR array was performed according to the manufacturer's instructions (#330231 PAMM-120ZA, Qiagen). This PCR array profiles 84 key genes involved in dysregulated tissue remodeling during the repair and healing of wounds. Roche®LightCycler®480 was used to performing the PCR procedure. Qiagen's online web analysis tool was utilized to analyze the data. *B2m* and *Hsp90ab1* were used as reference genes. The fold changes of gene expression were calculated by determining the ratio of HP group to AP group.

***qRT-PCR*:** To investigate the time-course dynamics of the transcription on *Rhoa, Rock1, Rock2*, *Tgfb1*, and *Thbs1* in atrial tissues following HP loading, we collected atrial "explants" at 1, 6, 24, and 72 hours (n = 3, at each time point for both groups) after the initiation of culture, and we purified total RNA as described above. For qRT-PCR, the first-strand cDNA was synthesized with SuperScript™ VILO™ MasterMix (Invitrogen) according to the manufacturer's recommendations, and the RT-PCR was performed using THUNDERBIRD®SYBR®qPCR MIX (TOYOBO) with the CFX96™ Real Time System (BIO-RAD). The gene expression was normalized by housekeeping gene *B2m*. Primers used for qPCR were the following: *Rhoa* (Forward: 5'- AGC TTG TGG TAA GAC ATG CTT G -3', Reverse:5'- GTG TCC CAT AAA GCC AAC TCT AC -3'); *Rock1* (Forward: 5'- AGC TTT TGT TGG CAA TCA GC -3', Reverse:5'- ACT TTC CTG CAA GCT TTT ATC CA -3'); *Rock2* (Forward: 5'- CAG TCC CTG GGT AGT TCA GC -3', Reverse:5'- GCC TGG CAT ATA CTC CAT C -3'); *Tgfb1* (Forward:5'-CTG CGC TTG CAG AGA TTA AA-3', Reverse:5'-GAA AGC CCT GTA TTC CGT CT-3'); *Thbs1* (Forward:5'-GGA ACG GAA AGA CAA CAC TG-3', Reverse:5'-AGT TGA GCC CGG TCC TCT TG-3').

Monitoring the outgrowth of stromal cells from atrial tissues: To further investigate the effect of HP loading on stromal cells, atrial tissues from mice were collected into 6-cm dish and minced into small fragments as described above. Then, the minced tissue fragments were randomly moved onto fibronectin-coated 6-cm dishes (a total of 40 pieces of minced tissue fragments/dish) and then cultured as "explants" with daily loading to 50 mmHg for 3 hours (HP group) or without pressure loading (AP group). The outgrowth of stromal cells from atrial "explants" was observed every other day, and we counted the number of "explants" with cell outgrowth at different time points (Supplemental Table I). The number of "explants" with cell outgrowth was divided by the total number of seeded "explants" at each time point, and then, the percentiles were used to draw the cell growth curves. Next, we collected the outgrowth cells at 12 days after the initiation of culture, and the total number of outgrowth cells was counted using a NucleoCounter cell-counting device (ChemoMetecA/S, Denmark). Three independent experiments were performed (n = 3 for both AP and HP groups).

Immunofluorescence staining: We also investigated the expression of CD105, CD90, and α-SMA in the outgrowth cells by immunofluorescence staining as described previously.[10] Briefly, the first-passaged outgrowth cells were cultured in 8-well chamber slides (1×10^4 /well, Lab-Tek, Thermo Scientific Nunc) coated with 15 ug/mL fibronectin (CORNING). Next, the cells were fixed with 4% paraformaldehyde phosphate buffer solution (Wako). After blocking, the cells were incubated with rabbit anti-mouse CD90 antibody (1:50 dilution, Abcam), rabbit anti-mouse CD105 antibody (1:50 dilution, Abcam), or rabbit antimouse α-SMA antibody (1:100 dilution, Abcam), respectively. Positive staining was detected using Alexa Fluorescent 546 goat antirabbit Ig (1:400 dilution, Dako) secondary antibody. The nuclei were stained with 4',6-diamidino-2-phenylindole (DAPI, Thermo Scientific). The immunofluorescence was examined under a microscope (FV10CW3, Olympus). We counted the positively stained cells or measured mean intensity in ten images of each experiment. The percentage of positive cells or mean intensity from three independent experiments was used for

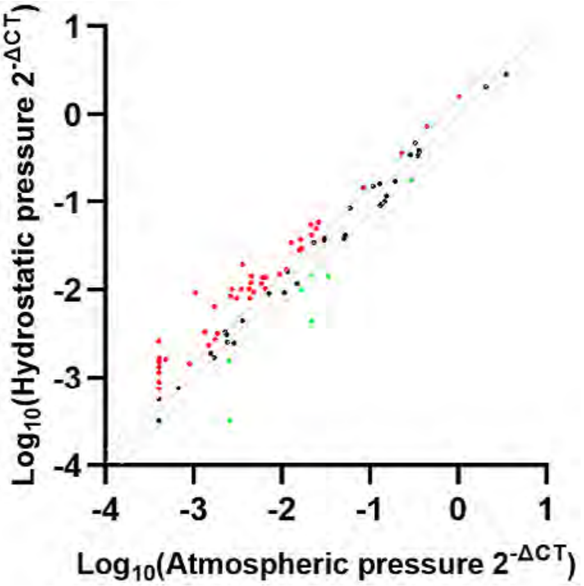

Figure 1. PCR array analysis on the expression of fibrosis-related genes in atrial tissues after 24 hours culture under 50 mmHg HP and AP. The scatter plots describe the relative expression between groups. Genes with more than 1.5-fold upregulation (red dots) and downregulation (green dots) are highlighted.

statistical analysis.

Statistical analysis: All the values were presented as the mean ± SD. For comparison of multiple sets of data, one-way analysis of variance followed by Tukey's test (Dr. SPSS II, Chicago, IL) was used for statistical analyses. For comparison of two sets of data, unpaired two-tailed t-test was used for statistical analyses. All analyses were carried out with the SPSS19.0 statistical software (IBM SPSS Co., USA). A *P*-value of less than 0.05 was accepted as significant.

Results

Loading the atrial tissues to 50 mmHg prevalently upregulated the expression of profibrotic genes: We first screened the overall changes in the expression of fibrosis-related genes in atrial "explants" loaded with 50 mmHg HP using the mouse RT^2 Profiler PCR array (Supplemental Table II). A scatter plot showed that 24 hours loading of atrial tissues to 50 mmHg upregulated many fibrosis-related genes by more than 1.5-fold (Figure 1), although a few genes showed a downregulation by more than 1.5-fold. We further categorized these genes according to their biological functions (Figure 2A) and noticed that these genes that functionally related to the ECM and cell adhesion molecules (Figure 2B), Inflammatory cytokines and chemokines (Figure 2C), TGF-β superfamily members (Figure 2D), Transcription factors (Figure 2E), and growth factors (Figure 2F) were widely upregulated.

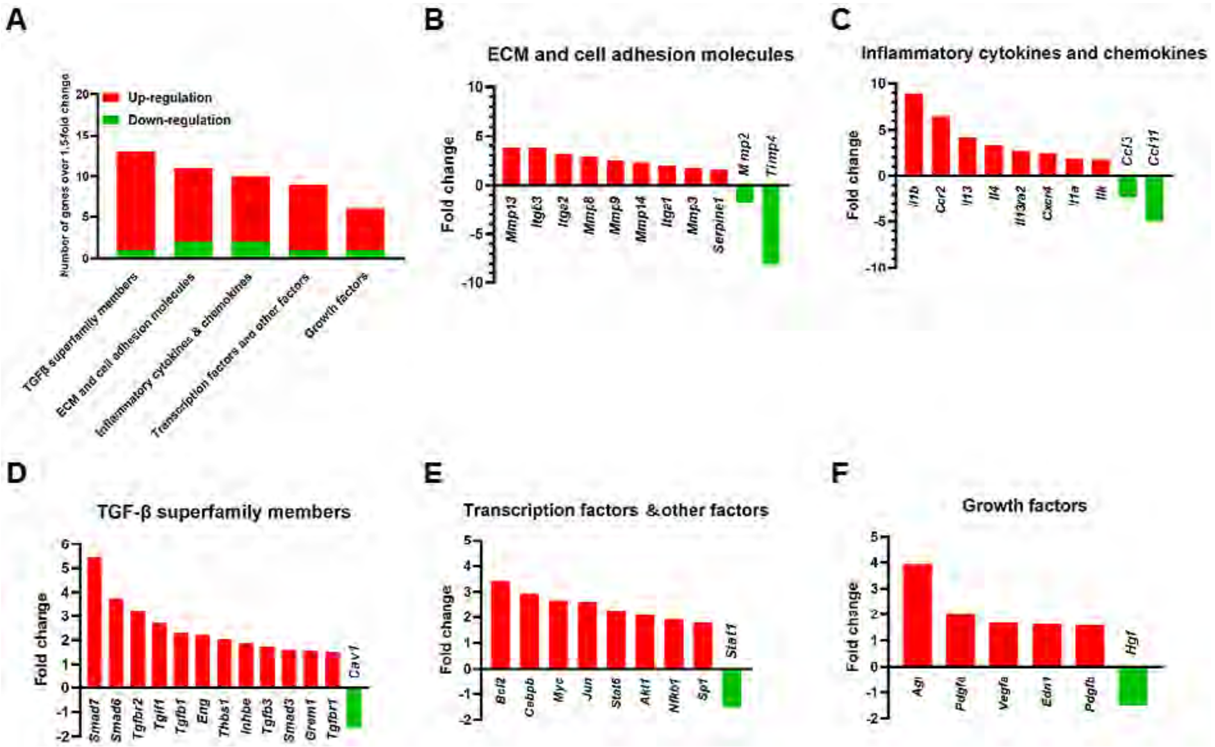

Figure 2. The functional categorization on the fibrosis-related genes included in PCR array analysis. **A:** The number of genes that upregulated and downregulated over 1.5-fold in atrial tissues after 24 hours culture under 50 mmHg HP. **B-F:** Data are also presented by dividing these genes into different categorizations according to their biological functions. Fold change of each gene functionally belongs to ECM and cell adhesion molecules (**B**), inflammatory cytokines and chemokines (**C**), TGF-β superfamily members (**D**), transcription factors (**E**), and growth factors (**F**).

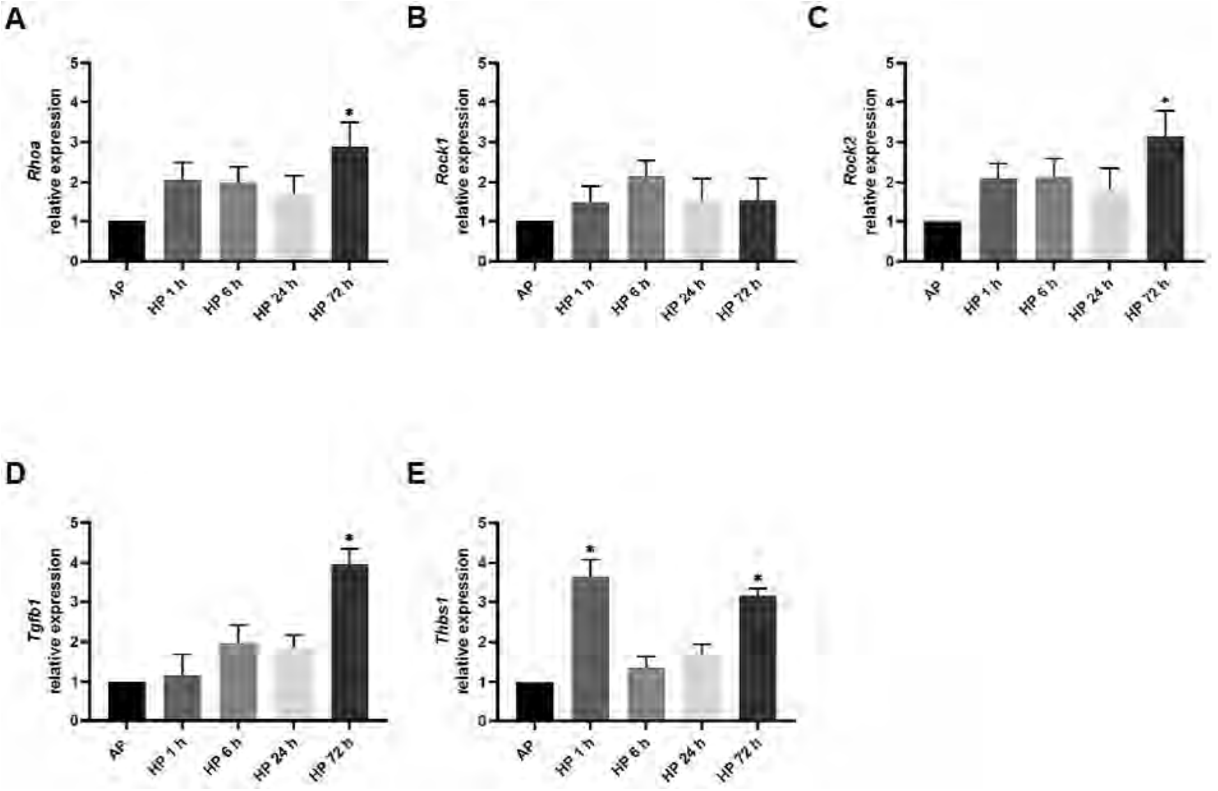

Figure 3. Time-course dynamics on the expression of *Rhoa*, *Rock1*, *Rock2*, *Tgfb1*, and *Thbs1* in atrial tissues followed by *ex vivo* loading to 50 mmHg HP. Quantitative RT-PCR data shows the relative expression of *Rhoa* (**A**), *Rock1* (**B**), *Rock2* (**C**), *Tgfb1* (**D**), and *Thbs1* (**E**) at 0, 1, 6, 24, 72 hours after culture. Data are represented by three independent experiments at each time point. $^*P < 0.01$ versus AP group. AP indicates atmosphere pressure; and HP, hydrostatic pressure.

Loading the atrial tissues to 50 mmHg activated the TGF-β signaling pathway: Based on the changes of the PCR fibrosis array, we found that TGF-β is the most affected pathway; thus, we tried to check the dynamics of mechanotransduction in response to HP through this pathway. We loaded the atrial tissues with either 0 or 50 mmHg for 1, 6, 24, and 72 hours. Then, we evaluated the gene expression of *Rhoa*, *Rock1*, *Rock2*, *Tgfb1*, and *Thbs1* at each time point. Our qRT-PCR data showed that, as a mechanosensitive multicomponent target of TGF-β noncanonical signaling pathways, the expression of *Rhoa* and *Rock2* was significantly enhanced at 72 hours by 50 mmHg loading ($P < 0.01$, Figure 3A, C). However, as another downstream target of *Rhoa*, the expression of *Rock1* was not changed much at any time point following 50 mmHg loading (Figure 3B). Interestingly, the expression of *Thbs1* was quickly induced at 1 hour, but it declined at 6-24 hours, and then increased again at 72 hours after 50 mmHg loading (Figure 3E). In contrast, the expression of *Tgfb1* was not induced at the early time windows, but it was robustly enhanced at 72 hours after 50 mmHg loading ($P < 0.01$, Figure 3D).

Daily loading of the atrial tissues to 50 mmHg accelerated the outgrowth of stromal cells: The outgrowth of fibroblast-like stromal cells from atrial "explants" was observed mostly at 3-5 days after the initiation of culture, but the outgrowth cells from some "explants" in the HP group could be observed even at the second day of culture (Figure 4A). By plotting the percentiles of "explants" with cell outgrowth, we found that the cell outgrowth from "explants" was significantly earlier in HP group than AP group (Figure 4B). Next, we harvested all the outgrowth cells 12 days after the initiation of culture, and the total number of outgrowth cells was also significantly increased by daily loading the atrial tissue to 50 mmHg for 3 hours ($P = 0.03$, Figure 4C).

Further, we investigated the phenotypic characteristics of these cells that outgrew from atrial "explants" by immunostaining on the expression of CD90, CD105, and α-SMA (Figure 5). Extensive expression of CD90 and CD105 (almost 90%) was observed in these outgrowth cells (Figure 5A, B), suggesting a mesenchymal stem cell-like phenotype. Although the expression of α-SMA tended to slightly increase in these outgrowth cells from the HP group, no significant difference was found between groups ($P = 0.07$, Figure 5C).

Discussion

Clinical practice and animal experiments indicate that pressure overload-induced atrial fibrosis and remodeling play a vital role in the pathology of rhythm disturbance.[12) In addition to endothelial cells undergoing additional shear stress, cardiac tissue is mainly exposed to mechani-

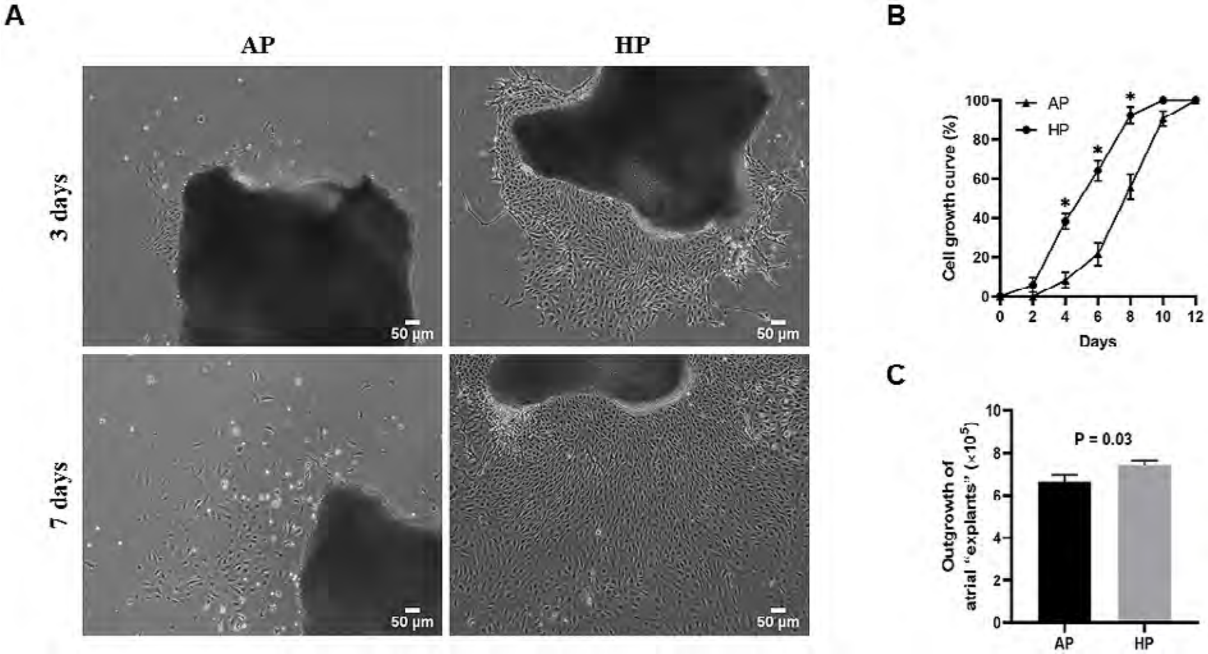

Figure 4. The outgrowth of stromal cells from atrial tissues with daily *ex vivo* loading to 50 mmHg HP for 3 hours. **A:** Representative images show the cells outgrowing from the atrial "explants" at 3 and 7 days after initiation of culture. **B:** The curve lines appear the percentiles of "explants" with cell outgrowing at different time points after the initiation of culture. **C:** The total number of outgrowth cells harvested at 12 days after the initiation of culture. Data are represented by three independent experiments. *$P < 0.05$ versus AP group. AP indicates atmospheric pressure; and HP, hydrostatic pressure.

cal compression stress. It is well known that mechanical stretch induces profibrotic fibroblast phenotypes, which is thought to promote the development of AF.[13,14] Recent studies also showed that HP involves in atrial remodeling.[15,16] However, the molecular and cellular mechanisms of atrial fibrosis in response to HP have not yet been well understood.

By *ex vivo* loading the atrial tissues from healthy mice to 50 mmHg HP, we confirmed the extensive enhancement on the expression of profibrotic genes. We further functionally classified these genes according to RT^2 Profiler PCR array manufacturer's instructions. Among these genes associated with ECM and cell adhesion molecules, the most upregulated genes were integrin and matrix metalloproteinase (MMP) family members. Indeed, previous studies showed that mechanical stress increases the mechanosensitive integrin subunit and induces the expression of *Mmp8, Mmp9*, and *Mmp13* in fibroblasts.[17-19] Mechanical stress can also induce the expression of transcription factors associated with inflammatory response and tissue remodeling, such as *Myc, Jun, Nfκb*.[20,21] Coincidentally, the loading of atrial tissues to HP also enhanced the expression of many transcription factors known as the master regulators of inflammatory cytokines and growth factors in our study. A computer biology model applied in a recent study demonstrated that the mechanosignaling network in the heart can be started from the mechanosensing step by several mechanosensors, such as integrin and angiotensin receptor, then induces the activation of multiple signaling cascades, such as TGF-β and RhoA/ROCK pathway, and finally alters the transcription of related genes to induce remodeling.[22]

TGF-β signal pathway is considered as the core in mechanotransduction of fibrogenesis in response to pressure overload to the heart. As an important signal isoform, TGF-β_1 can trigger the activation of cardiac fibroblasts, induce profibrotic genes through the canonical signaling pathway with activation of Smad2/3, or the noncanonical signaling pathways with activation of Rho/ROCK.[6] Recent studies further demonstrated that intermittent compressive force induces TGF-β_1 expression in human periodontal fibroblasts.[23,24] As a branch of TGF-β noncanonical signaling pathways, Rho/ROCK signaling plays a crucial role in various cellular processes, such as cell proliferation and migration. ROCK2 is known to be involved in angiotensin II-induced cardiac hypertrophy, and ROCK2-deficient mice are resistant to pressure overload-induced cardiac hypertrophy.[26,27] Moreover, a recent study further demonstrated that specific ROCK2 deficiency in cardiac fibroblasts protects the heart from angiotensin II-induced cardiac fibrosis.[28] Consistent with these previous studies, our data supported the mechanotransductive role of RhoA/ROCK2 in cardiac fibrosis. Although it has also been reported that the potential role of ROCK1 in the heart in response to mechanical stress,[29] we did not find the induction of ROCK1 in atrial tissues by *ex vivo* loading to 50 mmHg within 72 hours follow-up. We speculate that the mechanical stress threshold may be higher for inducing ROCK1 compared to ROCK2.

TSP-1, a mechanosensitive multi-functional matricellular protein of the TGF-β superfamily, has been identified to play a major role in cardiac fibrosis, mainly by ac-

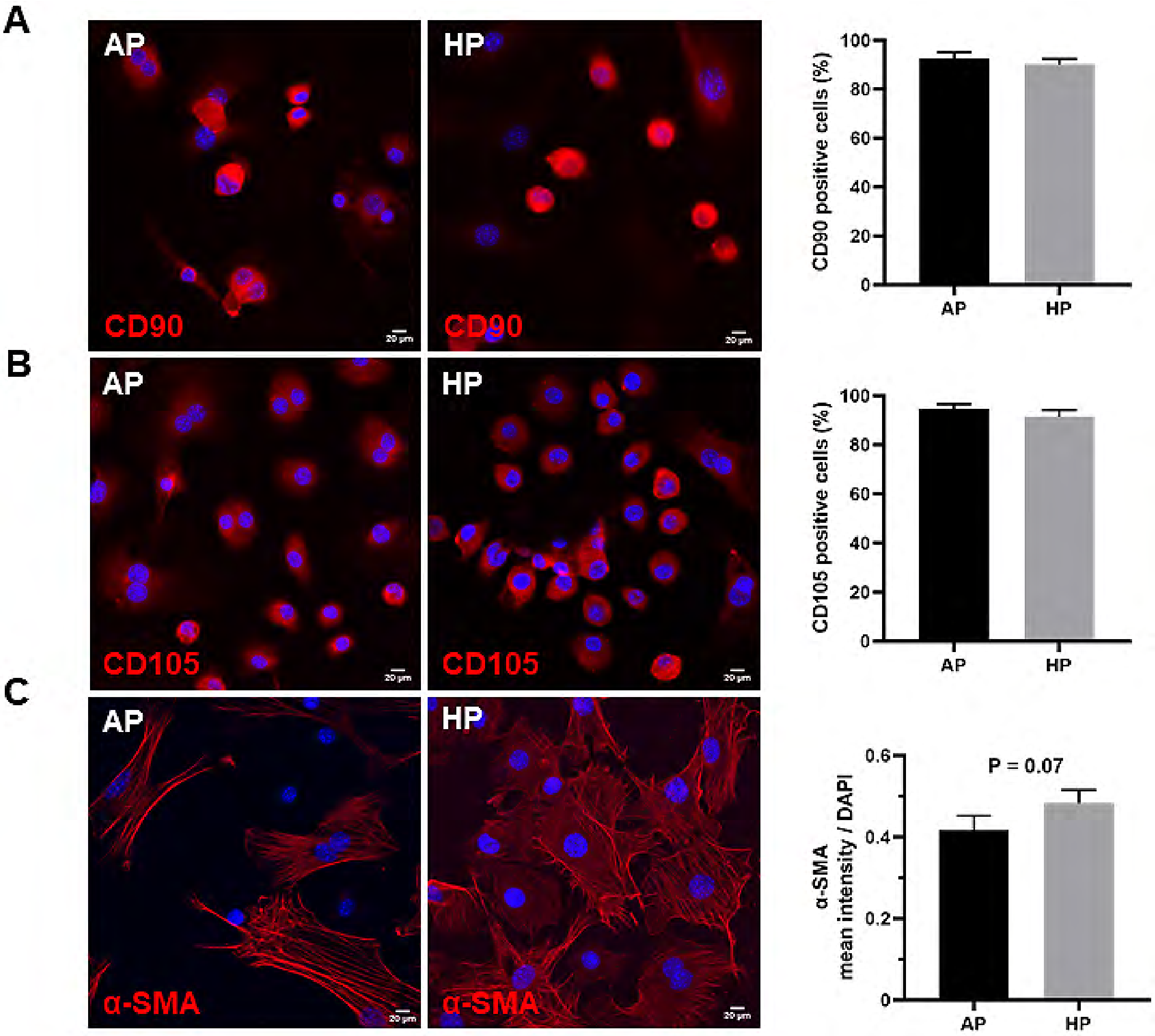

Figure 5. Immunocytochemical analysis on the expression of CD90, CD105, and α-SMA in the outgrowth cells. Representative images (left) and quantitative bar graph data (right) show the expression of CD90 (**A**), CD105 (**B**), and α-SMA (**C**) in the outgrowth cells from atrial "explants." Scale bar: 20 μm. AP indicates atmospheric pressure; and HP, hydrostatic pressure.

tivating the TGF-β isoforms, which in turn induces TSP-1 expression.[30-32] A recent study in mice demonstrated that TSP-1 deletion leads to the maladaptive remodeling of the aorta in response to pressure overload,[33] suggesting the protective role of TSP-1 in response to mechanical stress. Interestingly, our data showed that *ex vivo* loading atrial tissues to 50 mmHg quickly induced the expression of *Thbs1*; however, the expression of *Thbs1* increased again at 72 hours after the loading to 50 mmHg. The biphasic changes of TSP-1 in response to mechanical stress may represent dual roles of TSP-1 in the heart. In other words, instead of the cardioprotection about the increased TSP-1 soon after suffering from mechanical stresses, a delayed increase of TSP-1 may promote fibrogenesis in the heart with a persistent pressure overload. As we purified total RNA from the outgrowth cells together with the "explants" for the qRT-PCR analysis, data from our study reflected the comprehensive response of atrial tissues to HP.

Stromal cells, such as fibroblasts, within the defined tissues/organs, are known to be the key player of fibrogenesis. A recent study demonstrated that the increased stretch force or matrix stiffness promotes the proliferation and activation of cardiac fibroblasts.[14] Based on our observative data, HP loading accelerated the cell outgrow from "explants" (Figure 3B) and increased the yield of outgrowth cells (Figure 4C), suggesting the potential role of stromal cells in the atrial fibrosis in response to pressure overload. Although we did not further evaluate the regulatory role of RhoA, Rocks, and TSP-1 on outgrowth cells at a protein level, the upregulated mRNA expression suggests the probable role on the proliferation, migration, and other biological characteristics of resident stromal cells in response to HP.

We previously reported that cardiac-derived mesenchymal stem-like cells positively express CD90 and CD105, two markers commonly used for detecting mesenchymal stem stromal cells.[34] The extensive expression of CD105 and CD90 in these outgrowth cells suggests the mesenchymal stem-like cell characteristics. Although researchers previously reported the heterogeneity on the expression of CD90 in cardiac-derived stromal cells from human beings,[35] HP loading barely changed the expression of CD90 and CD105 in outgrowth cells in this study. As we did not evaluate the proliferative activity in this study, whether HP loading could change the proliferation of stromal cells is kept unknown. Researchers recently reported that the exposure of human cardiac fibroblasts to 200 mmHg for 8 hours significantly suppresses α-SMA expression.[36] Unexpectedly, as a typical marker of myofibroblasts, the expression of α-SMA was not significantly induced in response to loading of atrial tissues to 50 mmHg. The magnitude and duration of HP and the difference in experimental methods might affect the phenotypic shift of stromal cells.

This study exhibits some limitations. First, PCR array analysis was performed only once by using a mixture of RNA from three independent samples. Second, due to the tiny size of mouse atrial tissues, we could not collect enough protein to perform Western blotting analysis for further confirming the relevant molecular mechanism on our findings. Third, we only used 50 mmHg HP for all experiments, and optimizing the experimental conditions in future studies is necessary.

Conclusion

Our data showed the induction of profibrotic transcription of atrial tissues by HP loading, likely by activating TGF-β signal pathway and stromal cells. Data from the *ex vivo* experimental approach provided indirect evidence on the common pathological features of atrial fibrosis following pressure overload.

Disclosure

Conflicts of interest: The authors declare no competing financial interests.

References

1. Kirchhof P. The future of atrial fibrillation management: Integrated care and stratified therapy. Lancet 2017; 390: 1873-87.
2. Travers JG, Kamal FA, Robbins J, Yutzey KE, Blaxall BC. Cardiac fibrosis: The fibroblast awakens. Circ Res 2016; 118: 1021-40.
3. Creemers EE, Pinto YM. Molecular mechanisms that control interstitial fibrosis in the pressure-overloaded heart. Cardiovasc Res 2011; 89: 265-72.
4. Yuan J, Liu H, Gao W, *et al*. MicroRNA-378 suppresses myocardial fibrosis through a paracrine mechanism at the early stage of cardiac hypertrophy following mechanical stress. Theranostics 2018; 8: 2565-82.
5. Romani P, Valcarcel-Jimenez L, Frezza C, Dupont S. Crosstalk between mechanotransduction and metabolism. Nat Rev Mol Cell Biol 2021; 22: 22-38.
6. Dobaczewski M, Chen W, Frangogiannis NG. Transforming growth factor (TGF)-beta signaling in cardiac remodeling. J Mol Cell Cardiol 2011; 51: 600-6.
7. Shimizu T, Liao JK. Rho kinases and cardiac remodeling. Circ J 2016; 80: 1491-8.
8. Yamashiro Y, Thang BQ, Shin SJ, *et al*. Role of Thrombospondin-1 in mechanotransduction and development of thoracic aortic aneurysm in mouse and humans. Circ Res 2018; 123: 660-72.
9. Mennens SFB, van den Dries K, Cambi A. Role for mechanotransduction in macrophage and dendritic cell immunobiology. Results Probl Cell Differ 2017; 62: 209-42.
10. Peng YH, Xiao J, Yan C, Luo L, Li TS. Potential role of the resident mesenchymal stem-like cells in renal fibrogenesis after ureteral obstruction. Stem Cells Int 2019; 2019: 2543171.
11. Luo L, Yan C, Urata Y, *et al*. Dose-dependency and reversibility of radiation-induced injury in cardiac explant-derived cells of mice. Sci Rep 2017; 7: 40959.
12. Saucerman JJ, Tan PM, Buchholz KS, McCulloch AD, Omens JH. Mechanical regulation of gene expression in cardiac myocytes and fibroblasts. Nat Rev Cardiol 2019; 16: 361-78.
13. Yoshida K, Ulfarsson M, Oral H, *et al*. Left atrial pressure and dominant frequency of atrial fibrillation in humans. Heart Rhythm 2011; 8: 181-7.
14. Herum KM, Choppe J, Kumar A, Engler AJ, McCulloch AD. Mechanical regulation of cardiac fibroblast profibrotic phenotypes. Mol Biol Cell 2017; 28: 1871-82.
15. Wei W, Rao F, Liu F, *et al*. Involvement of Smad3 pathway in atrial fibrosis induced by elevated hydrostatic pressure. J Cell Physiol 2018; 233: 4981-9.
16. Li X, Deng CY, Xue YM, *et al*. High hydrostatic pressure induces atrial electrical remodeling through angiotensin upregulation mediating FAK/Src pathway activation. J Mol Cell Cardiol 2020; 140: 10-21.
17. Hannafin JA, Attia EA, Henshaw R, Warren RF, Bhargava MM. Effect of cyclic strain and plating matrix on cell proliferation and integrin expression by ligament fibroblasts. J Orthop Res 2006; 24: 149-58.
18. Takahashi I, Nishimura M, Onodera K, *et al*. Expression of MMP-8 and MMP-13 genes in the periodontal ligament during tooth movement in rats. J Dent Res 2003; 82: 646-51.
19. Fujisawa T, Hattori T, Takahashi K, Kuboki T, Yamashita A, Takigawa M. Cyclic mechanical stress induces extracellular matrix degradation in cultured chondrocytes via gene expression of matrix metalloproteinases and interleukin-1. J Biochem 1999; 125: 966-75.
20. Olson AK, Ledee D, Iwamoto K, *et al*. C-Myc induced compensated cardiac hypertrophy increases free fatty acid utilization for the citric acid cycle. J Mol Cell Cardiol 2013; 55: 156-64.
21. Manabe I, Shindo T, Nagai R. Gene expression in fibroblasts and fibrosis: Involvement in cardiac hypertrophy. Circ Res 2002; 91: 1103-13.
22. Tan PM, Buchholz KS, Omens JH, McCulloch AD, Saucerman JJ. Predictive model identifies key network regulators of cardiomyocyte mechano-signaling. PLoS Comput Biol 2017; 13: e1005854.
23. Manokawinchoke J, Pavasant P, Sawangmake C, *et al*. Intermittent compressive force promotes osteogenic differentiation in human periodontal ligament cells by regulating the transforming growth factor-beta pathway. Cell Death Dis 2019; 10: 761.
24. Manokawinchoke J, Limjeerajarus N, Limjeerajarus C, Sastravaha P, Everts V, Pavasant P. Mechanical force-induced TGFB1 increases expression of SOST/POSTN by hPDL cells. J Dent Res 2015; 94: 983-9.
25. Burridge K, Monaghan-Benson E, Graham DM. Mechanotransduction: From the cell surface to the nucleus via RhoA. Philos Trans R Soc Lond B Biol Sci 2019; 374: 20180229.
26. Sunamura S, Satoh K, Kurosawa R, *et al*. Different roles of myocardial ROCK1 and ROCK2 in cardiac dysfunction and postcapillary pulmonary hypertension in mice. Proc Natl Acad Sci USA 2018; 115: E7129-38.
27. Okamoto R, Li Y, Noma K, *et al*. FHL2 prevents cardiac hypertrophy in mice with cardiac-specific deletion of ROCK2.

FASEB J 2013; 27: 1439-49.

28. Shimizu T, Narang N, Chen P, *et al*. Fibroblast deletion of ROCK2 attenuates cardiac hypertrophy, fibrosis, and diastolic dysfunction. JCI Insight 2017; 2: e93187.
29. Zhang YM, Bo J, Taffet GE, *et al*. Targeted deletion of ROCK1 protects the heart against pressure overload by inhibiting reactive fibrosis. FASEB J 2006; 20: 916-25.
30. Murphy-Ullrich JE, Suto MJ. Thrombospondin-1 regulation of latent TGF-beta activation: A therapeutic target for fibrotic disease. Matrix Biol 2018; 68: 28-43.
31. Krishna SM, Golledge J. The role of thrombospondin-1 in cardiovascular health and pathology. Int J Cardiol 2013; 168: 692-706.
32. Zhao C, Isenberg JS, Popel AS. Transcriptional and post-transcriptional regulation of Thrombospondin-1 expression: A computational model. PLOS Comput Biol 2017; 13: e1005272.
33. Yamashiro Y, Thang BQ, Ramirez K, *et al*. Matrix mechanotransduction mediated by thrombospondin-1/integrin/YAP in the vascular remodeling. Proc Natl Acad Sci USA 2020; 117: 9896-905.
34. Li TS, Cheng K, Malliaras K, *et al*. Direct comparison of different stem cell types and subpopulations reveals superior paracrine potency and myocardial repair efficacy with cardiosphere-derived cells. J Am Coll Cardiol 2012; 59: 942-53.
35. Cheng K, Malliaras K, Smith RR, *et al*. Human cardiosphere-derived cells from advanced heart failure patients exhibit augmented functional potency in myocardial repair. JACC Heart Fail 2014; 2: 49-61.
36. Tanaka R, Umemura M, Narikawa M, *et al*. Hydrostatic pressure suppresses fibrotic changes via Akt/GSK-3 signaling in human cardiac fibroblasts. Physiol Rep 2018; 6: e13687.

Supplemental Files

Supplemental Tables I, II

Please see supplemental files; https://doi.org/10.1536/ihj.21-481

日中笹川医学奨学金制度＜学位取得コース＞評価書
課程博士：指導教官用

Supported by 日本財団 THE NIPPON FOUNDATION

第44期　研究者番号：G4411　作成日　：2024年3月　11日

氏　名	李 佩霖	LI PEILIN	性別	M	生年月日　1994/08/21

所属機関（役職）	長崎大学大学院医歯薬学総合研究科（大学院生）
研究先（指導教官）	長崎大学大学院医歯薬学総合研究科医療学専攻移植・消化器外科学（江口 晋　教授）
研究テーマ	小分子誘導肝前駆細胞（CLiP）からの3D胆管形成 3D bile duct formation from small molecule induced liver progenitor cells(CLiPs)
専攻種別	□論文博士　☑課程博士

研究者評価（指導教官記入欄）

成績状況	優　良　可　不可 学業成績係数=	取得単位数 取得単位数／取得すべき単位総数 27
学生本人が行った研究の概要	He mainly conducted research on chemically induced bile duct differentiation of liver progenitor cells. Liver cells isolated from human liver have bidirectional differentiation potential after reprogramming with a combination of chemical molecules. Using this progenitor cell for differentiation, the bile duct system was established in vitro, and combined with mature liver cells, the in vitro bile duct-hepatocyte system was established, which can be used for in vitro drug and metabolic analysis. In addition, the other studies include the generation of the hepatobiliary organoids in vitro, pharmacological treatment of small intestinal drug injury, and the use of hepatobiliary organoids for microplastic metabolic analysis.	
総合評価	【良かった点】 He works hard in research and could conduct multiple studies well, discovering problems and solving them in his research. 【改善すべき点】 Communicate more and improve Japanese. 【今後の展望】 I hope him to achieve better results in research and learn more skills in clinical practice after graduation.	
学位取得見込	He could get the Ph. D degree in Sep. 2024 and graduate earlier.	

評価者（指導教官名）　Susumu Eguchi, MD, PhD

日中笹川医学奨学金制度＜学位取得コース＞報告書
研究者用

Supported by 日本財団 THE NIPPON FOUNDATION

第44期　研究者番号：G4411　作成日：2024年3月 02 日

氏名	李 佩霖	LI PEILIN	性別	M	生年月日 1994/08/21
所属機関(役職)	長崎大学大学院医歯薬学総合研究科(大学院生)				
研究先(指導教官)	長崎大学大学院医歯薬学総合研究科医療学専攻移植・消化器外科学(江口 晋 教授)				
研究テーマ	小分子誘導肝前駆細胞(CLiP)からの3D胆管形成 3D bile duct formation from small molecule induced liver progenitor cells(CLiPs)				
専攻種別	論文博士	□	課程博士	☑	

1. 研究概要(1)

1)目的(Goal)

2)戦略(Approach)

3)材料と方法(Materials and methods)

4)実験結果(Results)

5)考察(Discussion)

6)参考文献(References)

1. Purpose:
To form the three-dimensional bile duct structure and integrated duct-hepatocyte tissue from human CLiPs.

2. Backgrounds:
The integrity of liver cell function depends on the integrity of the total triad. Portal triads are composed of three major tubes. Branches of the hepatic artery carry oxygenated blood to the hepatocytes, while branches of the portal vein carry blood with nutrients from the small intestine. The bile duct carries bile products away from the hepatocytes to the larger ducts and gall bladder. Therefore, it is necessary to form the structure including the material supply and metabolic waste discharge in regenerative liver tissue so that the hepatic tissue can maintain completed hepatic function for a long term. Herein, we have been able to successfully use rat CLiPs (a small chemical-induced liver progenitor cells developed by Dr. Katsuda) to induce 3D bile duct structure. If we want to form human liver tissue including bile duct and vascular, we have to establish the human 3D bile duct, but we have not yet completed the differentiation of human CLiPs into 3D bile duct structure. Therefore, we need to use human CLIP to induce 3D bile duct.

3. Method:
1.Human CLIPs were induced to form 3D bile duct structure in 3D culture system: MEF cell as feeder cell and Matrigel provides with 3D environment.
2.BIM (bile duct induced medium) combinate with growth factors (HGF and EGF) would be investigated.

Result:
1.Phase image and RT-qPCR showed that the FAC can successfully induce cryohepatocytes to human CLiPs.
2.Inducing human CLiPs to cholangiocytes and formation of the 3D bile duct structures: the combination of MEF feeder cells and Matrigel can induce the human CLiPs to cholangiocytes and form some 3D bile duct structure, which had positive expressions of biliary genes and concentration of Rhodamine123 in BIM medium with HGF.
3.The BIM+HGF had higher efficiency for the formation of the bile duct from hCLiPs compared with the other conditions.
4.The integrated bile-hepatocyte tissue expressed the bile acid transporter proteins and accumulated CLF into biliary lumen from the culture medium via hepatocytes canaliculi.

4. Summary:
we formed the functional bile duct from hCLiPs induced from hMHs by molecules combination with FBS. These hCLiPs expressed typical HPCs markers EpCAM, KRT-19, SOX-9, CD133 and gradually downregulated hMHs markers ALB, CYP7A1, and HNF4A during induction. These purified hCLiPs were then used to induce the generation of a 3D bile duct-like structure with lumens in a 3D culture environment with MEF. The bile duct expressed typical biliary epithelial cell markers CK-7, GGT1, CFTR and EpCAM and it had the ability to transport the bile-like substance rhodamine 123 into the lumen of the bile duct. Subsequently, bile ducts were co-cultured with hMHs for two days and bile salt analogues,CLF, were transported into bile duct and aggregate within the lumen from culture medium through the hMHs. The integrated tissue expressed the bile bile canaliculi marker and transporter protein.

1．研究概要(2)

1.Tanimizu N, Nakamura Y, Ichinohe N, et al. Hepatic biliary epithelial cells acquire epithelial integrity but lose plasticity to differentiate into hepatocytes in vitro during development. J Cell Sci. 2013;126:5239-46. doi:10.1242/jcs.133082
2.O'Hara SP, Tabibian JH, Splinter PL, et al. The dynamic biliary epithelia: molecules, pathways, and disease. J Hepatol. 2013;58:575-82. doi:10.1016/j.jhep.2012.10.011
3.Alpini G, McGill JM, LaRusso NF. The pathobiology of biliary epithelia. Hepatology. 2002;35:1256-68. doi:https://doi.org/10.1053/jhep.2002.33541
4.Cao W, Chen K, Bolkestein M, et al. Dynamics of Proliferative and Quiescent Stem Cells in Liver Homeostasis and Injury. Gastroenterology. 2017;153:1133-47. doi:10.1053/j.gastro.2017.07.006
5.Strazzabosco M, Fabris L, Spirli C. Pathophysiology of cholangiopathies. J Clin Gastroenterol. 2005;39:S90-S102. doi:10.1097/01.mcg.0000155549.29643.ad
6.Lazaridis KN, LaRusso NF. The Cholangiopathies. Mayo Clin Proc. 2015;90:791-800. doi:10.1016/j.mayocp.2015.03.017
7.Buisson EM, Jeong J, Kim HJ, et al. Regenerative Medicine of the Bile Duct: Beyond the Myth. Int J Stem Cells. 2019;12:183-94. doi:10.15283/ijsc18055
8.Huang Y, Sakai Y, Hara T, et al. Bioengineering of a CLiP-derived tubular biliary-duct-like structure for bile transport in vitro. Biotechnol Bioeng. 2021;118:2572-84. doi:10.1002/bit.27773
9.Yan J, Tai Y, Zhou H. Culture of Mouse Liver Ductal Organoids. Methods Mol Biol. 2022;2455:117-29. doi:10.1007/978-1-0716-2128-8_11
10.Wang Z, Faria J, van der Laan LJW, et al. Human Cholangiocytes Form a Polarized and Functional Bile Duct on Hollow Fiber Membranes. Front Bioeng Biotechnol. 2022;10:868857. doi:10.3389/fbioe.2022.868857

1.The intrahepatic bile ducts (BDs) play an important role in the modification and transport of bile, and the integration between the BD and hepatocytes is the basis of the liver function. However, the lack of a source of cholangiocytes limits in vitro research. The aim of the present study was to establish three-dimensional BDs combined with human mature hepatocytes (hMHs) in vitro using chemically induced human liver progenitor cells (hCLiPs) derived from hMHs. In this study, we formed functional BDs from hCLiPs using hepatocyte growth factor and extracellular matrix. BDs expressed the typical biliary markers CK-7, GGT1, CFTR and EpCAM and were able to transport the bile-like substance rhodamine 123 into the lumen. The established three-dimensional BDs were cocultured with hMHs. These cells were able to bind to the BDs, and the bile acid analog CLF was transported from the culture medium through the hMHs and accumulated in the lumen of the BDs. The BDs generated from the hCLiPs showed a BD function and a physiological system (e.g., the transport of bile within the liver) when they were connected to the hMHs. We present a novel in vitro three-dimensional BD combined with hMHs for study, drug screening and the therapeutic modulation of the cholangiocyte function.

2.Biliary tubular-hepatocyte system accumulates polystyrene microplastic (PS-MP)-induced hepatotoxicity and mitigate through bile extraction.
Background: Microplastic particles are ubiquitous in daily life and can bioaccumulate in the liver via the hepatic-intestinal axis through dietary sources. The presence of microplastics has been associated with liver abnormalities, particularly in lipid metabolism, and has been documented in nonalcoholic steatohepatitis (NASH). Animal studies have demonstrated that bioaccumulation of microplastics can also lead to abnormalities in lipid and bile metabolism in the liver. However, there is currently no available data on the accumulation and metabolic pathways of microplastics in the liver. The in vitro model is an effective tool for investigating liver diseases and metabolism. To address this gap, we propose to study the metabolism of polystyrene microplastics (PS-MP) in the liver using an in vitro tissue model of bile duct-hepatocytes.
Method:
1.Establish an in vitro biliary tubular-hepatocyte tissue with the biliary and hepatic functions. (Confirm the characteristic of the tissue by proteins (IF and IHC), gene expressions (Rt-qPCR) and function assay (Rhodamine 123 and CLF))
2.Expose the hepatic tissue with the PS-MP for 1 hours, 24 hours and 48 hours. In order to confirm the hepatotoxicity of the exposing to the PS-MP, the markers of the liver metabolism would be detected, as well as the hepatotoxicity markers.
3.The bile efflux would affect the extraction of the PS-MP in the liver, the bile acid and cholesterol transporters inhibition and stimulation experiments would be carried out.
Results:
1.The biliary tubular-hepatocyte tissue from the rat CLiPs was successful, which have the functions of the bile transportation and the hepatocyte.
2.The human hepatic organoid from human CLiPs was established at the same time and the hepatic organoid contain the biliary tubular structure and the mature hepatocytes. The hepatic organoid also up-take the PS-MP and it seems to be transported into the bile duct. The YAC-HO absorbing the PS-MP cause the hepatotoxicity.
3.UDCA facilitates the excretion of the PS-MP excretion into bile ducts and attenuates hepatotoxicity.

2. 執筆論文 Publication of thesis ※記載した論文を添付してください。Attach all of the papers listed below.

論文名 1 Title	Therapeutic effect and mechanism of Daikenchuto in a model of methotrexate-induced acute small intestinal mucositis				
掲載誌名 Published journal	PLOS ONE				
	2023 年 3 月	18 巻(号)	e0283626 頁 ～ 頁	言語 Language	English
第1著者名 First author	Peilin Li	第2著者名 Second author	Yusuke Inoue	第3著者名 Third author	Daisuke Miyamoto
その他著者名 Other authors	Toshiyuki Adachi, Satomi Okada,Tomohiko Adachi,Akihiko Soyama,Masaaki Hidaka,Kengo Kanetaka,Shinichiro Ito,Daichi Sadatomi,Sachiko Mogami,Naoki Fujitsuka,Weili Gu,Susumu Eguchi				
論文名 2 Title	Three-dimensional human bile duct formation from chemically induced human liver progenitor cells				
掲載誌名 Published journal	Frontiers in Bioengineering and Biotechnology				
	2023 年 8 月	11 巻(号)	頁 ～ 頁	言語 Language	English
第1著者名 First author	Li,Peilin	第2著者名 Second author	Miyamoto,Daisuke	第3著者名 Third author	Huang,Yu
その他著者名 Other authors	Adachi Tomohiko,Hidaka Masaaki,Hara Takanobu,Soyama Akihiko,Matsushima Hajime,Imamura Hajime,Kanetaka Kengo,Gu Weili,Eguchi,Susumu				
論文名 3 Title	Feasibility of Organ Transportation by a Drone: An Experimental Study Using a Rat Model				
掲載誌名 Published journal	Transplantation Proceedings				
	2023 年 9 月	巻(号)	頁 ～ 頁	言語 Language	English
第1著者名 First author	Enjoji, Takahiro	第2著者名 Second author	Soyama, Akihiko	第3著者名 Third author	Fukumoto, Masayuki
その他著者名 Other authors	Peilin, Li Matsuguma, Kunihito Imamura, Hajime Maruya, Yasuhiro Hara, Takanobu Matsushima, Hajime Kugiyama, Tota Adachi, Tomohiko Hidaka, Masaaki Hamamoto, Sho Takashima, Shiro Maeda,Takahiro Kanetaka, Kengo				
論文名 4 Title					
掲載誌名 Published journal					
	年 月	巻(号)	頁 ～ 頁	言語 Language	
第1著者名 First author		第2著者名 Second author		第3著者名 Third author	
その他著者名 Other authors					
論文名 5 Title					
掲載誌名 Published journal					
	年 月	巻(号)	頁 ～ 頁	言語 Language	
第1著者名 First author		第2著者名 Second author		第3著者名 Third author	
その他著者名 Other authors					

3. 学会発表 Conference presentation ※筆頭演者として総会・国際学会を含む主な学会で発表したものを記載してくだ

※Describe your presentation as the principal presenter in major academic meetings including general meetings or international me

学会名 Conference	The 67th Annual Congress of International College of Surgeons Japan Section		
演 題 Topic	An animal model of methotrexate-induced acute intestinal mucositis for drug therapy		
開催日 date	2022 年 6 月 4 日	開催地 venue	Tokyo
形式 method	☑ 口頭発表 Oral □ ポスター発表 Poster	言語 Language	□ 日本語 ☑ 英語 □ 中国語
共同演者名 Co-presenter	Peilin Li, Yusuke Inoue, Daisuke Miyamoto, Akihiko Soyama, Tomohiko Adachi, Kazuma Kobayashi, Shinichiro Ito, Masaaki Hidaka, Kengo Kanetaka, Susumu Eguchi		
学会名 Conference	Digestive Disease Week 2023; Session: AGA Basic Mechanisms of Tissue Injury, Repair and Fibrosis		
演 題 Topic	Therapeutic effect and mechanism of Daikenchuto in a model of methotrexate-induced acute small intestinal mucositis		
開催日 date	2023 年 5 月 6 日	開催地 venue	Chicago
形式 method	□ 口頭発表 Oral ☑ ポスター発表 Poster	言語 Language	□ 日本語 ☑ 英語 □ 中国語
共同演者名 Co-presenter	Peilin Li, Yusuke Inoue, Daisuke Miyamoto, Akihiko Soyama, Tomohiko Adachi, Kazuma Kobayashi, Shinichiro Ito, Masaaki Hidaka, Kengo Kanetaka, Susumu Eguchi		
学会名 Conference	The 68th Annual Congress of International College of Surgeons Japan Section		
演 題 Topic	A life-saving case report of hemolytic uremic syndrome by performing subtotal colorectal resection		
開催日 date	2023 年 6 月 10 日	開催地 venue	Tokyo
形式 method	☑ 口頭発表 Oral □ ポスター発表 Poster	言語 Language	□ 日本語 ☑ 英語 □ 中国語
共同演者名 Co-presenter	Peilin Li; Toshiyuki Adachi; Yusuke Inoue; Satomi Okada; Akihiko Soyama; Tomohiko Adachi; Kazuma Kobayashi; Masaaki Hidaka; Kengo Kanetaka;		
学会名 Conference			
演 題 Topic			
開催日 date	年 月 日	開催地 venue	
形式 method	□ 口頭発表 Oral □ ポスター発表 Poster	言語 Language	□ 日本語 □ 英語 □ 中国語
共同演者名 Co-presenter			

4. 受賞(研究業績) Award (Research achievement)

名 称 Award name				
	国名 Country		受賞年 Year of	年 月
名 称 Award name				
	国名 Country		受賞年 Year of	年 月

5. 本研究テーマに関わる他の研究助成金受給 Other research grants concerned with your resarch theme

受給実績 Receipt record	■ 有　　□ 無
助成機関名称 Funding agency	
助成金名称 Grant name	
受給期間 Supported period	年　月 ～　年　月
受給額 Amount received	円
受給実績 Receipt record	□ 有　　□ 無
助成機関名称 Funding agency	Japanese Society of Gastroenterology
助成金名称 Grant name	JSGE (Japanese Society of Gastroenterology) Overseas Young Physician Study/Training Grant System 2023
受給期間 Supported period	2023 年 4 月 ～ 2024 年 3 月
受給額 Amount received	500,000 円

6. 他の奨学金受給 Another awarded scholarship

受給実績 Receipt record	■ 有　　□ 無
助成機関名称 Funding agency	Nagasaki University
奨学金名称 Scholarship name	2023 Nagasaki University Special Research Student Scholarship
受給期間 Supported period	2023 年 4 月 ～ 2024 年 3 月
受給額 Amount received	600,000 円

7. 研究活動に関する報道発表 Press release concerned with your research activities

※記載した記事を添付してください。Attach a copy of the article described below

報道発表 Press release	□ 有　　□ 無	発表年月日 Date of release	
発表機関 Released medium			
発表形式 Release method	・新聞　・雑誌　・Web site　・記者発表　・その他（　　　　）		
発表タイトル Released title			

8. 本研究テーマに関する特許出願予定 Patent application concerned with your research theme

出願予定 Scheduled	□ 有　　□ 無	出願国 Application	
出願内容（概要） Application contents			

9. その他 Others

指導責任者（記名）　江口　晋

Feasibility of Organ Transportation by a Drone: An Experimental Study Using a Rat Model

Takahiro Enjoji[a], Akihiko Soyama[a*], Masayuki Fukumoto[a], Li Peilin[a], Kunihito Matsuguma[a], Hajime Imamura[a], Yasuhiro Maruya[a], Takanobu Hara[a], Hajime Matsushima[a], Tota Kugiyama[a], Tomohiko Adachi[a], Masaaki Hidaka[a], Sho Hamamoto[b], Shiro Takashima[c], Takahiro Maeda[d], Kengo Kanetaka[a], and Susumu Eguchi[a]

[a]Department of Surgery, Nagasaki University Graduate School of Biomedical Sciences, Nagasaki, Japan; [b]Soraya Inc., Nagasaki, Japan; [c]All Nippon Airways Company Limited (ANA) Holdings Inc., Tokyo, Japan; and [d]Department of General Medicine, Nagasaki University Graduate School of Biomedical Sciences, Nagasaki, Japan

ABSTRACT

Background. Recently, the successful delivery of organs for transplantation using drones was reported. We investigated the influence of transportation by drones on the quality of liver grafts using a rat model.

Methods. Livers of 12 rats (8 and 32 weeks old) were divided into 2 groups of six. Livers were split into 2 parts and allocated to the drone or control groups (both n = 12). The drone experiment was conducted between islands in Nagasaki Prefecture, Japan. The distance between the islands was 12 km. Livers of the drone group were transported by a multicopter at a speed of 30 km-40 km/h over 60 m above sea level. Transported liver quality was analyzed by histology, and biochemistry data were compared between groups.

Results. Cold ischemia time did not differ between groups (902 min and 909 min, respectively). There were no differences in macroscopic findings regarding coloration and damage between groups. Aspartate aminotransferase (AST), alanine aminotransferase (ALT), and alkaline phosphatase (ALP) in preservation fluid were graft weight-corrected and compared, and no significant differences were found between groups: AST/g (4.61 vs 4.81 IU/L), ALT/g (2.78 vs 2.92 IU/L), and ALP/g (39.1 vs 37.0 IU/L). Immunochemical staining showed no significant difference between groups for terminal deoxynucleotidyl transferase dUTP nick and labeling staining (141 vs 113 cells), CD163 (818 vs 870 cells), and TNF-α (1.25 vs 1.41 scores).

Conclusions. The simulation experiment of organ transport for transplantation by drones was successfully conducted. There were no differences in the quality of livers transported by drones or other means. Further studies including large-animal experiments could lead to future clinical applications.

IN transplantation medicine, the graft ischemic time has a significant effect on outcomes [1−3]. Therefore, it is very important to plan for more appropriate logistics of organ transportation. In Japan, current organ transportation often involves chartered aircraft or helicopters for heart transplants, whereas other organs are often transported using public transport. Thus, the organ transportation system is based on a complex network comprising public transport, private transport, and medical workers in transplantation medicine [4].

If public transport is used, time adjustments are necessary because of the use of scheduled flights. In addition, there is a risk that traffic congestion will affect transportation. Therefore, the timing of organ transplants is often dependent on public transport.

---

*Address correspondence to Akihiko Soyama, MD, PhD, Nagasaki University Graduate School of Biomedical Sciences, 171, Sakamoto, 852-8501, Nagasaki, Japan. E-mail: soyama@nagasaki-u.ac.jp

230 Park Avenue, New York, NY 10169

0041-1345/20
https://doi.org/10.1016/j.transproceed.2023.08.018

The accumulation of time resulting from this complex network can make transplantation impossible [5]. In recent years, pilot clinical studies of organ delivery by unmanned aerial systems were reported to solve these problems [6,7]. Unmanned aerial systems enable faster organ transplantation through smoother connections to aircraft and time saving by avoiding traffic jams [8,9]. They also improve access to transplantation in various situations, such as when major roads are closed to traffic due to accidents or disasters. The availability of unmanned aerial systems may also have the advantage of reducing the risk of accidents associated with the transport of organs for transplantation by transplant physicians and transplant-related staff.

There have been no reports of organ transportation by drones in Japan. In this study, we conducted an experiment to test the feasibility of transplant organ transportation by drones in Japan, using an animal model in cooperation with local governments and companies.

MATERIAL AND METHODS

Animal Model

Livers were obtained from model rats at the Nagasaki University Animal Research Facility (approval number: 211202-1). Twelve male Wister rats (six 8-week-old and 6 32-week-old rats) were set up as models. Whole livers from model rats were obtained and University of Wisconsin (UW) solution was administered in 40 mL-50 mL flushes through the portal vein to perfuse the liver. The livers were split into 2 parts, weighed, grouped into drone and control groups, and then packed in accordance with the protocol of the Japanese Society for Transplantation (1st layer: 100 mL of UW solution, 2nd layer: 100 mL of saline solution, 3rd layer: no solution). Packed livers were stored in a cold container with ice. The above operations were performed on 12 rats per group. The rats were transported to the drone experiment site by a high-speed jetfoil and car.

Drone Transport Experiment

The experiment was conducted between Fukue Island and Hisaka Island, Goto City. The drone used was a multicopter type with a payload capacity of 5 kg and a maximum flight speed of 10 m/s (Fig 1). The livers in the drone group were transported by drone over a distance of approximately 12 km, whereas those in the control group were transported by high-speed vessel and car. Management and decision-making related to drones, such as drone operation and route determination, were carried out by a team of drone specialists. The criteria for the drone used in this study to be deemed flight-worthy was set at a maximum wind speed of 10 m/sec, and it flew along a predetermined route using autonomous navigation. The drone's position was constantly monitored using a Global Positioning System, and it was programmed to switch to manual control in case of any abnormalities. The transportation time and temperature inside the containers during transportation were recorded. After the transportation experiment between the islands was completed, specimens were transported to the Nagasaki University Experimental Facility by high-speed vessel and car, and the specimens were processed.

Fig 1. The six-winged multicopter drone used in this study.

Biochemical Examination in Preservation Solution

The UW solution (packing layer 1) was collected after transport, stored at −30°C, and measured for aspartate aminotransferase (AST), alanine aminotransferase (ALT), and alkaline phosphatase (ALP) enzyme activities, which were evaluated as values per liver weight.

Histopathological Analyses

Liver tissues were processed for optical microscopy. For this, specimens were fixed in 4% formaldehyde for 48 hr-72 hr, encased in paraffin, and 5 μm-thick sections were prepared. Hematoxylin-eosin (HE) staining and immunohistochemical (IHC) staining were performed. Immunohistochemical staining was performed with Dako Target Retrieval Solution, Tris/EDTA solution (pH = 9.0), Dako REAL Peroxidase-Blocking Solution (Cat. No. S2023, Agilent Technologies, Santa Clara, CA), Protein Block Serum-Free Ready-to-use (Cat. No. X0909), Dako REAL Antibody Diluent (Cat. No. S2022), and Dako REAL EnVision/HRP secondary antibodies, Rabbit/Mouse (Cat. No. K5007). These procedures were performed in accordance with the protocol provided by Dako. After visualization with diaminobenzidine, the sections were counterstained with hematoxylin. The stained specimens were observed using an Olympus BX53 microscope (Olympus, Tokyo, Japan). The primary antibodies used were as follows: rabbit anti-CD163 antibody (Cat. ab182422, Abcam Inc., Cambridge, MA; 1:500) and anti-TNF-α antibody (Cat. ab220210, Abcam Inc.; 1/500).

Terminal deoxynucleotidyl transferase dUTP nick and labeling staining. Terminal deoxynucleotidyl transferase dUTP nick and labeling (TUNEL) staining was performed using a TUNEL Assay kit (Cat. ab206386, Abcam Inc., Cambridge, MA) in accordance with the manufacturer's instructions.

Histopathological and TUNEL staining evaluation. Hematoxylin-eosin staining staining was evaluated on the basis of the number of cases with findings of necrosis caused by external damage, balloon-like hepatocytes, and edema.

CD163 and TUNEL staining were evaluated quantitatively by counting the number of positive cells in 5 randomly selected fields of view (× 200). TNF-α was evaluated semiquantitatively by scoring on a 4-point scale (0-3) as follows: 0: no expression, 1: mild overexpression, <25% of hepatocytes, 2: moderate overexpression, 25%-50% of hepatocytes, and 3: high overexpression, >50% of hepatocytes.

Statistical Analysis

The data for continuous variables were expressed as means with standard deviation. Data of biochemical, histopathological, and TUNEL staining data were analyzed by two-tailed t test using JMP Pro (SAS Institute Inc., Cary, NC). A P value <.05 was considered statistically significant.

Table 1. Liver Weight and Cold Ischemia Time in Each Group

	Drone		Control		
Age in weeks	Young	Old	Young	Old	*P* value
Number of samples	6	6	6	6	-
Liver weight(g)	4.3±0.2	6.9±0.5	9.3±0.4	14.8±2.3	<.01
CIT(min)	895±32	909±26	903±34	915±29	.57

RESULTS

Liver Weight and Cold Ischemic Time

The drone and control groups each consisted of 6 young rat livers and 6 old rat livers. The lighter weight split livers were assigned to the drone group. The mean liver weight was 4.3 ± 0.17 g for young rats and 6.9 ± 0.45 g for old rats in the drone group, and 9.3 ± 0.4 g for young rats and 14.8 ± 2.3 g for old rats in the control group. The mean cold ischemic time was 894 ± 32 min for young rat livers and 909 ± 26 min for old rat livers in the drone group, and 903 ± 34 min for young rat livers and 915 ± 29 min for old rat livers in the control group (Table 1). There was no significant difference in cold ischemia time between the drone and control groups (*P* = .57).

Temperature inside the container during transport. The outside temperature during the experiment was 12°C-16°C. The temperature inside the container in the drone group was maintained at 0°C-5°C and did not vary depending on the method of transportation (Fig 2).

Biochemical examination of preserved solution samples. The values of AST, ALT, and ALP (per liver weight) in the stored solution of the drone and control groups were AST/g: 4.61 ± 3.06 vs 4.84 ± 1.52 (*P* = .81), ALT/g: 2.78 ± 2.32 vs 2.92 ± 1.04 (*P* = .85), and LDH/g: 39.1 ± 31. 1 vs 37.0 ± 7.6 (*P* = .82), respectively (Table 2). There were no significant differences in the AST/g, ALT/g, and ALP/g in the preserved solution between the 2 groups.

Macroscopic findings. Macroscopic findings of the livers after transportation are shown in Fig 3. There were no differences in the macroscopic findings of livers from both groups based on necrosis, color change, or external damage.

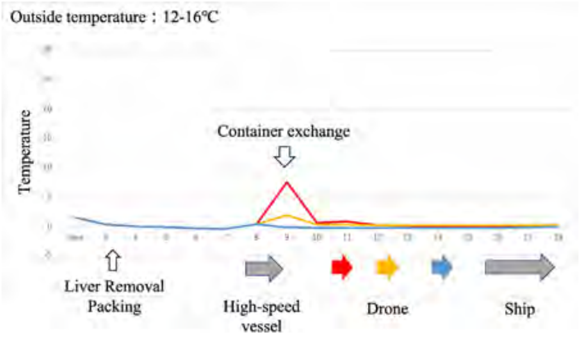

Fig 2. Temperature inside the container. The temperature inside the containers remained constant regardless of the transfer method.

Table 2. Biochemical Analysis

	Drone	Control	*P* value
AST/g	4.6±3.0	4.8±1.5	.81
ALT/g	2.8±2.3	2.9±1.0	.85
LDH/g	39.1±31.1	37.0±7.6	.82

HE staining. The results of HE staining are shown in Fig 4. There were no findings of necrosis caused by external damage, ballooning hepatocytes, or edema in any of the livers, and no findings suggestive of effects from drone transportation.

TUNEL staining and immunochemical staining. The results of TUNEL staining and immunochemical staining are shown in Fig 5. TUNEL staining showed that the mean quantitative values of the drone and control groups were 141 ± 274 vs 113 ± 211 cells (*P* = .78), and there was no significant difference between the 2 groups in the assessment of apoptosis. There were no significant differences in the number of Kupffer cells (818 ± 92 vs 870 ± 77 cells; *P* = .14) or inflammatory markers (CD163 and TNF-α) (1.25 ± 0.45 vs 1.41 ± 0.51 scores; *P* = .4).

DISCUSSION

An organ transportation experiment was conducted using a drone to transport rat livers. Temperatures were maintained at a constant level during transport, and no adverse effects of drone transportation were observed regarding the physiological or pathologic evaluation of the specimens. There was no significant effect on livers, confirming the safety of organ transportation by drones.

Regarding the current organ transportation system, there are various time issues associated with the use of public transport.

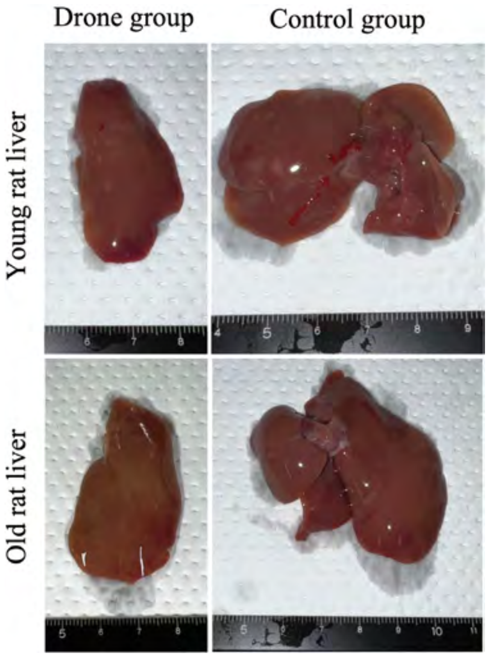

Fig 3. Macroscopic analysis of livers. There were no obvious findings of necrosis, color change, or external damage.

A

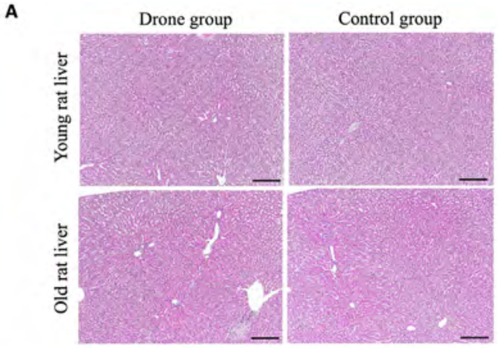

B

	Drone(n=12)		Control(n=12)		P value
	Young (n=6)	Old (n=6)	Young (n=6)	Old (n=6)	
necrosis	0	0	0	0	-
ballooning	0	0	0	0	-
edema	0	0	0	0	-

Fig 4. Hematoxylin-eosin (HE) staining. There were no cases of necrosis caused by external influences, balloon-like hepatocytes, or edema. Scale bar, 200 μm.

For example, staff transporting organs may have to wait because of traffic congestion or lose time because of limited numbers of flights. If drones can be used as a means of organ transportation, they can avoid traffic congestion and connections to scheduled flights in the shortest possible time by taking over the responsibility of transporting the organs from the hospital to the airport. As a result, the cold ischemia time could be shortened. In addition, if future improvements in drone performance enable long-distance, stable flights and direct inter-hospital transport, organ transport will be possible without relying on aircraft time, and further cold ischemia time reduction can be expected.

A

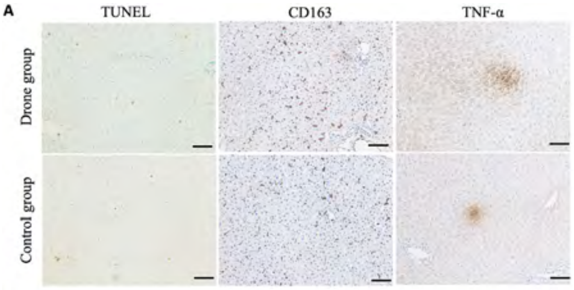

B

	Drone	Control	p value
TUNEL$_{\text{(cells)}}$	141±274	113±211	0.78
CD163$_{\text{(cells)}}$	818±92	870±77	0.14
TNF-α$_{\text{(scores)}}$	1.25±0.45	1.41±0.51	0.40

Fig 5. Terminal deoxynucleotidyl transferase dUTP nick and labeling (TUNEL) staining and immunochemical analyses. TUNEL staining and immunochemical staining in young rat livers are shown. No significant differences in staining were found between the drone and control groups. Scale bars, 100 μm.

Transplant medicine is considered a high-risk procedure in medicine. In 2007, 6 members of the University of Michigan organ transplantation team died during lung transportation [10]. In Japan in 2020, an organ removal team from the University of Tokyo crash-landed while transporting a heart by helicopter, resulting in serious injuries [11]. Thus, the current organ transportation system puts transplantation teams at risk of being involved in accidents. We think that unmanned drones can perform part of this transportation, thereby reducing the risk of accidents to the transplantation team.

In December 2022, the Japanese Civil Aeronautics Law was revised to allow unobserved flights in manned areas if certain conditions are met [12]. This may lead to increased opportunities for drones to be used in the future for the transportation of pharmaceuticals and medical materials, in addition to the delivery of food and other goods. This study provides basic data for considering the feasibility of organ transportation using drones in future transplantation medicine.

Regarding the temperature management of organs during transportation, currently drones do not have temperature control capabilities. Therefore, in this study, we placed a temperature logger inside the container storing the organs and checked the temperature with the logger after landing. Currently, even with conventional means of organ transportation, continuous temperature monitoring is not being conducted. Therefore, if continuous temperature monitoring becomes necessary for organ transportation by drones in the future, the development of a temperature management system would also be required.

The drone used in this study had a maximum payload capacity of 5 kg and was tested using livers from rats. A drone that can withstand a weight of about 10 kg is needed to transport grafted human livers in actual clinical practice. In addition, this experiment involved air transport by a drone over a distance of approximately 12 km. The longest distance achieved in recent drone-based organ transport experiments is approximately 14 km [6,7,13,14]. The safety of long-distance transportation using drones is still not fully understood. In terms of drone logistics, initially focusing on short-distance usage is desirable. Specifically, using drones for transportation between hospitals in urban areas or between hospitals and airports is a viable approach. This allows for the avoidance of risks associated with traffic congestion, disasters, and issues on roads, while enabling smooth connections to limited scheduled flights or charter aircraft. With the future improvement of drone performance and establishment of further safety measures in drone transport, it is anticipated that direct transportation between distant hospitals will become possible. This opens up opportunities for additional research in this field.

In conclusion, this study showed the feasibility of rat organ transport by a drone. Further simulation of organ delivery using larger organs may lead to the clinical use of drones in the future.

DATA AVAILABILITY

All data generated or analyzed during this study are included in this article. Further inquiries can be directed to the corresponding author.

DECLARATION OF COMPETING INTEREST

All the authors declare no known competing financial interests or personal relationships that could have appeared to influence the work reported in this paper.

ACKNOWLEDGMENTS

We thank J. Ludovic Croxford, PhD, from Edanz (https://jp.edanz.com/ac) for editing a draft of this manuscript.

REFERENCES

[1] Wiesner RH, Demetris AJ, Belle SH, Seaberg EC, Lake JR, Zetterman RK, et al. Acute hepatic allograft rejection: incidence, risk factors, and impact on outcome. Hepatology 1998;28:638–45.

[2] Busuttil RW, Farmer DG, Yersiz H, Hiatt JR, McDiarmid SV, Goldstein LI, et al. Analysis of long-term outcomes of 3200 liver transplantations over two decades: a single-center experience. Ann Surg 2005;241:905–16; discussion 916−8.

[3] Totsuka E, Fung JJ, Lee MC, Ishii T, Umehara M, Makino Y, et al. Influence of cold ischemia time and graft transport distance on postoperative outcome in human liver transplantation. Surg Today 2002;32:792–9.

[4] Chow EK, DiBrito S, Luo X, Wickliffe CE, Massie AB, Locke JE, et al. Long cold ischemia times in same hospital deceased donor transplants. Transplantation 2018;102:471–7.

[5] Stewart DE, Kucheryavaya AY, Klassen DK, Turgeon NA, Formica RN, Aeder MI. Changes in deceased donor kidney transplantation one year after KAS implementation. Am J Transpl 2016;16:1834–47.

[6] Scalea JR, Pucciarella T, Talaie T, Restaino S, Drachenberg CB, Alexander C, et al. Successful implementation of unmanned aircraft use for delivery of a human organ for transplantation. Ann Surg 2021;274:e282–8.

[7] Scalea JR, Restaino S, Scassero M, Blankenship G, Bartlett ST, Wereley N. An initial investigation of Unmanned Aircraft Systems (UAS) and real-time organ status measurement for transporting human organs. IEEE J Transl Eng Health Med 2018;6:4000107.

[8] Handford C, Reeves F, Parker P. Prospective use of unmanned aerial vehicles for military medical evacuation in future conflicts. J R Army Med Corps 2018;164:293–6.

[9] Lin CA, Shah K, Mauntel LCC, Shah SA. Drone delivery of medications: review of the landscape and legal considerations. Am J Health Syst Pharm 2018;75:153–8.

[10] Englesbe MJ, Merion RM. The riskiest job in medicine: transplant surgeons and organ procurement travel. Am J Transplant 2009;9:2406–15.

[11] Kotekawa T, Rikimaru S. The Asahi Shimbun. Copter carrying donated heart crash-lands in Fukushima, https://www.asahi.com/ajw/articles/13094525; 2020 [accessed 28.01.23].

[12] MILT Japan. Unmanned aircraft level 4 flight portal site, https://www.mlit.go.jp/koku/level4/; 2022 [accessed 28.01.23].

[13] Conny B, Amy L, Sarah Sonn. Mission GO. MissionGO & Minnesota team transports world's first human pancreas via unmanned aircraft, https://www.globenewswire.com/news-release/2021/05/11/2227226/0/en/MissionGO-Minnesota-Team-Transports-World-s-First-Human-Pancreas-via-Unmanned-Aircraft.html; 2021 [accessed 05.07.23].

[14] Adrianna R. USA TODAY. Drone carries human kidney over Las Vegas desert in what could be the future of organ transportation, https://www.usatoday.com/story/news/health/2020/09/28/drone-used-transport-human-kidney-airport-las-vegas-nevada/3528614001/; 2020 [accessed 05.07.2023].

PLOS ONE

RESEARCH ARTICLE

Therapeutic effect and mechanism of Daikenchuto in a model of methotrexate-induced acute small intestinal mucositis

Peilin Li[1,2], **Yusuke Inoue**[1], **Daisuke Miyamoto**[1], **Toshiyuki Adachi**[1], **Satomi Okada**[1], **Tomohiko Adachi**[1], **Akihiko Soyama**[1], **Masaaki Hidaka**[1], **Kengo Kanetaka**[1], **Shinichiro Ito**[1], **Daichi Sadatomi**[3], **Sachiko Mogami**[3], **Naoki Fujitsuka**[3], **Weili Gu**[2], **Susumu Eguchi**[1]*

1 Department of Surgery, Nagasaki University Graduate School of Biomedical Sciences, Nagasaki, Japan, **2** Department of Surgery, Guangzhou First People's Hospital, School of Medicine, South China University of Technology, Guangzhou, Guangdong, China, **3** Tsumura Kampo Research Laboratories, 2 Tsumura Advanced Technology Research, Tsumura & Co., Ibaraki, Japan

* sueguchi@nagasaki-u.ac.jp

Abstract

Background

Daikenchuto (DKT) has positive therapeutic effects on improving various gastrointestinal disorders. The present study investigated whether or not DKT has a potential therapeutic effect on chemotherapy-induced acute small intestinal mucositis (CIM) in a rat model.

Methods

Intraperitoneal injection of 10 mg/kg methotrexate (MTX) every 3 days for a total of 3 doses was used for induction of CIM in a rat model. The MTX and DKT-MTX groups were injected with MTX as above from the first day, and the DKT-MTX and DKT groups were administered 2.7% DKT via the diet at the same time. The rats were euthanized on day 15.

Results

The DKT-MTX group showed an improvement in the body weight and conditions of gastrointestinal disorders as well as increased levels of diamine oxidase in plasma and in the small intestinal villi. The pathology results showed that small intestinal mucosal injury in the DKT-MTX group was less severe than that in the MTX group. Immunohistochemistry for myeloperoxidase and malondialdehyde and quantitative real-time polymerase chain reaction (RT-qPCR) for TGF-β1 and HIF-1α showed that DKT attenuated peroxidative damage. The crypts in the DKT-MTX group contained more Ki-67-positive cells than MTX group. The zonula occluden-1 and claudin-3 results showed that DKT promoted repair of the mucosal barrier. RT-qPCR for the amino acid transporters EAAT3 and BO+AT also confirmed that DKT promoted mucosal repair and thus promoted nutrient absorption.

OPEN ACCESS

Citation: Li P, Inoue Y, Miyamoto D, Adachi T, Okada S, Adachi T, et al. (2023) Therapeutic effect and mechanism of Daikenchuto in a model of methotrexate-induced acute small intestinal mucositis. PLoS ONE 18(3): e0283626. https://doi.org/10.1371/journal.pone.0283626

Editor: Muhammad Shahid Riaz Rajoka, University of Maryland Baltimore, UNITED STATES

Received: January 11, 2023

Accepted: March 13, 2023

Published: March 30, 2023

Data Availability Statement: All relevant data are within the paper and its Supporting Information files.

Funding: This experiment was supported by Tsumura Kampo Research Laboratories, Tsumura & Co. The funder had no role in study design, data collection and analysis, decision to publish, or preparation of the manuscript.

Competing interests: The authors of Peilin Li, Yusuke Inoue, Daisuke Miyamoto, Toshiyuki Adachi, Satomi Okada, Tomohiko Adachi, Akihiko

Soyama, Masaaki Hidaka, Kengo Kanetaka, Shinichiro Ito and Susumu Eguchi received a research grant from Tsumura & Co. Daichi Sadatomi, Naoki Fujitsuka and Sachiko Mogami are employed by Tsumura & Co. All authors who took part in this study promised to avoid conflicts of interest (even superficial ones) with the company and the research process, and the results conformed to the research specification. All authors undertook to ensure that the personal conduct of all participants was in accordance with the guidelines and to report appropriately when there is a potential for any actual or potential conflict. All the other authors declared no competing interests. The funder provided support in the form of salaries for Daichi Sadatomi, Naoki Fujitsuka and Sachiko Mogami, but did not have any additional role in the study design, data collection and analysis, decision to publish, or preparation of the manuscript. The specific roles of these authors are articulated in the 'author contributions' section.

Conclusion

DKT protected against MTX-induced CIM in a rat model by reducing inflammation, stimulating cell proliferation, and stabilizing the mucosal barrier.

Introduction

Intestinal mucositis (IM) is a common and debilitating side effect of chemotherapy that manifests due to the inability of chemotherapy drugs to differentiate between normal and tumor cells, with the intestinal epithelial cells rapidly proliferating cells and often becoming the target of attack during chemotherapy treatments [1]. Chemotherapy-induced IM (CIM) occurs in as many as 25%-75% of cancer patients receiving different chemotherapy, leading to diarrhea, a decreased quality of life, treatment intolerance resulting in discontinuation, and even death [2]. Due to the complex and diverse clinical symptoms of CIM and the importance of the reducing this toxic complication of chemotherapy, developing new ways to alleviate or prevent CIM is important.

Methotrexate (MTX), a structural analogue of folic acid, is one of the most widely used therapeutic agents for the treatment of the tumors, malignant hematological disorders, and autoimmune diseases [3]. MTX causes inhibition of growth and repair activities of epithelium and mucosa where the dividing and proliferating activities are increased, inducing CIM, which is the main reason for limiting further use of this drug or prompting its use [4].

Daikenchuto (DKT) is a traditional Japanese medicine (Kampo) originally described in a Chinese classic article and independently developed in Japan. It is a mixture of extract powders from dried Japanese pepper, processed ginger, ginseng radix, and malt sugar powder and is reported to have the effects of improving gastrointestinal motility, activating anti-inflammatory, increasing intestinal blood flow, and altering the intestinal microbiome [5,6]. The main mechanism underlying the DKT-mediated contraction and improvement of gastrointestinal motility is modulation of intestinal contraction and relaxation via the release of acetylcholine, nitric oxide, releasing of acetylcholine from cholinergic nerves stimulated by 5-HT3R and 5-HT4R and other excitatory neurotransmitters [7,8]. The anti-inflammatory effect of DKT are attributed to the fact that DKT manages the downregulation of cyclooxygenase 2 (COX-2), the upregulation of endogenous adrenomedullin (ADM), and the suppression of eosinophil infiltration [9]. The regulation of intestinal blood flow by DKT is achieved by stimulating epithelial transient receptor potential ankyrin 1 (TRPA1) to induce endogenous ADM release [10]. Recent studies have suggested that DKT can alter the gut microbiota, thereby improving long-lasting dysbiosis and gastrointestinal dysfunction after bowel or liver surgery [11].

In addition to these effects, Wada et al. also demonstrated that DKT enhanced anastomotic healing via an anti-inflammatory effect and increased blood flow after intestinal surgery in rats [12]. DKT has been widely used clinically in patients with gastrointestinal symptoms, such as postoperative intestinal obstruction, inflammatory bowel disease, abdominal pain, and pain accompanied by abdominal flatulence [13–15]. DKT improves gastrointestinal motility disorders and reduces serum C-reactive protein levels in patients with grade B liver injury after hepatectomy and is an effective treatment after hepatectomy for hepatocellular carcinoma [16]. A previous report showed that DKT can suppress the adverse effects associated with irinotecan hydrochloride, an anticancer agent with debilitating side effect of severe diarrhea, and improve the function of tight junction proteins, including zonula occluden-1 (ZO-1), occludin and claudin-4 [17].

The lack of relevant medication for CIM is usually only alleviated by reducing the dose of chemotherapy drugs or stopping chemotherapy, and there is a lack of relevant drugs for complementary or supplementary treatment. Based on existing experiments and recent studies on DKT, we hypothesized that DKT could improve CIM through the above mechanisms. Therefore, the present study investigated whether or not DKT could improve CIM and promote recovery from CIM.

Methods

Animal

Male *Sprague-Dawley rats* (6 weeks, 160–190 g; CLEA Japan Inc., Tokyo, Japan) were used in this study. They were bred and housed at the rat facility in standard rat cages exposing to 12-h light-dark cycles and allowed *ad libitum* access to water and rat chow.

All animal experiments were conducted according to protocols approved by the institutional animal care committee of Nagasaki University and all methods were performed in accordance with the relevant guidelines and regulations of Nagasaki University. The study was reported in accordance with ARRIVE guidelines.

Experimental protocol

All animals were divided randomly into 4 groups: the control group (Col, n = 5), MTX-induced model group (MTX, n = 5), DKT treatment group (DKT-MTX, n = 5), and DKT-only group (DKT, n = 5). In the MTX and DKT-MTX groups, MTX was administered (10 mg/kg every 3 days, 3 times total) with intraperitoneal injection. In the MTX-DKT and DKT groups, DKT at 2.7% of the total mass (Tsumura & Co., Tokyo, Japan) mixed in the feed (CE-2 feed; CLEA Japan Inc.) was administered orally from the beginning of the administration of MTX, while the other two groups received non-DKT CE-2 feed. In the control group, the rats were intraperitoneally injected with the same volume of normal saline at the same time.

All rats had their body weight measured every three days. All surviving rats were euthanized by cutting the vena cava to induce exsanguination after abdominal collection of all of the small intestinal tissues under deep isoflurane (Wako Pure Chemical, Osaka, Japan) respiratory anesthesia (All-in-one Anesthetizer, Muromachi Kikai CO. LTD, Japan).

Intestinal histology

The rats were sacrificed under anesthesia at day 15, and the small intestinal tissues were collected immediately. The rat small intestinal tissue was fixed with 4% paraformaldehyde phosphate-buffered solution (PBS; Wako Pure Chemical, Osaka, Japan) for 3 days. Fixed tissues were embedded in paraffin, cut into 5-μm sections, and deparaffinized for standard histological staining with hematoxylin and eosin (HE). HE sections were evaluated blindly for intestinal inflammation, which comprised crypt length, architecture and abscesses, loss of goblet cells, tissue damage, and infiltration of leukocytes and neutrophils.

For immunohistochemistry staining, tissue sections of the small intestines were stained for claudin-3, ZO-1, neutrophil myeloperoxidase (MPO), malondialdehyde (MDA), Ki-67 and diamine oxidase (DAO) (The antibody information were attached to S1 Table). The percentage of total area of the small intestinal sections was measured using image J Software analysis at least 10 positions.

Quantitative real-time polymerase chain reaction (qRT-PCR)

Tissue samples were acquired at defined time point for mRNA extraction using spin columns according to the manufacturer's instructions (NucleoSpin RNA II; Macherey-Nagel, Duren, Germany). cDNA was synthesized from total RNA using a high-capacity cDNA reverse transcription kit (Applied Biosystems, Tokyo, Japan). In brief, PCR amplification was performed followed by Applied Biosystems (Taq-man was attached to S2 Table). The gene expression was normalized to that of GAPDH (control intestinal tissue was set as 1.0), and the mRNA expression was determined using the comparative cycle time (ΔΔCt) method.

Determination of plasma DAO activity by an enzyme-linked immunosorbent assay (ELISA)

Plasma of rats was separated in a refrigerated centrifuge and stored at −20˚C before determination of the DAO activity using the rat diamine oxidase ELISA Kit (FineTest; ER0895, Wuhan, China) according to the manufacturer's instructions. The DAO activity was calculated according to a standard curve and presented in units/L.

Statistical analyses

At least five rats were used for all experimental groups. The Data of RT-qPCR are represented as mean ± standard error of the mean from three biological replicates for each sample, while the mRNA sample would be collected at least three samples. The percentage contribution of positivity of IHC was calculated for at least 10 positions by image J Software (ImageJ 1.53k, NIH, USA). The data were expressed as the mean ± standard error of the mean (S.E.M). Statistical analyses were carried out with the GraphPad Prism software program (GraphPad Software, Inc., California, USA) using a one-way analysis of variance (ANOVA), t-test, or an analysis of variance with repeated measures when appropriate. The survival rate of the rats was shown with Log-rank (Mantel-Cox) test. Asterisks (*) indicate significant differences (* $P < 0.05$, ** $P < 0.01$, by t-test or one-way ANOVA).

Results

DKT can enhance the body weight recovery and ameliorate the symptoms of IM induced by MTX

MTX was used for induction of CIM, and the optimum dose and frequency (10 mg/kg every 3 days, 3 times total) of MTX to induce CIM was determined. The DKT treatment experiment was performed according to the diagram (**Fig 1A**). According to the lectures and the recommend dose for patients, 2.7% of the total mass mixed in the feed was administered orally from the beginning of the administration of MTX [18]. The body weight of the rats in the MTX and DKT-MTX groups decreased over time, compared with control group, but after day 12, the body weight of the rats in the DKT-MTX group significantly increased (**Fig 1B**). The changes in food intake were similar to those of the body weight, with rats in both the DKT-MTX and MTX groups showing reductions after the administration of MTX, compared to the control group, although values gradually increased in DKT-MTX group after day 12 (**Fig 1C**). There was also no significant difference in the survival rate between the MTX group and the DKT-MTX group on day 15 (**Fig 1D**).

The MTX group had severe diarrhea by day 15, while the rats in the DKT-MTX group had only slightly soft stool. When the small intestine was observed after euthanasia and opening, the small intestine in the MTX group was observed to be relatively pale in appearance (**Fig 1E**). Pathologic changes in the small intestine would be described in detail below.

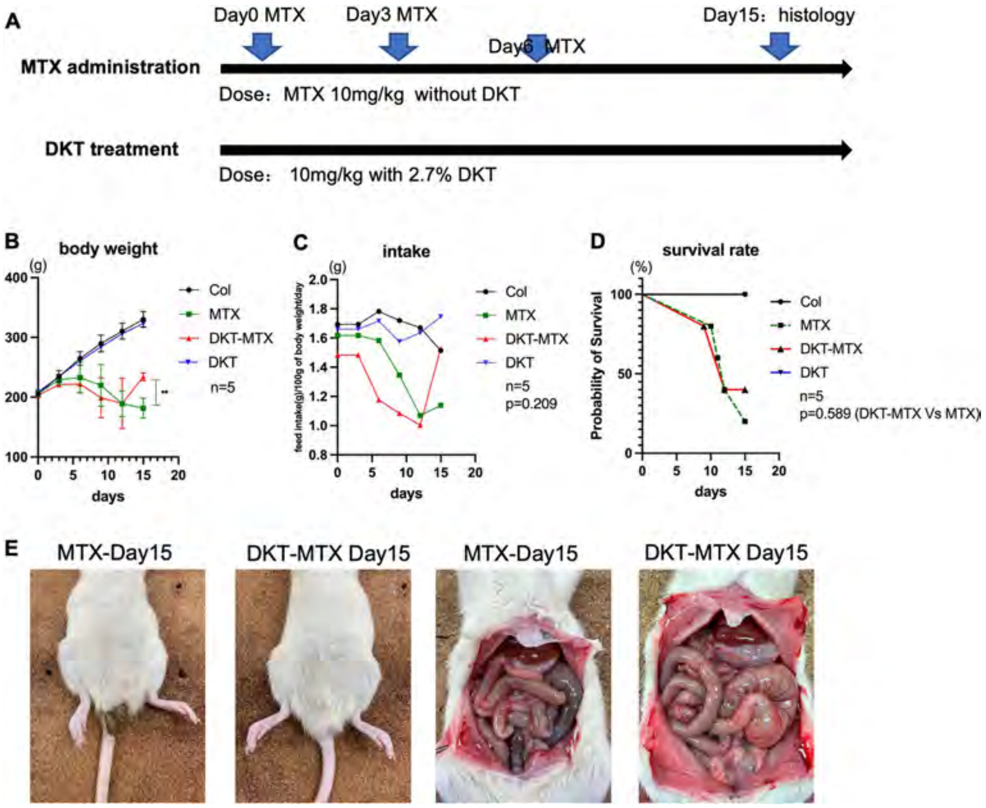

Fig 1. DKT enhanced the body weight recovery and ameliorated the symptoms of IM induced by MTX. **(A)** The experiment was performed according to the diagram. **(B)** The body weight of the rats was shown. Data are represented as mean ± standard error of the mean. One-way ANOWA test, followed by Tukey's multiple comparison test for day15, ns>0.05, **p < 0.001. **(C)** The food intake of the rats was shown. Data are represented as mean only, Student-t test for day 15 data, DKT-MTX Vs MTX, p = 0.209. **(D)** The survival rate of the rats in all groups was shown. Log-rank (Mantel-Cox) test, p value = 0.5890. **(E)** The rats in the DKT-MTX group had no obvious diarrhea, and the intestinal walls of the rats in the MTX group were thinned.

https://doi.org/10.1371/journal.pone.0283626.g001

DKT attenuated MTX-induced inflammation and mucosal damage in the small intestinal mucosa

Pathological and inflammation-related factors were used to evaluate the inflammation of the small intestinal mucosa and the therapeutic effect of DKT on acute CIM. HE staining showed that the MTX group had degeneration and vacuolization of the surface and crypt epithelium and villus structure in the jejunum, the digestion and dissolution of epithelial structures, and bleeding and edema in the lamina propria in the ileum. The DKT-MTX group showed the degeneration and vacuolization of the surface and crypt epithelium and villus structure in the jejunum and ileum. There were no marked changes in the control or DKT group (**Fig 2A**).

Immunohistochemical (IHC) staining for MPO and MDA showed that the DKT-MTX group had a lower percentage contribution of positivity than the MTX group in the jejunum and ileum, although there was no significant difference in the MDA in the jejunum (**Fig 2B–2D**). RT-qPCR showed that the expression of inflammation-related mRNA of TGF-β1 was up-regulated in the small intestine of the MTX group, compared with the DKT-MTX and control groups; however, there were no significant changes in the HIF-1α levels in any groups after DKT treatment (**Fig 2E**).

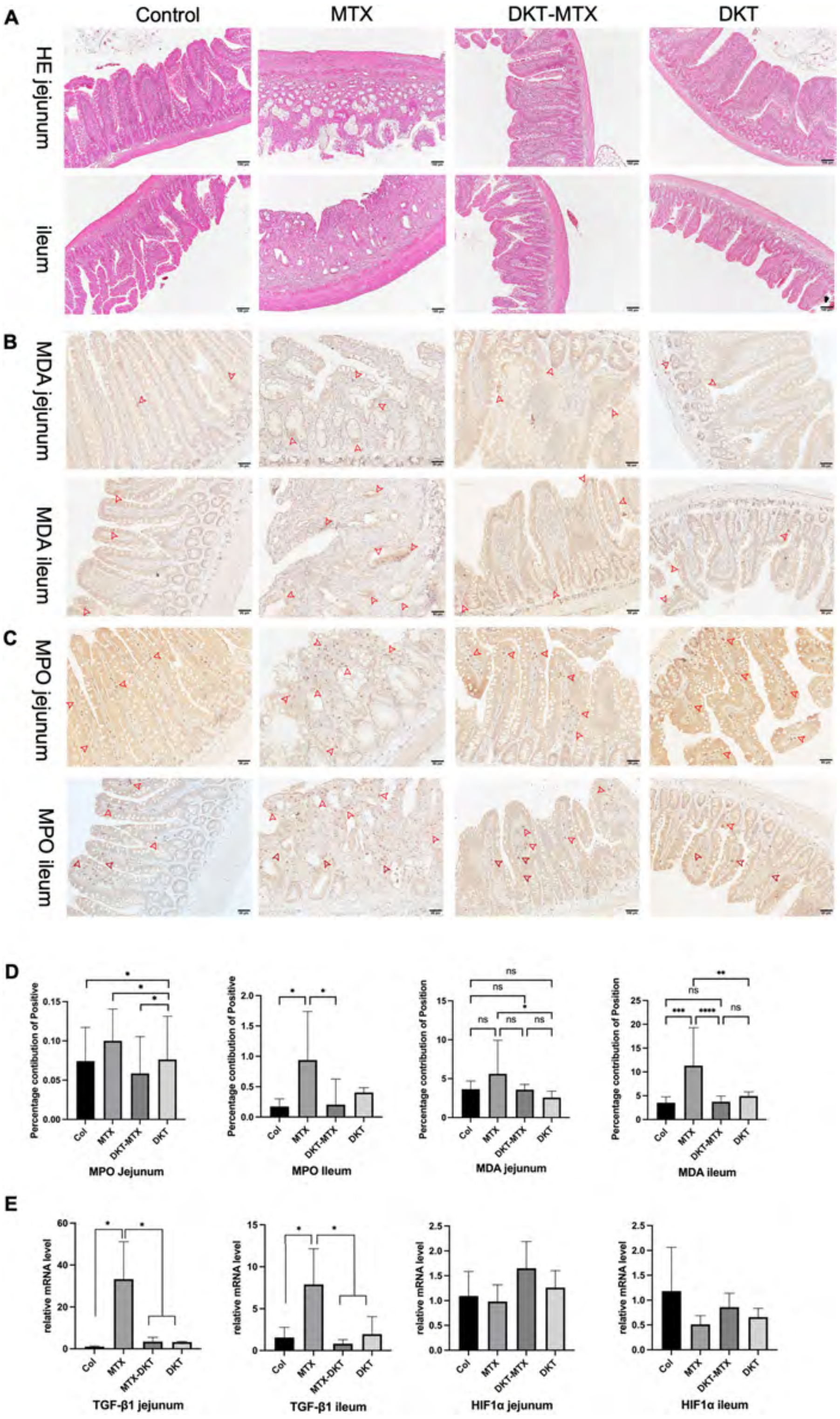

Fig 2. DKT attenuated MTX-induced inflammation and mucosal damage in the small intestinal mucosa. (A) HE staining showed the structural changes in all groups. Scale bar = 100 μm. **(B, C, D)** The immunohistochemistry results showed a lower percentage contribution of positivity for **(D)** MDA **(B)** and MPO **(C)** in the jejunum and ileum of the DKT-MTX group than in those of the MTX group. For each criterion, the percentage contribution of positivity was calculated for at least 10 positions. Scale bar = 50 μm. Data are represented as mean ± standard error of the mean. One-way ANOWA test, ns>0.05, $^*p < 0.05$. **(E)** RT-qPCR showed the expression of inflammation-related mRNA of TGF-

β1 and HIF-1α in the four groups. Values were determined relative to GAPDH and presented as fold-change relative to the control group. Data are represented as mean ± standard error of the mean from three biological replicates. One-way ANOVA test, ns >0.05, *p <0.05.

https://doi.org/10.1371/journal.pone.0283626.g002

DKT enhanced small intestinal crypt cell proliferation after administration of MTX

MTX induced small intestinal mucosal epithelial injury by inhibiting the proliferation of small intestinal mucosal crypt cells, which resulted in the suspension of small intestinal mucosal renewal. IHC staining for Ki-67 of the small intestinal tissue was used to evaluate the cell proliferation in the crypts and epithelia of the small intestinal mucosa, which could reflect the repair of the mucosa [19]. After treatment with DKT in the CIM models, the small intestinal mucosal crypts in the DKT-MTX group contained more Ki-67-positive cells than the MTX group (**Fig 3A**). Positive area counting using the image J software program (NIH, Wisconsin, USA) showed that the DKT-MTX group had a higher percentage contribution of Ki-67 positivity than the MTX group in crypts (**Fig 3B**). Normal villous crypt ratio (V/C) is 3 to 5:1 [20]. After the rats in the DKT-MTX group were administered with DKT, the small intestinal V/C ratio in the DKT-MTX group was significantly higher than that in the MTX group, which was close to 3 (**Fig 3C**).

DKT promoted the repair of the mucosal barrier and nutrient absorption functions

DAO can reflect the degree the mucositis induced by MTX. In DKT treatment experiments, the DAO level was decreased in both the MTX and DKT-MTX groups, compared with the control group but gradually recovered after 12 days in the DKT-MTX group (**Fig 4A**). IHC staining also showed the positions and relative level of DAO in the jejunum and ileum, with statistically significant differences being noted in the jejunum and ileum between the DKT-MTX and MTX groups (**Fig 4B and 4C**).

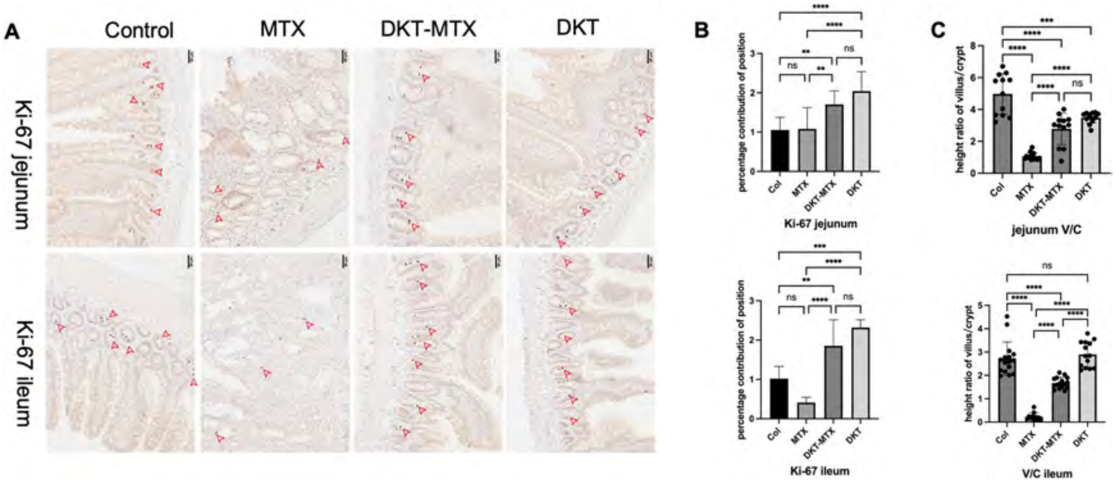

Fig 3. DKT enhanced the small intestinal crypt cell proliferation after the administration of MTX. **(A)** Immunohistochemical results showed that the small intestinal mucosal crypts in the DKT-MTX group contained more Ki-67-positive cells than the MTX group. **(B)** The DKT-MTX group had a higher percentage contribution of Ki-67 positivity than the MTX group. Scale bar = 50 μm. For each criterion, the percentage contribution of Ki-67 positivity was calculated for at least 10 positions using image J software. **(C)** The high ratio of villus to crypt was measured by image J software. Data are represented as mean ± standard error of the mean. One-way ANOVA test, ns >0.05, *p <0.05.

https://doi.org/10.1371/journal.pone.0283626.g003

To investigate the effect of DKT on the repair of the mucosal barrier function in MTX-induced IM, we examined the ZO-1 protein level in the intestinal tissue by immunofluorescence staining. ZO-1 was predominantly localized along the apical membrane of the intestinal villi in the control, DKT-MTX, and DKT groups. In contrast, a reduction in ZO-1 immunostaining was observed along the apical membrane of the intestinal villi, especially along the ileum, in the MTX group (**Fig 4D**). Additionally, the tight junction related factor associated to the intestinal permeability, cladin-3, was also investigated. The MTX-treated rats in the MTX group had decreased claudin-3 protein density in the intestinal mucosa, especially in the ileum. The DKT-MTX group had higher claudin-3 protein density in the intestinal mucosa of the rats compared with the MTX group (**Fig 4E**).

To investigate the effect of DKT on the repair of nutrient absorption function in MTX-induced IM, we examined the expression of genes related to the amino acid transport-related proteins excitatory amino acid transporter 3 (EAAT3) and broad neutral amino acid transporter (B0+AT) in the small intestinal mucosa. The relative gene expression of EAAT3 and B0+AT in the DKT-MTX group was significantly higher than that in the MTX group, especially in the jejunum (**Fig 4F**).

Discussion

IM is a common side effect of chemotherapy, and with the increasing number of cancer diagnoses and the prevalence of chemotherapy drug use, chemotherapy-associated mucositis has become increasingly common. MTX, as an anti-cancer drug widely used for leukemia and other malignancies, is a structural analogue of folic acid that can inhibit the metabolism of folic acid by competitively inhibiting dihydrofolate reductase, thereby inhibiting the *de novo* synthesis of purines and pyrimidines [21]. Over the past few decades, MTX has been successfully used alone or in combination with other drugs to treat various cancers and autoimmune diseases [22]. Unfortunately, however, due to its multi-organ toxicity, especially in the gastrointestinal system, the therapeutic potential of MTX can be reduced, with the drug typically having to be ceased in response to bone marrow toxicity, cardiotoxicity, nephrotoxicity, and liver toxicity [23,24]. Damage to the gastrointestinal mucosa following MTX treatment in cancer patients includes villus shortening and fusion, epithelial atrophy, crypt loss, inflammatory infiltration of the lamina propria, goblet cell depletion, and barrier dysfunction due to loss of mucosal integrity and reduced nutrient absorption [25].

MTX-induced IM not only causes direct damage by DNA copy inhibition but also induces inflammation and the generation of reactive oxygen species (ROS) [26]. A study has demonstrated that MPO and MDA levels are increased after treatment with MTX, suggesting the possible participation of neutrophil infiltration and ROS in MTX-induced IM [26]. In the present study, we found that levels of MPO, a marker of neutrophil accumulation and infiltration during intestinal mucosa damage, were increased in the epithelial mucosa of rats with IM induced by MTX. Kolli et al. also reported that oxidants such as MDA, which is a product of lipid peroxidation, were increased in MTX-induced small IM [27]. MPO is also an enzyme with peroxidative damage secreted by neutrophils after neutrophil, and it also causes peroxidative damage to tissues. According to our results, oral administration of DKT can inhibit the inflammatory process and ROS damage, as evidenced by the fact that DKT can reduce the production of MPO and MDA.

In addition to peroxidation-related factors, growth factors secreted from mucosa also played a role in this process. TGF-β1 and HIF-1α were reported to protect intestinal integrity [28,29]. The mRNA level of TGF-β1 in the DKT-MTX group was higher than that in the control group on day 15, but it was lower in the jejunum and ileum than in the MTX group. This

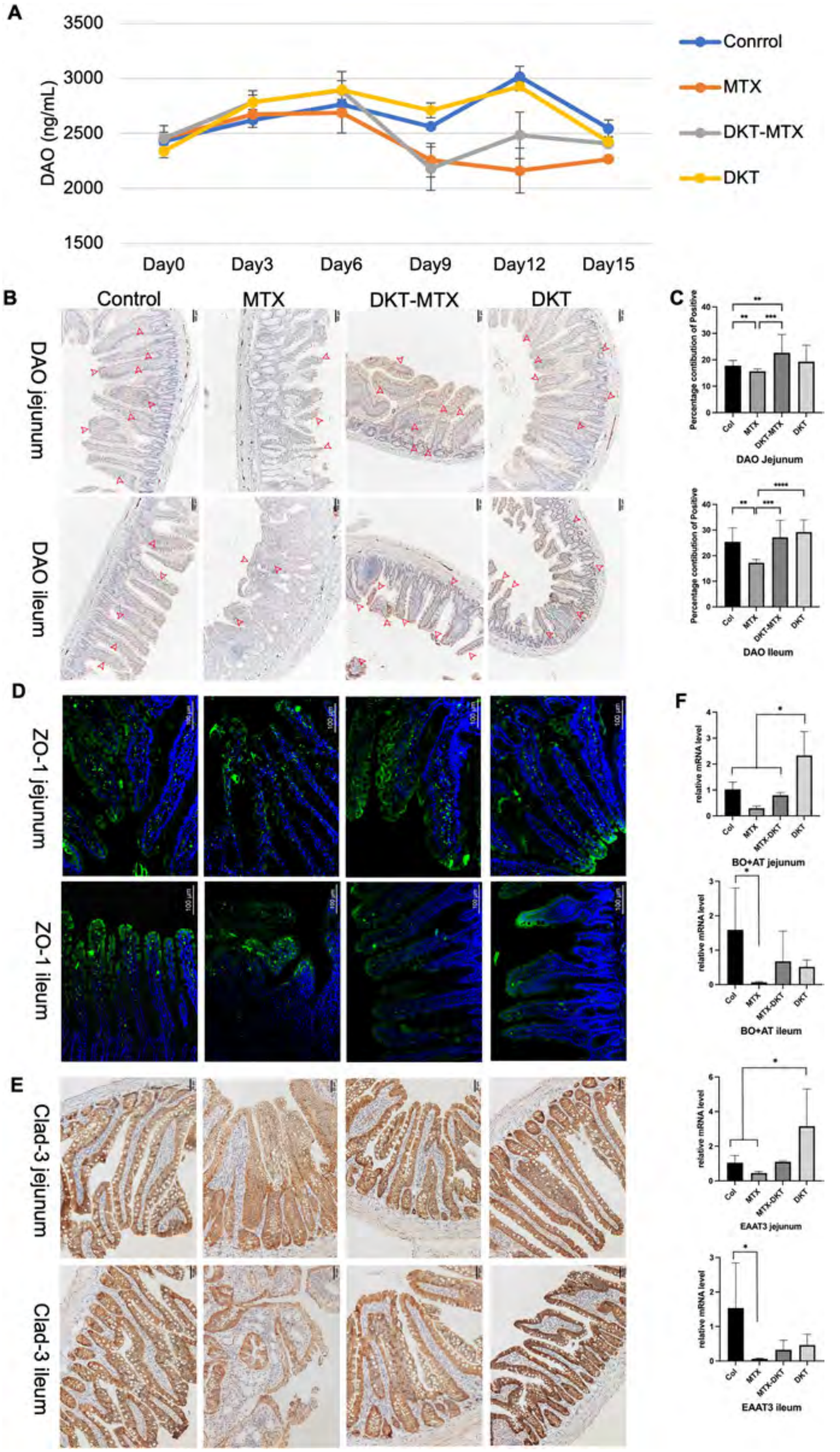

Fig 4. DKT promoted the repair of the mucosal barrier and nutrient absorption functions. **(A)** The plasma DAO level in the control, MTX, DKT-MTX, and DKT groups. The DAO level decreased in both the MTX and DKT-MTX groups compared with the control group but gradually recovered after day 9 in the DKT-MTX group. Units: ng/ml; DAO, diamine oxidase. **(B)** Immunohistochemical staining shows the positions and relative level of DAO in the jejunum and ileum of the control, MTX, DKT-MTX, and DKT groups, and **(C)** the percentage contributions of

positivity are shown. Scale bar = 100 μm. For each criterion, the percentage contribution of positivity was calculated for at least 10 positions. Data are represented as mean ± standard error of the mean. One-way ANOVA tests: ns>0.05, *p <0.05. **(D)** Immunofluorescence staining with the anti-Zo-1 antibody showed the expression and positions of the tight junction protein Zo-1. Bar = 100 μm, Zo-1, zonula occludens-1. **(E)** The tight junction related claudin-3 protein associated to the intestinal permeability was investigated by IHC staining. Scale bar = 50 μm **(F)** RT-qPCR showed the relative mRNA levels of BO+AT and EAAT3 in the jejunum and ileum. Values were determined relative to GAPDH and presented as fold-change relative to the control group. Data are represented as mean ± standard error of the mean from three biological replicates. One-way ANOVA: ns>0.05, *p <0.05. EAAT3: Excitatory amino acid transporter 3; B0+AT: Broad neutral amino acid transporter.

https://doi.org/10.1371/journal.pone.0283626.g004

method of mucosal repair was also verified in another experiment of DKT in the treatment of intestinal injury repair in rats [12].

The changes in the level and localization of ZO-1 induced by MTX may lead to disorder of the barrier function, which leads to increased intestinal permeability, resulting in intestinal mucosal barrier dysfunction [30]. ZO-1, as a tight junction scaffold protein, has been shown to render structure firmness and impermeability to the junction and functions as a link between occludin and actin, which are the major elements in the structure of the barrier of the small intestine [31]. However, Kuo et al. reported that the tight junction protein ZO-1 was dispensable for the barrier function but critical for intestinal mucosal repair [32]. Furthermore, redistribution of this tight junction function along the lateral plasma membrane sustained the epithelial barrier during cell shedding [33]. In the present study, an immunohistochemical analysis revealed that ZO-1 was predominantly localized along the apical membrane of the intestinal villi in the control and DKT groups. DKT has the potential to promote the expression of ZO-1 in the small intestinal mucosa epithelium to facilitate the repair of tight junctions and improve the mucosal nutrient absorption. These results were also confirmed by the immunostaining of the claudin-3.

The expression of genes related to the amino acid transport-related proteins EAAT3 and B0 +AT was up-regulated after the administration of DKT in the DKT-MTX group. A prospective study of the effects of DKT on the blood flow in the superior mesenteric artery and portal vein (PV) reported that DKT may modulate the SMA and PV blood flows by acting on intestinal micro-vessels [34]. The absorption of nutrients around the ileocecal region was related to the blood flow of the intestine and PV. A prospective open-labeled randomized exploratory study also demonstrated that DKT can improve the perioperative nutritional status of patients with colorectal cancer [35].

DAO is a highly active intracellular enzyme in the upper villi of the human and mammalian small intestinal mucosa that plays a role in the metabolism of histamine and various polyamines [36]. Plasma DAO activity was reported to be associated with the degree of small intestinal injury and had potential utility for measuring mucositis during chemotherapy [36,37]. A previous study showed that an increase of DAO activity in the intestine of mature rats leads to an increase in the degree of DAO activity in plasma [38]. In contrast, intestinal mucosal damage caused by hypertonic sodium sulfate solution or atrophy caused by a low-fiber diet reduces plasma DAO activity [39]. In the present study, with the occurrence of MTX-induced IM, the DAO content in rat plasma decreased, and with the onset of gastrointestinal tract symptoms aggravated and reduced to a lower level. In the DKT-MTX group, as DKT promoted the recovery of rat mucosa, the serum content of DAO was also increased. The IHC results also confirmed that the rat small intestinal mucosal epithelial villi of the DKT-MTX group contained higher DAO levels in the mature apical membrane than that in MTX group.

DKT is mainly composed of dried Japanese pepper extract, ginger extract, and ginseng extract. Ginger can reportedly improve ileum damage caused by MTX, shortened villus fusion, inflammatory cell infiltration, and goblet cell depletion [40]. As one of the main components of DKT, ginger extract has been verified to have a variety of intestinal effects, including anti-inflammatory and antioxidative effects in ulcerative colitis [41]. The mechanism underlying the restoration of the intestinal barrier function by ginger extract involves the increased expression of ZO-1 and claudin-1 protein [42]. Regarding dried Japanese pepper extract (*Zanthoxylum fructus*), there have been articles reporting that *Zanthoxylum fructus* extract inhibits the reduction in mast cell activation by inhibiting sphingosine kinase 1, mainly reducing the release of inflammatory mediators [43]. In research on DKT, it is reported that DKT depolarizes the pacemaker potential of Cajal interstitial cells in an internal or external Ca^{2+}-dependent manner by stimulating the 5-HT4 and muscarinic M3 receptors. Its main ingredients are ginseng and ginger root, which help DKT regulate the activity of the intestine and reduce the dysfunction of the small intestine [44]. Some researchers have screened cytoprotective agents against MTX-induced cell genotoxicity from among biologically active phytochemicals and found that agents, such as Siberian ginseng and curcumin have cytoprotective effects [45]. Total ginsenosides was reported to promote intestinal epithelial cell proliferation, presumably via the regulation of the cell cycle and of the expression of proliferation-related proteins by polyamines [46]. Specifically, DKT appears to be less effective in reducing rat mortality due to severe mucosal necrosis but shows marked efficacy in another aspect, such as reducing injury and promoting mucosal repair, as well as improving symptoms. Furthermore, DKT may also have some efficacy against chronic mucositis of the small intestine, so a further investigation regarding chronic mucositis in the clinical setting or as a daily disease will be needed in the future, with particular focus on the therapeutic effect of DKT on chronic mucositis of the small intestine.

In conclusion, DKT may be able to protect against MTX-induced acute small intestinal mucosal injury in a rat model via anti-peroxidation, stimulating cell proliferation, and stabilizing the mucosal barrier. Although DKT comprise numerous chemically diverse compounds with multi-target effects, it has been shown to be able to protect and treat intestinal injury, regardless of administration as a single component or a mixture of multiple components.

Supporting information

S1 Table. List of the first and secondary antibodies in the experiments.
(DOCX)

S2 Table. List of the Taq-man primer of Rt-PCR performed in the experiments.
(DOCX)

Author Contributions

Conceptualization: Peilin Li, Yusuke Inoue.

Data curation: Peilin Li, Daisuke Miyamoto, Satomi Okada, Masaaki Hidaka.

Formal analysis: Peilin Li, Yusuke Inoue, Toshiyuki Adachi, Satomi Okada, Tomohiko Adachi, Kengo Kanetaka, Shinichiro Ito, Weili Gu.

Investigation: Peilin Li.

Methodology: Peilin Li.

Project administration: Peilin Li, Akihiko Soyama, Susumu Eguchi.

Resources: Peilin Li, Daichi Sadatomi, Sachiko Mogami, Naoki Fujitsuka.

Software: Peilin Li.

Supervision: Susumu Eguchi.

Writing – original draft: Peilin Li.

References

1. Dahlgren D, Sjöblom M, Hellström PM, Lennernäs H. Chemotherapeutics-Induced Intestinal Mucositis: Pathophysiology and Potential Treatment Strategies. Front Pharmacol. 2021; 12:681417. https://doi.org/10.3389/fphar.2021.681417 PMID: 34017262
2. Peterson DE, Boers-Doets CB, Bensadoun RJ, Herrstedt J, Committee EG. Management of oral and gastrointestinal mucosal injury: ESMO Clinical Practice Guidelines for diagnosis, treatment, and follow-up. Ann Oncol. 2015; 26 Suppl 5:v139–51. https://doi.org/10.1093/annonc/mdv202 PMID: 26142468
3. Abolmaali SS, Tamaddon AM, Dinarvand R. A review of therapeutic challenges and achievements of methotrexate delivery systems for treatment of cancer and rheumatoid arthritis. Cancer Chemother Pharmacol. 2013; 71(5):1115–30. https://doi.org/10.1007/s00280-012-2062-0 PMID: 23292116
4. Tsukada T, Nakano T, Miyata T, Sasaki S. Life-Threatening Gastrointestinal Mucosal Necrosis during Methotrexate Treatment for Rheumatoid Arthritis. Case Rep Gastroenterol. 2013; 7(3):470–5. https://doi.org/10.1159/000356817 PMID: 24348319
5. Manabe N, Camilleri M, Rao A, Wong BS, Burton D, Busciglio I, et al. Effect of daikenchuto (TU-100) on gastrointestinal and colonic transit in humans. American journal of physiology Gastrointestinal and liver physiology. 2010; 298(6):G970–5. https://doi.org/10.1152/ajpgi.00043.2010 PMID: 20378829
6. Wada Y, Nishiyama M, Uehara H, Sato K, Hamamoto Y, Ogihara H, et al. Microbiome biomarkers associated with the gut contraction response elicited by the Japanese traditional medicine daikenchuto. Gene. 2022; 826:146262. https://doi.org/10.1016/j.gene.2022.146262 PMID: 35257788
7. Kikuchi D, Shibata C, Imoto H, Naitoh T, Miura K, Unno M. Intragastric Dai-Kenchu-To, a Japanese herbal medicine, stimulates colonic motility via transient receptor potential cation channel subfamily V member 1 in dogs. Tohoku J Exp Med. 2013; 230(4):197–204. https://doi.org/10.1620/tjem.230.197 PMID: 23892797
8. Nagano T, Itoh H, Takeyama M. Effects of Dai-kenchu-to on levels of 5-hydroxytryptamine (serotonin) and vasoactive intestinal peptides in human plasma. Biol Pharm Bull. 2000; 23(3):352–3. https://doi.org/10.1248/bpb.23.352 PMID: 10726893
9. Kogure Y, Kanda H, Wang S, Hao Y, Li J, Yamamoto S, et al. Daikenchuto attenuates visceral pain and suppresses eosinophil infiltration in inflammatory bowel disease in murine models. JGH Open. 2020; 4 (6):1146–54. https://doi.org/10.1002/jgh3.12410 PMID: 33319050
10. Kono T, Kaneko A, Omiya Y, Ohbuchi K, Ohno N, Yamamoto M. Epithelial transient receptor potential ankyrin 1 (TRPA1)-dependent adrenomedullin upregulates blood flow in rat small intestine. American journal of physiology Gastrointestinal and liver physiology. 2013; 304(4):G428–36. https://doi.org/10.1152/ajpgi.00356.2012 PMID: 23275609
11. Sasaki K, Sasaki D, Sasaki K, Nishidono Y, Yamamori A, Tanaka K, et al. Growth stimulation of Bifidobacterium from human colon using daikenchuto in an in vitro model of human intestinal microbiota. Sci Rep. 2021; 11(1):4580. https://doi.org/10.1038/s41598-021-84167-z PMID: 33633259
12. Wada T, Kawada K, Hirai K, Toda K, Iwamoto M, Hasegawa S, et al. Enhanced anastomotic healing by Daikenchuto (TJ-100) in rats. Sci Rep. 2018; 8(1):1091. https://doi.org/10.1038/s41598-018-19550-4 PMID: 29348453
13. Eguchi S, Hidaka M, Soyama A, Hara T, Kugiyama T, Hamada T, et al. A Pilot Study Evaluating the Effectiveness and Safety of Daikenchuto (TJ-100) for the Treatment of Postoperative Abdominal Pain or Bloating in Patients Undergoing Hepatectomy: Study Protocol for a Randomized, Open, Controlled Trial. Kurume Med J. 2021; 66(3):169–74. https://doi.org/10.2739/kurumemedj.MS663005 PMID: 34373384
14. Ohbe H, Jo T, Matsui H, Fushimi K, Yasunaga H. Effect of Daikenchuto for Mechanically Ventilated Patients With Enteral Feeding Intolerance: A Propensity Score-Matched Analysis Using a Nationwide Administrative Inpatient Database. JPEN J Parenter Enteral Nutr. 2021; 45(8):1703–13. https://doi.org/10.1002/jpen.2076 PMID: 33483948
15. Kono T, Maejima T, Ono Y, Ito T, Furukawa S, Nishiyama M, et al. Distinct effects of TU-100 (daikenchuto) on long-lasting dysbiosis in the small intestine in patients with colorectal cancer and inflammatory bowel disease. Gene. 2022; 820:146266. https://doi.org/10.1016/j.gene.2022.146266 PMID: 35134471
16. Shimada M, Morine Y, Nagano H, Hatano E, Kaiho T, Miyazaki M, et al. Effect of TU-100, a traditional Japanese medicine, administered after hepatic resection in patients with liver cancer: a multi-center, phase III trial (JFMC40-1001). Int J Clin Oncol. 2015; 20(1):95–104. https://doi.org/10.1007/s10147-014-0678-2 PMID: 24595550

17. Takasu C, Yismaw WG, Kurita N, Yoshikawa K, Kashihara H, Kono T, et al. TU-100 exerts a protective effect against bacterial translocation by maintaining the tight junction. Surg Today. 2017; 47(10):1287–94. https://doi.org/10.1007/s00595-017-1518-6 PMID: 28421347

18. Kong L, Hoshi N, Watanabe D, Yamada Y, Yasutomi E, Adachi S, et al. Effect of Daikenchuto On Spontaneous Intestinal Tumors in Apc(Min/+) Mice. Kobe J Med Sci. 2021; 66(4):E139–E48. PMID: 33994517

19. Potten CS, Booth C, Tudor GL, Booth D, Brady G, Hurley P, et al. Identification of a putative intestinal stem cell and early lineage marker; musashi-1. Differentiation. 2003; 71(1):28–41. https://doi.org/10.1046/j.1432-0436.2003.700603.x PMID: 12558601

20. Serra S, Jani PA. An approach to duodenal biopsies. J Clin Pathol. 2006; 59(11):1133–50. https://doi.org/10.1136/jcp.2005.031260 PMID: 16679353

21. Schmiegelow K. Advances in individual prediction of methotrexate toxicity: a review. Br J Haematol. 2009; 146(5):489–503. https://doi.org/10.1111/j.1365-2141.2009.07765.x PMID: 19538530

22. Paci A, Veal G, Bardin C, Levêque D, Widmer N, Beijnen J, et al. Review of therapeutic drug monitoring of anticancer drugs part 1—cytotoxics. Eur J Cancer. 2014; 50(12):2010–9. https://doi.org/10.1016/j.ejca.2014.04.014 PMID: 24889915

23. Morsy MA, Ibrahim SA, Amin EF, Kamel MY, Rifaai RA, Hassan MK. Curcumin ameliorates methotrexate-induced nephrotoxicity in rats. Adv Pharmacol Sci. 2013; 2013:387071. https://doi.org/10.1155/2013/387071 PMID: 24381587

24. Perez-Verdia A, Angulo F, Hardwicke FL, Nugent KM. Acute cardiac toxicity associated with high-dose intravenous methotrexate therapy: case report and review of the literature. Pharmacotherapy. 2005; 25(9):1271–6. https://doi.org/10.1592/phco.2005.25.9.1271 PMID: 16164401

25. Maiguma T, Hayashi Y, Ueshima S, Kaji H, Egawa T, Chayama K, et al. Relationship between oral mucositis and high-dose methotrexate therapy in pediatric acute lymphoblastic leukemia. Int J Clin Pharmacol Ther. 2008; 46(11):584–90. https://doi.org/10.5414/cpp46584 PMID: 19000557

26. Kolli VK, Abraham P, Rabi S. Methotrexate-induced nitrosative stress may play a critical role in small intestinal damage in the rat. Arch Toxicol. 2008; 82(10):763–70. https://doi.org/10.1007/s00204-008-0287-9 PMID: 18253714

27. Kolli VK, Abraham P, Isaac B, Kasthuri N. Preclinical efficacy of melatonin to reduce methotrexate-induced oxidative stress and small intestinal damage in rats. Digestive diseases and sciences. 2013; 58(4):959–69. https://doi.org/10.1007/s10620-012-2437-4 PMID: 23053903

28. Saeedi BJ, Kao DJ, Kitzenberg DA, Dobrinskikh E, Schwisow KD, Masterson JC, et al. HIF-dependent regulation of claudin-1 is central to intestinal epithelial tight junction integrity. Mol Biol Cell. 2015; 26(12):2252–62. https://doi.org/10.1091/mbc.E14-07-1194 PMID: 25904334

29. Xiao K, Cao S, Jiao L, Song Z, Lu J, Hu C. TGF-β1 protects intestinal integrity and influences Smads and MAPK signal pathways in IPEC-J2 after TNF-α challenge. Innate Immun. 2017; 23(3):276–84.

30. Hamada K, Shitara Y, Sekine S, Horie T. Zonula Occludens-1 alterations and enhanced intestinal permeability in methotrexate-treated rats. Cancer Chemother Pharmacol. 2010; 66(6):1031–8. https://doi.org/10.1007/s00280-010-1253-9 PMID: 20119715

31. Buckley A, Turner JR. Cell Biology of Tight Junction Barrier Regulation and Mucosal Disease. Cold Spring Harb Perspect Biol. 2018;10(1). https://doi.org/10.1101/cshperspect.a029314 PMID: 28507021

32. Kuo WT, Zuo L, Odenwald MA, Madha S, Singh G, Gurniak CB, et al. The Tight Junction Protein ZO-1 Is Dispensable for Barrier Function but Critical for Effective Mucosal Repair. Gastroenterology. 2021; 161(6):1924–39. https://doi.org/10.1053/j.gastro.2021.08.047 PMID: 34478742

33. Guan Y, Watson AJ, Marchiando AM, Bradford E, Shen L, Turner JR, et al. Redistribution of the tight junction protein ZO-1 during physiological shedding of mouse intestinal epithelial cells. Am J Physiol Cell Physiol. 2011; 300(6):C1404–14. https://doi.org/10.1152/ajpcell.00270.2010 PMID: 21346149

34. Watanabe S, Inoue M, Miyata M, Boda H. A prospective study of Daikenchuto on superior mesenteric artery and portal venous blood flows in extremely low birthweight infants. Research Square; 2022.

35. Fujita F, Torashima Y, Inoue Y, Ito S, Kobayashi K, Kanetaka K, et al. Daikenchuto improved perioperative nutritional status of the patients with colorectal cancer: A prospective open-labeled randomized exploratory study. Interv Med Appl Sci. 2019; 11(2):84–8. https://doi.org/10.1556/1646.11.2019.13 PMID: 32148910

36. Luk GD, Bayless TM, Baylin SB. Plasma postheparin diamine oxidase. Sensitive provocative test for quantitating length of acute intestinal mucosal injury in the rat. The Journal of clinical investigation. 1983; 71(5):1308–15. https://doi.org/10.1172/jci110881 PMID: 6406546

37. Fukudome I, Kobayashi M, Dabanaka K, Maeda H, Okamoto K, Okabayashi T, et al. Diamine oxidase as a marker of intestinal mucosal injury and the effect of soluble dietary fiber on gastrointestinal tract

toxicity after intravenous 5-fluorouracil treatment in rats. Med Mol Morphol. 2014; 47(2):100–7. https://doi.org/10.1007/s00795-013-0055-7 PMID: 24005798

38. Luk GD, Bayless TM, Baylin SB. Diamine oxidase (histaminase). A circulating marker for rat intestinal mucosal maturation and integrity. The Journal of clinical investigation. 1980; 66(1):66–70. https://doi.org/10.1172/JCI109836 PMID: 6772669

39. Nakao M, Ogura Y, Satake S, Ito I, Iguchi A, Takagi K, et al. Usefulness of soluble dietary fiber for the treatment of diarrhea during enteral nutrition in elderly patients. Nutrition. 2002; 18(1):35–9. https://doi.org/10.1016/s0899-9007(01)00715-8 PMID: 11827762

40. Abdul-Hamid M, Salah M. Intervention of ginger or propolis ameliorates methotrexate-induced ileum toxicity. Toxicol Ind Health. 2016; 32(2):313–22. https://doi.org/10.1177/0748233713500833 PMID: 24097362

41. Shin JK, Park JH, Kim KS, Kang TH, Kim HS. Antiulcer Activity of Steamed Ginger Extract against Ethanol/HCl-Induced Gastric Mucosal Injury in Rats. Molecules. 2020; 25(20). https://doi.org/10.3390/molecules25204663 PMID: 33066164

42. Guo XX, Zhang YD, Wang TC, Wang XL, Xu YY, Wang Y, et al. Ginger and 6-gingerol prevent lipopolysaccharide-induced intestinal barrier damage and liver injury in mice. J Sci Food Agric. 2022; 102 (3):1066–75. https://doi.org/10.1002/jsfa.11442 PMID: 34309869

43. Wang X, Kageyama-Yahara N, Hayashi S, Yamamoto T, Kadowaki M. Sphingosine kinase-1-dependent and -independent inhibitory effects of zanthoxyli fructus to attenuate the activation of mucosal mast cells and ameliorate food allergies in mice. Evid Based Complement Alternat Med. 2012; 2012:862743. https://doi.org/10.1155/2012/862743 PMID: 22719791

44. Kim H, Kim HJ, Yang D, Jung MH, Kim BJ. Depolarizing Effects of Daikenchuto on Interstitial Cells of Cajal from Mouse Small Intestine. Pharmacogn Mag. 2017; 13(49):141–7. https://doi.org/10.4103/0973-1296.196312 PMID: 28216898

45. Gu S, Wu Y, Yang J. Screening of cytoprotectors against methotrexate-induced cytogenotoxicity from bioactive phytochemicals. PeerJ. 2016; 4:e1983. https://doi.org/10.7717/peerj.1983 PMID: 27190706

46. Zhu Y, Wang A, Li R, Zhu H, Hu L, Chen W. Total ginsenosides promote the IEC-6 cell proliferation via affecting the regulatory mechanism mediated by polyamines. Saudi Pharm J. 2021; 29(10):1223–32. https://doi.org/10.1016/j.jsps.2021.09.007 PMID: 34744477

frontiers | Frontiers in Bioengineering and Biotechnology

TYPE Original Research
PUBLISHED 21 August 2023
DOI 10.3389/fbioe.2023.1249769

Check for updates

OPEN ACCESS

EDITED BY
Nic Davis Leipzig,
University of Akron, United States

REVIEWED BY
Delilah Hendriks,
Hubrecht Institute (KNAW), Netherlands
Soon Seng Ng,
Imperial College London,
United Kingdom

*CORRESPONDENCE
Susumu Eguchi,
✉ sueguchi@nagasaki-u.ac.jp

RECEIVED 29 June 2023
ACCEPTED 10 August 2023
PUBLISHED 21 August 2023

CITATION
Li P, Miyamoto D, Huang Y, Adachi T, Hidaka M, Hara T, Soyama A, Matsushima H, Imamura H, Kanetaka K, Gu W and Eguchi S (2023), Three-dimensional human bile duct formation from chemically induced human liver progenitor cells.
Front. Bioeng. Biotechnol. 11:1249769.
doi: 10.3389/fbioe.2023.1249769

Three-dimensional human bile duct formation from chemically induced human liver progenitor cells

Peilin Li[1,2], Daisuke Miyamoto[1], Yu Huang[1,2], Tomohiko Adachi[1], Masaaki Hidaka[1], Takanobu Hara[1], Akihiko Soyama[1], Hajime Matsushima[1], Hajime Imamura[1], Kengo Kanetaka[1], Weili Gu[2] and Susumu Eguchi[1]*

[1]Department of Surgery, Nagasaki University Graduate School of Biomedical Sciences, Nagasaki, Japan, [2]Department of Surgery, Guangzhou First People's Hospital, School of Medicine, South China University of Technology, Guangzhou, Guangdong, China

Background: The intrahepatic bile ducts (BDs) play an important role in the modification and transport of bile, and the integration between the BD and hepatocytes is the basis of the liver function. However, the lack of a source of cholangiocytes limits *in vitro* research. The aim of the present study was to establish three-dimensional BDs combined with human mature hepatocytes (hMHs) *in vitro* using chemically induced human liver progenitor cells (hCLiPs) derived from hMHs.

Methods: In this study, we formed functional BDs from hCLiPs using hepatocyte growth factor and extracellular matrix. BDs expressed the typical biliary markers CK-7, GGT1, CFTR and EpCAM and were able to transport the bile-like substance rhodamine 123 into the lumen. The established three-dimensional BDs were cocultured with hMHs. These cells were able to bind to the BDs, and the bile acid analog CLF was transported from the culture medium through the hMHs and accumulated in the lumen of the BDs. The BDs generated from the hCLiPs showed a BD function and a physiological system (e.g., the transport of bile within the liver) when they were connected to the hMHs.

Conclusion: We present a novel *in vitro* three-dimensional BD combined with hMHs for study, drug screening and the therapeutic modulation of the cholangiocyte function.

KEYWORDS

chemically induced progenitor cell, cholangiocyte, bile duct regeneration, bile canaliculi, hepatic organoid

1 Introduction

The liver consists of two types of endodermal epithelial cells, hepatocytes, and biliary epithelial cells (BECs), termed cholangiocytes, which differentiate from hepatoblasts during development (Tanimizu et al., 2013; O'Hara et al., 2013). The BECs form bile ducts (BDs) that connect the liver and the intestine to secrete bile, which is generated in hepatocytes, into the intestine (Alpini et al., 2002). BECs modify and transport the bile produced by hepatocytes so that they can protect the liver from bile-induced damage (O'Hara et al., 2013). The homeostasis of the connection between the BDs and the hepatocytes is therefore crucial for maintaining a normal liver function and preventing liver damage or disease (Cao et al., 2017). Functional impairment of BECs and the transportation of bile acids play an essential role in the development of various types of biliary disorders and liver failure, which can eventually only be treated by liver transplantation (Strazzabosco et al., 2005). However, the physiology and pathophysiology of cholangiopathies have not yet been fully elucidated (Strazzabosco et al., 2005; Lazaridis and LaRusso, 2015). This is mainly due to the lack of relevant *in vivo* and *in vitro* models for the study of biliary tract development, cholangiopathies and drug assays, especially for bile transport and drainage between BECs and hepatocytes in humans. The shortage of the cell source also limits the *in vitro* study of human BECs (hBECs) and the three-dimensional structural function of the BD (Buisson et al., 2019).

It has been proven to be feasible to use isolated BECs or stem cells as a source to establish a three-dimensional biliary network *in vitro* by bioengineering methods (Ramli et al., 2020; Huang et al., 2021; Sato et al., 2021; Roos et al., 2022; Wang et al., 2022; Yan et al., 2022). Currently, there has been significant improvement in the generation of functional hepatocytes from induced pluripotent stem cells (iPSCs). Several *in vitro* models of human hepatic disease have been established based on iPSCs (Olgasi et al., 2020; Kim et al., 2022; Park et al., 2022; Xu et al., 2022). Some researchers have also used chemically induced pluripotent stem cells to build various hepatocyte and cholangiocyte organoids (Si-Tayeb et al., 2010; Chen et al., 2018; Aizarani et al., 2019; Ramli et al., 2020; Wang et al., 2020; Carberry et al., 2022). Although there has been significant success in the induction of BECs and BD cysts from animal cell sources, the induction of human three-dimensional BDs (hBDs) has not fully progressed (Huang et al., 2020; Ramli et al., 2020; Huang et al., 2021). iPSCs or liver progenitor cells (LPCs) constitute BD epithelial cells, spheroids and biliary tubules in different cultural environments needed the different combinations of growth factors (Tanimizu et al., 2007; Tian et al., 2016). However, iPSCs with altered gene sequences and the isolation of BECs with limited sources still have limited clinical applications, although BECs and biliary organoids have shown great value in the treatment of biliary disease (Sampaziotis et al., 2021; Velazquez and Ebrahimkhani, 2021). Additionally, the present studies of BDs constructed *in vitro* usually ignore the relationship between BDs and hepatocytes. Hepatotoxicity studies based on hepatocytes are basically studies of the hepatocyte culture models or cystic hepatic organoids (Li et al., 2022; Park et al., 2022). Cystic organoids contain BECs and hepatocytes and exhibit corresponding characteristic cell functions. The multicellular tissue of BD combined with hepatocytes is a hepatic organoid that can represent the physiological state.

Katsuda et al. used a small molecule cocktail to chemically induce rodent mature hepatocyte (rMH) dedifferentiation into chemically-induced liver progenitor cells (CLiPs) with bidirectional differentiation potential of MHs and BECs, and on this basis, they and other researchers developed methods for human MHs (hMHs) (Katsuda et al., 2017; Katsuda et al., 2019; Kim et al., 2019). Human CLiPs (hCLiPs), chemically induced from hMHs, offer an appreciated cell source for regenerative medicine (Katsuda et al., 2019). The dilative and proliferative ability and bidirectional differentiation potential of hCLiPs bring considerable prospects for the treatment of end-stage liver disease. Huang et al. established biliary duct-like structure integrated hepatocyte tissues from rCLiPs, providing an excellent *in vitro* model for hepatobiliary disease research but not for humans (Huang et al., 2020; Huang et al., 2021). The BD-hepatocyte connected tissue as a cocultured organoid model provides a model for studying the integrated BD-hepatocyte and hepatocyte-cholangiopathy *in vitro*, which can be used to study the transport of bile and establish *in vitro* disease models.

In this study, the primary aim was to utilize hCLiPs to establish functional hepatic tissue with a three-dimensional BD connected to the hMHs. The connected tissue exhibits both structural and functional characteristics similar to BD-hepatocyte transporters and bile canaliculi. The interconnected tissue was capable of performing the crucial functions of bile transportation, collection, and delivery.

2 Methods

2.1 Cell culture and conversion

Human Cryo-Hepatocytes (CHHs) (Lot.416, Corning, Woburn, MA, United States) were seeded into collagen type-I-coated dishes (Asahi Techno Glass, Tokyo, Japan) at a density of 2×10^4 cells/cm^2 in STIM medium to promote attachment to the plate surface. The STIM medium was a hepatocyte culture media kit with 10 ng/μL epidermal growth factor (EGF) containing 1x penicillin–streptomycin-glutamine (100X) (Gibco™, Tokyo, Japan) and 10% fetal bovine serum (FBS, Gibco™, Tokyo, Japan). Four hours later, the culture medium was changed to small chemically reprogrammed culture medium. The small chemical reprogramming culture medium was DMEM/F12 containing 2.4 g/L $NaHCO_3$ and L-glutamine (Life Technologies, Tokyo, Japan) and supplemented with 5 mM HEPES, 30 mg/L L-proline, 0.05% BSA, 10 ng/mL EGF (all from Sigma–Aldrich Japan, Tokyo, Japan), insulin-transferrin-serine (ITS)-X (Life Technologies, Tokyo, Japan), 10–7 M dexamethasone (Dex) (Fuji Pharma Co. Ltd., Tokyo, Japan), 10 mM nicotinamide (Sigma–Aldrich, Tokyo, Japan), 1 mM ascorbic acid-2 phosphate (Wako Pure Chemical, Osaka, Japan), 100 U/mL penicillin, and 100 mg/mL streptomycin (Life Technologies, Tokyo, Japan) in addition to two small chemical molecules of 0.5 μM A-83–01 (Wako Pure Chemical, Osaka, Japan), 3 μM CHIR99021 (A10199, AdooQ BioScience, Irvine, CA, United States) and 10% FBS, which would be called FAC medium. The culture medium was changed 1 day after seeding and every two/3 days thereafter. It takes 14–16 days to generate hCLiPs at up to 90% confluence from CHHs.

2.2 Removal of fibroblasts and subculture of hCLiPs

The cultured cells reached ≥90% confluence and were treated with TrypLE Express (Life Technologies, Tokyo, Japan) for 15–20 min. The hCLiPs were expanded with an equivalent volume of preculture medium, and the cells were transferred to a 15 mL conical tube and centrifuged at 220 *g* for 5 min. The cell pellet was resuspended in 5 mL of culture medium, and the total number of cells and percent viability were determined using a hemocytometer. The isolated hCLiPs were seeded onto gelatin-coated culture plates (Asahi Techno Glass, Tokyo, Japan) at a density of 5.0×10^4 cells/cm^2 and incubated for 60 min. The cells in the medium were isolated and seeded onto collagen-coated plates at a density of 5.0×10^4 cells/cm^2 and incubated for 10 min. After 10 min, the cells were isolated and seeded onto collagen-coated plates at a density of 1.0×10^4 cells/cm^2. The cells seeded onto the third collagen-coated plates achieved an appreciable purity. This method was drived from the published patent [JP2020-162551 (P2020-162551A)].

2.3 Human BD formation from hCLiPs

BDs were differentiated and formed from hCLiPs as previously reported (Huang et al., 2021). Briefly, 1–2 days before collecting the hCLiP suspension, we used embryonic fibroblast feeder cells (MEFs) (Cat #PMEF-N, Merck Millipore, Billerica, MA United States) to form an MEF feeder layer by seeding $1–2 \times 10^5$ cells on collagen-coated 12-well plates (approximately 3×10^4 cells/cm^2) in DMEM containing 10% FBS. We plated the dissociated hCLiP suspension onto the MEF feeder layer at a density of $4–5 \times 10^5$ cells/well (1.2×10^5 cells/cm^2) in FAC medium for cell attachment for 1 day. Thereafter, we replaced the medium with BEC induction medium (BIM), which was mTeSR™1 Complete Kit (Catalog #85850, STEMCELL Technologies, Tokyo, Japan), including mTeSR™1 basal medium supplemented with TeSR™1 5X supplement, with the addition three small chemical molecules of 10 μM Y-27632, 0.5 μM A-83–01, 3 μM CHIR99021, hepatocyte growth factor (HGF, Sigma–Aldrich Japan, Tokyo, Japan) and EGF, every 2 days for 6 days, followed by BIM supplemented with 2% growth factor reduced Matrigel (Catlog 354230, Corning, Bedford, United States) for an additional 6–10 days, to facilitate the maturation of BECs and the formation of biliary structures.

2.4 Integrated BD structure to human hepatocytes

We plated CHHs onto three-dimensional BD at a density of 1×10^5 cells/12-well plate (2.5 × 104 cells/cm^2) for 1 day in hepatocyte-defined medium (Catlog 05449, Corning, Bedford, United States) supplemented with 10 μg/mL EGF and 10% FBS. We then replaced it with BIM supplemented with 2% Matrigel for another 2–4 days. The BD was automatically attached with hepatocytes with bile canaliculi to the biliary cells.

2.5 Gene expression analysis by quantitative reverse-transcription polymerase chain reaction (qRT–PCR)

Samples were cultured in dishes under various conditions, and mRNA was extracted using a spin column (NucleoSpin RNA II; Macherey-Nagel, Düren, Germany). Synthesis of cDNA was performed using a high-capacity cDNA reverse transcription kit (Applied Biosystems, Tokyo, Japan). Samples were then stored at −20°C until their analysis by polymerase chain reaction (PCR), which was performed using an Applied Biosystems StepOne Plus Real-time PCR System with TaqMan Gene Expression Assay Kits (Applied Biosystems, Tokyo, Japan) according to the manufacturer's instructions. Briefly, PCR mixtures contained 1 μL of cDNA, 1 μL of TaqMan Gene Expression Assay probe, 5 μL of TaqMan Fast Advanced Master Mix (both from Applied Biosystems), and 13 μL of nuclease-free water. All TaqMan gene primers are listed in Supplementary Table S1. The thermocycling conditions were 95°C for 20 s followed by 40 cycles of 95°C for 1 s and 60°C for 20 s. Expression levels were quantified using the comparative cycle time method. Cycle threshold (Ct) values were automatically determined by the Applied Biosystems StepOne Plus Real-Time PCR System, and fold changes in gene expression were calculated by the $2^{(-\Delta\Delta CT)}$ method. Expression levels were normalized to those of the housekeeping gene and internal control glyceraldehyde 3-phosphate dehydrogenase (GAPDH).

2.6 Immunofluorescence

Cultured cells were fixed with 4% paraformaldehyde in phosphate-buffered saline (PBS) (Wako Pure Chemical, Osaka, Japan) for 10 min. Fixed samples were then incubated in 0.1% Triton X-100 (Sigma–Aldrich, Tokyo, Japan) in PBS for 10 min and blocked in PBS containing 1% BSA for 1 h at room temperature. The cells were then incubated with primary antibodies diluted in PBS+1% BSA at 4°C overnight. After washing with PBS three times, they were incubated with appropriate secondary antibodies diluted in PBS+1% BSA for 2 h. All primary and secondary antibodies are listed in Supplementary Table S2. Nuclei were stained with 4′,6-diamidiono-2-phenylindole (DAPI) (DOJINDO, Kumamoto, Jaoan) for 30 min. They were washed for three times in PBS up to 30–60 min. Fluorescence and bright-field images were captured using a microscope (Ti-U and C-HGFI, Nikon, Tokyo, Japan).

2.7 Rhodamine 123 assay

The rhodamine 123 assay was performed. We incubated the cells with Hanks' balanced salt solution (HBSS) containing 100 μM rhodamine 123 (both from Sigma-Aldrich, Tokyo, Japan) for 30 min at 37°C and washed them with HBSS twice. To inhibit the transporter activity of multidrug-resistance protein 1 (Mdr1), we incubated the cells with 20 μM verapamil (Tokyo Chemical Industry Co., Ltd. Tokyo, Japan) at 37°C for 2 h before adding rhodamine 123. Fluorescence and bright-field images were captured using a microscope (Ti-U and C-HGFI, Nikon, Tokyo, Japan).

2.8 Definition of the biliary lumen by cell-tracking staining

Because of the functionality of the hCLiP-derived biliary-duct-like structures, they were able to metabolize a cell-tracking dye to ascertain the extent of the biliary lumen. Therefore, we used the sequential cell-tracking staining method to determine the tubular lumen in the induced biliary duct structures. Briefly, the induced

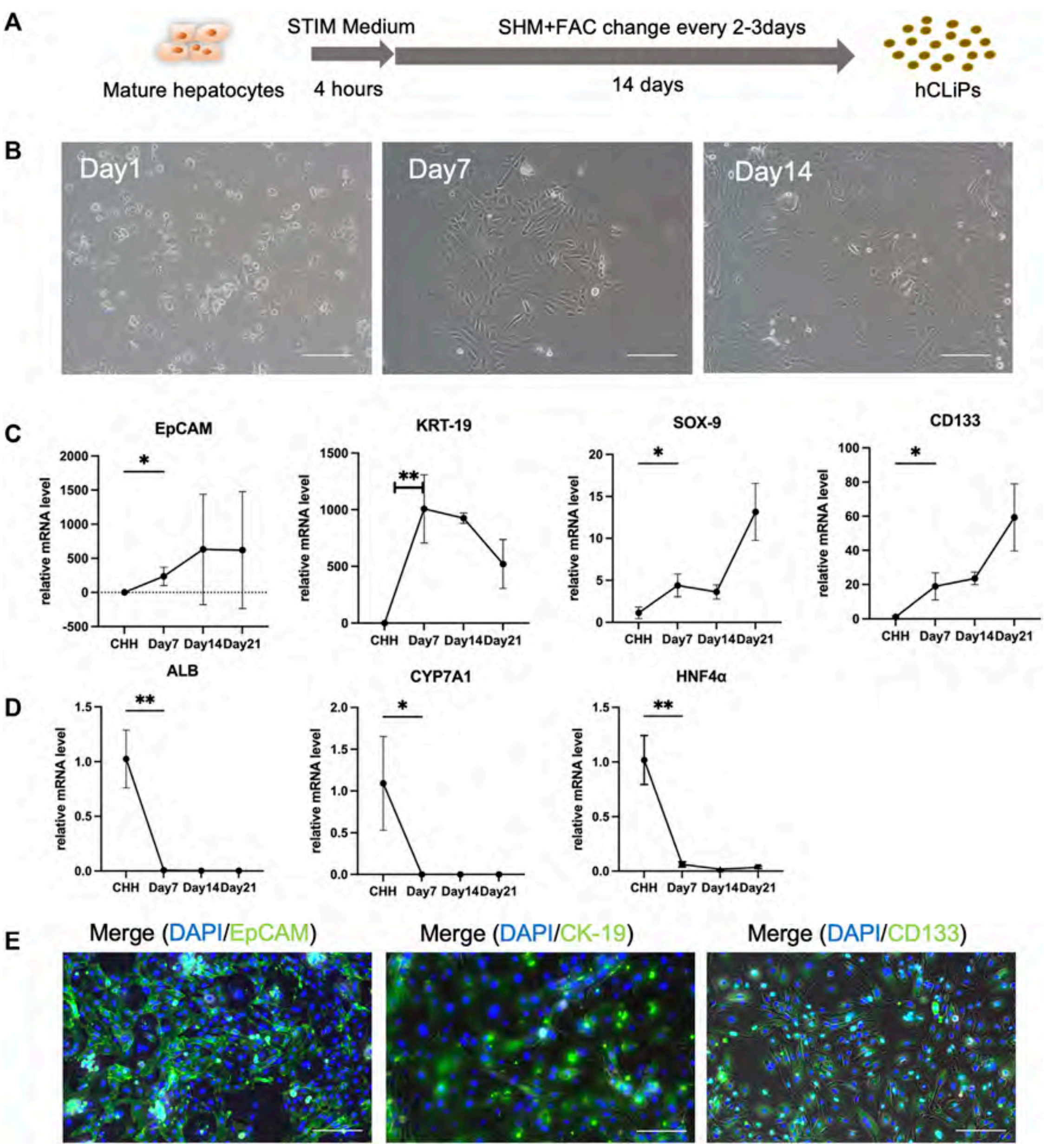

FIGURE 1
FAC medium converted human cryohepatocytes into hepatic progenitor cells. **(A)** FAC medium could induce human mature hepatocytes (MHs) into chemically induced liver progenitor cells (hCLiPs). **(B)** The morphology of the MHs gradually changed during 2 weeks of FAC culture. Scale bar = 100 μm. **(C, D)** RT-qPCR analysis showed that the hepatic progenitor cell (LPC)-related markers EpCAM, KRT-19, SOX-9, and CD133 gradually increased (*n* = 3–6), while the MH markers ALB, CYP7A1, and HNF-4α gradually decreased, which indicated that MHs were transferred to the hCLiP (*n* = 3–6). Data represent the mean values. Student's t-test, $*p < 0.05$, $**p < 0.01$. **(E)** Immunofluorescence staining of transformed cells was performed on day 14, and the cells expressed the LPC-related markers EpCAM, CK-19, and CD133. Scale bar = 200 μm.

biliary structures were incubated with 100 μM rhodamine 123 dye for 10 min at 37°C. Subsequently, the biliary-duct-like structures were cultured in BIM-2 medium (BIM-1 supplemented with 2% Matrigel) for 48 h, followed by incubation with 10 μM cell tracker orange (CTO, C34551; Invitrogen, Tokyo, Japan) dye for 10 min at 37°C. After washing twice with HBSS, images were captured using a microscope (Ti-U and C-HGFI, Nikon, Tokyo, Japan).

2.9 Cholyl-lysyl-fluorescein (CLF) dye assay

We loaded the cells with 1 μM CLF (Corning Life Sciences, Bedford, United States) for 30 min at 37°C and washed them twice with HBSS. We observed the cells and captured images using a confocal microscope. We replaced the cell medium with BIM medium to keep the cells alive for an extended period.

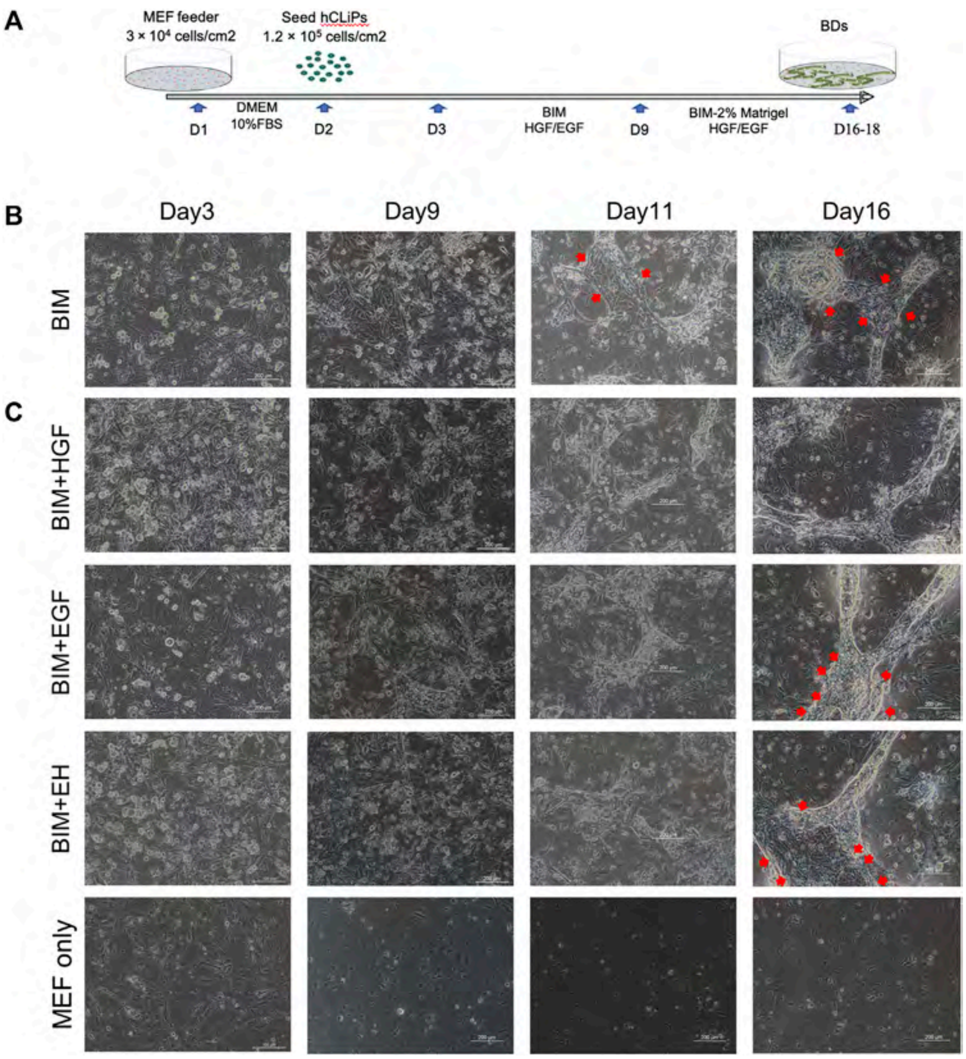

FIGURE 2
HGF promoted bile duct (BD) formation in three-dimensional culture. **(A)** Embryonic fibroblast feeder cells (MEFs) were used as a layer, and Matrigel was used to construct a three-dimensional culture environment as extracellular matrix (ECM) to induce the hCLiPs to create three-dimensional BDs in a two-step method. **(B)** The bile duct-induced medium (BIM) to induce BD from hCLiP was inefficient (the red arrow shows the untransformed cells). Scale bar = 200 μm. **(C)** In BIM, BIM + EGF, and BIM + EH, BDs were mixed with pieces of hCLiPs or transformed BECs, while BIM with HGF was more effective for forming BDs. Scale bar = 200 μm.

2.10 Statistical analysis

Statistical analyses were performed, and graphs were made using GraphPad Prism 8.0 (GraphPad Software Inc., San Diego, CA, United States). Data were analyzed by Student's t-test or a one-way ANOVA. Details of the statistical analyses and the associated values are described in the respective figure legends.

3 Results

3.1 FAC medium converted human cryo-hepatocytes into hepatic progenitor cells

The transformed cells, CHH, were utilized in the experiments and showed significant morphological changes after just 3 days of culture. Notably, the transformed cells displayed a higher capacity for proliferation compared to primary hepatocytes, achieving approximately 90% confluence within 14 days of culture (Figures 1A, B). Additionally, the proliferation of fibroblasts on the heterogeneous culture plate could be observed (Supplementary Figures S1A, B). The mRNAs of the transformed cells were extracted, and RT–qPCR was used to analyze the gene expression of the hepatocytes and LPCs. The results of Rt-qPCR confirmed that in transformed cells, the expression of LPC-related genes, including EpCAM, KRT-19, SOX-9, and CD133 (Figure 1C), and fibroblast-related genes, including ACTA2, TGF-β2 and MMP2, was gradually upregulated (Supplementary Figure S1C), while the relative gene expression of Alb, CYP7A1 and HNF4α in MHs was gradually downregulated (Figure 1D). Moreover, the transformed cells expressed the LPC protein markers EpCAM, CK-19 and CD133, while the heterogeneous cells expressed the α-SMA protein (Figure 1E; Supplementary Figure S1C). The data suggested that these transformed cells converted from CHH by a small molecule cocktail with FAC medium were LPCs.

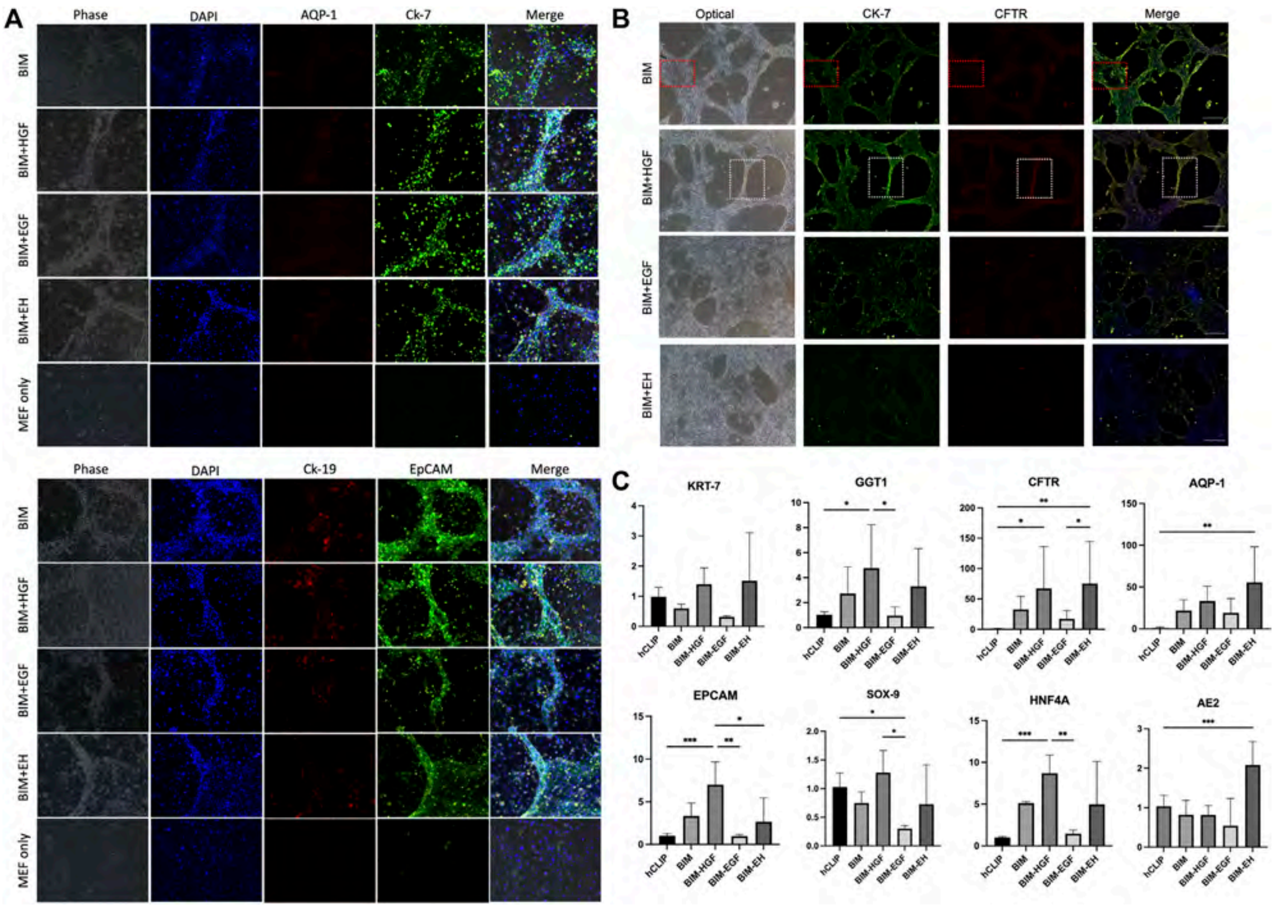

FIGURE 3
Bile duct-like structures expressed biliary markers. **(A)** The bile duct-related markers AQP-1, CK-7, CK-19, and EpCAM were expressed on all bile ducts. Scale bar = 200 μm.**(B)** The fluorescence intensity of bile duct-related markers CK-7, CFTR, and EpCAM appeared to differ in BIM with HGF, which is more pronounced in areas where bile ducts formed (the red box shows the negative zone, and the white box shows the high-intensity area). Scale bar = 500 μm. **(C)** RT-qPCR was used to assay the bile duct-associated genes KRT-7, GGT1, and CFTR and the progenitor cell-associated genes EPCAM, SOX9, and HNF4A and showed that BIM with HGF increased biliary genes and progenitor genes. ($n = 3–6$) Data represent the mean ± standard error of the mean. One-way ANOVA, $*p < 0.05$, $**p < 0.01$.

3.2 HGF promoted BD formation in three-dimensional culture

Three-dimensional BD formation was induced by a two-step method in a three-dimensional environment established with MEFs and Matrigel (Figure 2A). Since the direct use of BIM to induce BDs from hCLiPs was not efficient (Figure 2B), we introduced the growth factors HGF and EGF as supplements of BIM. (Tanimizu et al., 2007; Anzai et al., 2016; Kim et al., 2019). In heterogeneous cell culture dishes that induce hepatic progenitor cells, it is imperative to remove a large number of mixed fibrotic cells (Singh et al., 2013). It has been previously reported that many fibrotic cells produced during the induction of MHs are isolated using different culture medium (Miyoshi et al., 2022). When using hCLiPs to generate BDs, fibroblasts affect the formation of BD due to the rapid proliferation of fibroblasts (Supplementary Figure S2A), and the hCLiPs were enriched in purity without damage by multiple subcultures (Supplementary Figure S3A–C). BIM with HGF or EGF could generate BDs in 3D culture earlier (Day 11) in comparison to BIM alone. BIM with HGF was more effective in inducing the transformation of hCLiPs into BECs and the formation of BD tubular structures. In BIM, BIM with EGF, BIM with EH, BD were mixed with pieces of hCLiPs or transformed BECs (Figure 2C).

All four groups were subjected to immunofluorescence microscopy to determine whether the induced biliary-like structure was the BD structure. AQP-1, CK-7, CK-19, and EpCAM (BD-related markers) were expressed on all BDs (Figure 3A), but the fluorescence intensity of CK-7, CFTR, and EpCAM appeared to differ. This was more pronounced in areas where BDs formed (Figure 3B; Supplementary Figures S4). As described above, BD-associated proteins are more pronounced in regions of BD-like formation, and the condition of 3D culture supply with HGF is more helpful in inducing hCLiPs to form 3D BDs. This was also confirmed by RT–qPCR results for BD-associated genes (KRT-7, GGT1, and CFTR) and progenitor cell-associated genes (EPCAM, SOX9, and HNF4A) (Figure 3C).

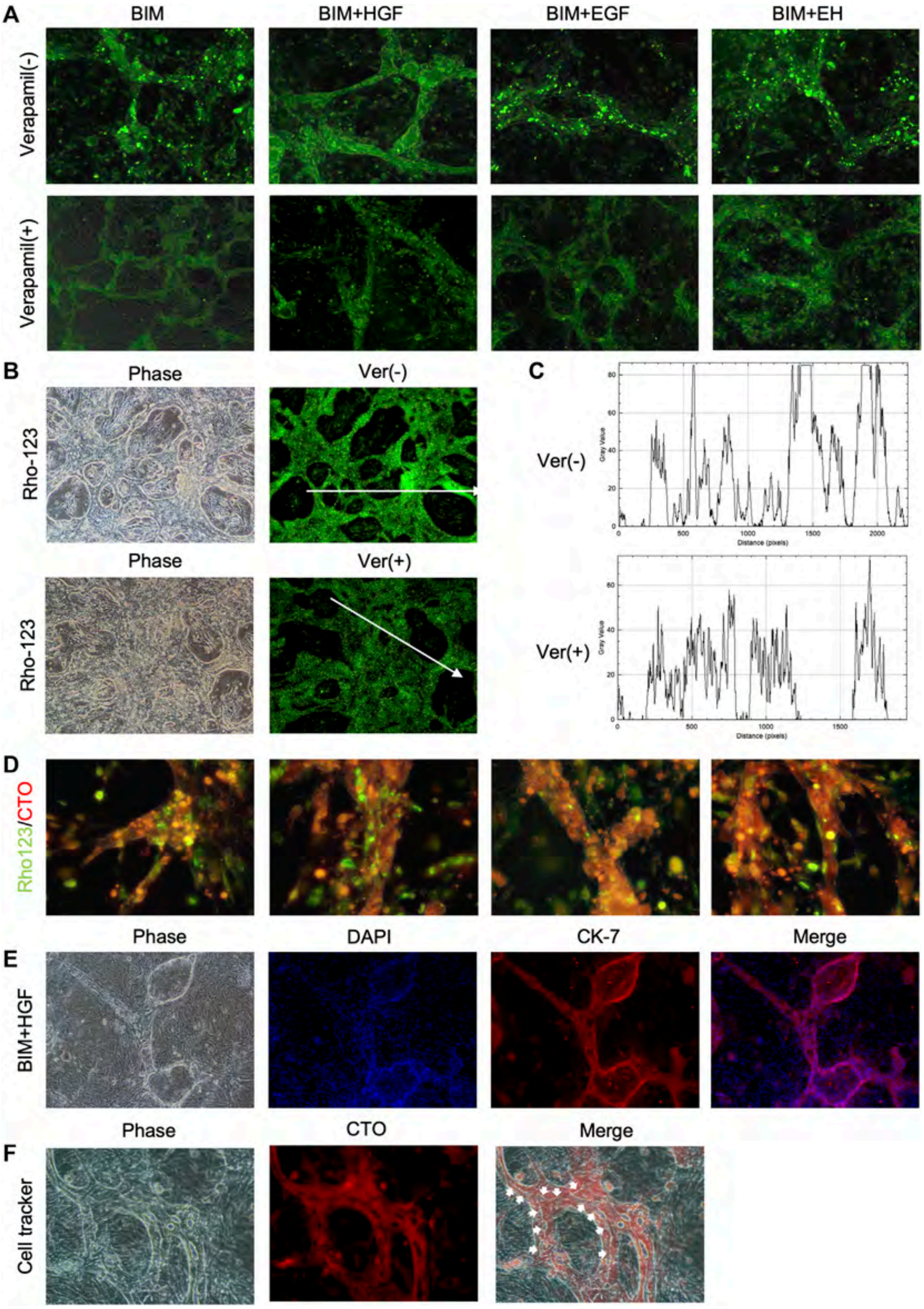

FIGURE 4
The function of the bile duct structure induced by hCLiPs resembles the biliary function. **(A)** Rhodamine-123 was transported into the BEC and accumulated in the lumen of the biliary duct structures. This could be inhibited by the MDR-1 inhibitor verapamil. **(B, C)** Rhodamine-123 was transported into the BEC and accumulated in the lumen of the biliary duct structures in BIM + HGF group, fluorescence intensity along the line was evaluated by ImageJ. **(D)** To further illustrate the presence of lumen in the bile ducts, after 24 h of staining Rhodamine-123, the dye was taken up by bile duct cells for 30 min using a cell tracker orange. **(E, F)** In the BIM + HGF group, CK-7 showed the structure of the bile duct, and cell-tracker staining analysis (30 min) of the bile duct in the BIM + HGF group showed the lumen in the bile duct.

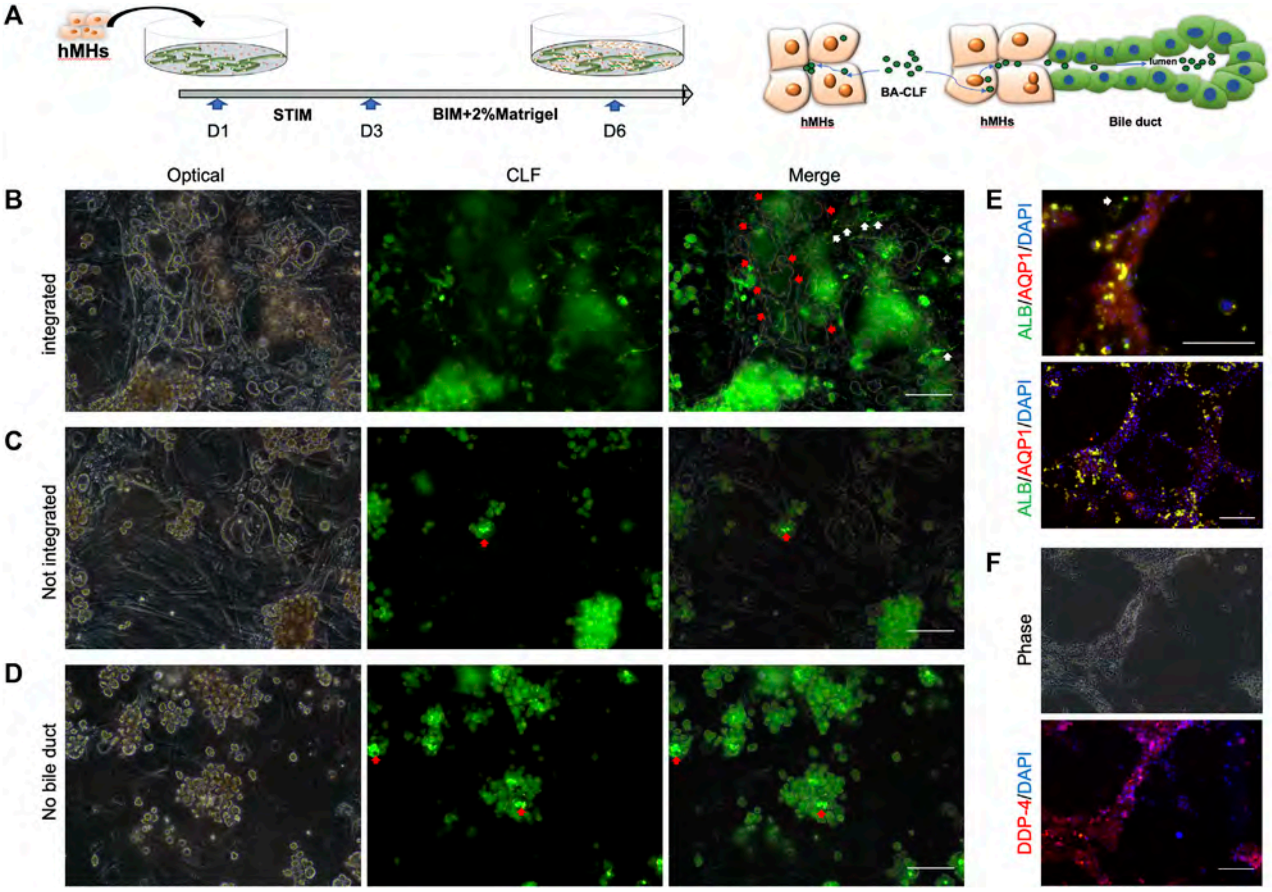

FIGURE 5
The human bile duct structure is integrated with hepatocytes. **(A)** In the bile duct structures combined with MHs, CLF could accumulate in the lumen from the culture medium through the MHs. Scale bar = 100 μm. **(B, C)** In hepatocytes that were not incorporated into a bile duct or in only MEF conditions, the CLF accumulated in the bile canaliculi formed by the hepatocytes. Scale bar = 100 μm. **(D, E, F)** The immunofluorescence results showed that the integrated MHs expressed albumin (ALB), a marker of mature hepatocytes, dipeptidyl peptidase-4 (DPP-4), a marker protein of the bile canaliculi, and the transporter AQP-1. In contrast, MHs unconnected to the bile duct structures expressed only ALB (the white narrow shows the unintegrated hepatocytes). Scale bar = 200 μm.

3.3 The functionality of the BD structure induced by hCLiPs resembled the biliary function

The functionality of the BD structure was assessed by determining multidrug resistance protein-1 (MDR1) activity, which was evaluated by the ability to transfer rhodamine-123 into the lumen. Rhodamine-123 was transported into the BECs and then accumulated in the lumen of the BD (Figure 4A). In contrast, as the MDR-1 transporter inhibitor, verapamil prevented rhodamine-123 from accumulating in the lumen of the BD, confirming the functional MDR-1 transport activity in the BD (Figure 4A). The bile duct uptake of rhodamine-123 in BIM + HGF group was further examined, and the bile duct uptake of rhodamine-123 could be inhibited by verapamil (Figures 4B, C). To further illustrate the presence of lumen in the BD, after 24 h of staining with rhodamine-123, the dye was taken up by BECs for 30 min using a cell-tracker, and BIM + HGF could be seen to have a more pronounced cavity when viewed under a fluorescence microscope (Figure 4D). In the BIM + HGF group, CK-7 showed the structure of the bile duct with cysts, and 30 min cell-tracker orange staining analysis in the BIM + HGF group showed the lumen in the bile duct in the BIM + HGF group (Figures 4E, F). These results suggested that BIM supplied with HGF could induce the formation of a functional BD with a lumen from hCLiPs.

3.4 The human BD structure is integrated with hepatocytes

The intrahepatic BD forms a complex three-dimensional network configured by cholangiocytes. The BD is responsible for bile acid collection and transplantation from the bile canaliculi among hepatocytes in the *in vivo* hepatic system. To investigate whether the BD structure induced by hCLiPs could collect bile acid from bile canaliculi and hepatocytes, we seeded human hepatocytes into the BD system generated from hCLiPs for 1 day in STIM and 3 days in BIM with HGF, which allowed hepatocytes to integrate into the BD (Figure 5A). Cholyl-l-Lysyl-Fluorescein (CLF) is a fluorescent bile salt derivative that is being developed as an agent for determining the *in vivo* liver function and *in vitro* hepatocyte function (Milkiewicz et al., 2000; de Waart et al., 2010; Huang et al., 2021). BD integrated with hepatocyte tissue could accumulate CLF in the lumen of the BD (Figure 5B). In contrast, the hepatocytes, which did not incorporate BD, accumulated CLF in the bile canaliculi formed by the hepatocytes (Figure 5C). The accumulation of CLF in the bile canaliculi of hepatocytes under MEF-only conditions also confirmed this finding (Figure 5D). Subsequently, immunofluorescence staining of BD-integrated MHs was performed, and the results showed that these MHs expressed albumin (ALB), dipeptidyl peptidase-4 (DPP-4), a marker protein of the bile canaliculi, and the transporter AQP-1 (Figures 5E, F). In contrast, MHs unconnected to the BD expressed only ALB (Figure 5E). The above results showed that the BD integrated the hMH and was able to transport the CLF from the MHs into the BD lumen.

4 Discussion

A combination of small molecules could convert MHs into LPCs, which had an unlimited self-renewal capacity and could be induced to differentiate into both MHs and BECs (Katsuda et al., 2017; Katsuda et al., 2019; Kim et al., 2019). In this study, we present a novel *in vitro* three-dimensional BD formed by hCLiPs induced from hMHs, which could combine with hMHs as an integrated tissue with the complete biliary function of the accumulation of the bile analog. This tissue represents a model of the human hepatic organoid that is close to the condition *in vivo*. These results demonstrate the functional properties of BECs and the physiological nature of bile transport in the liver, providing a valuable tool for the study of bile transport and metabolism and related diseases. In addition, this tissue-engineered model holds promise for the development of *in vitro* disease models and drug screening.

Previous studies have explored the use of human BECs *in vitro*; however, their practical application has been limited by a number of factors. The low proportion of BECs in the liver, difficulties in isolation, scarcity of donors, and ethical concerns have all hindered the direct utilization of BECs (Katayanagi et al., 1998; Chen et al., 2018; Huang et al., 2020). The use of small molecules to induce mature cell dedifferentiation has gained increased attention in recent times. Small molecule cocktails do not alter the genetic sequence of the cell, which is different from iPSCs, but instead manipulates the cell fate through alterations in the cell's epigenetics, offering a straightforward and highly controllable approach (Knyazer et al., 2021; Guan et al., 2022; Hou et al., 2022; Pan et al., 2022). For instance, the three-dimensional BD generated from hCLiPs demonstrated *in vitro* properties that resembled those of intrahepatic BDs, including the transport of the bile analogs CLF and rhodamine-123. Ramli et al. demonstrated the generation of a human hepatic organoid from iPSCs, in which the cells underwent progressive differentiation into hepatocytes and cholangiocytes within approximately 50 days of culture (Ramli et al., 2020).

When isolating mature hepatocytes by two-step perfusion using collagenase, fibrous cells, BD cells and other nonparenchymal cells are always mixed because of the heterogeneity of liver cells (Zhang et al., 2016; Aizarani et al., 2019). Induction cultures are often heterogeneous because of the presence of undifferentiated derivatives and nonparenchymal cells, thereby introducing variability, potential immunogenicity, and problems in directed differentiation (Singh et al., 2013; Miyoshi et al., 2022). When FAC medium induced hepatocyte dedifferentiation, fibroblast cells with strong growth ability grew on P0, gained a growth advantage during the passage process and interfered with the proliferation of hCLiPs after passaging, as shown in the supplemental data. When BDs were induced with hCLiPs without the removal of fibroblasts, the growth of BDs was inhibited by the massive proliferation of fibroblasts during induction. The fibroblast cells from FAC culture caused a high background and limited the growth space. In heterogeneous cell culture dishes that induce hepatic progenitor cells, it is particularly important to remove a large number of mixed fibrotic cells (Singh et al., 2013). The properties of stem cells themselves, which differ in their adhesion to different extracellular matrices, are generally weaker than those of fibrotic cells that are capable of secreting collagen (Wang et al., 2016; Aizarani et al., 2019). Stem cells do not inherently attach to the general surface, and there must be some functionalized surface to facilitate adhesion (Lam and Longaker, 2012). It has been previously reported that a large number of fibrotic cells produced during hepatoprostocyte induction are isolated using different culture media (Miyoshi et al., 2022). It seems feasible to select an appropriate adhesion surface for the separation of different cells, especially stem cells and fibrotic cells with large differences in adhesion ability (Wang et al., 2016). The collagen-coated dish can provide a proper adhesion surface for hCLiPs, but for the gelatin-coated dish, its adhesion ability is significantly weaker than that of ordinary fibroblasts, at least in the adhesion time (Miyoshi et al., 2022). After the one-time fibroblast cell removal procedure, the cells in the final collagen-coated dish were mainly EpCAM-positive cells, with only a small number of Desmin-positive cells. The cells in the gelatin dish were almost all Desmin-positive cells, with few EpCAM-positive cells.

When we attempted to use BIM, which was successfully used for rat BD formation in other studies, to induce directed differentiation of hCLiPs into BECs and subsequently construct three-dimensional BD with medium supplemented with Matrigel, the efficiency of BIM was found to be low (Figure 3) (Huang et al., 2021). The growth factors HGF and EGF were introduced into BIM to improve this situation. Other studies have confirmed that these growth factors promote the induction of three-dimensional BD, especially HGF, which can induce the tubular formation of BDs (Tanimizu et al., 2007; Anzai et al., 2016; Tian et al., 2016; Kim et al., 2019). Dong et al. summarized that the components of liver organoids, including R-spondin-1, forskolin, Wnt, EGF, fibroblast growth factor (FGF), HGF, and TGF-β inhibitors, promote the differentiation of LPCs into BECs. Tanimizu et al. demonstrated that PI3K activated by EGF in combination with HGF promoted proliferation during cyst morphogenesis, and tubular or cyst formation depended on the percentage of Matrigel in the total gel volume. According to some studies, hepatocyte growth factor (HGF) can promote the tube formation of endothelial cells and ductal structure formation of BD cells in three-dimensional culture conditions (Saiki et al., 2006; Tian et al., 2016). HGF can also stimulate the proliferation and differentiation of hepatocytes and induce the formation of hepatocyte-derived biliary epithelium *in vitro* (Limaye et al., 2008; Rose et al., 2021; Tanimizu et al., 2021). The biological responses of scatter, growth, and branching morphogenesis mediated by the HGF receptor are triggered by tyrosine phosphorylation of a single multifunctional docking site located in the carboxy-terminal tail of the receptor (Ponzetto et al., 1994; Boccaccio et al., 1998). The study demonstrated that the HGF receptor binds and phosphorylates Stat-3 and that the ensuing nuclear signaling is required to trigger differentiation for branching morphogenesis (Boccaccio et al., 1998). While HGF, EGF, and the combination of the two induce the transdifferentiation of hepatocytes to BECs, hepatocyte-to-BEC transdifferentiation is regulated by HGF and EGF receptors, and PI3 kinase–mediated signaling independent of AKT is a crucial component of the transdifferentiation process (Limaye et al., 2008). The activation of HGF-Met signaling induces diverse morphogenetic responses, including the formation of branching tubules, cell scattering, and invasion (Birchmeier et al., 2003; Christensen et al., 2005). Therefore, HGF may have a positive effect on BD formation *in vitro* and in three-dimensional culture. Moreover, the LPCs developed cysts with the central lumen in 40% Matrigel, and a lower percentage of Matrigel would form tubular structures (Tanimizu et al., 2007). Tian et al. reported that they had efficiently and controllably generated two-dimensional and three-dimensional BD from iPSC-derived spheroids. The three-dimensional BD structures were formed under control by HGF and EGF in a three-dimensional ECM constructed by Matrigel (Tian et al., 2016). Based on these findings, we compared the efficiency of HGF, EGF, and the combination of the two, and they could promote formation during tubular morphogenesis, but HGF only seemed more efficient. In another similar hCLiPs, Kim et al. reported that hCLiPs formed a tube-like branching morphology using BEC differentiation medium consisting of DMEM/F12 medium containing 10% FBS and 20 ng/mL HGF in a three-dimensional culture constructed with collagen gel (Kim et al., 2019). Indeed, the growth factors used in different culture systems and stem cells are different. Nevertheless, it is undeniable that EGF and HGF are culture components that can be considered to form tubular BD.

Bile is secreted from hepatocytes, extracted into bile canaliculi formed by hepatocytes and subsequently delivered to the intrahepatic BDs, where it is modified by BECs. The BECs form the intrahepatic BD and extrahepatic BD, which complete the modification, secretion, transportation, accumulation, and discharge of bile (Reshetnyak, 2013). Huang et al. and Katsuda et al. demonstrated that they generated rat BD or integrated tubule-hepatocyte tissues *in vitro* that could transport CLF, rhodamine 123 or fluorescein diacetate (Katsuda et al., 2017; Huang et al., 2021). This is the first reported instance of a tissue connection between the human tubular BD and hepatocytes and presents an excellent opportunity to develop an organoid model for studying diseases related to human biliary hepatocytes. *In vitro*, the functionality of the BD was assessed by determining MDR1 activity, which was evaluated by the ability to transfer rhodamine-123 into the lumen. The BD could collect rhodamine-123 in the BECs, which could accumulate in the lumen, and this could be inhibited by verapamil. Additionally, the P-gp transport function was evaluated by the active transport of rhodamine 123, and verapamil was also an inhibitor of the P-gp function (Wang et al., 2022). Milkiewicz et al. demonstrated that the transportation of CLF is mediated by ATP binding cassette subfamily C members 2 and 3 (ABCC2, 3), which encode canalicular multispecific organic anion transporters 2 and 3 (MRP2/3) (Milkiewicz et al., 2000). The bile canaliculi formed by the MHs without connecting BDs were also observed collecting CLF, while it was reported that this phenomenon was not observed in either the BEC monolayer or the BD without hepatocytes (Huang et al., 2021). Therefore, we speculated that the bile canalicular formed by the MHs formed a connection with BD and had the ability to transport the bile analog CLF. Subsequent immunofluorescence experiments also confirmed the presence of AQP-1 and DPP-4 proteins between the MHs and the BD, which are also bile transportation-related proteins. In conclusion, the connection of the MHs to the BD provided a microstructural basis for the excretion of bile.

Overall, this study provides a promising avenue for establishing a novel *in vitro* system that combines hMHs and BD using HGF and Matrigel. The functional BD, generated from the hCLiPs, displayed characteristics of BDs and were able to accumulate a bile analog, demonstrating their biliary function. By coculturing and connecting hMHs and functional BD, researchers can study various physiological and pathophysiological conditions and evaluate drug responses. The future study of the establishment of disease models from this model could provide a valuable tool for drug development and understanding disease mechanisms.

Data availability statement

The original contributions presented in the study are included in the article/Supplementary Material, further inquiries can be directed to the corresponding author.

Ethics statement

Ethical approval was not required for the studies on humans in accordance with the local legislation and institutional requirements because only commercially available established cell lines were used. Ethical approval was not required for the studies on animals in accordance with the local legislation and institutional requirements because only commercially available established cell lines were used.

Author contributions

PL designed the research study, performed experiments and data interpretation, and wrote the manuscript. DM and YH contributed to the data analysis. SE gave final approval of the manuscript. All authors contributed to the article and approved the submitted version.

Funding

This study was supported in part by the Japan China Sasakawa Medical Fellowship. This study was supported in part by the Grant-in-Aid for Scientific Research (21K08598).

Conflict of interest

The authors declare that the research was conducted in the absence of any commercial or financial relationships that could be construed as a potential conflict of interest.

Publisher's note

Supplementary material

The Supplementary Material for this article can be found online at: https://www.frontiersin.org/articles/10.3389/fbioe.2023.1249769/full#supplementary-material

SUPPLEMENTARY FIGURE S1

It was necessary to remove the fibroblast cells mixed with the hCLiPs. **(A)** The fibroblast cells would increase during the induction of hCLiPs by FAC medium. Scale bar = 500 μm. **(B)** If the fibroblast cells mixed in the culture dish were not removed, the fibroblast cells with rapid proliferation ability would overgrow in the culture dish after passaging. **(C)** Fibroblast-related genes, including ACTA2, TGF- β 2, and MMP2, were gradually upregulated during induction. (n = 3–6) Data represent the mean ± standard error of the mean. One-way ANOVA, $*p < 0.01$. **(D)** Heterogeneous cells expressed the EpCAM and α-SMA proteins. Scale bar = 200 μm.

SUPPLEMENTARY FIGURE S2

The fibroblast cells proliferated rapidly in a 3D culture environment, making it difficult to form or fragment 3D bile ducts. Scale bar = 500 μm.

SUPPLEMENTARY FIGURE S3

The hCLiPs were enriched in purity without damage by multiple subcultures. **(A)** Multiple subcultures were utilized to remove mixed fibroblast cells in the suspension of hCLiP. **(B)** Immunofluorescence staining of collagen dish-2 and a gelatin dish on day 8. Conversely to the gelatin dishes, fewer Desmin-positive cells were observed in Collagen dish-2 and most cells were EpCAM-positive. **(C)** RT-qPCR results showed that the fibrosis related genes ACTA2, TGF-β2, and MMP2 were more highly expressed in the fiber cells of the gelatin dishes than in the hCLiPs of collagen dish-2, while the LPC marker genes EpCAM, SOX-9, and CD133 were more highly expressed in the hCLiPs. Data represent the mean ± standard error of the mean. Student's t test, $*p < 0.05$,$*p < 0.01$.

SUPPLEMENTARY FIGURE S4

The immunofluorescence results showed that the EpCAM protein was expressed in the area of bile duct formation, while the EpCAM protein expression was lower in cells that failed to form tubular structures in the BIM+EGF and BIM+EH groups.

References

Aizarani, N., Saviano, A., Sagar, Mailly, L., Durand, S., Herman, J. S., et al. (2019). A human liver cell atlas reveals heterogeneity and epithelial progenitors. *Nature* 572, 199–204. doi:10.1038/s41586-019-1373-2

Alpini, G., McGill, J. M., and LaRusso, N. F. (2002). The pathobiology of biliary epithelia. *Hepatology* 35, 1256–1268. doi:10.1053/jhep.2002.33541

Anzai, K., Chikada, H., Tsuruya, K., Ida, K., Kagawa, T., Inagaki, Y., et al. (2016). Foetal hepatic progenitor cells assume a cholangiocytic cell phenotype during two-dimensional pre-culture. *Sci. Rep.* 6, 28283. doi:10.1038/srep28283

Birchmeier, C., Birchmeier, W., Gherardi, E., and Vande Woude, G. F. (2003). Met, metastasis, motility and more. *Nat. Rev. Mol. Cell. Biol.* 4, 915–925. doi:10.1038/nrm1261

Boccaccio, C., Andò, M., Tamagnone, L., Bardelli, A., Michieli, P., Battistini, C., et al. (1998). Induction of epithelial tubules by growth factor HGF depends on the STAT pathway. *Nature* 391, 285–288. doi:10.1038/34657

Buisson, E. M., Jeong, J., Kim, H. J., and Choi, D. (2019). Regenerative medicine of the bile duct: beyond the myth. *Int. J. Stem Cells* 12, 183–194. doi:10.15283/ijsc18055

Cao, W., Chen, K., Bolkestein, M., Yin, Y., Verstegen, M. M., Bijvelds, M. J., et al. (2017). Dynamics of proliferative and quiescent stem cells in liver homeostasis and injury. *Gastroenterology* 153, 1133–1147. doi:10.1053/j.gastro.2017.07.006

Carberry, C. K., Ferguson, S. S., Beltran, A. S., Fry, R. C., and Rager, J. E. (2022). Using liver models generated from human-induced pluripotent stem cells (iPSCs) for evaluating chemical-induced modifications and disease across liver developmental stages. *Toxicol Vitro* 83, 105412. doi:10.1016/j.tiv.2022.105412

Chen, C., Jochems, P. G. M., Salz, L., Schneeberger, K., Penning, L. C., van de Graaf, S. F. J., et al. (2018). Bioengineered bile ducts recapitulate key cholangiocyte functions. *Biofabrication* 10, 034103. doi:10.1088/1758-5090/aac8fd

Christensen, J. G., Burrows, J., and Salgia, R. (2005). c-Met as a target for human cancer and characterization of inhibitors for therapeutic intervention. *Cancer Lett.* 225, 1–26. doi:10.1016/j.canlet.2004.09.044

de Waart, D. R., Häusler, S., Vlaming, M. L., Kunne, C., Hänggi, E., Gruss, H. J., et al. (2010). Hepatic transport mechanisms of cholyl-L-lysyl-fluorescein. *J. Pharmacol. Exp. Ther.* 334, 78–86. doi:10.1124/jpet.110.166991

Guan, J., Wang, G., Wang, J., Zhang, Z., Fu, Y., Cheng, L., et al. (2022). Chemical reprogramming of human somatic cells to pluripotent stem cells. *Nature* 605, 325–331. doi:10.1038/s41586-022-04593-5

Hou, X., Ma, S., Fan, W., Li, F., Xu, M., Yang, C., et al. (2022). Chemically defined and small molecules-based generation of sinoatrial node-like cells. *Stem Cell. Res. Ther.* 13, 158. doi:10.1186/s13287-022-02834-y

Huang, Y., Sakai, Y., Hara, T., Katsuda, T., Ochiya, T., Gu, W., et al. (2021). Bioengineering of a CLiP-derived tubular biliary-duct-like structure for bile transport *in vitro*. *Biotechnol. Bioeng.* 118, 2572–2584. doi:10.1002/bit.27773

Huang, Y., Sakai, Y., Hara, T., Katsuda, T., Ochiya, T., Gu, W. L., et al. (2020). Differentiation of chemically induced liver progenitor cells to cholangiocytes: investigation of the optimal conditions. *J. Biosci. Bioeng.* 130, 545–552. doi:10.1016/j.jbiosc.2020.07.009

Katayanagi, K., Kono, N., and Nakanuma, Y. (1998). Isolation, culture and characterization of biliary epithelial cells from different anatomical levels of the intrahepatic and extrahepatic biliary tree from a mouse. *Liver* 18, 90–98. doi:10.1111/j.1600-0676.1998.tb00133.x

Katsuda, T., Kawamata, M., Hagiwara, K., Takahashi, R. u., Yamamoto, Y., Camargo, F. D., et al. (2017). Conversion of terminally committed hepatocytes to culturable bipotent progenitor cells with regenerative capacity. *Cell. Stem Cell.* 20, 41–55. doi:10.1016/j.stem.2016.10.007

Katsuda, T., Matsuzaki, J., Yamaguchi, T., Yamada, Y., Prieto-Vila, M., Hosaka, K., et al. (2019). Generation of human hepatic progenitor cells with regenerative and metabolic capacities from primary hepatocytes. *Elife* 8, e47313. doi:10.7554/eLife.47313

Kim, H., Im, I., Jeon, J. S., Kang, E. H., Lee, H. A., Jo, S., et al. (2022). Development of human pluripotent stem cell-derived hepatic organoids as an alternative model for drug safety assessment. *Biomaterials* 286, 121575. doi:10.1016/j.biomaterials.2022.121575

Kim, Y., Kang, K., Lee, S. B., Seo, D., Yoon, S., Kim, S. J., et al. (2019). Small molecule-mediated reprogramming of human hepatocytes into bipotent progenitor cells. *J. Hepatol.* 70, 97–107. doi:10.1016/j.jhep.2018.09.007

Knyazer, A., Bunu, G., Toren, D., Mracica, T. B., Segev, Y., Wolfson, M., et al. (2021). Small molecules for cell reprogramming: a systems biology analysis. *Aging (Albany NY)* 13, 25739–25762. doi:10.18632/aging.203791

Lam, M. T., and Longaker, M. T. (2012). Comparison of several attachment methods for human iPS, embryonic and adipose-derived stem cells for tissue engineering. *J. Tissue Eng. Regen. Med.* 6 (Suppl. 3), s80–s86. doi:10.1002/term.1499

Lazaridis, K. N., and LaRusso, N. F. (2015). The cholangiopathies. *Mayo Clin. Proc.* 90, 791–800. doi:10.1016/j.mayocp.2015.03.017

Li, M., Gong, J., Gao, L., Zou, T., Kang, J., and Xu, H. (2022). Advanced human developmental toxicity and teratogenicity assessment using human organoid models. *Ecotoxicol. Environ. Saf.* 235, 113429. doi:10.1016/j.ecoenv.2022.113429

Limaye, P. B., Bowen, W. C., Orr, A. V., Luo, J., Tseng, G. C., and Michalopoulos, G. K. (2008). Mechanisms of hepatocyte growth factor–mediated and epidermal growth factor–mediated signaling in transdifferentiation of rat hepatocytes to biliary epithelium. *Hepatology* 47, 1702–1713. doi:10.1002/hep.22221

Milkiewicz, P., Saksena, S., Cardenas, T., Mills, C. O., and Elias, E. (2000). Plasma elimination of cholyl-lysyl-fluorescein (CLF): a pilot study in patients with liver cirrhosis. *Liver* 20, 330–334. doi:10.1034/j.1600-0676.2000.020004330.x

Miyoshi, T., Hidaka, M., Miyamoto, D., Sakai, Y., Murakami, S., Huang, Y., et al. (2022). Successful induction of human chemically induced liver progenitors with small molecules from damaged liver. *J. Gastroenterol.* 57, 441–452. doi:10.1007/s00535-022-01869-5

O'Hara, S. P., Tabibian, J. H., Splinter, P. L., and LaRusso, N. F. (2013). The dynamic biliary epithelia: molecules, pathways, and disease. *J. Hepatol.* 58, 575–582. doi:10.1016/j.jhep.2012.10.011

Olgasi, C., Cucci, A., and Follenzi, A. (2020). iPSC-derived liver organoids: a journey from drug screening, to disease modeling, arriving to regenerative medicine. *Int. J. Mol. Sci.* 21, 6215. doi:10.3390/ijms21176215

Pan, T., Wang, N., Zhang, J., Yang, F., Chen, Y., Zhuang, Y., et al. (2022). Efficiently generate functional hepatic cells from human pluripotent stem cells by complete small-molecule strategy. *Stem Cell. Res. Ther.* 13, 159. doi:10.1186/s13287-022-02831-1

Park, Y., Thadasina, D., Bolujo, I., Isidan, A., Cross-Najafi, A. A., Lopez, K., et al. (2022). Three-dimensional organoids as a model to study nonalcoholic fatty liver disease. *Semin. Liver Dis.* 42, 423–433. doi:10.1055/a-1934-5588

Ponzetto, C., Bardelli, A., Zhen, Z., Maina, F., dalla Zonca, P., Giordano, S., et al. (1994). A multifunctional docking site mediates signaling and transformation by the hepatocyte growth factor/scatter factor receptor family. *Cell.* 77, 261–271. doi:10.1016/0092-8674(94)90318-2

Ramli, M. N. B., Lim, Y. S., Koe, C. T., Demircioglu, D., Tng, W., Gonzales, K. A. U., et al. (2020). Human pluripotent stem cell-derived organoids as models of liver disease. *Gastroenterology* 159, 1471–1486.e12. doi:10.1053/j.gastro.2020.06.010

Reshetnyak, V. I. (2013). Physiological and molecular biochemical mechanisms of bile formation. *World J. Gastroenterol.* 19, 7341–7360. doi:10.3748/wjg.v19.i42.7341

Roos, F. J. M., van Tienderen, G. S., Wu, H., Bordeu, I., Vinke, D., Albarinos, L. M., et al. (2022). Human branching cholangiocyte organoids recapitulate functional bile duct formation. *Cell. Stem Cell.* 29, 776–794.e13. doi:10.1016/j.stem.2022.04.011

Rose, S., Ezan, F., Cuvellier, M., Bruyère, A., Legagneux, V., Langouët, S., et al. (2021). Generation of proliferating human adult hepatocytes using optimized 3D culture conditions. *Sci. Rep.* 11, 515. doi:10.1038/s41598-020-80019-4

Saiki, A., Watanabe, F., Murano, T., Miyashita, Y., and Shirai, K. (2006). Hepatocyte growth factor secreted by cultured adipocytes promotes tube formation of vascular endothelial cells *in vitro*. *Int. J. Obes. (Lond)* 30, 1676–1684. doi:10.1038/sj.ijo.0803316

Sampaziotis, F., Muraro, D., Tysoe, O. C., Sawiak, S., Beach, T. E., Godfrey, E. M., et al. (2021). Cholangiocyte organoids can repair bile ducts after transplantation in the human liver. *Science* 371, 839–846. doi:10.1126/science.aaz6964

Sato, K., Zhang, W., Safarikia, S., Isidan, A., Chen, A. M., Li, P., et al. (2021). Organoids and spheroids as models for studying cholestatic liver injury and cholangiocarcinoma. *Hepatology* 74, 491–502. doi:10.1002/hep.31653

Si-Tayeb, K., Lemaigre, F. P., and Duncan, S. A. (2010). Organogenesis and development of the liver. *Dev. Cell.* 18, 175–189. doi:10.1016/j.devcel.2010.01.011

Singh, A., Suri, S., Lee, T., Chilton, J. M., Cooke, M. T., Chen, W., et al. (2013). Adhesion strength-based, label-free isolation of human pluripotent stem cells. *Nat. Methods* 10, 438–444. doi:10.1038/nmeth.2437

Strazzabosco, M., Fabris, L., and Spirli, C. (2005). Pathophysiology of cholangiopathies. *J. Clin. Gastroenterol.* 39, S90–S102. doi:10.1097/01.mcg.0000155549.29643.ad

Tanimizu, N., Ichinohe, N., Sasaki, Y., Itoh, T., Sudo, R., Yamaguchi, T., et al. (2021). Generation of functional liver organoids on combining hepatocytes and cholangiocytes with hepatobiliary connections *ex vivo*. *Nat. Commun.* 12, 3390. doi:10.1038/s41467-021-23575-1

Tanimizu, N., Miyajima, A., and Mostov, K. E. (2007). Liver progenitor cells develop cholangiocyte-type epithelial polarity in three-dimensional culture. *Mol. Biol. Cell.* 18, 1472–1479. doi:10.1091/mbc.e06-09-0848

Tanimizu, N., Nakamura, Y., Ichinohe, N., Mizuguchi, T., Hirata, K., and Mitaka, T. (2013). Hepatic biliary epithelial cells acquire epithelial integrity but lose plasticity to differentiate into hepatocytes *in vitro* during development. *J. Cell. Sci.* 126, 5239–5246. doi:10.1242/jcs.133082

Tian, L., Deshmukh, A., Ye, Z., and Jang, Y. Y. (2016). Efficient and controlled generation of 2D and 3D bile duct tissue from human pluripotent stem cell-derived spheroids. *Stem Cell. Rev. Rep.* 12, 500–508. doi:10.1007/s12015-016-9657-5

Velazquez, J. J., and Ebrahimkhani, M. R. (2021). Cholangiocyte organoids as a cell source for biliary repair. *Transpl. Int.* 34, 999–1001. doi:10.1111/tri.13902

Wang, X., Ni, C., Jiang, N., Wei, J., Liang, J., Zhao, B., et al. (2020). Generation of liver bipotential organoids with a small-molecule cocktail. *J. Mol. Cell. Biol.* 12, 618–629. doi:10.1093/jmcb/mjaa010

Wang, Y., Zhang, W., Yuan, J., and Shen, J. (2016). Differences in cytocompatibility between collagen, gelatin and keratin. *Mater Sci. Eng. C Mater Biol. Appl.* 59, 30–34. doi:10.1016/j.msec.2015.09.093

Wang, Z., Faria, J., van der Laan, L. J. W., Penning, L. C., Masereeuw, R., and Spee, B. (2022). Human cholangiocytes form a polarized and functional bile duct on hollow fiber membranes. *Front. Bioeng. Biotechnol.* 10, 868857. doi:10.3389/fbioe.2022.868857

Xu, X., Jiang, S., Gu, L., Li, B., Xu, F., Li, C., et al. (2022). High-throughput bioengineering of homogenous and functional human-induced pluripotent stem cells-derived liver organoids via micropatterning technique. *Front. Bioeng. Biotechnol.* 10, 937595. doi:10.3389/fbioe.2022.937595

Yan, J., Tai, Y., and Zhou, H. (2022). Culture of mouse liver ductal organoids. *Methods Mol. Biol.* 2455, 117–129. doi:10.1007/978-1-0716-2128-8_11

Zhang, C. Y., Yuan, W. G., He, P., Lei, J. H., and Wang, C. X. (2016). Liver fibrosis and hepatic stellate cells: etiology, pathological hallmarks and therapeutic targets. *World J. Gastroenterol.* 22, 10512–10522. doi:10.3748/wjg.v22.i48.10512

公益財団法人日中医学協会
ＴＥＬ　０３－５８２９－９１２３
ＦＡＸ　０３－３８６６－９０８０
E-MAIL iryo@jpcnma.or.jp
〒101-0032 東京都千代田区岩本町 1-4-3
住泉ＫＭビル６階
URL：https://www.jpcnma.or.jp/